Microscopic origin of the rheological and surface properties of embryonic cell aggregates

Tomita Vasilica Stirbat

Université Claude Bernard Lyon 1

UNIVERSITÉ DE LYON

N° d'ordre **171 - 2012**

Année 2012

THESE DE L'UNIVERSITE DE LYON

Délivrée par

L'UNIVERSITE CLAUDE BERNARD LYON 1

ECOLE DOCTORALE

ED 52 – PHAST (Physique et Astrophysique)

DIPLOME DE DOCTORAT

(arrêté du 7 août 2006)

soutenue publiquement le 28.09.2012

par

Mlle Tomita Vasilica STIRBAT

Microscopic origin of the rheological and surface properties of embryonic cell aggregates

Directeurs de thèse : Jean-Paul RIEU
Hélène DELANOE-AYARI

Jury : Françoise BROCHARD-WYART (Rapporteur)
Albrecht OTT (Rapporteur)
Sylvie DUFOUR (Examinatrice)
François GRANER (Examinateur)
Catherine BARENTIN (Invitée)

RESUME en français

Ces travaux de thèse portent sur l'étude expérimentale des propriétés physiques et de la biomécanique des agrégats cellulaires embryonnaires. Le but de cette thèse était d'une part de mieux comprendre l'origine biologique de la viscosité et de la tension de surface tissulaire, d'autre part d'étudier quantitativement en détail l'élasticité cellulaire par des nouvelles mesures de rhéologie en cisaillement.
Un premier chapitre concerne les mesures de tension de surface tissulaire par la méthode de compression et de viscosité tissulaire par analyse de la cinétique de fusion de deux agrégats en faisant varier comme paramètre principal la contractilité cellulaire que certains suspectent comme étant la principale origine biologique de ces paramètres. Nous utilisons le formalisme du DITH (Haris, 1976: Differential Interfacial Tension Hypothesis) pour interpréter les données.
Le deuxième chapitre concerne les mesures rhéologiques en cisaillement à l'aide d'un rhéomètre commercial plan-plan sur plusieurs centaines ou milliers d'agrégats cisaillés ensembles. Nous montrons que les cellules deviennent moins rigides pour une déformation minimale d'environ 4%, mais sur l'échelle de l'heure les cellules sont capables de se rigidifier à nouveau. Ces expériences sont analysées à l'aide d'un modèle de ressorts qui cassent sous contrainte puis se ressoudent à contrainte nulle.

TITRE en anglais

Microscopic origin of the rheological and surface properties of embryonic cell aggregates

RESUME en anglais

This thesis focuses on the experimental study of physical properties and biomechanics of embryonic cell aggregates. The aim of this thesis was on one hand to better understand the biological origin of tissue viscosity and tissue surface tension, and on the other hand to study quantitatively in detail cell elasticity by means of new rheological measurements in shear.
A first chapter deals with measurements of tissue surface tension by tissue compression method and tissue viscosity by analysis of the fusion kinetics of two aggregates. We vary key parameters such as cell contractility that some people suspect to be the main biological origin of these parameters. We use the formalism of DITH (Haris, 1976: Differential Interfacial Tension Hypothesis) to interpret the data.
The second chapter deals with rheological measurements in shear using a commercial plate-plate rheometer over several hundred of aggregates. We showed that cells become softer after a minimal deformation of 4% is reached, and can harden again on the timescale of hour. These experiences are analyzed using a model of springs that break under stress and then reattach at zero strain.

DISCIPLINE

Biophysics/Biophysique

MOTS-CLES en anglais et français

Cell aggregates, surface tension, viscosity, cell adhesion, cytoskeleton contractility, cell rearrangements, visco-elasto-plasticity, softening, yield stress.
Agrégats cellulaires, tension de surface, viscosité, adhésion cellulaire, contractilité du cytosquelette, réarrangements cellulaires, visco-élasto-plasticité, ramollissement, contrainte seuil.

INTITULE ET ADRESSE DE L'U.F.R. OU DU LABORATOIRE :

Laboratoire de Physique de la Matière Condensée et Nanostructures UMR 5586
Université Claude Bernard Lyon 1 et CNRS
43 boulevard du 11 novembre 1918
69622 Villeurbanne Cedex

Acknowledgments - Remerciements

Il y a beaucoup de personnes que je voudrais remercier pour leur aide et leur soutien au cours de ces trois années de thèse.

Tout d'abord, mes remerciements s'adressent aux membres du jury qui ont accepté de juger ce travail. Je remercie Françoise Brochard-Wyart et Albrecht Ott d'avoir accepté d'être mes rapporteurs ainsi que Sylvie Dufour et Catherine Barentin d'avoir bien voulu faire partie de mon jury. Un merci particulier à François Graner, qui m'a fait l'honneur de présider le jury et pour ses remarques toujours très intéressantes accompagnées d'un enthousiasme contagieux.

Je tiens à exprimer ma profonde et sincère gratitude à mes deux directeurs de thèse. Je remercie vivement Jean-Paul Rieu pour m'avoir accueillie dans son équipe. Je n'ai jamais trouvé les mots pour vous remercier de m'avoir donné cette opportunité et de m'avoir fait confiance. Un grand merci à Hélène Delanoë-Ayari qui a consacré énormément de son temps à encadrer ma thèse. J'ai toujours apprécié ta passion pour la recherche, ton enthousiasme et dynamisme et également, ta franchise. Je vous remercie tous les deux pour vos conseils avisés, pour votre aide précieuse (pendant la rédaction également), pour votre disponibilité et votre soutien tout au long de ces trois années aussi bien sur le plan scientifique qu'humain.

Je voudrais aussi remercier Catherine Barentin pour sa contribution à ce travail. J'ai beaucoup apprécié nos discussions et votre soutien.

Le temps passé dans le laboratoire a été très agréable et pour cela je tiens à remercier toute l'équipe « Liquides@Interfaces » et particulièrement Catherine et Charlotte, pour leur gentillesse, chaleur et pour leur aide inconditionnelle. Merci aussi à Baudouin pour l'aide avec le Carbopol et l'organisation des expériences et merci à Gilles et Guillaume pour leur aide technique, toujours rapide et efficace. Un grand merci à Christelle, notre chère secrétaire, qui m'a beaucoup aidé et cela, toujours avec le sourire.

Un grand merci à Sham et Thibault car ma thèse a beaucoup évolué grâce à eux, à leur enthousiasme.

Merci au tout petit groupe Biophysique grâce à qui les moments passés dans la salle de culture ont été plus agréables (merci Antoine et Magalie!).

Merci aux collègues de bureau : Ludivine, Guido, Alejandro, Priyanka, Joseph et tout particulièrement, merci Clara, Marie-Julie et Antoine pour votre gentillesse, votre bonne humeur, merci de m'avoir attendue tant de fois pour aller déjeuner et pour tous les beaux moments passés ensemble. Cela a été un vrai plaisir de vous connaitre.

Mes pensées vont aussi vers mes anciens professeurs, mes anciens collègues et actuels amis (Livia, Ionut, Bogdan, Magda) et je voudrais remercier particulièrement Ana-Maria : merci d'avoir cru en moi et de m'avoir aidée professionnellement et personnellement aussi.

Je tiens à remercier également mes très chères copines qui n'ont pas pu être à mes côtés pendant la thèse mais qui m'ont toujours soutenu : Iulia (merci pour tout et merci d'être venue à la soutenance), Anca (… pour ton belle amitié et pour les longues discussions), Maria (… pour ta bonne humeur et ton soutien) et Irina (… pour tout… et je n'oublierai pas la glace au café).

Je voudrais remercier particulièrement mes parents et mon frère *(mama și tata, mulțumesc pentru tot ceea ce ați făcut pentru mine și pentru tot ceea ce mi-ați oferit)* mais aussi toute ma chère famille (mes tantes, mes cousins et cousines et mes grands-parents…) dont le soutien a toujours été présent, malgré la distance qui nous sépare. Vous me manquez beaucoup.

Enfin, je dédie ce manuscrit à Ovidiu. C'est grâce à toi que je suis devenue plus forte. Merci de tout mon cœur pour ta confiance, pour tes mots d'encouragement, pour ton soutien en tout moment et pour ton amour si beau.

Microscopic origin of the rheological and surface properties of embryonic cell aggregates

Preface

Both physicists and biologists are showing a growing interest in the study of multicellular spheroids (*i.e.*, aggregates of dissociated and reaggregated cells), whose applications in developmental biology, oncology and tissue engineering are continuously emerging.

It is now well admitted that mechanics plays a fundamental role in tissue organization and genesis [1]. To get to their final position, cells need to move or more exactly "to flow" [2]. But what are the characteristic timescales and what are the physical forces driving or resisting these movements? Finally, what are the microscopic ingredients explaining them?

The pioneer work of M. S. Steinberg [3] on cell aggregates constitutes an interesting starting point. Steinberg demonstrated that certain embryonic tissues mimic the behavior of viscous liquids or fluids [4]. Classical experiments on the relaxation of embryonic chicken aggregates subjected to mechanical deformations, either by centrifugation [5] or by compression [6], demonstrated that tissues relax as elastic materials on short time scales (seconds) and as viscous liquids on long time scales (hours). At long time scales, cell aggregates may round, spread over the surface of one another, or sort out when two distinct tissues are randomly intermixed. Tissues possess therefore a tissue surface tension (TST) that drives these processes exactly as liquid droplets do.

The first TST measurements were performed on different chicken embryonic tissues using a parallel plate compression apparatus (tensiometer). These measurements predicted the mutual corresponding envelopment behavior of the tissues [7]. Later, the same authors demonstrated that aggregate surface tensions are a direct, linear function of cadherin (proteins responsible of cell adhesion) expression level using L cell aggregates transfected with N-, P- or E-cadherin in varied, measured amounts [8]. The authors concluded that tissues exhibit perfect fluidity at long time scales and that rearrangements during cell sorting, tissue spreading or rounding represent self-assembly processes guided by the diminution of adhesion energy directly dependent on the cadherin expression.

However, some of these conclusions were questioned several times recently and according to new experimental data reported, TST is likely to depend as well on the cytoskeleton contractility [9–12]. The Differential Interfacial Tension Hypothesis (DITH) [9,13–15]

relates the tissue surface tension to the tension along the edges of individual cells. It was first introduced by Harris in the seventies [13] but never fully tested experimentally to our best knowledge.

Quantitatively, the elastic properties of cell aggregates at short time scales are not better known. Moreover, although classically modeled as fluid at long time scales, yield stresses and plasticity seem also to play an important role in the reorganization and rheology of embryonic cellular aggregates [16]. Foams, emulsions, ketchup, gels, granular materials, paints are example of everyday life complex and disordered materials presenting such properties. Their intermediate fluid/solid behavior is fundamentally difficult to describe: at rest they behave like an elastic solid, but they are able to flow like a liquid under sufficient applied stress, the *so-called* yield stress. Altogether the flow and deformation of such systems involve a combination of elasticity, plasticity and viscous relaxation. Plasticity is classically associated with an irreversible change in the macroscopic shape of a system after a sufficient stress. In foams, it is associated with the irreversible T1 processes (neighbor changes between bubbles). A yield stress exists to overcome the barrier to change neighbors and induce cell flow.

A major question concerning cell aggregates is the relevance of such an elasto-plastic scenario of soft glasses to describe their rheological properties.

In this context, the purpose of this work was on one hand to better understand the biological origin of viscosity and surface tension, and on the other hand to study quantitatively in details the visco-elasto-plastic behavior of cell aggregates using new rheological protocols in shear experiments.

This manuscript is divided into four chapters.

Chapter 1 is an introduction to the subject, with some basic concepts of rheology of cells and cell tissues.

In chapter 2 we describe the molecular and pharmacological approaches together with the experimental system that we used in our study and we give details about the different experimental procedures.

Chapter 3 deals with measurements of tissue surface tension by tissue compression method and of tissue viscosity by analysis of fusion kinetics of two cell aggregates. We vary key parameters such as cell contractility that some people suspect as the main biological origin of these parameters and we use the formalism of DITH to interpret the data. We present in this chapter results which allowed us to state that we can reach a fine tuning of tissues' viscosity and surface tension through contractility, and we will show the role of a key protein of the cell-cell adhesive structure: α-catenin.

The experimental results obtained using a parallel-plate commercial rheometer and a model helping for the understanding of these results are presented and discussed in chapter 4. One of the main motivations for the work presented in this chapter was to probe in more details the intra-cellular rearrangements by shearing thousands of aggregates at the same time.

Finally, in Conclusions and Perspectives chapter we draw the general conclusions and we give several suggestions for future directions of the research presented in this thesis, mainly the use of complementary techniques, such as two-photon microscopy to study cell rearrangements inside the aggregates at large deformations.

One appendix comes to complete the manuscript, in which we present supplementary experimental rheological curves obtained by varying different parameters in our system.

1. Lecuit, T. & Lenne, P. Cell surface mechanics and the control of cell shape, tissue patterns and morphogenesis. *Nature reviews. Molecular cell biology* **8**, 633–44 (2007).

2. Cui, C., Yang, X., Chuai, M., Glazier, J. A. & Weijer, C. J. Analysis of tissue flow patterns during primitive streak formation in the chick embryo. *Developmental biology* **284**, 37–47 (2005).

3. Steinberg, M. S. Reconstruction of tissues by dissociated cells. Some morphogenetic tissue movements and the sorting out of embryonic cells may have a common explanation. *Science* **141**, 401–408 (1963).

4. Beysens, D. A., Forgacs, G. & Glazier, J. A. Cell sorting is analogous to phase ordering in fluids. *Cell* (2000).

5. Phillips, H. & Steinberg, M. S. Embryonic tissues as elasticoviscous liquids. I. Rapid and slow shape changes in centrifuged cell aggregates. *Journal of cell science* **30**, 1 (1978).

6. Forgacs, G., Foty, R. A., Shafrir, Y. & Steinberg, M. S. Viscoelastic Properties of Living Embryonic Tissues : a Quantitative Study. *Biophysical journal* **74**, 2227–2234 (1998).

7. Foty, R. A., Pfleger, C. M. C. M., Forgacs, G. & Steinberg, M. S. Surface tensions of embryonic tissues predict their mutual envelopment behavior. *Cell* **1620**, 1611–1620 (1996).

8. Foty, R. A. & Steinberg, M. S. The differential adhesion hypothesis: a direct evaluation. *Developmental biology* **278**, 255–63 (2005).

9. Krieg, M. *et al.* Tensile forces govern germ-layer organization in zebrafish. *Nature cell biology* **10**, 429–36 (2008).

10. Mgharbel, A. Physique et rhéologie des agrégats cellulaires embryonnaires. (2009).

11. Manning, M. L., Foty, R. a, Steinberg, M. S. & Schoetz, E.-M. Coaction of intercellular adhesion and cortical tension specifies tissue surface tension. *Proceedings of the National Academy of Sciences of the United States of America* **107**, 12517–22 (2010).

12. Jakab, K. *et al.* Relating cell and tissue mechanics: implications and applications. *Developmental dynamics: an official publication of the American Association of Anatomists* **237**, 2438–49 (2008).

13. Harris, A. K. Is cell sorting caused by differences in the work of intercellular adhesion? A critique of the Steinberg hypothesis. *Journal of Theoretical Biology* **61**, 267–285 (1976).

14. Graner, F. Can surface adhesion drive cell-rearrangement? Part I: Biological cell-sorting. *Journal of theoretical biology* **164**, 455–455 (1993).

15. Brodland, G. W. The Differential Interfacial Tension Hypothesis (DITH): A Comprehensive Theory for the Self-Rearrangement of Embryonic Cells and Tissues. *Journal of Biomechanical Engineering* **124**, 188 (2002).

16. Marmottant, P. *et al.* The role of fluctuations and stress on the effective viscosity of cell aggregates. *Proceedings of the National Academy of Sciences of the United States of America* **106**, 17271–5 (2009).

Chapter 1

Physics and Rheology of cell aggregates: State of the art

Aggregates of dissociated and reaggregated cells (also often called multicellular spheroids) are more and more used for biological (developmental biology), cancer or biomedical applications (tissue regeneration) or just as models of complex cellular fluids. All these applications require a better understanding of the physical properties of cell aggregates in order to be able to propose a few macroscopic physical and mechanical quantities or rheological laws that are capable of describing the behavior of tissues. For the moment, very little is known about the rheology of cell aggregates and to be able to reach the desired level of comprehension in this field, a lot of work still needs to be done.

We will start this introductive chapter with a small review of the applications of cell aggregates in cell biology and for biomedical purpose. We will pursue by a description of their known physical properties at different time scales and in particular their fluid properties at long time scales.

Foremost, it is very important to have an overall view on the characterization and on the rheological properties of single cells before stepping in the context of multicellular systems. Thus, in the last section of this introductive chapter, different experimental results obtained at the cellular scale will also be presented. An important question which arises is to what extent these single cell properties can account for the effects observed in whole tissues.

1.1 Cell aggregates: structure, biological and biomedical applications

1.1.1 Structure of cell aggregates

Various embryonic tissues and organ pieces can be dissociated into suspension of discrete, viable cells following treatment with Ca- and Mg-free saline solutions and trypsin [1]. If we take dissociated cells and put them in a suspension, some types of cells will be capable to re-establish contacts between each other, reassemble and to give rise to agglomerations whose internal structure evolves with the maturations of links between cells in order to create a compact aggregate which mimics the structure of an embryonic tissue. A wide range of normal and malignant cell lines can be aggregated. Since the late 1950s, these multicellular aggregates of malignant cells have been analyzed for proliferation, differentiation, invasion potential and structural similarity to human tumors [1]. Explants (*i.e.*, living tissue transferred from an organism to an artificial medium for culture) can also be directly used without trypsinization once they recovered and got rounded after they were dissected from their initial parental tissue.

Because cell lines form often nearly perfect sphere-shaped aggregates (Fig. 1.1 A), they were called "spheroids" [2]. Histological examination of these spheroids revealed striking similarities between their structure and that of naturally occurring human tumors. Furthermore, the response of 3D culture models to cancer therapy is so similar to the response obtained in humans that many investigators consider spheroids useful for studying cancer cells' basic biological properties [3,4].

Many protocols exist to prepare aggregates (centrifugation, hanging drops, self aggregation in confined spaces or wells). Most of these methods offer a control of the aggregate size from the concentration of dissociated cells in the suspension (Fig. 1.1 A). Due to their range of size (typically 100~500 µm in diameter), aggregates can be easily manipulated (Fig. 1.1 C).

The internal cell density is determined by the cell type and by the adhesive links between the cells. These adhesive links are maintained by adhesion molecules or proteins localized at the cells' surface such as cadherins [5,6]. The epithelial embryonic carcinoma cell aggregates used in this work (F9 cell line) present cell-to-cell adhesion which is mediated by epithelial cadherins (usually named E-cadherins) which are membrane proteins. Figure 1.1 B shows immunofluorescent staining of β-catenin inside and at the external surface of a section of such a F9 cell aggregate. As β-catenin colocalizes with cadherins near the cell membrane, this staining is also representative of the cadherin distribution. It is equally present all around the cells with little difference between the bulk and the external boundary of the aggregate. Figure 1.1 D shows a live optical section by 2-photon confocal microscopy of the same F9

aggregate at 37 °C. The staining with sulforhodamine B draws all cell contours exactly as do *β*-catenin in Fig. 1.1 B. The cell density is very high and virtually all cells are in close packing. This dense structure resembles the packing of bubbles in foams.

The surface of the aggregates could be rather smooth (Fig. 1.1 A-D, F) or rough as for CHO cell aggregates (Fig. 1.1 E). It is assumed that a larger roughness indicates lower cell cohesion [7]. Note also that the cohesion of CHO aggregates is mediated by the interaction between another type of adhesion molecules, the integrins, with the extra-cellular matrix present into the aggregates [8].

Behind adhesion molecules, inside the cells we find a skeleton of proteins which is relatively rigid and dynamic. It is named the actin cytoskeleton and it gives to the cell its shape. The cadherin-cytoskeleton complex allows the cell to probe its mechanical environment and develop forces with the purpose of providing movement. Despite the compact structure, at a long time scale, cells are capable to move and reorganize inside the aggregate. But these movements are so slow and the 3D aggregates so dense that still little is known about cell-cell rearrangements and 3D motility.

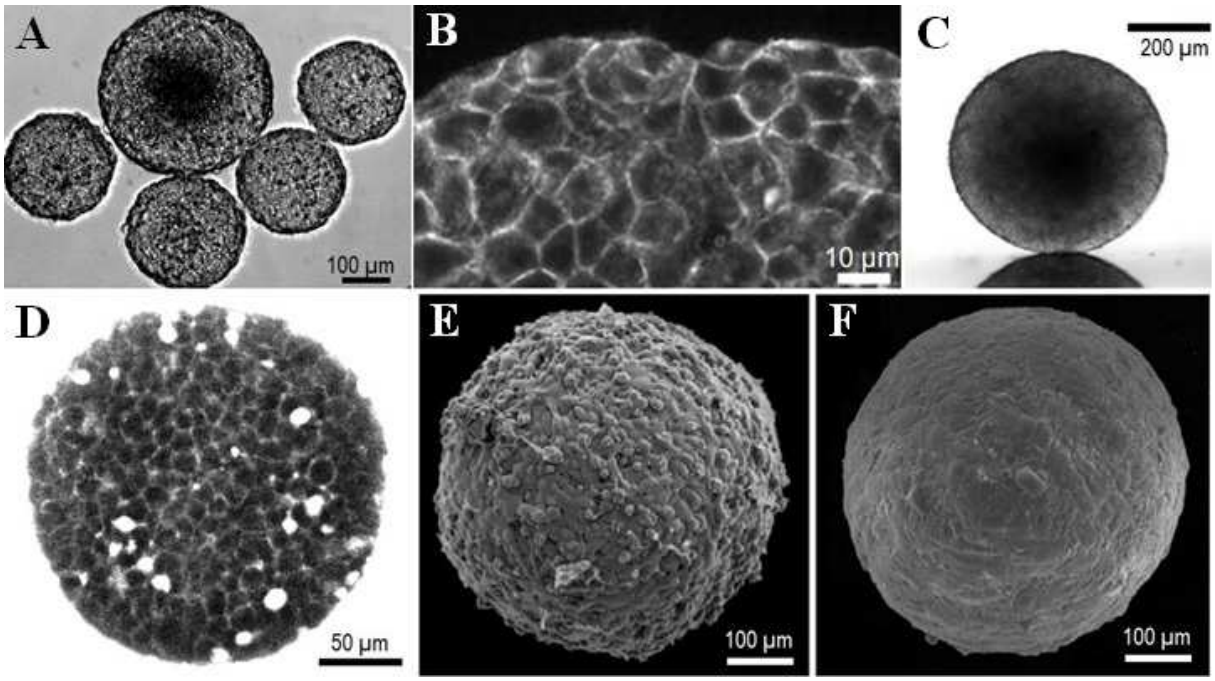

Fig. 1.1: *(A-D) F9 WT cell aggregates. (A) Optical microscopy image of aggregates of cells taken two days after the beginning of the aggregation. (B) Cross section of a cell aggregate (the staining is for β-catenin). (C) Side view from our tensiometer setup. (D) Middle plane of a slightly compressed aggregate by 2-photons confocal microscopy (staining with sulforhodamine B showing all cell contours). (E-F) Scanning electron microscopy images of CHO (Chinese hamster ovary) (E) and HUSMC (Human Umbilical Vein Smooth Muscle Cell) (F) cell aggregate surfaces. The berry-like shape of many of the CHO cells reveals limited*

adhesion between surface and subsurface cells. The flattened shape of HUSMCs implies that they strongly adhere to subsurface cells (from [7]).

1.1.2 Developmental biology

1.1.2.1 Morphogenesis

Morphogenesis is the phase during which the tissues and organs will be set up in order to give the body its final form. The ability of cells to flow (*i.e.*, tissue liquidity) is a key ingredient in morphogenesis, as directed cell movements allow their organization into tissues that will eventually form the organs.

Embryonic development usually starts after fertilization of an egg by sperm. Thus, embryogenesis starts from a single cell whose genetic code is executed, emerging into a highly complex living organism. Right after fertilization, the cell divides very quickly and then a massive rearrangement takes place at a cellular and tissue level, known as the gastrulation stage [9]. This process drives the formation of a trilaminar structure (*i.e.*, the gastrula) composed by the ectoderm, mesoderm and endoderm. Each layer gives rise to specific tissues and organs in the developing embryo. The ectoderm, which is the most superficial, gives rise to epidermis, integumentary structures and nervous system. The mesoderm, found between the ectoderm and the endoderm, gives rise to muscles, cartilage, bone and connective tissue, blood and blood vessels. Finally, the endoderm gives rise to the epithelium of the digestive and respiratory systems and the organs associated with, such as liver, pancreas and lungs.

To better illustrate the different stages of embryonic development, we will consider here the example of zebrafish development.

The zebrafish or Danio (Danio rerio) [10] is the most current model in developmental biology, as it allows a genetic analysis and a classical embryological approach facilitated by the transparency of embryos and their rapid development (gastrulation after 5h of development).

After the egg fertilization, which is the first step in the embryonic development, the first cell will undergo a series of synchronous divisions (Fig. 1.2), while reducing their size, leading to a set of identical and totipotent cells. Until the midblastula transition (1024 cells), development is under control of maternal information [11]. During this stage, the zygotic transcription takes place and cells become mobile. Cells situated at the animal pole (the head of the embryo) will begin to divide asynchronously and will gradually cover the vitelline reserve (yolk) (Fig 1.2 F) during the phenomenon of epiboly (*i.e.*, expansion of one cell sheet over other cells). When 50% of the yolk is covered by embryonic cells, gastrulation begins in

order to transform the unstructured blastula into an embryo with three defined layers: ectoderm, endoderm and mesoderm. During gastrulation, three movements necessary for the establishment of these three primary layers, are to be considered: the epiboly movement that continues until all the yolk reserve is covered by embryonic cells, the movement of invagination of the cells of the margin that will allow the formation of the two deep germ layers, endoderm and mesoderm, and the convergence movement that leads the ventral cells to the dorsal surface of the embryo where the embryonic axis lengthens [12].

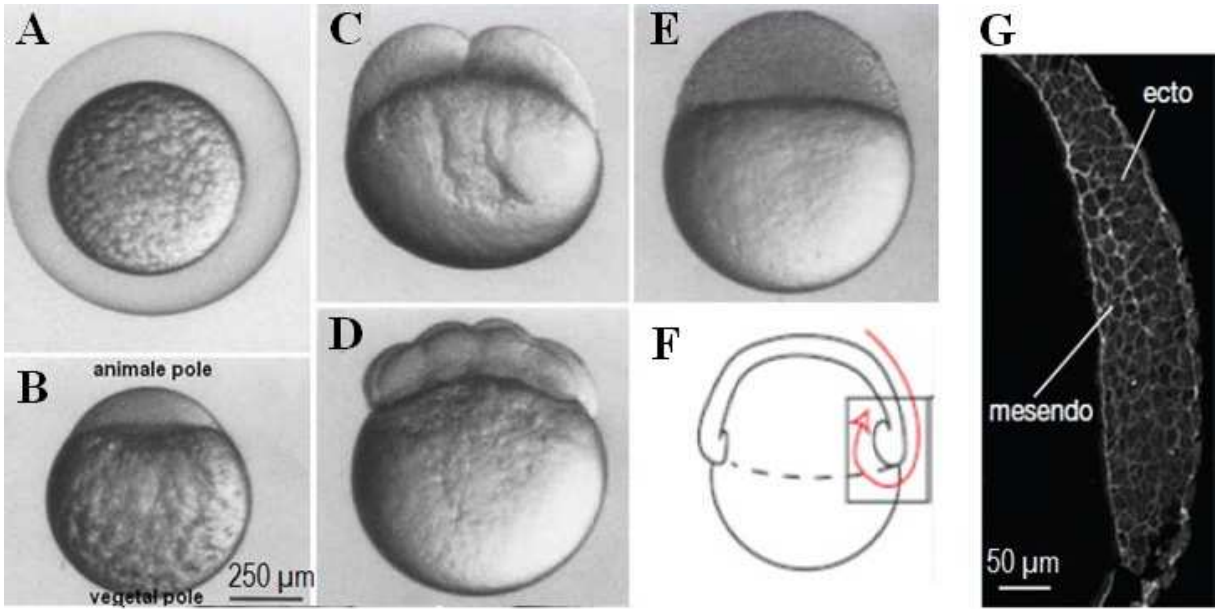

Fig. 1.2: *(A-B) Views of a fertilized zebrafish egg. (A) With protective chorion. (B) After chorion removal, on the animal pole, we can identify the first cell, at the top of the image. (C-D) Example of an embryo image after the first cell divisions. (C) 2 cells stage. (D) 16 cells stage. The cell size decreases at each division with the increase in the number of embryonic cells. (E) Blastula stage embryo (between "high and oblong stage"). (F-G) Sagittal section of the dorsal germ-ring margin of a shield stage wild-type embryo (6 hpf; schematic drawing in F) fluorescently stained with an E-cadherin antibody. Picture was taken by confocal microscopy. Taken and modified from* [13].

During morphogenesis, cell movements is governed by genetic information secreting molecular factors, and requires the intervention of mechanical [14] and biochemical signals. These signals allow cells to probe their environment and respond to instructions in order to "flow" to their destination within the organism. In order to understand these complex processes, it is useful to perform *in-vitro* experiments with dissected explants or aggregates of reaggregated cells in controlled environmental conditions [13].

1.1.2.2 Tissue affinity and the Differential Adhesion Hypothesis (DAH)

When multiple types of cells from a primitive animal or an embryo are dissociated, randomly intermingled, and then reaggregated, they are able to rearrange, to reestablish coherent homotypic domains, and sometimes to reconstitute an entire animal. This rearrangement of cells, known as regeneration or cell sorting, offers insight into the mechanisms governing morphogenesis. Sorting has long been studied using organisms including hydra [15] or sponges [16] who have a strong regenerative capacity.

In the middle of last century, the embryologists Holtfreter and Townes tried to explain the self-organization of tissues in the amphibian embryo, and they came to the conclusion that the transformation of a single fertilized egg into a patterned body was due to a certain tissue affinity [17,18]. Support for this idea had come from cell culture experiments, in which Holtfreter had shown rounding-up of tissue fragments, the spread of one tissue over another and the sorting out of completely dissociated cells, rearranging in a formation which would resemble the correct anatomical structure in the amphibian embryo. Furthermore, the various cell types investigated did not only have specific affinities for one cell type but not another, they also preferred particular positions within a multicellular aggregate.

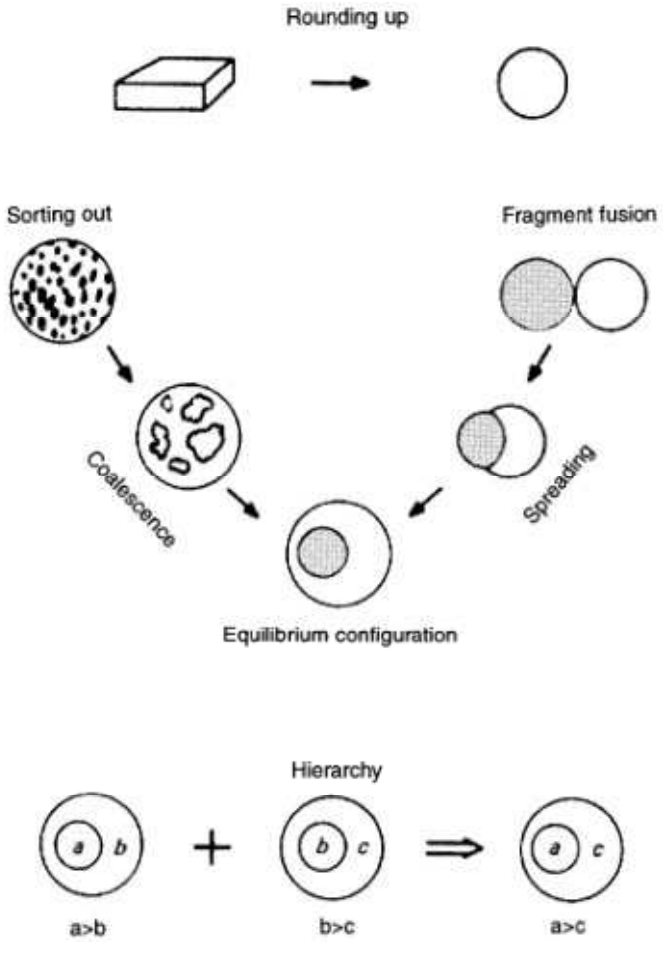

Fig. 1.3: *Behaviors displayed both by embryonic cell aggregates and by ordinary liquids or immiscible liquid pairs. (Top) A mass of arbitrary shape rounds up to form a sphere, minimizing its surface area. (Middle) Intermixed phases sort out by a process of coalescence, forming a continuous externalizing phase which envelops, to a greater or lesser degree, a discontinuous, internalizing phase. When touched together as separate masses, the same two phases spread, one over the other, to approach the same (equilibrium) configuration approached by sorting-out. (Bottom) In a set of mutually immiscible phases, the tendencies of one phase to spread over another are transitive; i.e., if b tends to spread over a and c tends to spread over b, then c will tend to spread over a. From* [19,20].

In the sixties, the Differential Adhesion Hypothesis (DAH) was proposed by M. S. Steinberg to explain all these observations. The central idea of the DAH is the analogy between biological tissues and ordinary liquids. The DAH proposes that tissues can be treated as liquids on long times scales with surface and interface tensions, since they are composed of motile, cohesive subunits (cells) and show typical fluid behavior [21]. The term surface tension is used to describe the forces acting along the interphase between a tissue and the cell culture medium, and interfacial tension is used to describe the forces acting along the interphase between two tissues. These tensions trigger cell rearrangements in tissues and predict the final equilibrium configuration of tissues exactly as ordinary (immiscible) liquids that reach an equilibrium configuration of minimal surface energy.

The rounding up of tissue fragments into spheres, the fusion, the sorting or the envelopment between two different tissues (mutual envelopment behavior with the less cohesive cells enveloping the more cohesive ones) are all phenomena already observed by Holtfreter and Townes [17,18] and explained by the DAH (Fig. 1.3).

1.1.2.3 What we may learn from equilibrium configuration after mixing cell populations

To test the predictions of the DAH, Steinberg and Takeichi [22] combined two populations of L cells transfected with P-cadherin and expressing this homophilic adhesion molecule in substantially differing amounts. When the two cell populations were intermixed, they segregated to approach a sphere within a sphere configuration, the cell population expressing more P-cadherin forming islands which fused to become an internal "medulla". When the two cell populations were first formed into separate aggregates which were subsequently allowed to fuse (spreading assay), the cell population expressing more P-cadherin was enveloped by its partner. Steinberg and co-workers also demonstrated that for primary cells dissected from different chick embryonic tissues, the relative values of tissues surface tensions (TST) consistently predicted the mutual spreading tendencies of aggregates [23] (Fig. 1.4). Fukunaga *et al.* [24] used a similar spreading assay to predict the lower cohesion of *β*-catenin Plakoglobin deficient cell line as compared to the parent F9 cell line but did not measured TSTs. In this manuscript, in chapter 3, we will provide a supplementary example: α-catenin deficient cells whose TST value is lower are surrounding the parent F9 cells with higher TST. This indicates that simple *in-vitro* sorting or spreading assays with cell aggregates enables to get important information on cell cohesiveness.

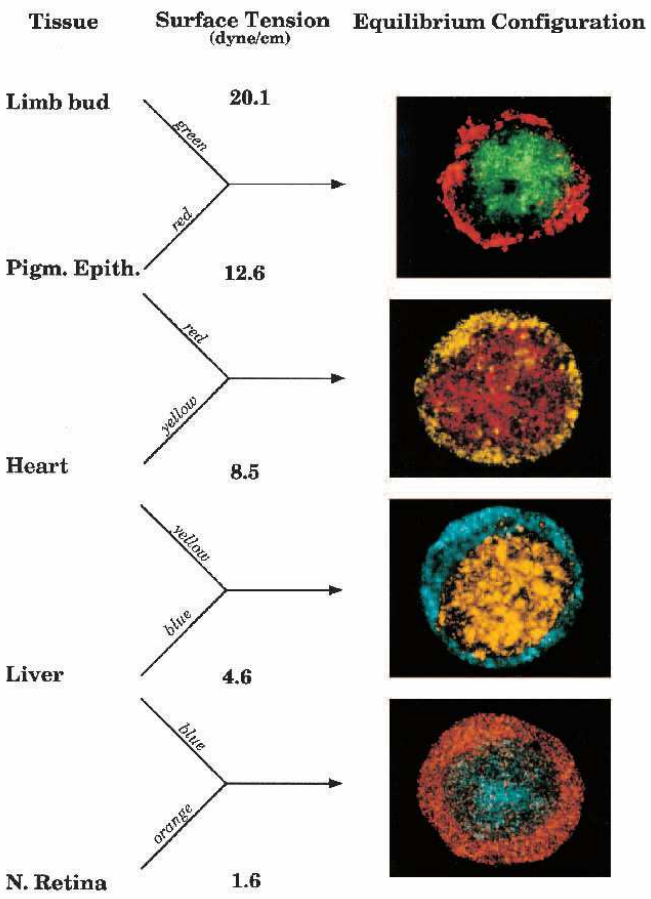

Fig. 1.4: *Chick embryonic tissue surface tensions were determined by tissue tensiometry. The surface tension values are increasing more than an order of magnitude from neuronal retina tissue to limb bud tissue. The envelopment hierarchy corresponds exactly with the measured tissue surface tensions and confirms the transitive hierarchy of surface tensions and cell sorting. Taken from* [23].

During gastrulation, both cell adhesion and cell contractility have long been implicated in germ-layer formation; however, their relative contribution to these processes is still a matter of debate [13]. Two series of *in vitro* cell sorting experiments with germ-layer progenitors were performed in *Rana pipiens* (amphibian) and zebrafish embryos by the groups of M. S. Steinberg and C. P. Heisenberg respectively. In both systems, it was found that ectoderm cells are surrounded by mesoderm or endoderm cells and mesoderm cells are surrounded by endoderm cells. But while in zebrafish, a higher actomyosin-dependent cell-cortex tension (and not a higher cell-cell adhesion) was found to correlate with ectoderm progenitor sorting to the inside of a heterotypic aggregate [13], Steinberg *et al.* found in the amphibian that the TST values predict the sorting hierarchy [25]. Perhaps the key to understand these different experimental results is to admit that TST does not depend only on cell-cell adhesion but also on cortical tensions as postulated by the Differential Interfacial Tension Hypothesis (DITH, [13,26–28]). We will come back to this discussion latter in this chapter and we will examine in detail the cortical tension dependence of TST in chapter 3.

To finish this section about the advantages and possibilities offered by aggregate technology to the field of developmental biology, one should keep in mind that, *in-vivo*, morphogenesis often departs from a sphere within a sphere configuration. Elongated and layered structures are quickly formed in the course of development. In the amphibian, the

observations of Winklbauer and co-worker of tissue separation at gastrulation in *Xenopus* indicate more complex mechanisms than those postulated by the DAH or the DITH [29]. Instead, it involves localized responses to signals exchanged at the tissue boundary and an attachment/detachment cycle which allows for cell migration across a cellular substratum [30].

In the avian vertebrate retina, a powerful reaggregation model available for the analysis of tissue regeneration, the complete arrangement of retinal layers is not only a result of cell sorting. Reaggregated cells also proliferate and differentiate to establish a structured tissue. This process can be achieved only if the dispersed retinal cells are young and they are supplemented with soluble factors from either the retinal pigmented epithelium or radial glia [31].

1.1.3 Biomedical applications

1.1.3.1 Oncology

In oncology, cell aggregates offer a very interesting model system for the study of dissemination of cancer tumors.

As known, when a cell undergoes an alteration of its genome, an abnormal development of cancer cells will occur. The uncontrolled proliferation will disrupt the organization of the tissue and loosing cohesion determines the migration of these cancer cells towards different tissues in the human body (metastasis).

Cell proliferation deregulation is a hallmark of tumorigenesis and the knowledge of the mechanisms of its regulation of is fundamental to a better understanding of the consequences of their misregulation in, as well as to manipulate them in cancer therapy [32]. The study of these mechanisms already contributed to a large extent to the improvement of targeted therapies.

However, many studies performed so far relied on in vitro analyses of rapidly growing cancer cell lines in monolayer. These 2D models do not take into account tissue heterogeneity, cellular interactions and tumor microenvironment that have been shown to be of major relevance in tumor development [33,34]. Multicellular tumor spheroids (MCTS) generated from cancer cells are attractive models to study cancer proliferation in 3D [32]. Indeed these 3D complex multicellular systems reproduce cell-cell and cell-matrix interactions as found in solid tumors [35]. Moreover, MCTS can grow to diameters of several hundred micrometers, progressively developing a gradient of proliferating cells (Fig. 1.5) similar to that found in nonvascularised micro-regions of a tumor: dividing cells are located in the outer layers and quiescent cells are located more centrally in regions that are hypoxic and receive few nutrients [36,37].

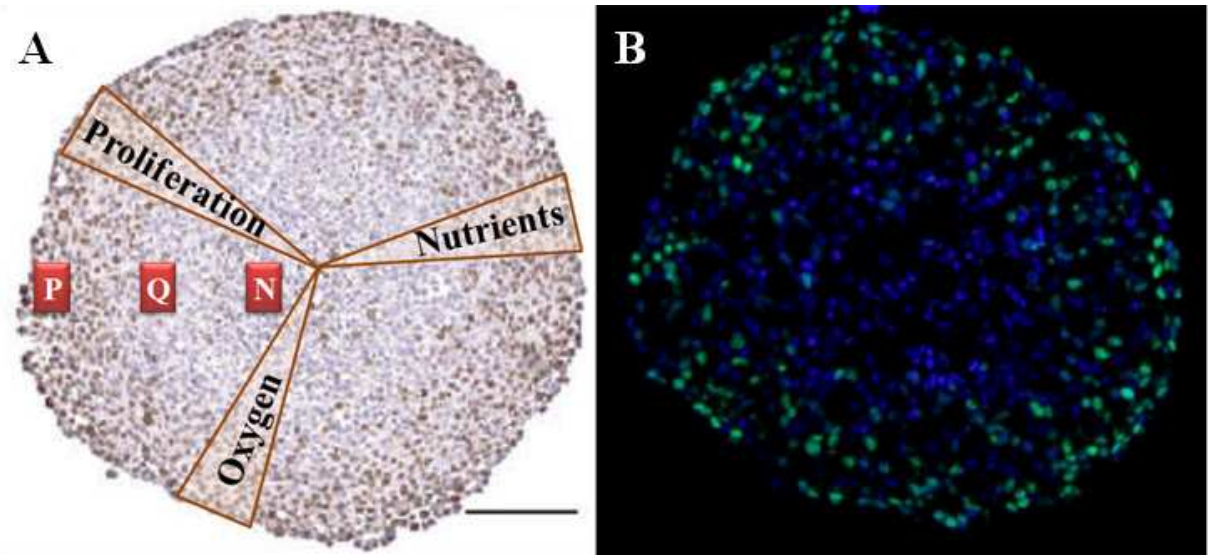

Fig. 1.5: *MCTS integrates microtumor organization with nutrients, hypoxia and proliferation gradients. (A) Proliferation, hypoxia and nutrients gradient are sketch over Ki-67 IHC staining of a HCT116 colon adenocarcinoma multicellular tumor spheroid. Proliferative, quiescent and necrotic regions are represented with P, Q and N. (B) Detection of proliferating cells and of nuclei on a HCT116 spheroid cryosection after EdU incorporation and fluorescent detection (green) and DAPI staining (blue) of the nuclei. Scale bar, 100 µm. Modified from* [38]*. Data from* [38–42]*.*

1.1.3.2 Tissue engineering

"Tissue engineering" is a concept attributed to the bioengineering pioneer Y. C. Fung of the University of California, San Diego, which is also regarded as the founding figure of "Modern Biomechanics".

By exploiting biological morphogenesis, tissue engineering aims to repair, replace or regenerate damaged tissues or organs, having a great contribution in regenerative medicine. In the biomedical research, tissue engineering also helps for a better understanding of the fundamental mechanisms and principles of biological organization in general and organogenesis in particular.

A novel approach in tissue engineering is organ printing, a rapid prototyping method. It has been shown that the self assembly driven structural organization of cell aggregates can be employed in the evolving technology of organ printing [43–46].

Technological advances [47–49] combined with the concept of tissue liquidity have shown that, rather than individual cells (usually deposited on biocompatible hydrogels [50]), it is preferred to use cell aggregates as droplets of bioink which upon embedding into scaffolds have the ability to fuse into 3D structures of specified morphology. The aggregates can be obtained by using genetically transformed cells with controlled adhesive properties.

The postprinting cell rearrangements are highly dependent on the embedding gel, the "biopaper" (collagen, gelatin or hyaluronan) whose composition can be controlled in order to obtain chemical and mechanical characteristics that will promote cell survival and postprinting self assembly.

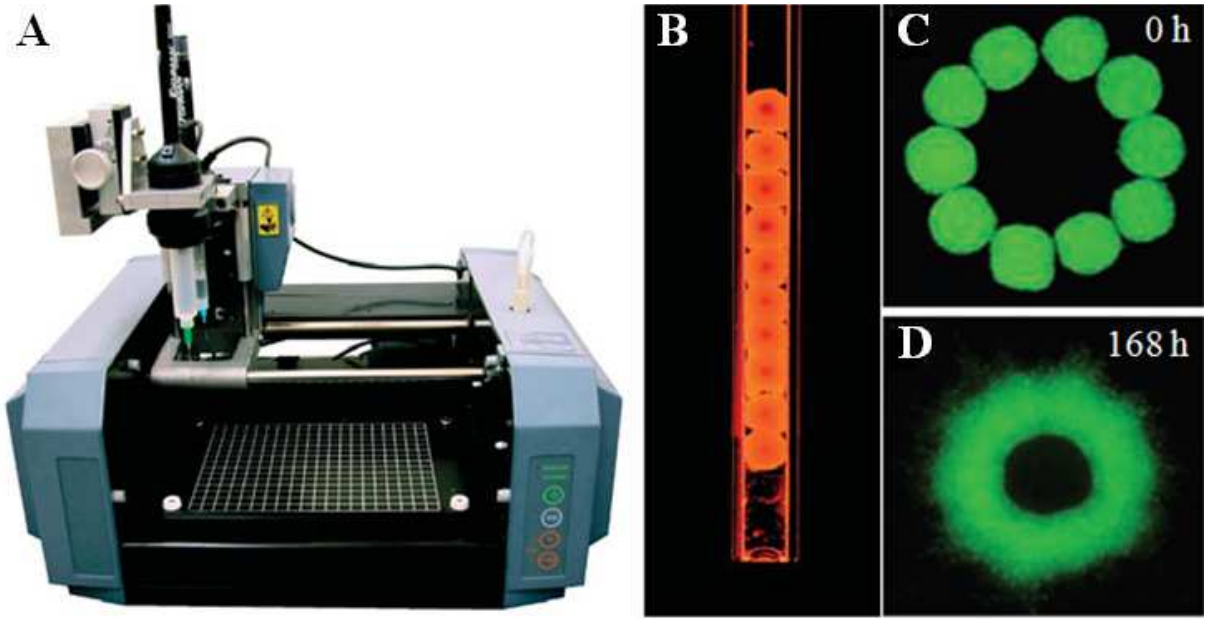

Fig. 1.6: *Tissue engineering* [44]*. (A) Special purpose 3D bioprinter with two mechanically driven extruders. One of the extruders hosts the bio-ink cartridge, which is a micropipette housing the spherical aggregate-bioink particles. The other extruder prints the biopaper-hydrogel scaffold. The x-y stage and the z directional motion of the extruders are fully computer controlled. (B) A detailed view of the bioprinter's cartridge loaded with 500 μm diameter bio-ink droplets. (C-D) Time evolution of a cellular pattern. Initial (C) and final (D) configurations of a CHO cell aggregate embedded in a collagen gel of concentration 1 mg/ml. The nuclei of the cells are fluorescently labeled and the average diameter of the aggregates is 500 μm. Taken from* [44,51].

1.2 Physical properties of cell aggregates – From the macroscopic to the microscopic scale

1.2.1 Fluids or solids, a matter of scale

It is well known that qualitatively on short time scales, aggregates behave as elastic solids while at long times they behave as fluids [52,53]. Quantitatively, the detailed material and rheological properties of cell aggregates and their biological origin is much less known and that's a major aim of this PhD work to try add a contribution to the field.

We already largely commented in the previous section the analogy with liquids at long times: in the absence of any external forces, aggregates formed by reaggregation of cells can round up in a spherical shape, sort when two populations are intermixed or fuse when they are put in direct contact [54]. Figure 1.7 shows a visual example of the fusion of two mouse carcinoma F9 cell aggregates (the embryonic epithelial cell line used throughout this work), which is very similar to the coalescence of two liquid droplets.

Hence, cell aggregates possess an apparent tissue surface tension (TST or σ, see also next subsection) and also an apparent tissue viscosity η. Hydrocapillary laws predicting the kinetics of rounding or of coalescence of Newtonian fluid droplets enable the measurements of a characteristic liquid time $t_{Liq}=\sigma R/\eta$ where R is the aggregate radius.

Several studies demonstrated that these hydrodynamical laws are satisfactorily fitting the experimentally kinetics of rounding or fusion of cell aggregates. The measured time are of the order of a few hours to a few tenths hours [54–58]. We will come back to these viscocapillary measurements in chapter 3.

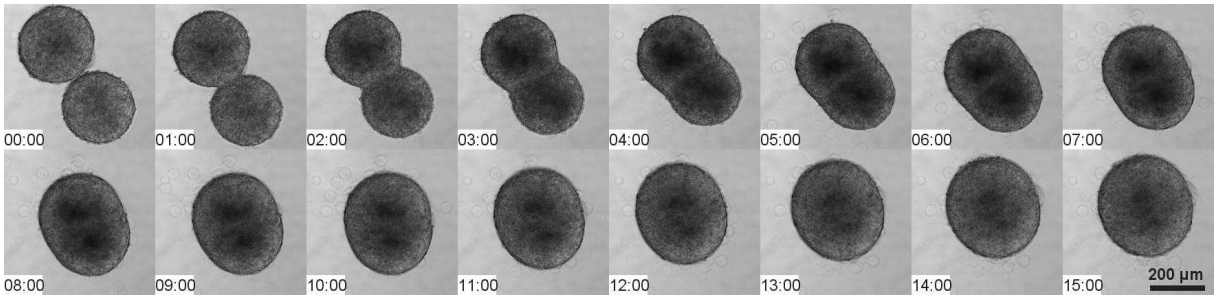

Fig. 1.7: *Timelapse images every 1 hour of the fusion of two mouse carcinoma F9 cell aggregates that were put into contact at t=0.*

Already in the late 70s, Phillips and Steinberg qualitatively observed the viscoelastic characteristics of aggregates at short times, by mechanically deforming them using centrifugation against solid substrata [20,59].

For example, Leghorn embryo cell aggregates subjected to brief centrifugation periods (8–16 min) flatten quickly (cell shapes flatten too), and round up quickly (in <2 min) once centrifugal forces are removed, reaching a shape very similar to the initial one [20]. Such brief centrifugation experiments provide some support for a simple elastic-solid model in which aggregate shape changes are accompanied by cell deformations rather than cell rearrangements.

In contrast, during prolonged centrifugation (1 day), the same aggregates continue to flatten more slowly (while cells gradually regain their original shapes) [59,60]. Once centrifugal forces are removed, these aggregates round up slowly (in ~1 day), like a viscous liquid.

Furthermore, by applying prolonged centrifugation, it was shown that an initially very flat aggregate (freshly cut, as a thin square, from an embryo) and an initially round aggregate (obtained after incubating and shaking overnight the flat piece of embryo) adopted the same final intermediate shape [20]. In this long term experiments, aggregate behavior is explained by their liquid properties and the fact that they are able to flow and change neighbors at long time scales, relaxing the compression-induced stress.

The behavior of living tissues in terms of standard models of viscoelasticity was analyzed by Forgacs and co-workers [52]. They got some quantitative details about tissue rheology by following the viscoelastic response of mechanically compressed aggregates in terms of characteristic relaxation times and elastic and viscous parameters. A generalized Kelvin model of viscoelasticity was proposed to describe the measured relaxation curves.

During his PhD thesis in the laboratory, Abbas Mgharbel used the compression apparatus as a simple rheometer by recording the shape relaxation of aggregates initially compressed to a given height h_{comp} (corresponding to a deformation ε_{comp}) during a time t_{comp}. The aggregate deformation is defined by the height change, $\varepsilon = (h_0-h)/h_0$ where h_0 is the aggregate's initial height (*i.e.*, diameter), corresponding to the plate separation at the time of first contact; h is its current height ($h < h_0$). For F9 mouse embryonic cell aggregates, Fig.8A shows the absolute deformation after a prolonged compression (duration t_{comp}), followed by a sudden free decompression (at time taken as t = 0). All curves show an initial fast relaxation (in ~10^2 s) but the aggregate does not recover completely its initial shape during a recording time of about 30 min to 1 h (Fig.1.8 C). The compression has thus promoted irreversible, plastic-like deformations. To recover the initial shape, it is necessary to wait a much longer time, corresponding to the surface tension driven rounding time. These irreversible changes in the aggregate shape occurring at intermediate times were called apparent plasticity [61].

When successive compressions with the same compression time and the same initial relative deformation are applied to an aggregate, plasticity progressively accumulates (Fig. 1.8 A). The relaxation kinetics appear very similar when plotted by using, as a reference height for each compressed aggregate, the final height of the previous step (*i.e.*, relative deformation, Fig.1.8 B) rather than the initial aggregate height. Cells store therefore the same relative plasticity during each compression and release the same relative amount of deformation between two compressions. The viscoelastic response depends only on the relative deformation rate not on the history of the aggregate.

From a physical point of view, cellular aggregates are therefore complex fluids presenting a very complex visco-elasto-plastic behaviour [61].

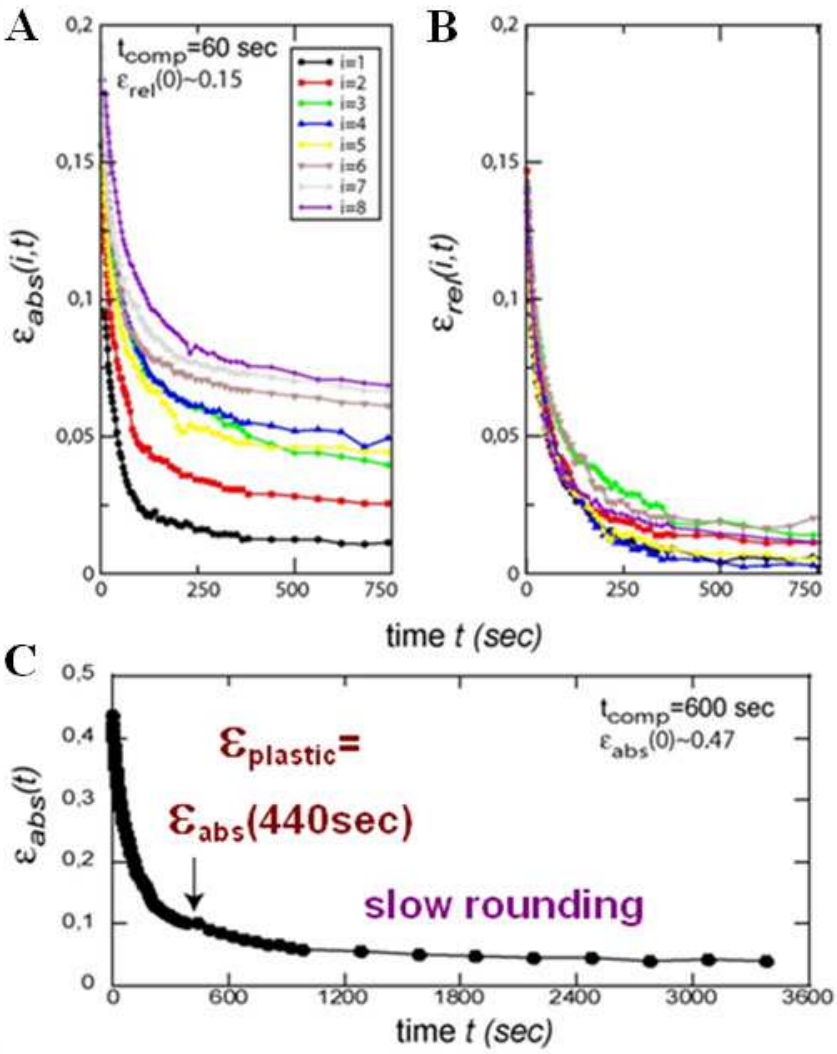

Fig. 1.8: *Aggregate height versus time for F9 cells during free shape relaxation after compression. (A) Absolute deformation* $\varepsilon_{abs}(t) = (h_{ag} - h(i,t))/h_{ag}$*, where* $h(i,t)$ *is the height of the aggregate during relaxation after* i *compressions. For each of eight successive compressions, the compression (*t_{comp} *= 1 min, relative deformation* $\varepsilon_{rel}(0) = 0.15$*) is followed by a sudden decompression at* $t = 0$ *during* t_{decomp} *= 1,600 s. Each curve shows a fast initial relaxation (~*10^2 *s) and then a slower regime. Plasticity is progressively stored during successive compressions. (B) Same data, plotted as relative deformation* $\varepsilon_{rel}(t) = (h_0(i) - h(i,t))/h_0(i)$*, where* $h_0(i)$ *is the height of aggregate just before the* i^{th} *compression:* $h_0(1) = h_{ag}$*,* $h_0(i) = h(i\text{-}1, t=1600\ s)$*. For a given relative deformation, the height relaxation mechanism seems the same for all compressions. (C) Absolute deformation for a single larger and longer compression* $\varepsilon_{abs}(0) = 0.47$*,* t_{comp} *= 10 min. Taken from* [62].

1.2.2 Apparent plasticity and cell-cell rearrangements

Until recently the only direct experimental evidence that cells could relax their stress by changing neighbors was made by Phillips and Steinberg [20]. They showed by electron

microscopy that cells in leghorn embryo cell aggregates submitted to a brief centrifugation (~10 min) are flattened while they regain their original polyhedral shapes when there are submitted to a very long (~1 day) centrifugation period. But this experiment was done on fixed aggregates at these only two extreme time points. No direct observation of cell displacements and rearrangements was therefore available at intermediate time scales.

Abbas Mgharbel showed that two-photon microscopy provides a means to visualize the shape of live fluorescent cells deeply inside aggregates. The intercellular space between cells was stained by the soluble dye sulforhodamine B (SRB) injected in the culture medium and quickly diffusing inside aggregates (the dye also fills completely dead cells that become permeable to SRB). Fig. 1.9 shows two-photon microscopy images at different times of the middle plane of an aggregate just after a 27% compression. Cell 1 initially in proper focus in this plane is moving to another plane to relax stress. A complete analysis of the "amount of rearrangements" in the course of time is needed (this is a complex task as optical contrast is weak and rearrangements occur in 3D), but it is clear that rearrangements start as soon as aggregates are compressed and continue during at least 15 min (the total experimental recording time for this experiment). The fusion of a pair of aggregates was also recorded by confocal microscopy and constitutes a spectacular example of cell rearrangements in the contact area (A. Mgharbel *et al.*, to be published).

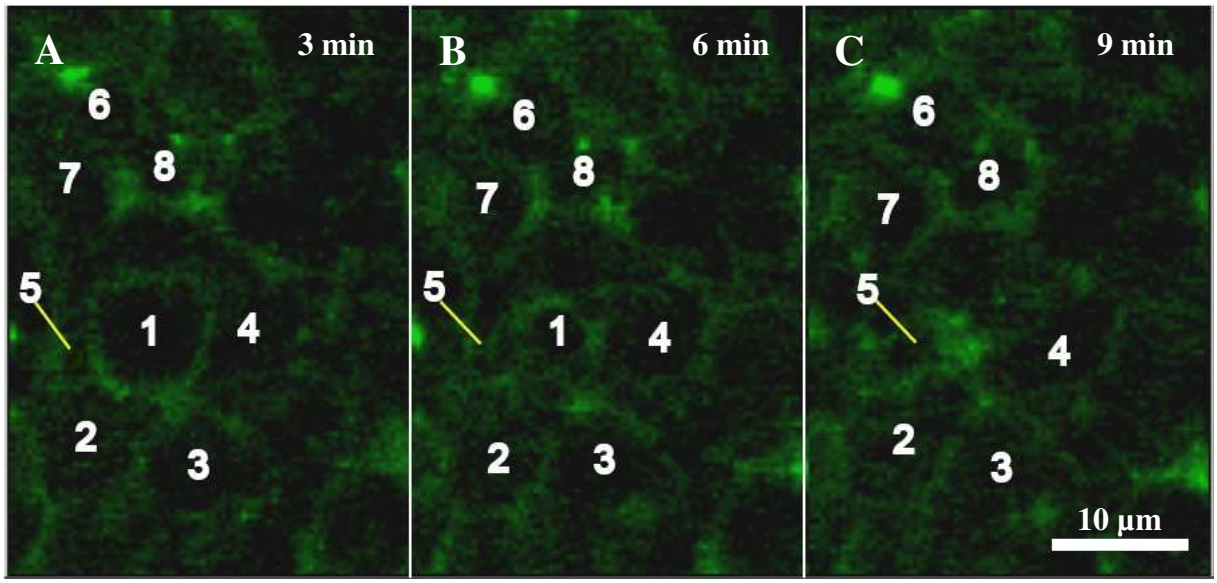

Fig 1.9: *Sketch of cell rearrangements into an inner zone of the middle plane of a compressed cell aggregate. Cells are indicated by numbers to guide the eye and aid to track them during rearrangement. 3 min after the beginning of the compression, cell 1 starts to disappear into another plane (A). At the same time stretching can be identified for cells 4, 5, 6, 7 and 8 inside the imaging plane (B-C). 6 min after, 5 enter into contact with 4, when the interface 3/1 was broken down and gives place to the establishment and growth of the contact between 2 and 4. Taken from* [62].

Cell rearrangements during prolonged stress (for instance compression as in Fig. 1.8) induce apparent plasticity. It was chosen conventionally to quantify the plasticity 440 s after decompression (Fig. 1.8 C, a time much smaller than the liquid time). Then the plastic deformation is given by $\varepsilon_{plastic} = (h_{ag} - h_p)/h_{ag}$, where $h_p = h\ (440s)$.

Fig. 1.10 B summarizes the experimental plasticity measurements as a function of time as well as initial deformation of aggregates. The higher or the longer the compression step, the larger is the remaining plasticity. For example, the apparent plastic deformation after 440 s in the case of Fig. 1.8 C ($\varepsilon_{comp}(0) = 0.47$ and $t_{comp} = 10$ min), is about $\varepsilon_{plastic} = 10\%$.

The solid lines are fitted by a continuum model of cell rearrangements induced by applied stress developed in collaboration with P. Marmottant [61]. The model simply assumes that: (i) cells possess an elastic modulus E; (ii) in order to change neighbors (rearrangements), a cell has to overcome an energy barrier $\Delta\varepsilon$ (as a T1 process in a foam [63]); (iii) both applied stress and fluctuations ξ (effective temperature) help cell to overcome this barrier.

This "Eyring" model displays a characteristic stress and viscosity, τ^* and η^*, which depend on microscopic and kinematic parameters and a characteristic time scale $t_c = \eta^*/E \sim \exp(\Delta\varepsilon / \xi)$. It predicts the stress relaxation during a compression at constant deformation (TST measurements, Fig. 1.10 A) with an initial stress τ_0:

$$\tau(t) = 2\tau^* \tanh^{-1}\left[\tanh\left(\frac{\tau_0}{2\tau^*}\right)\exp\left(-\frac{t}{t_c}\right)\right] \qquad \text{(Eq.1)}$$

The apparent plasticity of Fig. 1.10 is obtained by subtracting the elastic deformation to the initial compression:

$$\varepsilon_{plastic} = \varepsilon_{comp} - \frac{\tau(t_{comp})}{E} \qquad \text{(Eq. 2)}$$

However, by fitting these two types of experiments, two very different time scales were obtained: t_c = 10 min from stress relaxation (Fig. 1.10 A), t_c = 5 hours from apparent plasticity (Fig. 1.10 B). The second one is a liquid time scale associated with cell rearrangements but the first one was interpreted as mostly intra-cellular rearrangements (cytoskeleton). Probing in more detail these intra-cellular rearrangements was one of the main motivations of the rheological experiments performed in a shear geometry in the present work (chapter 4).

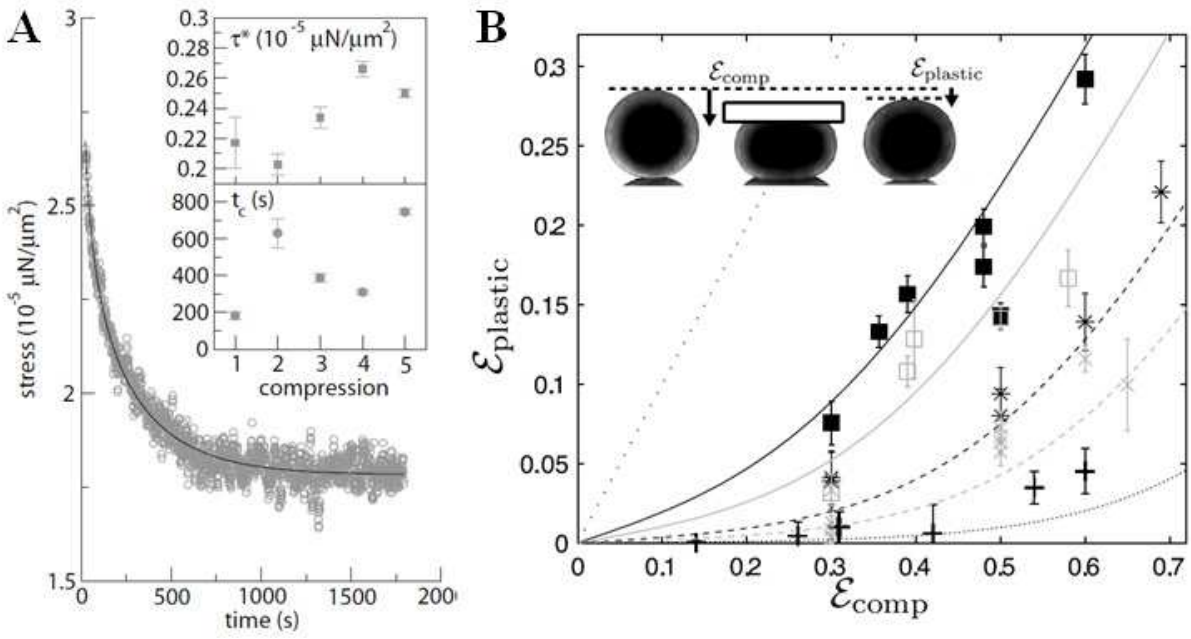

Fig. 1.10: *(A) Stress relaxation while the compression plate is quickly displaced then kept fixed (constant distance h: ''step-strain''). Gray circles, measured stress; solid line, fit from Eq. 1 after subtraction of the asymptotic plateau value. (Inset) Characteristic stress τ* and stress relaxation time t_c fitted for five successive compressions. (B) Apparent plasticity. An aggregate is compressed at a fixed height h_{comp} during a time t_{comp} and then the upper plate is removed and the aggregate is left free to relax. Symbols indicate t_{comp}: black+, 1 min; gray ×, 5 min; black *, 10 min; gray open squares, 30 min; filled squares, 60 min. Lines: prediction of Eq. 1 and 2 plotted with t_c = 5h and τ*/E = 0.13; thin straight dotted line: prediction with $t_{comp} = \infty$, i.e., $\varepsilon_{plastic} = \varepsilon_{comp}$. (Inset) Images of aggregates before compression (h_{ag}), during compression (h_{comp}), and after decompression (h_p); $\varepsilon_{comp} = (h_{ag} - h_{comp})/h_{ag}$, $\varepsilon_{plastic} = (h_{ag} - h_p)/h_{ag}$. h_p is defined and measured as the height h measured by convention after 440 s (Fig. 1.8). Each error bar is estimated on only one aggregate decompression experiment with the uncertainty on the optical measurement of h_{ag}, h_p and h_{comp}; it depends on image resolution and aggregate roughness as well as the possible slight aggregate rotation and translation after decompression. Taken from* [62].

1.2.3 Tissue surface tension

The tissue surface tension (TST) is a macroscopic reflection of the intercellular cohesion and acts to minimize the exposed area of the aggregate. It is a physical quantity that provides a direct quantification of tissue cohesion without any assumption on the microscopic interactions between the cells. One of the goals of this thesis is to find out the biological origin of this property (chapter 3).

1.2.3.1 How to measure TST?

In a general way, the surface tension of liquids is the result of a misbalance in intermolecular cohesion forces between bulk and interfaces. Because surface tension is a positive quantity, its most current manifestation is the formation of spherical droplets that minimize the overall surface area (Fig. 1.11).

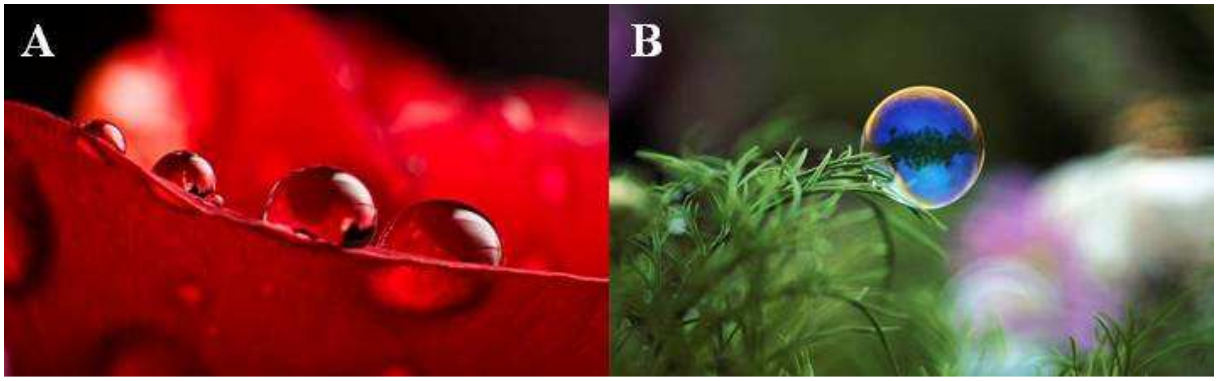

Fig. 1.11: *Typical manifestation of the surface tension on water droplets deposited on different surfaces.*

In the case of aggregates, TST is the result of a misbalance in intercellular forces between bulk and interface. If we forget for a while the eventual role of the cytoskeleton and focus on the role of the adhesion between cells, TST is due to the absence of cell-cell adhesive links at the aggregate medium/interface and reflects intercellular cohesion.

For both a liquid and a tissue, one can ask how to measure internal cohesivity (or cohesion)? It is very important to make the difference between the adhesion energy and the force necessary to detach two adhesive surfaces, which is fundamentally very different. If only adhesion is to be considered, surface tension can be envisioned either as the difference of free energy between two states (attached and not attached) or as the work necessary to separate two surfaces initially in contact. The difference in free energy is linked to the difference in intermolecular interactions at the surfaces. Designing an experiment for trying to apply the second definition is unfortunately impossible. As if one would want to calculate surface tension by applying a force to separate the two surfaces (for calculating a work), one should do that in a quasi-static way, which on biological systems is clearly impossible. So, one should not interpret experiments on the pulling of cell doublets -through AFM cantilever or by aspiration- as experiments giving access to surface tension. In this case, people are quantifying what is often called as the ”strength of the contact” but which is an undefined mixture between equilibrium and dynamical quantities.

Indeed, results are clearly influenced by the pulling rate as the remodeling of the contact zone while stretching can be very important. Thus, as pointed out by Steinberg, the

measurement of surface tension with a tensiometer as developed for the first time by Foty [64] is one of the only ways to get access to this equilibrium quantity. In this sense, surface tension is much easier to understand as a difference in free energy between two states attached or not attached. The surface tension measurement is also the only way to get access to the adhesion energy and to clearly separate equilibrium quantities from dynamical ones (such as viscosity).

The very first quantitative measurement of a tissue's surface tension was made in 1984 by Davis, who performed compression experiments on the mesoderm, the ectoderm and the endoderm of amphibian embryonic cells. The very next work in this field was done by G. Forgacs, R. Foty and M. S. Steinberg, who in 1994 designed their own tensiometer. Using chicken embryos, they showed that indeed the values of the apparent surface tension can predict the envelopment of different types of tissue [22,23,52,64], as stated by the DAH. Since, other groups have been using different approaches of this technique [7,65].

Together with the compression plate tensiometry [64,66], two other methods exist to measure TST: axisymmetric drop shape analysis of centrifuged aggregates [67,68] and aspiration of cell aggregates in a micropipette [69].

In the followings, a very brief description of each method will be presented.

a) The axisymmetric drop shape analysis of centrifuged aggregates

For a long time, centrifugation of cell aggregates was performed only for qualitative purposes [19] . Later on the method became quantitative by combining it with the axisymmetric drop shape analysis for imperfect profile (ASDA-IP) [67] or with the standard axisymmetric drop shape analysis (ASDA) [68].

During these experiments the centrifugal force that tends to flatten the aggregates is balanced by the surface tension of the tissue which tends to round the aggregate, and these two parameters determine the shape of the aggregate in equilibrium. This force balance is governed by the Laplace equation of capillarity. Therefore, the ASDA methods are simply based on the numerical fit between the shape of the experimental cell aggregate (width, height and volume) and the mathematical model given by the classical Laplace equation of capillarity. The surface tension measured is independent of the centrifugal forces and aggregate size.

b) Aspiration of cell aggregates in a micropipette

Guevorkian *et al.* used this approach a few years ago and developed a model which is based on the viscoelastic behavior and surface tension of cell aggregates [69]. The micropipette can vary in diameter between 40 and 70 µm (*i.e.*, 3 to 5 times that of a single cell) and a large range of pressures can be attained (0.1 to 5 kPa).

As the spheroid is aspirated inside the pipette at a constant pressure, in this case the applied stress is constant and the tissue flows, continuously stretching the cells. Thus the

viscoelastic properties can be deduced from the strain variation. The authors emphasize the existence of two distinct regimes: a fast elastic deformation which is followed by a viscous flow. According to their results, the aggregate surface tension is stress dependent, with reinforcement in tissue cohesion. They also suggest that the reinforcement of the surface tension is actually a signature of an active cellular response to mechanical forces leading to cytoskeletal remodelling.

c) The compression plate tensiometry

The compression plate tensiometry remains however the most widely used quantitative method. In this case, the strain is constant and the stress relaxes to an equilibrium state. It is based on the fact that, at long time scales, once elastic forces are relaxed, the surface tension can be measured by assuming that cell aggregates verify the same physical laws of capillarity as liquid droplets.

Besides the surface tension which is measured after force relaxation, this technique can also give access to tissue's viscosity by analyzing shape relaxation after an imposed deformation [56].

In our study we chose to use this method and more details can be found in the Materials and methods chapter 2.

1.2.3.2 A true surface tension?

Published measurements of surface tension are usually robust and do not depend on compression magnitude and duration, nor on aggregate size [52,64,65,70] and our new results with F9 cell line in chapter 3 confirm this robustness. In addition, as discussed previously, TST values often predict equilibrium configurations of mixed aggregates.

However, TST measurements are often delicate to perform due to the long equilibration times that are necessary to be sure to measure a steady state quantity. The time between two successive compressions is usually between 30 min and 2 h [58,64]. When using a compression plate apparatus, an equilibrium force seems to be attained 2–10 min after compression [52,61]. This time is probably large enough to relax internal contributions (cytoskeleton reorganization) and we will indeed see in this thesis that cells are immediately flowing when stress is applied. But, unlike what is assumed for instance in [52], Abbas Mgharbel showed that only a limited number of rearrangements have taken place during that time (see 1.2.2). So flow of cells will be stopped by surface tension, and it will be triggered again by surface tension forces when the compression force is released. This will lead to the relatively rapid shape relaxation of the aggregate, which could be interpreted as a pseudo-elasticity, but which is however not perturbing the surface tension measurement.

In principle, we could check in more details this hypothesis of complete elastic relaxation through cell flow by designing robust experimental set-up for which each compression step could be followed by a long resting period (overnight or day if necessary). We have found in this work by performing long term rheological experiments (chapter 4) that our aggregates remain in good conditions (same rheological properties) during such a long times. The tissue tensiometer should be therefore designed to be able to measure TST after such long resting times.

1.2.3.3 Hypotheses to explain tissue surface tension

M. S. Steinberg postulated that TST arises from difference in cell-cell adhesion and cell-external medium adhesion. In 2005, Foty and Steinberg measured a perfect linear correlation between cadherin expression level and aggregate surface tension [71]. The authors concluded that TST arises only from the energies of intercellular adhesions. They also stated that so far non-convincing experimental data indicated any another microscopic dependence. However this conclusion and statement were questioned several times recently and according to new experimental data reported, TST is likely to depend as well on the cytoskeleton contractility [13,58,62,72]. The Differential Interfacial Tension Hypothesis (DITH) [13,26–28] relates the tissue surface tension to the tension along the edges of individual cells. It was first introduced by Harris in the 70s [26] and then developed by other researchers in several studies [13,27,28].

We will discuss in more details these issues in the introduction of chapter 3.

1.3 Rheology of the cell - State of the art

Where do all rheological cell properties come from? Even though the present thesis is concerned primarily with the rheological characterization of cell aggregates, in order to achieve a good understanding of this issue, some basic knowledge of the structural elements in a single cell which might influence its mechanical behaviour is crucial.

Each eukaryotic cell is surrounded by the plasma membrane, which is a thin membrane consisting of a bilayer of phospholipids, whose mechanical behavior is however highly modified by the actin cortex, a network of filamentous acto-myosin anchored just underneath. Beyond this membrane we find the body of the cell together with the nucleus. While we believe that cytoskeletal components are more likely to dominate the rheological properties of cells, the nucleus can also play a significant role in the rheological behavior of

single cells or aggregate of cells, depending on the compression rate or the deformation rate. However, not much is known on this issue.

The cell body is composed mainly by the cytoskeleton but the mitochondria, the endoplasmic reticulum and the Golgi apparatus are also present in the cytoplasm. All these structures play important roles in the cellular functioning and activity but herein after we will refer only to the cytoskeleton as being the main component of the cell influencing its mechanical properties.

The cytoskeleton is a filamentous protein network and it constitutes the scaffold of a cell, determining the mechanical deformation characteristics [73–75]. The actomyosin cytoskeleton is represented by networks of fiber-like actin filaments which are cross-linked by different proteins and put under tension by myosin II molecular motors. While very little information exists on the influence of intermediate filaments and microtubules (which are also a consistent part of the cytoskeleton), the most studied candidate for playing a decisive role in the rheology of cells is actin, which is the major protein constituent of the cytoskeleton.

Many different techniques have been employed to measure the mechanical properties of cells under stress (Fig. 1.12). Kasza *et al.* made a very good review of this subject [76].

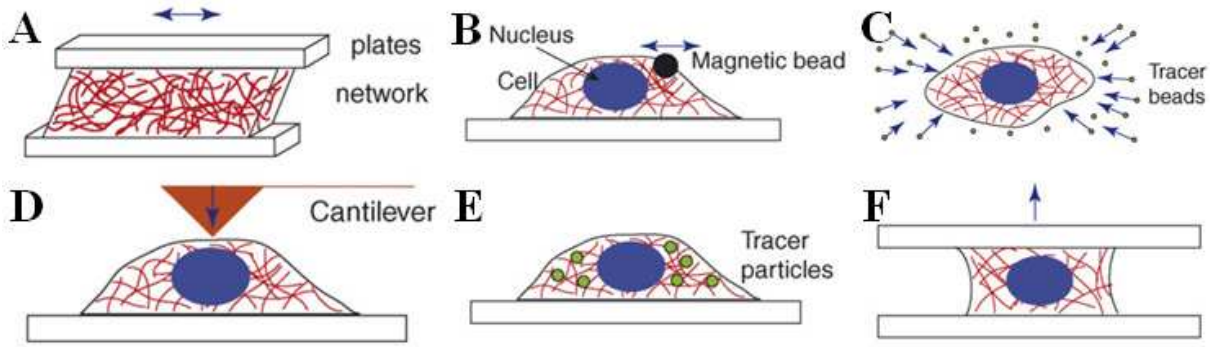

Fig. 1.12: *Common physical methods to probe mechanical properties of cells. (A) Bulk rheology: a material is sheared between two plates using an oscillatory stress to probe the shear elastic, G' (in-phase) and viscous, G" (out-of-phase) moduli. (B) Magnetic bead cytometry: an external magnetic field applies a stress to a magnetic bead. The bead is position tracked to determine the response. (C) Traction force microscopy: cell contractions deform a flexible substrate. Forces are estimated from bead displacements. (D) Atomic force microscopy: a cantilever applies stress to the cell. The cantilever deflection is measured by laser reflection. (E) Microrheology: the motion of probe particles is measured using either video or laser tracking techniques. Particle motion is either driven externally or thermally induced and is interpreted to yield the viscoelastic modulus. (F) Whole cell stretching: a cell is attached to two surfaces. A force is applied to one surface and the plate separation is measured. Taken from* [76].

Many authors have claimed to have measured some kind of universal law describing the behavior of cells but we still can find some discrepancies in the literature. We will try to summarize here a few of the results obtained on the rheology of reconstituted network or cells.

1.3.1 Linear rheology: G'(ω) , G''(ω)

A few years ago, Hofmann *et al.* claimed that there was a consensus among all the different measurements done on cells, and showed that two regimes could be observed [77]. At high frequencies, cells present a power law with an exponent ¾, whereas at low frequencies the exponent is much weaker and will depend on the network which is being probed (cortical/lamellar versus intracellular one).

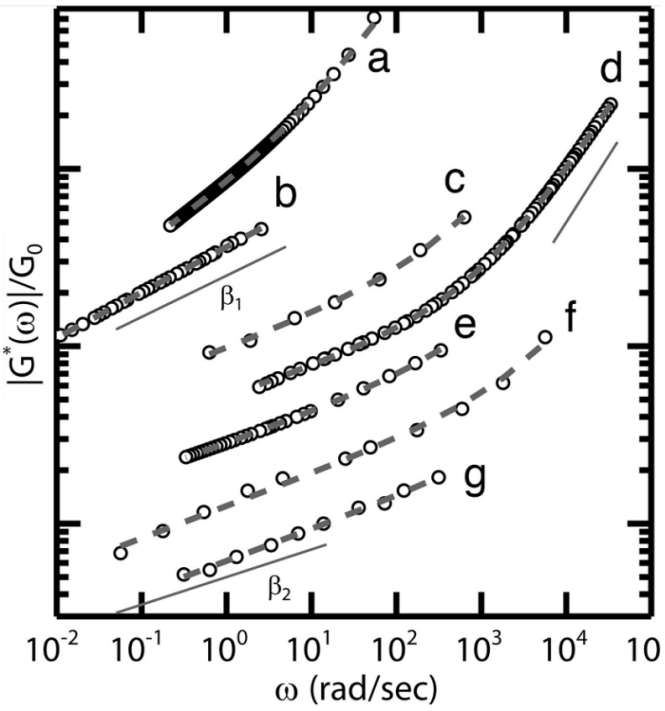

Fig. 1.13: *Summary of literature shear moduli versus frequency, offset vertically for clarity. From top to bottom: mechanical measurements from cell creep (magnetic pulling)* [78] *(a), uniaxial rheometry* [79] *(b), atomic force microscopy* [80] *(c), LTM in the lamellae* [81] *(d), cell creep (magnetic bead twisting)* [82] *(e), MTC* [83] *(f), and optical tweezers* [84] *(g). All data are well fit to a sum of power laws (the generalized Stokes–Einstein relation). Magnetic pulling and uniaxial rheometry (a and b) results have fit slopes of 0.29 and 0.26 (comparable to the mechanical response of intracellular cytoskeletal networks obtained in* [77]*), whereas others (c–g) have slope of 0.16–0.18 (comparable to the response of cortical networks). Taken from* [77].

Using four different rheological techniques (MTC – Magnetic Twisting Cytometry, TPM – Two point Microrheology, internal LTM – Laser Tracking Microrheology, external LTM), the authors obtained a consensus regarding the frequency dependence and compartmented nature of the mechanical response. However, the absolute stiffness of either structure does not provide a good agreement (TPM technique provides a model-independent stiffness while LTM requires a Stokes-like boundary condition model which is not quantitatively accurate). While differences in stiffness of the cell type, and not differences in

frequency dependence could explain this discrepancy, authors suggest that errors in modeling the cytoskeletal deformation field and structure near tracer probes are more likely to cause this disagreement.

It seems that now we may have to consider even a third behavior at very low frequency. In a recent review on particle tracking rheology, Wirtz explained the regime as a function of the actin network dynamics [85]. He is using creep compliance (*i.e.*, a measurement of strain over stress γ/σ while a fixed stress is applied to the system), which can enable to calculate back through Fourier or Laplace transform G', G''.

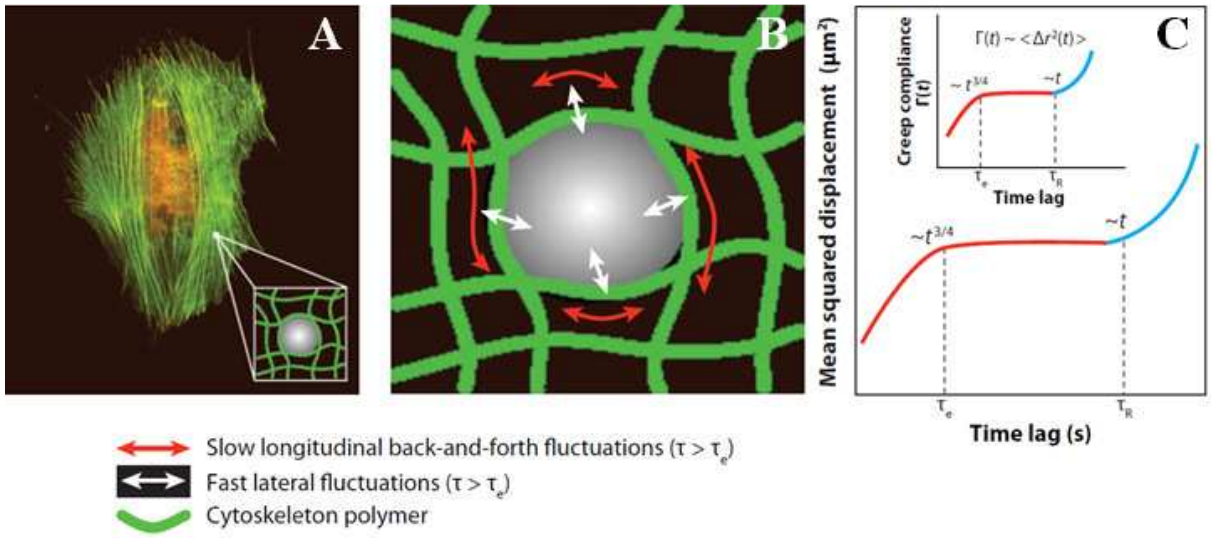

Fig. 1.14: *Physical origin of the displacements of beads in the cytoplasm. (A) Ballistically injected beads are lodged within the cytoskeleton. The size of the beads is larger than the average mesh size of the cytoskeleton network, which is ~50 nm in fibroblasts. (B) The spontaneous movements of the cytoskeleton filaments that surround each bead induce displacements of the beads. At short timescales, the displacements of the beads are predominantly induced by the fast lateral bending fluctuations of the cytoskeleton filaments. At long times, the displacements of the beads are predominantly induced by the slow longitudinal back-and-forth lateral fluctuations of the cytoskeleton filaments. Finally, filaments move sufficiently to allow beads to escape the cage to move to the next cage. (C) Accordingly, the mean squared displacements (MSDs) of the beads show a $t^{3/4}$ power-law dependence at short timescales, a quasi plateau value at intermediate timescales between τ_e and τ_R, and a linear dependence at long times caused by the slow viscous diffusion of the beads. (Inset) The deformability of the cytoplasm [creep compliance, $\Gamma(t)$] is proportional to the MSD of the beads, $\langle \Delta r^2(t) \rangle$. Taken from* [85].

Thus, over the full range of timescales that include physiologically relevant frequencies, cells exhibit multiple regimes which cannot be described by a single power-law.

Another example of transition between power-law regimes that occur over a well-defined timescale can be found in [86]. Stamenovic *et al.* found that $|G^*|$ versus f relationships

exhibited two distinct power-law regimes: one less frequency-dependent (10^0-10^3 Hz) with exponent α_1=0.2 and the other more (10^{-3}-10^{-1} Hz) with α_2=0.33, separated by a third well defined plateau regime (10^{-1}-10^0 Hz) (Fig. 1.15), where no power-law behavior can be seen. Moreover, the transition time appears to be cell type-specific.

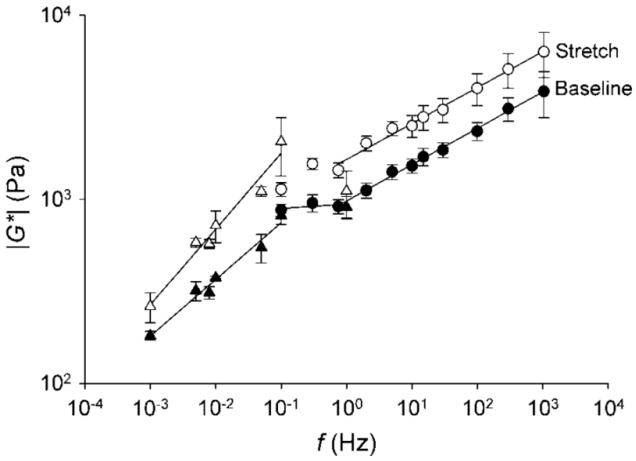

Fig. 1.15: *The magnitude of the dynamic modulus (|G*|) versus frequency (f) relationship measured in cultured HASM cells at the baseline (solid symbols) and after cell stretching by an ~12% uniform substrate strain (open symbols) using oscillatory magnetic cytometry. Cells displayed two power-law regimes at 10^0–10^3 Hz and at 10^{-3}–10^{-1} Hz, separated by a plateau (10^{-1}–10^0 Hz). Each regime was fitted by a function ~f^{α} (solid lines). Data are means ± SE of median values of |G*| obtained from 180 to 500 magnetic beads distributed in 3–5 different wells for each condition (circles and triangles indicate data from two protocols). Taken from* [86].

The authors propose an explanation for the mechanism responsible for the plateau behavior: it could be due to a limited-length distribution of the actin filaments when analyzed at high frequencies (as usually the plateau can occur when one power-law regime saturates). At lower frequencies, limited-length distributions of intermediate filaments and/or microtubules can explain the power-law regime.

A model which has been proposed to describe the rheological behavior of living cells is the soft glass rheology (SGR) theory [82,83,87–89] derived from soft matter physics. It remarkably captures the linear rheology and the fluidization responses to stretch of living cell [83,89].

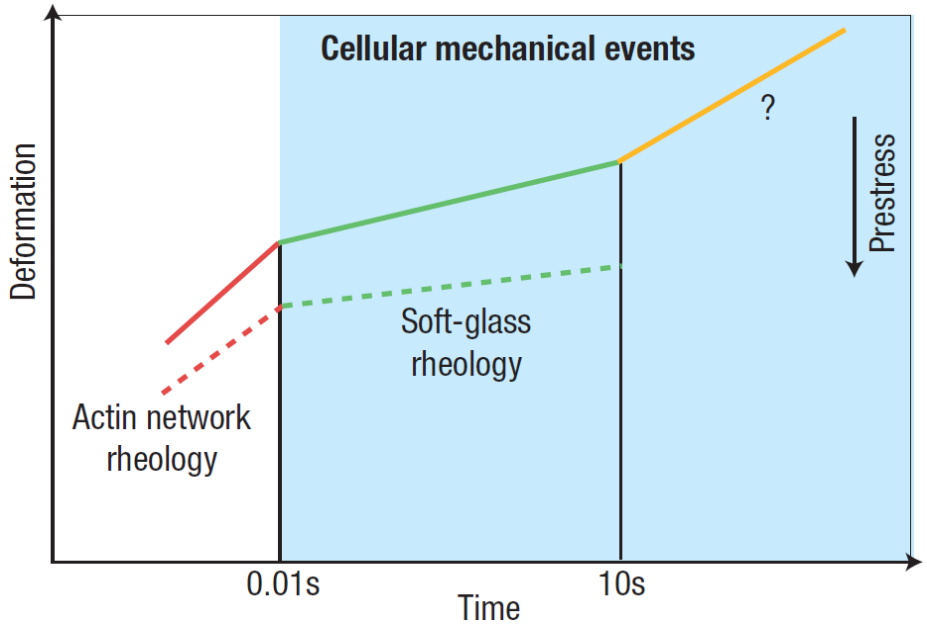

Fig. 1.16: *A log–log plot of the creep response - a time course of cell deformation produced by a constant applied stress - summarizes the current understanding of cell rheology. The creep response is characterized by three regimes: an initial fast creep (~0–0.01 s) governed by the viscoelastic behavior of the semi-flexible actin network (scales with the power-law exponent α = 0.75 indicated by the red segment)* [88,90]*; a very slow creep (~0.01–10 s) governed by the SGR dynamics (α ≈ 0.05–0.35, indicated by the green segment)* [83,87,88,91]*, and an intermediate slow creep (above ~10 s, indicated by the yellow segment) governed by mechanisms that are still unknown (α ≈ 0.5)* [79,92]*. The slope of each of the segments is indicative of the corresponding α. An increase in prestress (direction of the increase indicated by the arrow) causes a decrease in deformation (that is, an increase in stiffness) and a decrease in α, as indicated by the dashed lines* [83,88,91,93]*. Integrated mechanical events of the cell (spreading, crawling, contracting, reorienting, invading and so on) are set within timescales that correspond to the intermediate–slow time regimes. Taken from* [94].

Let's finally mention, the study by Goldmann and Ezzel [95], which was conducted on the same cell type as used in this thesis: F9 WT (and F9 vinculin-deficient (5.51) cells, not used here). Cells are exposed to controlled cantilever loads of the AFM. Using the Hertz model they found the average calculated elastic values of cantilever loads being ~ 3.83 and ~ 2.47 kPa for WT and 5.51 cells, respectively.

They also used rotation disc rheometry and by applying an oscillatory shear force, they detected a plateau regime of G'(ω) for WT cells at lower frequencies ($\omega = 5x10^{-3}$ - 10^{-2} rad/s) and a power-law behavior of $G' \sim \omega^{1/5}$ for higher frequencies ($\omega = 10^{1} - 5x10^{1}$ rad/s). On the other side, for the 5.51 cells no plateau at G' has been obtained and the power-low behavior reduced to $G' \sim \omega^{1/8}$. Both moduli G' and G" are lower for 5.51 than for WT cells (Fig. 1.17).

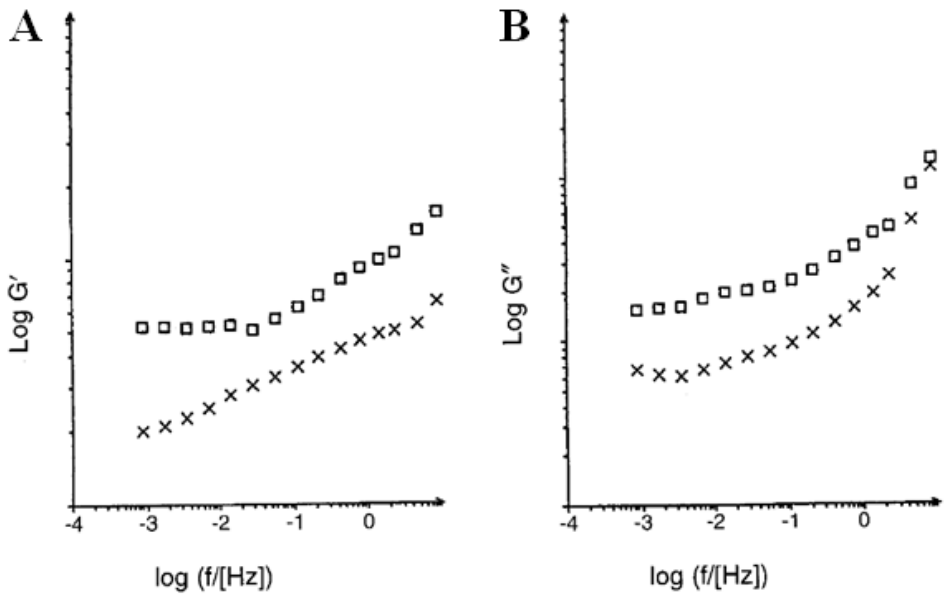

Fig. 1.17: *The log–log plots G'(ω) and G"(ω) against frequency represent the average of three reproducible measurements of F9 WT cells (open squares) and vinculin-deficient (5.51) cells (crosses), demonstrating only the relative differences between the storage (G') (A) and the loss (G") modulus (B) of a pellet of ~55*10^6 F9 WT and vinculin-deficient (5.51) cells. Note: to measure absolute values for G' and G" much higher shear forces need to be applied. Taken from* [95].

Showing there is a clear difference in the viscoelastic behavior of both cells, the authors raised the question whether vinculin provides a mechanical link between the cell surface and the cytoskeleton.

The main conclusion one can raise from this linear rheology studies is that G' and G'' are piece-linear function in a log-log representation. Let's turn now to an even more complex problem: non linear rheology.

1.3.2 Non-linear rheology: Stiffening and softening

How do exactly cells adapt to stress? This complex phenomenon has been extensively studied and several descriptions of the dynamics of cell mechanical response under stress have been proposed.

1.3.2.1 Stiffening

a) Active stiffening

It has been shown that by applying local forces on cells, their rigidity increases [96] and the actin remodels near the applied force [97,98]. Icard-Arcizet *et al.* [99] quantified, using A549

human alveolar epithelial cells and C2C12 mice myoblastic cells, the dynamics of cell stiffening and actin recruitment in response to a controlled external stress (force applied through an Arg-Gly-Asp coated bead adhering on the cell and trapped in optical tweezers).

They showed that the kinetics of stiffening and actin recruitment exhibit a strong correlation, with a typical timescale of around 600 s [99]. This behavior is clearly active and is due to cell mechanosensitive capacity.

b) Passive stiffening

It has been measured in different biopolymer networks cells and tissues. It can either arise from fibers alignment along the directions of deformation or from the nonlinear force-elongation relationship of individual semiflexible filaments.

This stiffening has already been for example reported in cells by Fernandez *et al.*[100], Trepat *et al.* [101] and Kollmansberger *et al.* [102].

1.3.2.2 Softening

However, recently the group of Fredberg proposed that softening (or fluidization) is a more evident strategy deployed by cells in order to respond to stress [89]. They indeed measured such behaviors in several cell types. For that, they stressed cell monolayers plated on an elastic substrate which can be homogeneously stretched and measured the elastic cell parameters after relaxation of the stress using OMTC (ferromagnetic beads attached to the cell surface are submitted to a magnetic oscillating field).

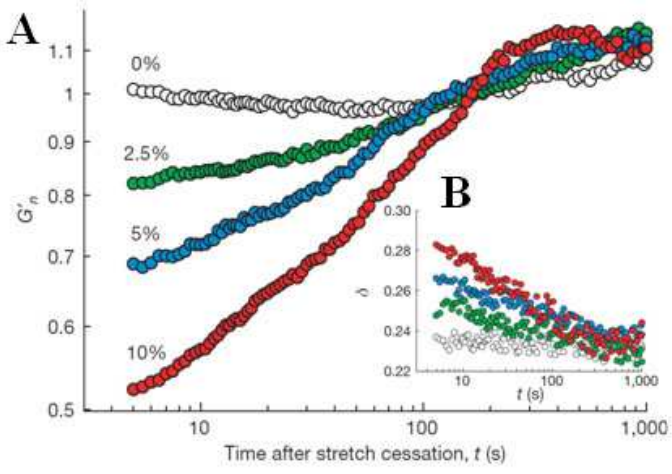

Fig. 1.18: *A single transient stretch drives fractional stiffness G'_n down and the phase angle δ up, indicating fluidization of the cytoskeleton. (A) Evolution of G'_n of HASM cells after a single transient stretch of 0% (no stretch, open circles), 2.5% (green), 5% (blue) and 10% (red). The response of each bead was normalized to its pre-stretch value. (B) Evolution of the phase angle after stretch application. Taken from* [89].

They showed that the extent of fluidization depends on the state of a system before being subjected to transient stretch: the closer was the system to a solid-like state, the greater the extent of fluidization and the faster its subsequent resolidification. Making an analogy to

dynamics in inert glassy systems, authors suggest that this behavior can be predicted by the soft glassy rheology model.

1.3.2.3 Reconciling both behaviors

a) Active stiffening and softening

To find out which one of these factors prevails over the other, Krishnan *et al.* [103] used the CMR (Cell Mapping Rheometry) approach on airway smooth muscle cells, mapping in space and in time the traction stress response to well-defined imposed stretch. Thus, combining cell stretch (indentation of the gel on which cells are plated on) with traction force microscopy, authors show that the fluidization response is always occurring while the reinforcement only happens when the applied stretch was anisotropic.

One has to emphasize that using the pulse technique developed by the authors where the elastic modulus is measured at no stress, no passive stiffening could be ever measured.

b) Passive stiffening and softening

Wolff *et al.* [104] recently showed that one behavior (softening) could mask the other (stiffening) in controlled cyclic shear rate experiment (strain is linearly increased and then decreased at a specific shear rate), if strain amplitude or shear rate are too low. If one wants to unravel the stiffening signature higher shear rate and amplitude should be used.

1.3.3 Cells versus networks of filamentous F-actin

Networks of filamentous actin (F-actin) formed under physiological conditions (thus at physiological concentration) can provide a good experimental toolbox in the analysis of the cytoskeleton's mechanical properties [105–108].

A strain hardening behavior was found to characterize the actin filaments networks [109]. Xu *et al.* showed that the dynamic cross-linking protein α-actinin plays an important role in the rheology of F-actin reconstituted networks, as it enhances the strain hardening of F-actin (particularly at high rates of shear, where filaments do not have sufficient time to slide past one another) and also, it allows F-actin to withstand larger deformations. However, both the levels of elasticity at low strain amplitudes and the extent of strain hardening given by *in-vivo* measurements are higher in single cells [81,110,111], indicating that a system formed by F-actin and α-actinin is not sufficient to reconstitute the full mechanical response of cells and that some other proteins may be required.

Later, studies have shown that the type of crosslinkers will change the stiffening behavior: scruin, which rigidly crosslinks the network, shows a stiffening exponent of 1.5 with stress [90], while networks with more compliant crosslinkers such as filamin, however, exhibit a linear dependence of stiffness on stress, and show a decrease in the power law exponent with increasing stress [108], much more in agreement with what has been observed in cells [102,112].

We will end this description of the literature on cell rheology by a citation of Kollmansberger *et al.* [102]:

"Due to the structural complexity of the cytoskeleton, however, a single crosslinker alone such as filamin cannot account for the nonlinear rheological properties of the cell. Instead, the fact that stress stiffening, power-law rheology and fluidization are observed in a wide variety of biological and biopolymer systems of different molecular compositions but similar structural architecture leads to the conclusion that the common rheological features have no specific molecular but rather a structural origin, such as dynamic bond turnover."

We will use this concept later on.

References:

1. Moscona, A. The development in-vitro of chimeric aggregates of dissociated embryonic chick and mouse cells. *Proceedings of the National Academy of Sciences of the United States of America* **43**, 184–94 (1957).

2. Sutherland, R. M., McCredie, J. A. & Inch, W. R. Growth of multicell spheroids in tissue culture as a model of nodular carcinomas. *Journal of the National Cancer Institute* **46**, 113–20 (1971).

3. Mueller-Klieser, W. Multicellular spheroids. A review on cellular aggregates in cancer research. *Journal of cancer research and clinical oncology* **113**, 101–22 (1987).

4. Weigelt, B. & Bissell, M. J. Unraveling the microenvironmental influences on the normal mammary gland and breast cancer. *Seminars in cancer biology* **18**, 311–21 (2008).

5. Duguay, D., Foty, R. A. & Steinberg, M. S. Cadherin-mediated cell adhesion and tissue segregation : qualitative and quantitative determinants. *Cell* **253**, 309 –323 (2003).

6. Leckband, D. & Sivasankar, S. Mechanism of homophilic cadherin adhesion. *Current Opinion in Cell Biology* 587–592 (2000).

7. Norotte, C., Marga, F., Neagu, A., Kosztin, I. & Forgacs, G. Experimental evaluation of apparent tissue surface tension based on the exact solution of the Laplace equation. *EPL (Europhysics Letters)* **81**, 1–6 (2008).

8. Robinson, E. E., Zazzali, K. M., Corbett, S. A. & Foty, R. A. Alpha5beta1 integrin mediates strong tissue cohesion. *Journal of cell science* **116**, 377–86 (2003).

9. Pourquié, O. *Biologie du développement*. (Editions Hermann: 2002).

10. Froese, R. & Pauly, D. http://www.fishbase.org. *FishBase. World Wide Web electronic publication.* (2012).

11. Thisse, B. & Thisse, C. Établissement des axes embryonnaires au cours du développement du poisson zèbre PA. *Med Sci (Paris)* **18**, 193–204 (2002).

12. Kimmel, C. B. & Warga, R. M. Tissue-specific cell lineages originate in the gastrula of the zebrafish. *Science (New York, N.Y.)* **231**, 365–8 (1986).

13. Krieg, M. *et al.* Tensile forces govern germ-layer organization in zebrafish. *Nature cell biology* **10**, 429–36 (2008).

14. Pouille, P.-A., Ahmadi, P., Brunet, A.-C. & Farge, E. Mechanical signals trigger Myosin II redistribution and mesoderm invagination in Drosophila embryos. *Science signaling* **2**, ra16 (2009).

15. Armstrong, P. B. Cell sorting out: the self-assembly of tissues in vitro. *Critical reviews in biochemistry and molecular biology* **24**, 119–49 (1989).

16. Wilson, H. V. On some phenomena of coalescence and regeneration in sponges. *Journal of Experimental Zoology* **5**, 245–258 (1907).

17. Townes, P. L. & Holtfreter, J. Directed movements and selective adhesion of embryonic amphibian cells. *Journal of Experimental Zoology* **128**, 53–120 (1955).

18. Holtfreter, J. A study of the mechanics of gastrulation. *Journal of Experimental Zoology* **95**, 171–212 (1944).

19. Phillips, B. Y. H. M. & Steinberg, M. S. Equilibrium measurements of embryonic chick cell adhesiveness, i. shape equilibrium in centrifugal fields*. 121–127 (1969).

20. Phillips, H. & Steinberg, M. S. Embryonic tissues as elasticoviscous liquids. I. Rapid and slow shape changes in centrifuged cell aggregates. *Journal of cell science* **30**, 1 (1978).

21. Steinberg, M. S. Reconstruction of tissues by dissociated cells. Some morphogenetic tissue movements and the sorting out of embryonic cells may have a common explanation. *Science* **141**, 401–408 (1963).

22. Takeichit, M. & Steinberg, M. S. Experimental specification of cell sorting , tissue spreading , and specific spatial patterning by quantitative differences in cadherin expression. *Proc Natl Acad Sci USA* **91**, 206–209 (1994).

23. Foty, R. A., Pfleger, C. M., Forgacs, G. & Steinberg, M. S. Surface tensions of embryonic tissues predict their mutual envelopment behavior. *Development* **122**, 1611 (1996).

24. Fukunaga, Y., Liu, H., Shimizu, M., Komiya, S. & Kawasuji, M. Defining the Roles of b-catenin and Plakoglobin in Cell-cell Adhesion : Isolation of b-catenin / plakoglobin-deficient F9 Cells. *Cell Structure and Function* **34**, 25–34 (2005).

25. Davis, G. S., Phillips, H. M. & Steinberg, M. S. Germ-Layer Surface Tensions and "' Tissue Affinities '" in Rana pipiens Gastrulae : Quantitative Measurements. *Developmental Biology* **644**, 630–644 (1997).

26. Harris, A. K. Is cell sorting caused by differences in the work of intercellular adhesion? A critique of the Steinberg hypothesis. *Journal of Theoretical Biology* **61**, 267–285 (1976).

27. Graner, F. Can surface adhesion drive cell-rearrangement? Part I: Biological cell-sorting. *Journal of theoretical biology* **164**, 455–455 (1993).

28. Brodland, G. W. The Differential Interfacial Tension Hypothesis (DITH): A Comprehensive Theory for the Self-Rearrangement of Embryonic Cells and Tissues. *Journal of Biomechanical Engineering* **124**, 188 (2002).

29. Wacker, S., Grimm, K., Joos, T. & Winklbauer, R. Development and control of tissue separation at gastrulation in Xenopus. *Developmental biology* **224**, 428–39 (2000).

30. Rohani, N., Canty, L., Luu, O., Fagotto, F. & Winklbauer, R. EphrinB/EphB signaling controls embryonic germ layer separation by contact-induced cell detachment. *PLoS biology* **9**, e1000597 (2011).

31. Dietrich, J. *et al.* Of layers and spheres : the reaggregate approach in tissue engineering. *Trends in Neurosciences* **25**, 131–134 (2002).

32. Lorenzo, C. *et al.* Live cell division dynamics monitoring in 3D large spheroid tumor models using light sheet microscopy. *Cell division* **6**, 22 (2011).

33. Wang, F. *et al.* Phenotypic reversion or death of cancer cells by altering signaling pathways in three-dimensional contexts. *Journal of the National Cancer Institute* **94**, 1494–503 (2002).

34. Wang, F. *et al.* Reciprocal interactions between β1-integrin and epidermal growth factor receptor in three-dimensional basement membrane breast cultures: A different perspective in epithelial biology. *Proceedings of the National Academy of Sciences* **95**, 14821–14826 (1998).

35. Desoize, B. & Jardillier, J.-C. Multicellular resistance: a paradigm for clinical resistance? *Critical reviews in oncology/hematology* **36**, 193–207 (2000).

36. Hirschhaeuser, F. *et al.* Multicellular tumor spheroids: An underestimated tool is catching up again. *Journal of Biotechnology* **148**, 3–15 (2010).

37. Sutherland, R. Cell and environment interactions in tumor microregions: the multicell spheroid model. *Science* **240**, 177–184 (1988).

38. Lobjois, V., Frongia, C., Jozan, S., Truchet, I. & Valette, A. Cell cycle and apoptotic effects of SAHA are regulated by the cellular microenvironment in HCT116 multicellular tumour spheroids. *European journal of cancer (Oxford, England : 1990)* **45**, 2402–11 (2009).

39. Truchet, I. *et al.* Estrogen and antiestrogen-dependent regulation of breast cancer cell proliferation in multicellular spheroids: Influence of cell microenvironment. *International journal of oncology* **32**, 1033–9 (2008).

40. Frongia, C. *et al.* 3D imaging of the response to CDC25 inhibition in multicellular spheroids. *Cancer biology & therapy* **8**, 2230–36 (2009).

41. Aressy, B., Bugler, B., Valette, A., Biard, D. & Ducommun, B. Moderate variations in CDC25B protein levels modulate the response to DNA damaging agents ND SC CE RIB ND ES SC RIB. **7**, 2234–2240 (2008).

42. Brezak, M.-C. *et al.* IRC-083864, a novel bis quinone inhibitor of CDC25 phosphatases active against human cancer cells. *International journal of cancer. Journal international du cancer* **124**, 1449–56 (2009).

43. Marga, F., Neagu, A., Kosztin, I. & Forgacs, G. Developmental Biology and Tissue Engineering. **328**, 320–328 (2008).

44. Jakab, K., Neagu, A., Mironov, V., Markwald, R. R. & Forgacs, G. Engineering biological structures of prescribed shape using self-assembling multicellular systems. (2004).

45. Jakab, K. *et al.* Tissue engineering by self-assembly of cells printed into topologically defined structures. *Tissue engineering. Part A* **14**, 413–21 (2008).

46. Jakab, K. *et al.* Tissue engineering by self-assembly and bio-printing of living cells. **022001**, (2010).

47. Wilson, W. C. & Boland, T. Cell and organ printing 1: protein and cell printers. *The anatomical record. Part A, Discoveries in molecular, cellular, and evolutionary biology* **272**, 491–6 (2003).

48. Boland, T., Mironov, V., Gutowska, A., Roth, E. A. & Markwald, R. R. Cell and organ printing 2: fusion of cell aggregates in three-dimensional gels. *The anatomical record. Part A, Discoveries in molecular, cellular, and evolutionary biology* **272**, 497–502 (2003).

49. Mironov, V., Boland, T., Trusk, T., Forgacs, G. & Markwald, R. R. Organ printing: computer-aided jet-based 3D tissue engineering. *Trends in Biotechnology* **21**, 157–161 (2003).

50. Liu, V. A. & Bhatia, S. N. Three-Dimensional Photopatterning of Hydrogels Containing Living Cells. *Biomedical Microdevices* **4**, 257–266 (2002).

51. Neagu, A., Jakab, K., Jamison, R. & Forgacs, G. Role of Physical Mechanisms in Biological Self-Organization. *Physical Review Letters* **95**, 1–4 (2005).

52. Forgacs, G., Foty, R. A., Shafrir, Y. & Steinberg, M. S. Viscoelastic Properties of Living Embryonic Tissues : a Quantitative Study. *Biophysical journal* **74**, 2227–2234 (1998).

53. Beysens, D. A., Forgacs, G. & Glazier, J. A. Cell sorting is analogous to phase ordering in fluids. *Cell* (2000).

54. Gordon, R., Goel, N. S., Steinberg, M. S. & Lawrence, L. W. Gordon et al. - 1972 - A rheological mechanism sufficient to explain the kinetics of cell sorting.pdf. *Journal of theoretical biology* **37**, 43–73 (1972).

55. Rieu, J., Barentin, C., Sawai, S., Maeda, Y. & Sawada, Y. Cell Movements and Mechanical Force Distribution During the Migration of Dictyostelium Slugs. 345–364 (2004).

56. Mombach, J. C. M. *et al.* Rounding of aggregates of biological cells: Experiments and simulations. *Physica A: Statistical and Theoretical Physics (Amsterdam)* **352**, 525–534 (2005).

57. Raufaste, C., Marmottant, P. & Graner, F. Discrete rearranging disordered patterns: Prediction of elastic and plastic behavior, and application to two-dimensional foams. *Physical Review E* **81**, 1–13 (2010).

58. Jakab, K. *et al.* Relating cell and tissue mechanics: implications and applications. *Developmental dynamics: an official publication of the American Association of Anatomists* **237**, 2438–49 (2008).

59. Phillips, H., Steinberg, M. S. & Lipton, B. Embryonic tissues as elasticoviscous liquids. II. Direct morphological evidence for cell slippage in centrifuged aggregates. *Dev. Biol* 124–134 (1977).

60. Yang, J. & Brodland, G. W. Estimating interfacial tension from the shape histories of cells in compressed aggregates: a computational study. *Annals of biomedical engineering* **37**, 1019–27 (2009).

61. Marmottant, P. *et al.* The role of fluctuations and stress on the effective viscosity of cell aggregates. *Proceedings of the National Academy of Sciences of the United States of America* **106**, 17271–5 (2009).

62. Mgharbel, A. Physique et rhéologie des agrégats cellulaires embryonnaires. (2009).

63. Weaire, D. & Rivier, N. Soap, cells and statistics—random patterns in two dimensions. *Contemporary Physics* **25**, 59–99 (1984).

64. Foty, R. A., Forgacs, G., Pfleger, C. M. & Steinberg, M. S. Liquid properties of embryonic tissues: measurement of interfacial tensions. *Physical review letters* **72**, 2298–2301 (1994).

65. Mgharbel, A., Delanoë-Ayari, H. & Rieu, J.-P. Measuring accurately liquid and tissue surface tension with a compression plate tensiometer. *HFSP journal* **3**, 213–21 (2009).

66. Hegedüs, B., Marga, F., Jakab, K., Sharpe-Timms, K. L. & Forgacs, G. The interplay of cell-cell and cell-matrix interactions in the invasive properties of brain tumors. *Biophysical journal* **91**, 2708–16 (2006).

67. Kalantarian, A. *et al.* Axisymmetric drop shape analysis for estimating the surface tension of cell aggregates by centrifugation. *Biophysical journal* **96**, 1606–16 (2009).

68. David, R., Ninomiya, H., Winklbauer, R. & Neumann, A. W. Tissue surface tension measurement by rigorous axisymmetric drop shape analysis. *Colloids and surfaces. B, Biointerfaces* **72**, 236–40 (2009).

69. Guevorkian, K., Colbert, M.-J., Durth, M., Dufour, S. & Brochard-Wyart, F. Aspiration of Biological Viscoelastic Drops. *Physical Review Letters* **104**, 1–4 (2010).

70. Foty, R. A., Pfleger, C. M. C. M., Forgacs, G. & Steinberg, M. S. Surface tensions of embryonic tissues predict their mutual envelopment behavior. *Cell* **1620**, 1611–1620 (1996).

71. Foty, R. A. & Steinberg, M. S. The differential adhesion hypothesis: a direct evaluation. *Developmental biology* **278**, 255–63 (2005).

72. Manning, M. L., Foty, R. a, Steinberg, M. S. & Schoetz, E.-M. Coaction of intercellular adhesion and cortical tension specifies tissue surface tension. *Proceedings of the National Academy of Sciences of the United States of America* **107**, 12517–22 (2010).

73. Janmey, P. a Mechanical properties of cytoskeletal polymers. *Current opinion in cell biology* **3**, 4–11 (1991).

74. Zhu, C., Bao, G. & Wang, N. Mechanical Response, Cell Adhesion, and Molecular Deformation. *Physiology* 189–226 (2000).

75. Alberts, B. *et al. Molecular biology of the cell*. (Garland Science Taylor & Francis Group: 2002).at <citeulike-article-id:691434>

76. Kasza, K. E. *et al.* The cell as a material. *Current opinion in cell biology* **19**, 101–7 (2007).

77. Hoffman, B. D., Massiera, G., Citters, K. M. V. & Crocker, J. C. The consensus mechanics of cultured mammalian cells. *Sciences-New York* **2006**, (2006).

78. Feneberg, W., Aepfelbacher, M. & Sackmann, E. Microviscoelasticity of the apical cell surface of human umbilical vein endothelial cells (HUVEC) within confluent monolayers. *Biophysical journal* **87**, 1338–50 (2004).

79. Desprat, N., Richert, A., Simeon, J. & Asnacios, A. Creep function of a single living cell. *Biophysical journal* **88**, 2224–33 (2005).

80. Alcaraz, J. *et al.* Microrheology of human lung epithelial cells measured by atomic force microscopy. *Biophysical journal* **84**, 2071–9 (2003).

81. Yamada, S., Wirtz, D. & Kuo, S. C. Mechanics of living cells measured by laser tracking microrheology. *Biophysical journal* **78**, 1736–47 (2000).

82. Lenormand, G., Millet, E., Fabry, B., Butler, J. P. & Fredberg, J. J. Linearity and time-scale invariance of the creep function in living cells. *Journal of the Royal Society, Interface / the Royal Society* **1**, 91–7 (2004).

83. Fabry, B. *et al.* Scaling the Microrheology of Living Cells. *Physical Review Letters* **87**, 1–4 (2001).

84. Balland, M., Richert, A. & Gallet, F. The dissipative contribution of myosin II in the cytoskeleton dynamics of myoblasts. *European biophysics journal : EBJ* **34**, 255–61 (2005).

85. Wirtz, D. Particle-tracking microrheology of living cells: principles and applications. *Annual review of biophysics* **38**, 301–26 (2009).

86. Stamenović, D. *et al.* Rheological behavior of living cells is timescale-dependent. *Biophysical journal* **93**, L39–41 (2007).

87. Bursac, P. *et al.* Cytoskeletal remodelling and slow dynamics in the living cell. *Nature materials* **4**, 557–61 (2005).

88. Deng, L. *et al.* Fast and slow dynamics of the cytoskeleton. *Nature materials* **5**, 636–40 (2006).

89. Trepat, X. *et al.* Universal physical responses to stretch in the living cell. *Nature* **447**, 592–5 (2007).

90. Gardel, M. L. *et al.* Elastic behavior of cross-linked and bundled actin networks. *Science (New York, N.Y.)* **304**, 1301–5 (2004).

91. Lenormand, G. & Fredberg, J. J. Deformability, dynamics, and remodeling of cytoskeleton of the adherent living cell. *Biorheology* **43**, 1–30 (2006).

92. Overby, D. R., Matthews, B. D., Alsberg, E. & Ingber, D. E. Novel dynamic rheological behavior of individual focal adhesions measured within single cells using electromagnetic pulling cytometry. *Acta biomaterialia* **1**, 295–303 (2005).

93. Stamenovic, D., Suki, B., Fabry, B., Wang, N. & Fredberg, J. J. Rheology of airway smooth muscle cells is associated with cytoskeletal contractile stress. *Journal of applied physiology (Bethesda, Md. : 1985)* **96**, 1600–5 (2004).

94. Mechanics, C. & Stamenovic, D. Two regimes, maybe three? *Group* **5**, 597–598 (2006).

95. Goldmann, W. H. & Ezzell, R. M. Viscoelasticity in wild-type and vinculin-deficient (5.51) mouse F9 embryonic carcinoma cells examined by atomic force microscopy and rheology. *Experimental cell research* **226**, 234–7 (1996).

96. Wang, N. & Ingbert, D. E. Control of Cytoskeletal Mechanics by Extracellular Matrix , Cell Shape , and Mechanical Tension. *Biophysical Journal* **66**, 2181–2189 (1994).

97. Deng, L., Fairbank, N. J., Fabry, B., Smith, P. G. & Maksym, G. N. Localized mechanical stress induces time-dependent actin cytoskeletal remodeling and stiffening in cultured airway smooth muscle cells. *American journal of physiology. Cell physiology* **287**, C440–8 (2004).

98. Matthews, B. D., Overby, D. R., Mannix, R. & Ingber, D. E. Cellular adaptation to mechanical stress: role of integrins, Rho, cytoskeletal tension and mechanosensitive ion channels. *Journal of cell science* **119**, 508–18 (2006).

99. Icard-Arcizet, D., Cardoso, O., Richert, A. & Hénon, S. Cell stiffening in response to external stress is correlated to actin recruitment. *Biophysical journal* **94**, 2906–13 (2008).

100. Fernández, P. & Ott, A. Single Cell Mechanics: Stress Stiffening and Kinematic Hardening. *Physical Review Letters* **100**, 2–5 (2008).

101. Trepat, X. *et al.* Viscoelasticity of human alveolar epithelial cells subjected to stretch. *American journal of physiology. Lung cellular and molecular physiology* **287**, L1025–34 (2004).

102. Kollmannsberger, P., Mierke, C. T. & Fabry, B. Nonlinear viscoelasticity of adherent cells is controlled by cytoskeletal tension. *Soft Matter* **7**, 3127 (2011).

103. Krishnan, R. *et al.* Reinforcement versus fluidization in cytoskeletal mechanoresponsiveness. *PloS one* **4**, e5486 (2009).

104. Wolff, L., Fernández, P. & Kroy, K. Resolving the stiffening-softening paradox in cell mechanics. *PloS one* **7**, e40063 (2012).

105. Janmey, P. A., Hvidt, S., Lamb, J. & Stossel, T. P. Resemblance of actin-binding protein/actin gels to covalently crosslinked networks. *Nature* **345**, 89–92 (1990).

106. Ruddies, R., Goldmann, W. H., Isenberg, G. & Sackmann, E. The viscoelastic moduli of actin/filamin solutions: a micro-rheologic study. *Biochemical Society transactions* **21**, 37S (1993).

107. Wachsstock, D. H., Schwarz, W. H. & Pollard, T. D. Cross-linker dynamics determine the mechanical properties of actin gels. *Biophysical journal* **66**, 801–9 (1994).

108. Gardel, M. L. *et al.* Stress-Dependent Elasticity of Composite Actin Networks as a Model for Cell Behavior. **088102**, 12–15 (2006).

109. Xu, J., Tseng, Y. & Wirtz, D. Strain hardening of actin filament networks. Regulation by the dynamic cross-linking protein alpha-actinin. *The Journal of biological chemistry* **275**, 35886–92 (2000).

110. Wang, N., Butler, J. P. & Ingber, D. E. Mechanotransduction across the cell surface and through the cytoskeleton. *Science* **260**, 1124–1127 (1993).

111. Bausch, A. R., Mo, W., Sackmann, E. & Möller, W. Measurement of local viscoelasticity and forces in living cells by magnetic tweezers. *Biophysical journal* **76**, 573–9 (1999).

112. Fernández, P., Pullarkat, P. a & Ott, A. A master relation defines the nonlinear viscoelasticity of single fibroblasts. *Biophysical journal* **90**, 3796–805 (2006).

Chapter 2

Materials and Methods

This thesis focuses on the experimental study of physical properties and biomechanics of embryonic cell aggregates. The purpose of this work was on one hand to better understand the biological origin of viscosity and surface tension, and on the other hand to study quantitatively in details the visco-elasto-plastic behavior of cell aggregates using new rheological protocols in shear experiments.

We describe in this chapter the materials used in our study and give details about the different experimental procedures.

We first present the molecular and pharmacological approaches and the experimental system we used and we continue with the description of the experimental protocols needed for each type of experiments (fusion, segregation, compression plate tensiometry and rheology).

2.1 Cell lines: molecular and pharmacological approaches and the experimental system

2.1.1 Cell lines: F9 WT, $F9^{(\alpha-/-)}$ and F9 cells

The mouse embryonic carcinoma F9 cell line and its derivatives (Fig. 2.1) were a generous gift from A. Nagafuchi (Kumamoto University, Japan) [1] and D. Riveline (University of Strasbourg, France).

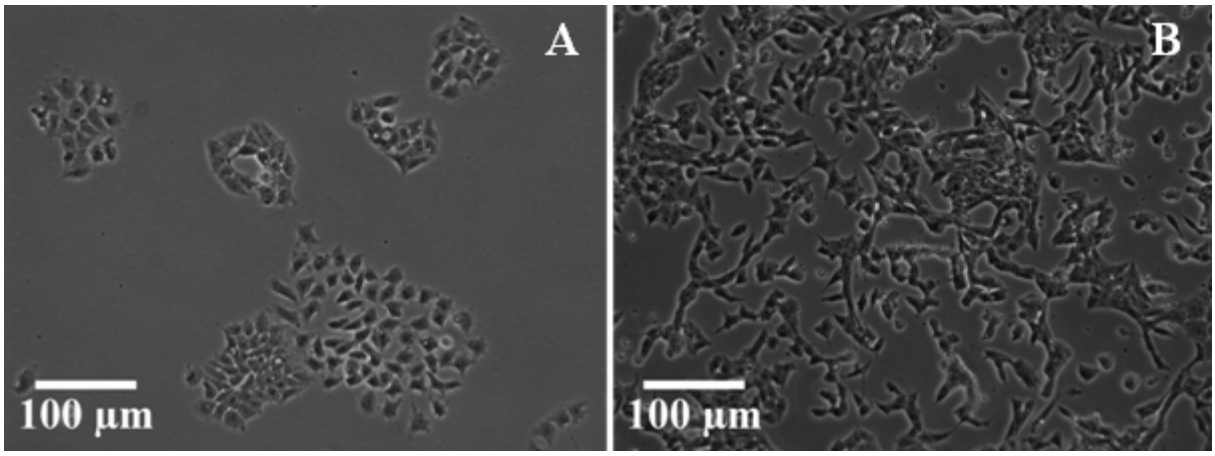

Fig. 2.1: *Optical microscopy images presenting differences between cells in culture. (A) F9 WT cells. (B)* $F9^{(\alpha-/-)}$ *cells.*

$F9^{(\alpha-/-)}$ cells represent knocked out cells with the cadherin-actin bond disrupted (for a representation, see the cartoons in Fig. 3.7 E-F in chapter 3). The loss of α-catenin does not change the level of cadherin expressed by F9 cells [2] as shown by the western blotting and immunoprecipitation analysis of Fig. 2.2.

However, the change in the interaction between cadherin and the cytoskeleton is relevant to our study, as catenin has an essential biological role in cell adhesion.

In culture, even when there is no complete confluence, F9 WT cells have the tendency to form islands (Fig. 2.1 A) which further develop into 3D structures, while $F9^{(\alpha-/-)}$ cells spread all over the culture dish (Fig. 2.1 B).

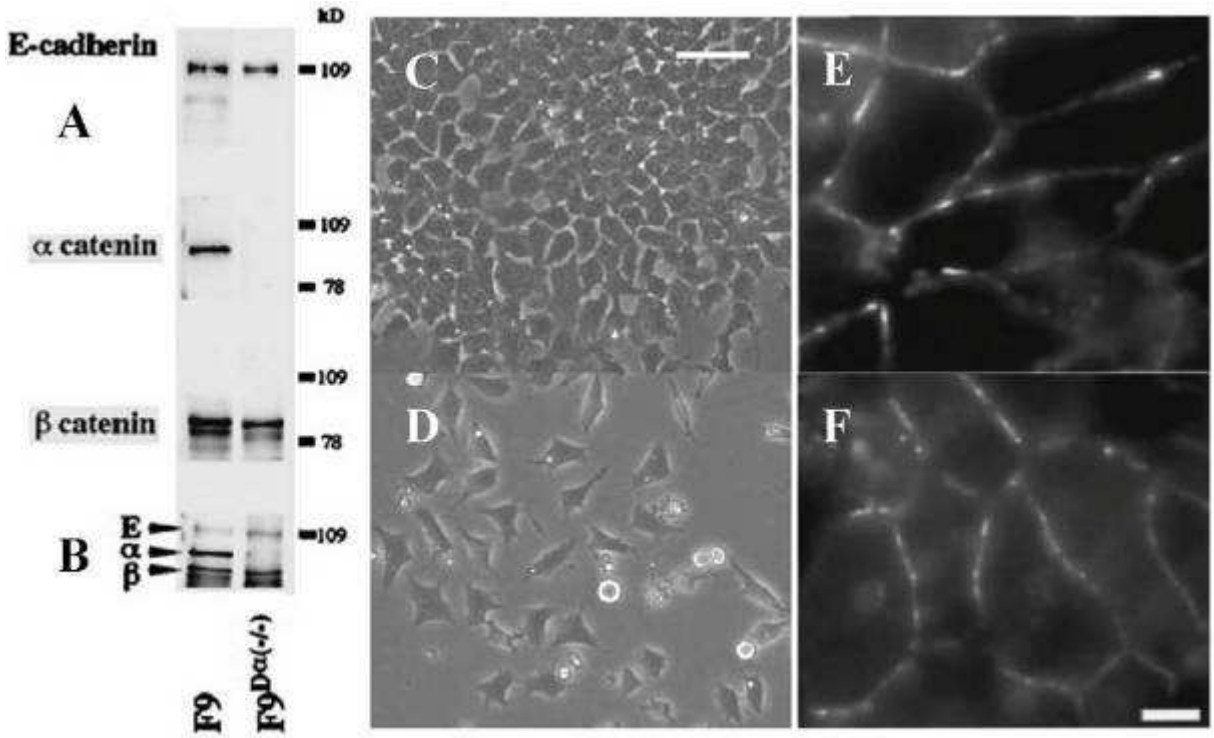

Fig. 2.2: *Immunological and morphological differences between F9 and F9$^{(\alpha-/-)}$ cells. (A) Western blotting analysis of F9 and F9$^{(\alpha-/-)}$ cell clone with anti-E-cadherin, anti-α-catenin and anti-β-catenin mAb. (B) Immunoprecipitation analysis of each cell clone with anti-E-cadherin mAb. E, E-cadherin; α, α-catenin; β, β-catenin* [3]*. (C-D) Phase contrast image of F9 (C) and F9$^{(\alpha-/-)}$ (D) adherent cells showing different morphologies: parental F9 cells form small and compact colonies while F9$^{(\alpha-/-)}$ cells present a scattered morphology, suggesting dysfunction of their cadherin-catenin adhesion. Scale bar, 50μm. (E-F) Immunostaining with the anti-E-cadherin mAb ECCD-2 of α-catenin positive control cells (similar to F9 cells) (E) and F9$^{(\alpha-/-)}$ cells (F): the antigens are concentrated in the boundary between cells in both case. Scale bar, 25μm. Printed from* [3].

For the cell sorting-out and envelopment studies, we use F9 cells labeled with Histon-GFP (referred to as F9) [4]. Histone GFP DNA was again a generous gift from A. Nagafuchi. Details on this vector can be found in ref [4]. For the transfection step, the same protocol as described in [4] was followed; expression vectors were transfected using the lipofectamine 2000 system (GIBCO). A 24-well culture plate was used for transfection. After one day the transfected cells were transferred into culture dishes. After two days culture medium was exchanged for one containing antibiotics (400 μg/ml G418) for selection. Culture medium was changed every day for a week. And then, medium change was done every two or three days. Two or three weeks after transfection, colonies could be isolated.

2.1.2 Cell culture

As previously described [5], cells were plated on plastic tissue culture dishes pre-coated for 15 min with gelatin (2%, Sigma, G1393) diluted to 0.2% in PBS and incubated at 37 °C and 5% CO_2 in DMEM (GIBCO, 41965-039) supplemented with 10% fetal bovine serum (PANSera ES, Dutscher 500105ES) and 1% antibiotics (Penicillin Streptomycin, GIBCO Invitrogen corporation, Cat. no. 15140- 122).

2.1.3 Cell storage

The cells can be cryopreserved and this procedure allows us to store them for different periods of time in order to have flexibility in scheduling the experiments.

At early passages, we trypsinize confluent cells, resuspend in fresh medium (DMEM prepared as previously described) and then centrifuge them. The freezing medium contains 10% dimethyl sulfoxide DMSO (Sigma, D8779) and 90% FBS serum (Biotech GmbH, 2902 P-241021).

The cryogenic screw cap vials (Fischer Scientific, PA) containing the cells are kept for maximum 2 hours in a freezer at -20 °C and then transferred either to a -80 °C freezer (FRYKA – Kältetechnik GmbH, B 30-85), either to a liquid nitrogen tank (Air Liquide, GT 11) for long term storage.

For the thawing of frozen cells, after keeping the vials for a very short time at room temperature (or directly in a 37 °C water bath), we put the cells in warm fresh medium, we centrifuge and then resuspend them using warm prepared DMEM in Petri culture dishes pre-coated with gelatin following the protocol previously described. After several hours (or as soon as the cells have attached) the medium has to be changed in order to get rid of all the remaining DMSO, which is very toxic for the cells.

2.1.4 Drugs acting on the signaling pathways that regulate cell contractility

In the compression plate tensiometry and fusion experiments, we investigated and quantified the effects of three different drugs, with opposed actions on the cell cytoskeleton.

The first one, nocodazole (Sigma, M1404), is expected to indirectly increase stress fiber contractility by inhibiting microtubule dynamics and activating the rho kinase pathway [6]. The enhancement of cell contractility is achieved in a cadherin independent manner.

In opposition to nocodazole, the second drug we exposed our aggregates to, Y-27632 dihydrochloride monohydrate (Sigma, Y0503) is known as a selective inhibitor of Rho-associated protein kinases (ROCK-I and ROCK-II), thus should imply a decrease in cell contractility [7].

Finally, to test whether Y-27632 provides the right amount of inhibition effect on cell contractility, we used blebbistatin (Sigma, B0560), which is a cell permeable, specific inhibitor of nonmuscle myosin II [8].

For rheology experiments, apart from nocodazole and Y-27632, we also used an inhibitor of the ATP expecting a passive response of our cells similar to that of a non biological complex fluid.

Moreover, in order to inhibit actin polymerization we exposed our aggregates to latrunculin A (L5163-100UG, Sigma) after confirming its reversible effect in cell culture. In our case, there was no need to remove the serum from the CO_2 independent medium, nor to use a large concentration of drug, as its effects appeared in cell culture starting even at a concentration of 1 µM latrunculin A.

In summary, for compression plate tensiometry and fusion experiments, aggregates were treated with nocodazole, Y-27632 or blebbistatin at 1µM, 10µM and 10 µM respectively for different time intervals before or during the experiments or left untreated. For rheology experiments, aggregates were treated with 1µM nocodazole, 10µM Y-27632, ATP inhibitor or 1µM latrunculin A just before placing them in the measuring system and were left exposed to drugs during the entire experiment as the drugs are added in the medium which surrounds them and the system does not allow us, for the moment, to refresh or to change the medium during an experiment.

2.1.5 Aggregate preparation protocol

To generate spherical aggregates, cells were dissociated and then reassembled in 15 µl hanging drops [9] (Fig. 2.3). To dissociate the cells, we rinsed the cell culture Petri dishes with a phosphate buffered saline solution (DPBS, Pan Biotech, P04-36500), we added trypsin 1X (Gibco/Invitrogen 25050) 0.1% and incubated for 3 min. We resuspended the cells and we centrifuged them at 636g (2500 rpm) for 5 min, then we diluted in order to have different cell concentrations in the final solution.

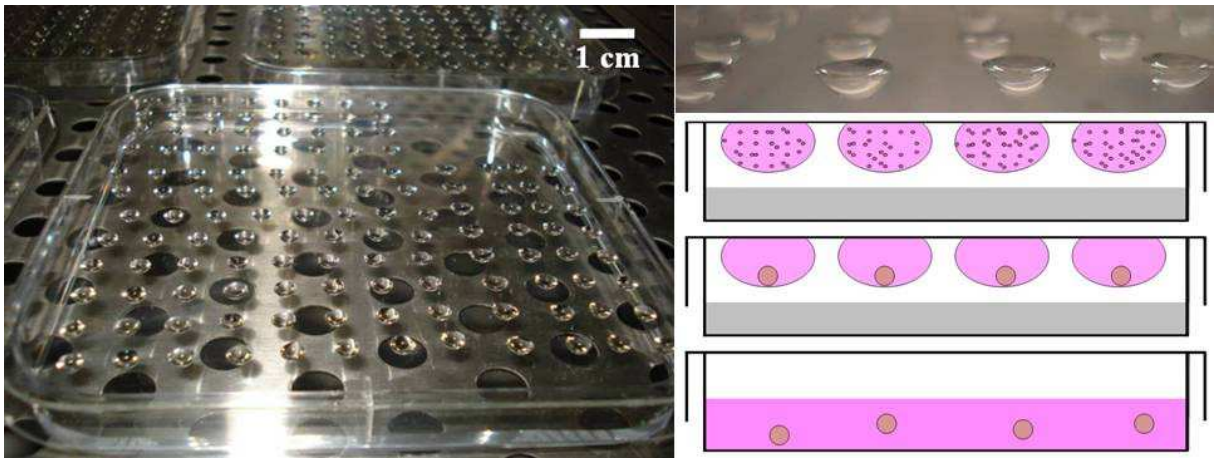

Fig. 2.3: *The hanging drop technique for the preparation of cell aggregates. Square dishes with hanging drops on an incubator shelf (left). Different steps of the hanging drop method (right). 15µl drops of medium containing from 1500 to 35000 cells are placed on the top of a Petri dish containing water or PBS, then turned, allowing the cells, by gravity, to form an aggregate at the bottom of the drop which will finally be "fish-out" and transferred in a new dish, containing cell culture medium.*

After two days, the newly formed aggregates were transferred into fresh culture medium filled sterile non-treated plastic Petri dishes and then incubated on a gyratory shaker (at 160 rpm, 5% CO_2, 37 °C). Depending on the cellular type, the entire procedure took from three (for F9 WT) to five days (for $F9^{(\alpha-/-)}$) and yielded spherical aggregates ranging between 180 and 500µm in diameter, each containing from 1500 to 35000 cells. For each cell concentration in the suspension we obtain 3D cellular aggregates of similar sizes.

After two days in hanging drops, the recently formed aggregates present different shapes when comparing the two cell lines (Fig. 2.4).

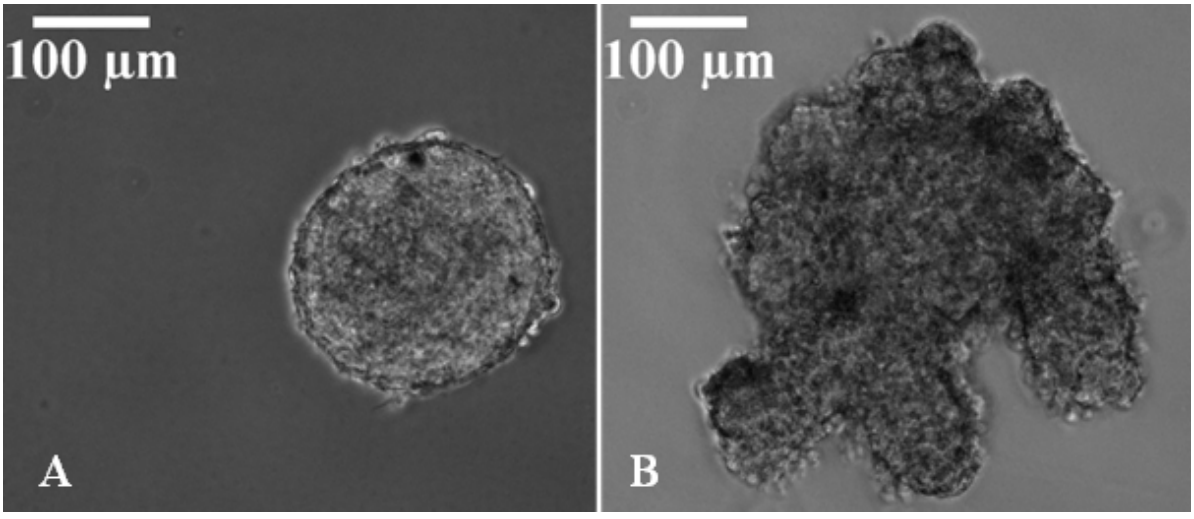

Fig. 2.4: *Typical optical microscopy images showing significant differences in the morphology of F9 WT (A) and $F9^{(\alpha-/-)}$ (B) cell aggregates just after two days in hanging drops.*

F9 WT cells form already spherical aggregates which don't need further gyration (Fig. 2.4 A), whereas $F9^{(\alpha-/-)}$ cells remain in various shape agglomerations (Fig. 2.4 B) which become spherical after approximately one day on the gyratory shaker. We can however try to leave the $F9^{(\alpha-/-)}$ cell aggregates in hanging drops for a longer period of time but this would alter their properties due to hypoxia or lack of nutrients for the cells situated in the center of the spheroids.

The gyration is a very important step before using the aggregates for experimental procedures. While it helps for the rounding of $F9^{(\alpha-/-)}$ especially, it also prevents the adhesion of aggregates on the dish surface or the fusion between small distance situated aggregates. This last phenomenon can be visualized in Fig. 2.5, where a large number of aggregates have fusioned while the gyratory shaker was accidentally turned off.

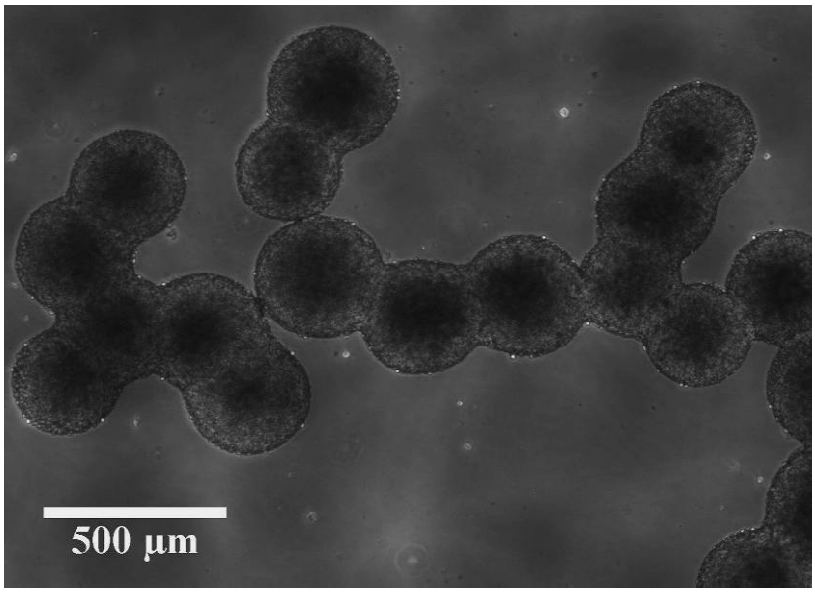

Fig. 2.5: *Fusion between F9 WT aggregates after the gyratory shaker in the incubator was accidentally turned off.*

All experimental observations require for the cell aggregates to be transferred to CO_2 independent medium (GIBCO, 18045-054) supplemented with the same components as the culture medium (serum, antibiotics) and 2% L-Glutamine (200mM, Pan Biotech, P04-80400).

For the rheology experiments, a great number of cell aggregates (between approximately 1000 and 2000) needs to be prepared.

For experiments using drugs, drugs were added in the CO_2 independent medium once aggregates were prepared.

2.2 Visualization of cross-sections of cell aggregates

Cross sections through the aggregates were carried out in collaboration with Hichem Mertani (CLB, Lyon), Selena Bodennec and Karine Ferri at the "Laboratoire de Biologie Intégrative et Moléculaire" in Lyon. The resulting sections have the thickness of a cell layer. They allow us to study the internal morphogenetics of cells and to prepare cell monolayers for histological marking.

2.2.1 Protocol for cross-sections

In the protocol for preparing the sections, for each cell type, a thousand aggregates must be prepared and fixed. To do so, we collected the aggregates in a 15 ml tube, we centrifuged for 2 minutes at 1200 rpm and we waited for the sedimentation of aggregates. The supernatant was carefully removed. Next, the aggregates were fixed using 4% PFA (30 minutes), rinsed with PBS (4 times, 5 minutes with gentle agitation) and dehydrated in a graded ethanol series (70%, 95%, 100%, one hour each) and butanol (30 minutes) before embedding in paraffin / xylene (v/v) solution (60 °C, overnight). The aggregates were submitted to three steps of pure paraffin embedding (1 hour, 60 °C) and air-dried. Sections (5 µm thick) were made using a microtome (Leica Microsystems) and transferred to glass slides.

2.2.2 Immunohistochemistry

The aggregate sections were deparaffinized using xylene (twice for 15 minutes under the hood, in a glass tube), 100% and 95% EtOH (twice for 10 minutes under the hood) and rehydrated in PBS. From this point the slides may be kept longer in the refrigerator. The sections were incubated in PBS with 10% BSA for 30 min before incubation with antibody against β-catenin (sc-7199, Santa Cruz Biotechnology, Inc.) at 1:300 dilution (90 minutes, RT). The sections were then washed with PBS and incubated with Alexa Fluor 488 goat anti-rabbit IgG (Invitrogen Molecular Probes) at 1:1000 dilution (1 hour, RT). Slides were mounted with fluorescent mounting medium and observed under a Nikon Eclipse 2000 fluorescence microscope. After mounting, the slides can be kept sealed at 4 °C for about 3 weeks in the dark.

2.3 The compression plate tensiometer

In order to measure the surface tension of our aggregates, compression experiments were done on a surface tension apparatus designed and built previously in our team[10]. The resulting force and the side profile of cell aggregates subjected to the compression are recorded simultaneously and the surface tension is measured using capillary laws.

2.3.1 Measuring the TST

Methods like the axisymmetric drop shape analysis of centrifuged aggregates [11,12] or the aspiration of cell aggregates in a micropipette [13] have been already used to measure the tissue surface tension. Details of each of these techniques are briefly presented in the introduction chapter.

In this study we chose to use the compression plate tensiometry, which is at the moment the most widely used quantitative method [14,15]. As already mentioned in introduction, this method is based on the fact that, at long time scales, once elastic forces are relaxed, we can measure the surface tension (σ) if we assume that cell aggregates verify the same physical laws of capillarity as liquid droplets.

During compression, the rotational symmetry around z-axis and the reflection symmetry with respect to the equatorial plane of the cell aggregate, allows one to determine precisely the two radii of curvature R_1 and R_2 (see also Fig. 2.6 A,D). These two parameters can be measured using a horizontal stereo-microscope. According to Laplace equation and capillarity laws, the force the aggregate is subjected to, during a compression experiment, is proportional to surface tension and to a geometrical parameter L containing the two radii of curvature (Fig. 2.6 C). After successive compressions one may plot L versus the deflection of the cantilever (Fig. 2.6 E).

Thus, measuring the force and analyzing the shape parameters at equilibrium (which corresponds to the time when a plateau in the force is reached, Fig. 2.6 B) allows one to obtain the value of the tissue surface tension using Laplace equation.

For the profile's analysis, different methods can be used to calculate the different radii of curvatures. In previously published studies several methods have been described: the CA method (based on the circular arc approximation) [16,17] and the Exact Laplace Profile (ELP) method (based on the exact solution of Laplace equation and on the only measurements of the contact angle, distance between compression plates and radius of the compressed aggregate R_1) [18]. In our study, for aggregate profile calculation we use the LPF (Local Polynomial Fit, second order polynomial fit at median plane for R_2) method, which is a direct, robust and

angle independent method. A more detailed description and its advantages were previously presented [10]. We now describe the different parts of our tissue tensiometer (Fig. 2.7).

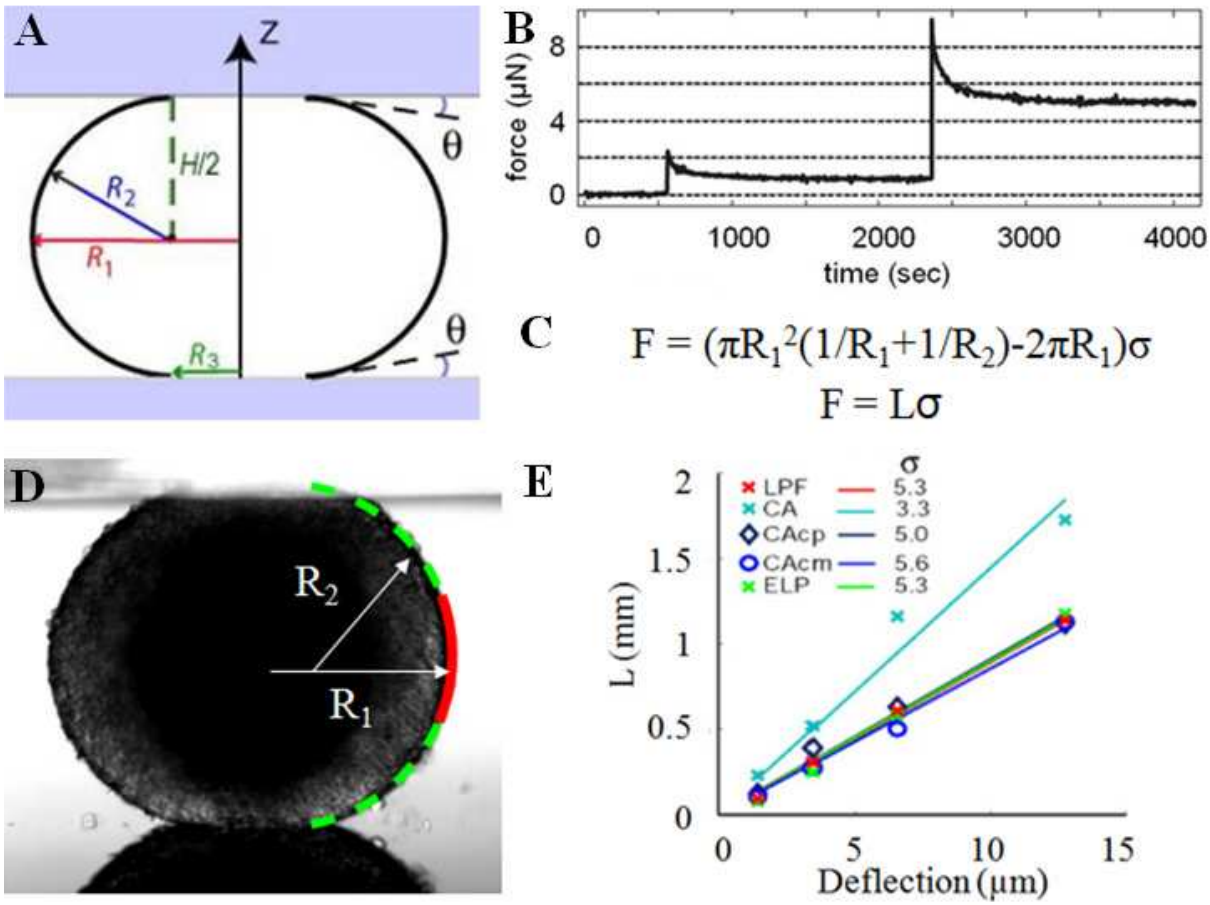

Fig. 2.6: *(A) Schematic representation of a compressed aggregate with the different parameters of importance R_1 and R_2 the principal radii of curvature, R_3 is the radius of the aggregate's circular area of contact with either of the compression plates, H is the distance between the upper and the lower compression plate and θ is the complementary contact angle between the surface and the adhering aggregate. (B) Typical force signal obtained when subjecting an aggregate to 2 successive compressions. (C) Mechanical force exerted between each aggregate parts along middle-plane (Laplace + contact line capillary contributions). (D) Side view on a stereomicroscope of a F9 WT aggregate in CO_2 independent culture medium at 37 °C placed between the two parallel plates with the schematic representation of R_1 and R_2. (E) Plot of the geometrical parameter $L = \pi R_1^2 (1/R_1 + 1/R_2) - 2\pi R_1$ as a function of cantilever deflection δ for a F9 WT aggregate with legend displaying the values (in mN/m) of tissue surface tension obtained using the different methods tested (abbreviations are as follows: ELP - Exact Laplace Profile; LPF - Local Polynomial Fit; CA - Circular Arc; CAcm - Circular Arc with force calculated at median plane; CAcp - Circular Arc with force calculated on plates). The tissue surface tension is given by the slope of the obtained linear fits, with L defined in the equation represented in (B) and δ = F/k (with k, the cantilever spring constant, varying between 0.36 and 0.67 N/m depending on the experiment).*

2.3.2 Description of the experimental set-up

The aggregate, located between two parallel glass plates, is subjected to several successive compressions of steps going from 25 to 50 µm. The choice in the number and the amplitude of steps of compression depends on the aggregate's volume. For the measure to be valid (not affected by stress induced dead cells), we have to keep the total compression rate lower than half the size of the aggregate (as evaluated from the amount of dead cells observed by 2-photon confocal microscopy in [5]).

The two compression plates consist of a 2-mm thick borosilicate glass for the lower one (LCP) and of a cover glass surface for the upper one (UCP). To ensure a minimal aggregate adhesiveness, surfaces are prepared and treated following the protocol described in [5]. After cleaning them with soap (2% Microson detergent, Fisher Bioblock, France) and water (sonicated for 30 min), we make them hydrophobic by silanization with perfluorosilane (ABCR, F06179). Then we incubate them in 10 mg/ml Pluronic F-127 (Sigma, P2443) for 5 min and finally we rinse them briefly with water and let them dry.

The LCP is located at the bottom of a medium chamber while a tungsten or inox wire, with diameter 0.1 and 0.8 mm respectively, connects the UPC to a copper-beryllium cantilever which has a spring constant varying between 0.36 and 0.67 N/m. The cantilever deflection is measured with a non-contact eddy current displacement and position measurement sensor (DT 3701-U1-A-C3, micro-epsilon). The calibration of the cantilever is done using light-weight curved wires attached to the UPC.

A NewStep^{TM} Motion Control System (NewPort) controls the z direction of the LCP through the movement with a controlled velocity of a cylindrical rod that traverses a CO_2 independent filled chamber in which aggregates are deposited. The same chamber can be moved in the x,y,z directions to center the sample on the optical axis by an electronic micromanipulator (MP285, Sutter Instrument). It is made in Teflon-inox with a pair of slide glasses glued on the sides to enable optical visualization. Evaporation of the medium is prevented by covering the free-open surface with a thick mineral oil layer (Sigma 330779-1L).

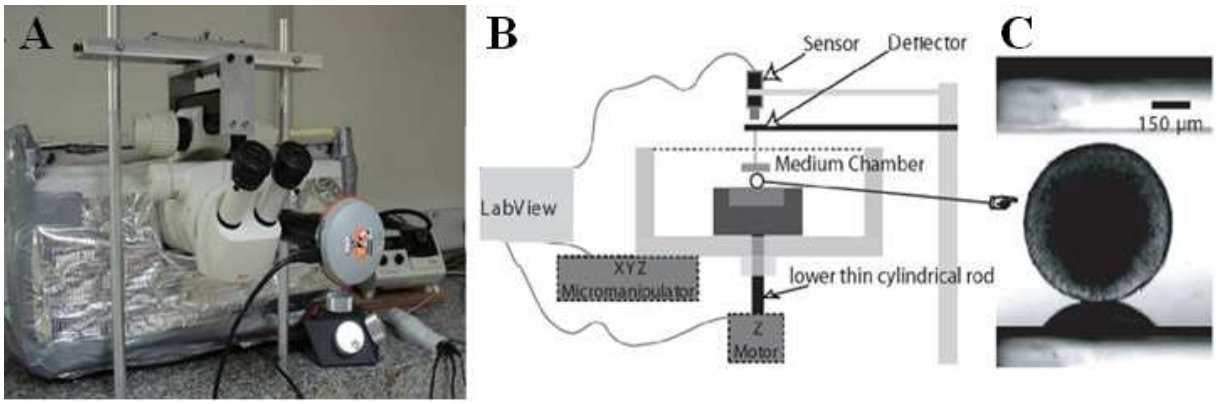

Fig. 2.7: *(A) Picture of the surface tension apparatus designed and built previously in our team embedded in a thermally isolated chamber maintained at 37 °C. (B) Schematic view of the setup: force is measured by a copper-beryllium cantilever (deflector) and an eddy current position sensor. Deposited aggregate on the LCP (shown in C, before compression) is positioned in the center of the optical axis thanks to a xyz manipulator and moved up thanks to a supplementary z step-motor.*

The whole setup is embedded in a thermally isolated chamber maintained at the desired temperature (*i.e.*, 37 °C) by a resistance traversed by a current that is modulated by a temperature controller (331; Lakeshore).

The monitoring of aggregates' shape is done using a stereomicroscope (MZ16 binocular, Leica) and a digital camera (A686M, Pixelink). We use a KL 1500 LCD cold light source (Schott) with "flexible tubes" to adjust the lightning.

The main advantages of this system are given by the fact that it offers easy and convenient manipulations (changing the sample from one experiment to another) and also, its resolution and optics enable very accurate measurements of the surface tension.

The whole setup is controlled with Labview (National Instruments), and image analysis is performed with Matlab (The MathWorks) and ImageJ (National Institutes of Health, Bethesda).

2.4 Segregation assays

For segregation assays we used the GFP labeled F9 cell line (F9), as it is suitable for visualization and evaluation by eye due to its fluorescence properties.

2.4.1 Cell sorting

For cell sorting assays, aggregates were prepared using a cell suspension containing two different cell types: $F9^{(\alpha-/-)}$ and F9 or the control F9 and F9. To evaluate whether the cell sorting takes place we observed the newly formed aggregates on a Nikon Eclipse 2000 fluorescence microscope at different stages of the phenomenon. Right after preparation and in between the images taking, the aggregates are incubated at 37 °C and 5% CO_2.

2.4.2 Tissue envelopment

Spreading of one cellular type over another one was tested by using the same pairs of cells as for the sorting out assays, only in this case, the interaction took place between preformed spherical aggregates containing only one type of dissociated cells. We tried two different methods to bring in contact the two distinct aggregates: placing them side-by-side on an agar bed or putting them together in a unique hanging drop. Both methods worked equally fine and we monitored the combined aggregates every several hours.

2.5 Fusion of two symmetric cell aggregates assays

The measurement of apparent viscosity requires the recording of the kinetics of two fusing aggregates. For this to be achieved, before each experiment, a 48 well plate is coated with 1% agar (Sigma A1296) prepared and deposited following the Sigma protocol in order to prevent adhesion of aggregates. Afterwards, the wells are filled with CO_2 independent medium and according to the type of experiment we can also add 1 µM nocodazole, 10 µM Y-27632 or 10 µM blebbistatin right before the transfer of aggregates.

A pair of aggregates prepared under same physiological and experimental conditions and chosen as to have approximately the same diameter, is transferred in each well and we record, with periods from 5 to 10 minutes, the kinetics of the fusing process on a motorized Nikon Eclipse TE 2000 E microscope using NIS Elements.

Experiments are carried out at thermal equilibrium, as the microscope is enclosed in a home-made polystyrene chamber, heated using a radiator controlled by a circulating water bath thermostated at 37 °C.

Image analysis (*i.e.*, extraction of the neck's radius X) is performed with Matlab (The MathWorks) and ImageJ (National Institutes of Health, Bethesda).

When placed in contact on the agar bed, the two identical aggregates will slowly fuse. To describe the fusion kinetics we consider that the initial regime of the process may be described by the Frenkel's equation [19] $X^2 = t*R_0*\sigma/\eta$ where X is the radius of the circle of contact between both aggregates, t is the time, R_0 is the initial radius of the aggregates, σ is the surface tension and η is the tissue viscosity. The gravity is neglected and we only fit one parameter (*i.e.*, the slope of the squared of the radius of contact between two aggregates *versus* time).

As pointed out in [9], in the original work by Frenkel [19], there was a mistake about incompressibility, detected by Eshelby (page 806 of the discussion of [20], who removed the extra prefactor 2/3 on the right-hand side. A calculus error on the line above Frenkel's equation (7) was also detected [9], so an extra prefactor $1/\pi$ was removed. The corrected formula therefore does not contain any numerical prefactor. This is consistent with a more extensive calculation of the fusion process at large times [21,22].

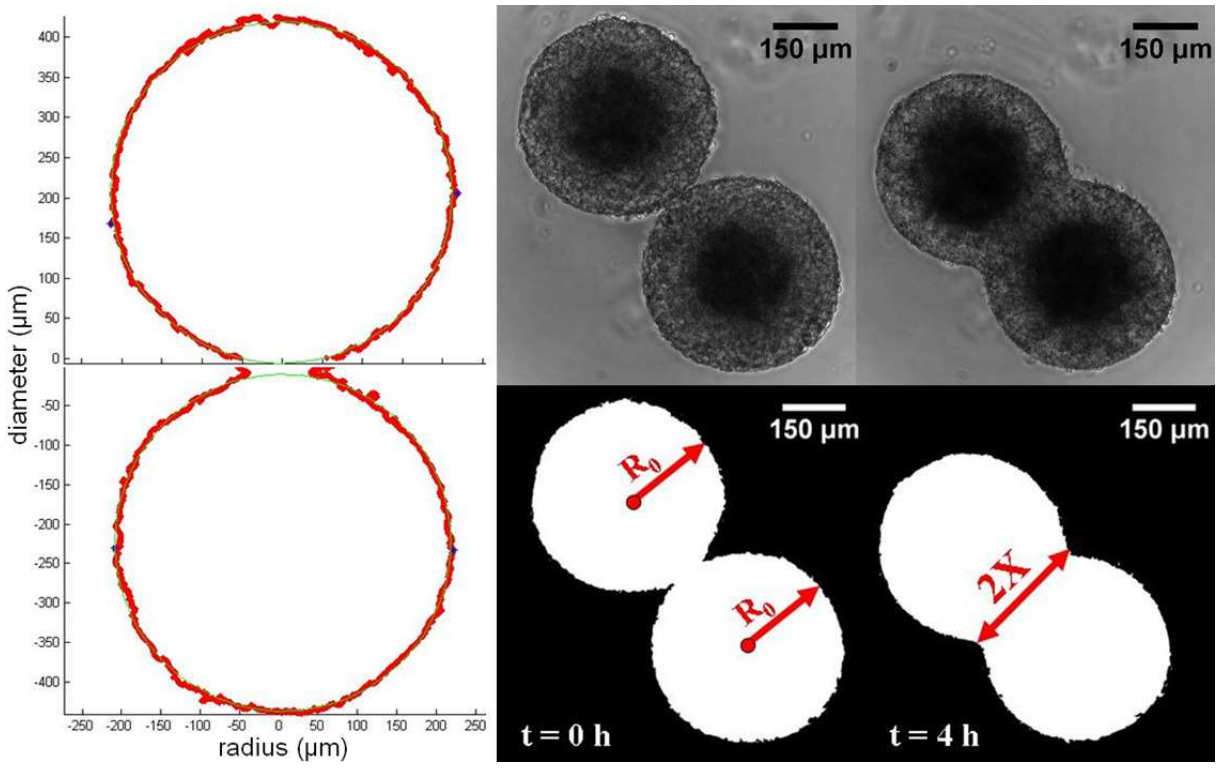

Fig. 2.8*: Schematic view of two fusing aggregates. (Left) Image analysis in Matlab allowing the estimation of the initial radius of the two identical cell aggregates. For each aggregate the radius is obtained and the final value of the initial radius is given by the mean of the two*

of them. (Right) Phase contrast and corresponding analyzed images allowing the extraction of the neck's radius X during the fusion process.

The fusion assay gives very reliable values of the ratios (σ/η) as long as we limit each measurement to $X_{limit} = (2/3)R_0$, which is the expected boundary for application of capillary law in the case of two liquid droplets [21], even though the total time to complete the process is longer.

To differently quantify the fusion process we also tried to fit our data using another non linear model presented in [23]:

$$X^3 = \alpha \frac{W_{CS}}{\eta} t R_0^2$$

This law is first derived for the spreading of soft viscoelastic polymeric beads [24] and was recently used to describe the early stages of spreading dynamics for both complete and partial wetting regimes of cell aggregates on a solid substrate coated with fibronectin or with a mixture at different percentages of fibronectin and PEG-PLL. The ratios $\alpha \frac{W_{CS}}{\eta}$ give the characteristic velocities W*, with W_{CS} being the cell-substrate adhesion energy per unit area, α being a numerical coefficient and η, the viscosity of the aggregate.

If we want to test whether the fusion of our aggregates could exhibit a similar scaling, we only have to replace W_{CS} by the TST σ.

2.6 Protocol for profile roughness measurements

We measured the roughness of aggregates by analyzing their contour shape. F9 and $F9^{(\alpha-/-)}$ cell aggregates were prepared as presented above and after two days of gyration in the incubator we transferred them into CO_2 independent-medium filled culture dishes. There was no need to treat the culture dishes in order to avoid adhesion, as the timescale of the entire procedure does not allow for this phenomenon to take place. We took phase contrast images on a motorized Nikon Eclipse TE 2000 E microscope using NIS Elements. Image analysis was performed with Matlab (The MathWorks). We convert our images to binary images, based on threshold. We use exponential curve fitting and we measure the areas given by the distance between the original contour and its curve fitting. To avoid areas in the contour where dead cells appear, we chose to analyze for the same aggregate several areas of different sizes. All analyzed images correspond to the same time in aggregate culture.

2.7 Rheology of embryonic cell aggregates

In this work, we have performed to our best knowledge the first rheological study of embryonic aggregates under shear stress.

2.7.1 Description of the experimental set-up: the rheometer

We used a commercial controlled stress rheometer (Anton Paar MCR301 - Modular Compact Rheometer) (Fig. 2.9) with a parallel-plate geometry coupled to an optical macroscopic observation system.

Fig. 2.9: *View of the Anton Paar MCR301 rheometer in the absence of the upper rotor but with the plexiglass hood chamber during a temperature calibration test (wire is the one of an external temperature controller).*

The parallel-plate system consists of two smooth glass surfaces with a roughness of approximately 2 nm (AFM measurements performed by Agnès Piednoir, LPMCN). The lower one is fixed while the upper one (Anton Paar PP43/136.5/GL-SN11471) can turn.

The rheometer is equipped with a Peltier System allowing us to control the desired temperature, *i.e.*, 37 °C. We completed our setup by using a homemade plexiglass hood chamber which covers the measuring system, avoiding medium evaporation and allowing fast and accurate temperature control.

The advantage of the transparency of glass plates is that it allows us to see the distribution and the number of the deposited aggregates. The macroscopic monitoring of aggregates is done using an USB 2 uEye SE camera (IDS Imaging Development Systems GmbH) equipped with a simple lens (or with a Computar TV LENS, 16 mm, 1:1.4, 119289), both placed underneath the measuring system (not visible in Fig. 2.9 but inserted in an open space behind the rheometer display and button panel).

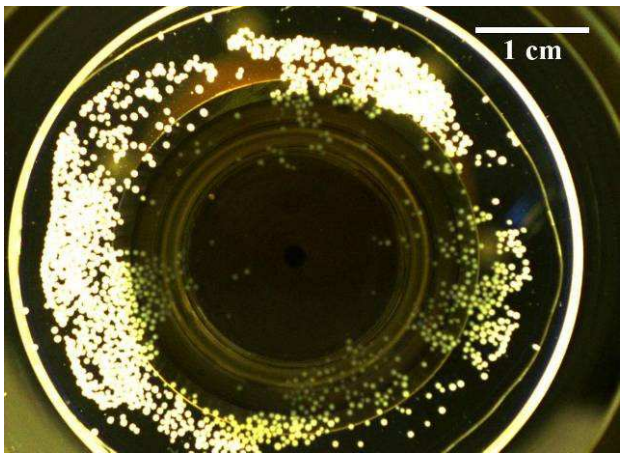

Fig. 2.10: *Visualizations of aggregates corresponding to a gap of 500 µm. Aggregates are surrounded by CO_2 independent medium.*

We control the entire system and we record our data using RheoPlus software (Anton Paar). Image recording is done using uEye Demo Application (IDS Imaging Development Systems GmbH) and image analysis is performed with Matlab (The MathWorks), ImageJ (National Institutes of Health, Bethesda) and VirtualDub.

2.7.2 Surface functionalization

For some experiments, in order to ensure a proper aggregate adhesiveness, the glass surfaces are treated with Poly-L-Lysine (Poly-L-lysine hydrobromide, P1274-25MG, Sigma) following the protocol described in [25]. We incubate the surfaces with the Poly-L-Lysine 0.1 mg/ml in water for at least 20 minutes. We rinse three times with distilled water and we let them dry for 1 to 2 hours.

2.7.3 Description of the experimental protocol and some technical issues

Before each experiment we perform a number of steps in order to always have the same departure state for the rheometer.

Thus, we begin by determining the inertia of the drive and of the measuring system and after we perform a long motor adjustment (for approximately 15 minutes).

An essential requirement for reliable data when performing rheological measurements on cells is to have an accurate, constant temperature of 37 °C. Thus, we have to wait for approximately a couple of hours for the entire setup to reach this condition before we begin any manipulation of our biological sample.

After the constant temperature is reached, we deposit our aggregates uniformly on the fixed lower surface and we fill the remaining space with CO_2-independent medium. The macroscopic observation allows us to visualize and to make an approximation of the number of deposited aggregates, as they appear as white or yellow approximately round structures on the images we record using the camera placed underneath them (Fig. 2.10).

It is very important to have a considerable number of aggregates that are subjected to shear in order to obtain a signal of a magnitude greater than the one produced by the meniscus which gives an elastic deformation and which is usually formed at the periphery of the studied surface. We point here that the viscosity of the CO_2 independent medium surrounding the aggregates is comparable with that of water (*i.e.*, 10^{-3} Pa.s) which gives a maximum torque in the order of 10^{-10} N.m. This value is below the sensitivity of our rheometer which is capable of measuring minimum 10^{-7} N.m but the meniscus could however induce a weak signal. That is why the number of deposited aggregates plays a determining role in obtaining the rheological signal. Thus, even though the very first experiments were carried out with a small number of aggregates (see Fig. 2.11 A), in most of the experiments and especially in the ones we present in this chapter we used a large number of aggregates (Fig. 2.11 B), up to several thousand for each case.

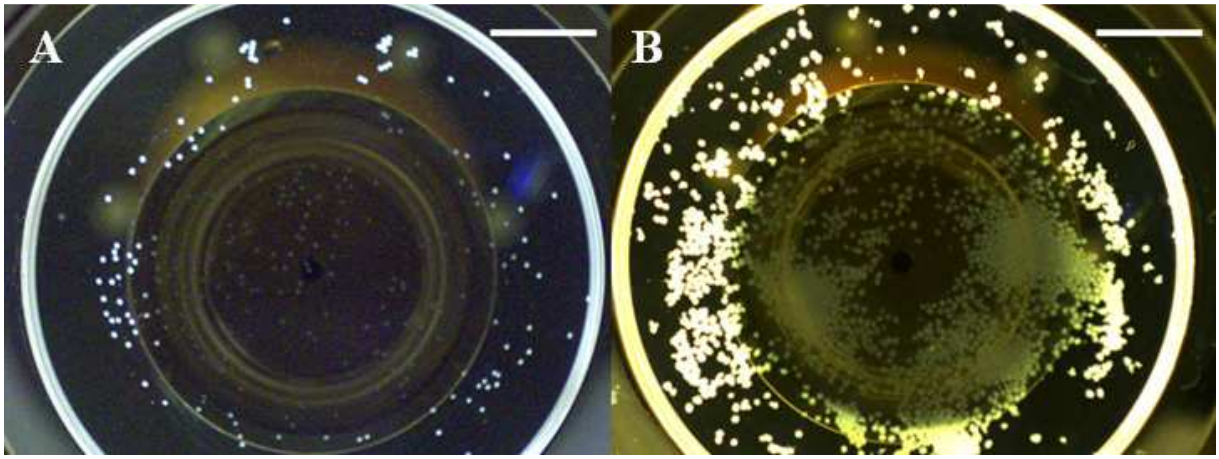

Fig. 2.11: *Images for two distinct experiments showing the difference between the number of aggregates deposited between the two parallel plates. The images correspond to the beginning of the experiment. Scale bars, 1 cm.*

Once the aggregates are deposited on the lower plate, we then bring the upper rotating surface in contact with our sample, imposing a gap whose values depend on the diameter of our aggregates and vary from one experiment to another. Usually, the two surfaces are

separated by 200 up to 300 µm. To avoid the formation of bubbles, we impose a very small velocity of the upper surface when approaching it to the lower one, whose order of magnitude varies according to the Table 2.12. This small velocity also avoids that aggregates would be subjected to a very high stress.

Position (mm)	**Velocity** (µm/s)	**Normal Force** (N)
0.2	5	40
0.6	10	40
1	100	40
2	500	40
5	1000	40
10	8000	5
12.5	8000	5

Table 2.12: *Gap setting parameters composing the active profile for measuring position (Speed controlled and Normal Force limited).*

As the timescale for some experiments is relatively large, we need to prevent the evaporation of the medium, as this phenomenon causes a displacement of the meniscus, which will shrink, creating a high drift on our rheology curves as shown in blue on Fig. 2.13.

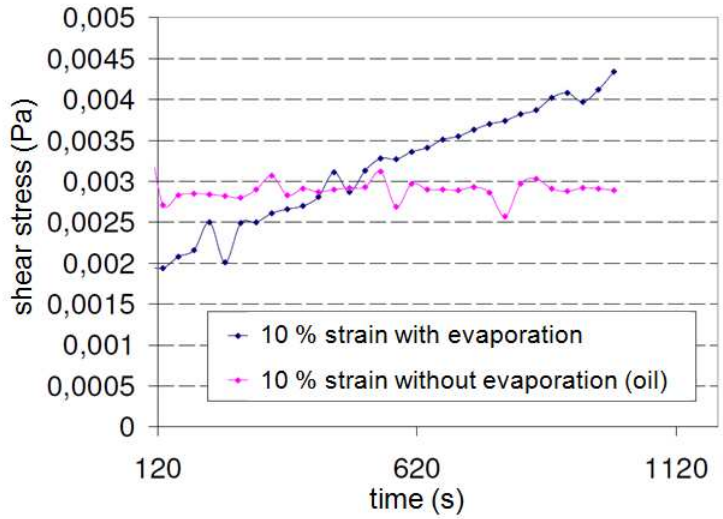

Fig. 2.13: *Evaporation phenomenon on a shear stress rheology curve (in blue). The experiment is done using PBS. In pink we represent the shear stress rheology curve when a ring of oil is used to avoid evaporation.*

Thus we decided to cover the free-open surface between the parallel plates with a ring shaped thick mineral oil layer (Sigma 330779-1L). The same type of rheological curve, represented in pink on Fig. 2.13, will no longer present a drift.

To be sure that this element has no influence on the results we obtain, we performed the same type of experiment using only PBS surrounded by the mineral oil layer. Comparing experiments with and without aggregates (Fig. 2.14), we obtained a comfortable factor 10 between this experiment (Fig. 2.14 A) and the classical one, where aggregates are sheared (Fig. 2.14 B).

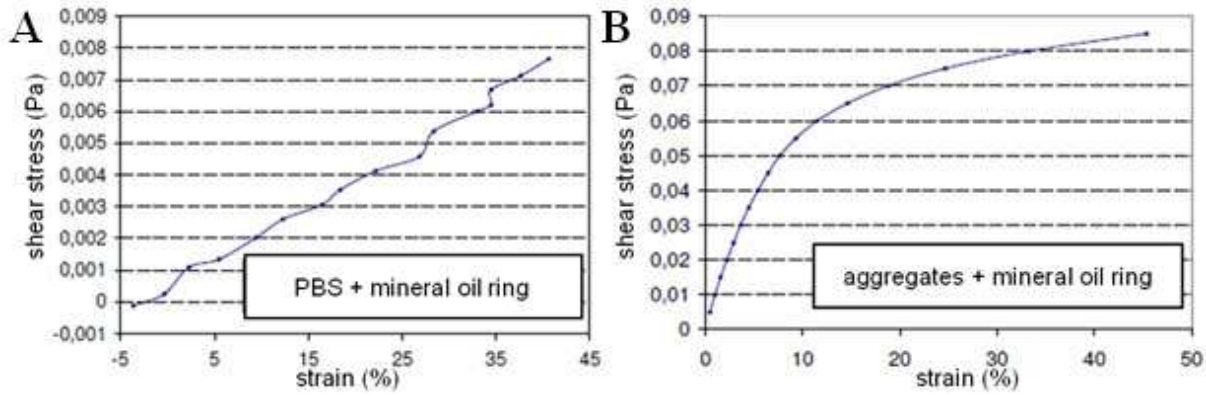

Fig. 2.14: *Comparison between the same type of experiment using PBS (A) and aggregates in CO_2 independent medium (B) surrounded by a ring of mineral oil. We can note the existence of a factor 10 between the two situations.*

The aggregates, located between the two parallel glass plates, are usually subjected to a deformation in simple shear. One of the risks which may appear when shearing the aggregates is to see them slip from the two glass surfaces, which then causes a sudden jump in the deformation. This is illustrated in Fig. 2.15, where we present a classical experiment of pulses of shear stress. We imposed pulses of shear stress varying from 3 to 10 seconds and separated by 1 or 10 minutes, depending on the experiment, and we recorded the deformation of our sample. One can see that after around 1200 seconds, the aggregates detached from the lower surface and turned with the upper one.

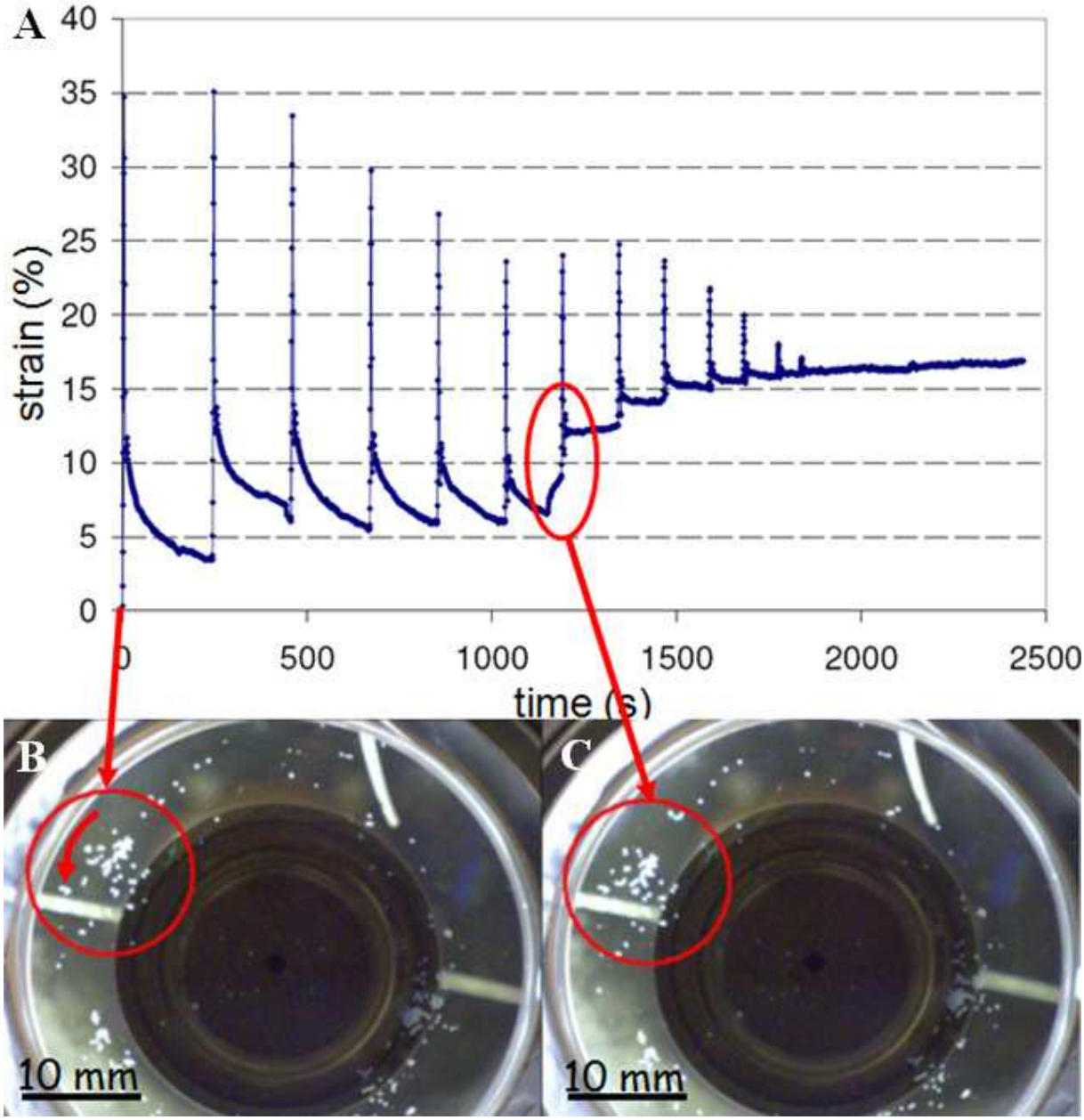

Fig. 2.15: *Visualization of the slipping phenomenon. (A) Typical rheological curve. The red ellipse shows the change in the baseline on the signal. (B-C) Corresponding images. The red arrow on the left corresponds to the beginning of the experiment (B) and the one on the right corresponds to the moment just after the aggregates' detachment (C). On each image, the red circle is surrounding the sliding region. The direction of sliding is represented with the red curved arrow in (B).*

To minimize these phenomena, besides functionalizing the rheometer's surfaces, we also have to wait for two hours after depositing the aggregates and approached the two glass surfaces, before starting any other manipulation. Cells situated at the outside of the aggregates will then have time to adhere firmly to the two surfaces and stay this way throughout the entire experiment. Hence, we can ensure that the aggregates are sheared, and do not just slide in block.

In our rheometer configuration, the lower plate is fixed while the upper one can turn, and we note the deformation induced by this rotation, measured at the periphery of the disk (in % of the gap e).

For each experiment, the rheometer allows us to have access to many variables, including the strain (γ), the shear rate ($\dot{\gamma}$), and the shear stress (τ) exerted by the rheometer to the fluid, which are the main recorded variables of interest.

Two major types of experiments are then possible: we can fix a deformation (or shear rate) and we look at how the shear stress changes or we can maintain a constant shear stress on the sample and we look at the evolution of the deformation that the rheometer applies as to maintain the constant stress.

However, the rheometer can also perform oscillation experiments. We will then have access to the elastic modulus G', which represents the elastic response of our sample, and the loss modulus G", which represents the viscous response. The value of one over the other tells us the rather elastic or viscous behavior of our sample.

2.7.4 How to get the real stress underwent by aggregates?

Even though geometrically, the parallel plate configuration is the simplest one, mathematically however it is more complex to analyze than the cone-plate configuration.

In this thesis, we will present our results for controlled shear rate or shear stress experiments in terms of shear stress or strain over time. But what our controlled stress rheometer (CSR) is actually measuring is not the stress, but the torque.

The shear stress σ_{rh} given by the rheometer (maximal shear stress at external radius of the plate) is given by the following relation for a simple fluid:

$$\sigma_{rh} = \Gamma * \mathrm{Css},$$

with C_{SS} a numerical factor which will correspond to the exact relation between the maximal shear stress at the periphery of the disk and the measured torque.

In the case of a simple fluid where the stress is given by the relation: $\sigma(r) = \eta\dot{\gamma}(r) = \eta\frac{\omega r}{e}$, where ω is the angular speed, e is the gap between the two plates, η the viscosity and r the distance to the center of the parallel plate, one can compute the torque as:

$$\Gamma = \int_0^{R_{max}} \sigma\,(r) 2\pi r^2 dr = \frac{\pi}{2}\,\eta\,\dot{\gamma}_{max} R^3 = \frac{\pi}{2} R^3 \sigma_{max}.$$

Thus, $C_{SS} = \frac{2}{\pi R^3} = 64.44$ Pa/(mNm), where R, the external radius of the parallel plates is equal to 2.1456 cm and $\sigma_{max} = \sigma_{rh}$.

If we want to get back to the real stress generated by biological aggregates while being sheared we have to make some hypothesis on the nature of the stress and we will have to get access to the distribution of the aggregates.

For simplicity, let make the hypothesis that the aggregates' stress is simply elastic, which is a rather reasonable approximation as far as typical experimental time is not larger than a few minutes as discussed in the introduction chapter:

$$\sigma(r) = E\gamma(r) = E\gamma_{max}\frac{r}{R} = \sigma_{el}\frac{r}{R}.$$

Let $\epsilon(r)$ be the distribution function of aggregates under the parallel plates. Then,

$$\Gamma = \int 2\pi r^2 \sigma(r)\epsilon(r)dr = \frac{2\pi}{R}\sigma_{el}\int r^3\epsilon(r)dr.$$

We can then write using the relation between torque and maximal shear stress σ_{rh} given by the rheometer:

$$\sigma_{el} = \frac{R^4\sigma_{rh}}{4\int r^3\epsilon(r)dr}$$

σ_{el} and σ_{rh} are of the same order of magnitude.

- In the case where the deformation is imposed, there is no divergence, because when the number of aggregates is small, $R^4\sigma_{rh}$ is small and so is $\int r^3\epsilon(r)dr$.

- In the case where the stress is imposed, we have to be careful if the number of aggregates is small or if they are not well distributed, the stress on each aggregate can be very high.

Let's do the calculus in two simple cases:

a) Homogeneous distribution $\epsilon(r)$=1: $\sigma_{el} = \sigma_{rh}$.

b) Distribution on a disk of width e at mean distance $r = r_0$, $\sigma_{el} = \frac{R^4\sigma_{rh}}{4r_0^3 e}$.

In all cases, $\sigma_{el} \geq \sigma_{rh}$.

In the case of a random distribution which is the case of our experiments, as we are recording a video of the full field of view of the shearing parallel plates, we have developed a simple routine to threshold images and get the experimental $\epsilon(r)$ distribution and automatically calculate the correction factor between the stress given by the rheometer, and the maximum elastic stress.

However, to be fully rigorous, we would also have to take into account the fact that some of the aggregates may not be adhering to both plates, and may not contribute to the shear stress signal.

Finally, the crudest approximation is the fact that we assume a purely linear elastic relation between the stress and the strain, which is as we will show clearly not the case.

For these reasons, we decided to present in this thesis the direct shear results given by the rheometer. And we hope that when we will have a full and complete picture of the rheology of our system, we will be able to get back to real numbers thanks to our knowledge of the aggregates distribution. But a little more work remains to be done…

References:

1. Nagafuchi, A., Shirayoshi, Y., Okazaki, K., Yasuda, K. & Takeichi, M. Transformation of cell adhesion properties by exogenously introduced E-cadherin cDNA. *Nature* **329**, 341–3 (1987).

2. Maeno, Y. *et al.* α-catenin-deficient F9 cells differentiate into signet ring cells. *American Journal of Pathology* **154**, 1323 (1999).

3. Yoshito Maeno, S. M. *et al.* alpha-Catenin-Deficient F9 Cells Differentiate into Signet Ring Cells. *American Journal of Pathology* **154**, 1323–1328 (1999).

4. Fukunaga, Y. *et al.* Defining the roles of beta-catenin and plakoglobin in cell-cell adhesion: isolation of beta-catenin/plakoglobin-deficient F9 cells. *Cell Struct Funct* **30**, 25–34 (2005).

5. Mgharbel, A. Physique et rhéologie des agrégats cellulaires embryonnaires. (2009).

6. Brevier, J., Vallade, M. & Riveline, D. Force-Extension Relationship of Cell-Cell Contacts. *Physical Review Letters* **268101**, 98–101 (2007).

7. Omelchenko, T., Vasiliev, J. M., Gelfand, I. M., Feder, H. H. & Bonder, E. M. Rho-dependent formation of epithelial "leader" cells during wound healing. *Proceedings of the National Academy of Sciences of the United States of America* **100**, 10788–93 (2003).

8. Kovács, M. *et al.* Mechanism of blebbistatin inhibition of myosin II. *The Journal of biological chemistry* **279**, 35557–63 (2004).

9. Marmottant, P. *et al.* The role of fluctuations and stress on the effective viscosity of cell aggregates. *Proceedings of the National Academy of Sciences of the United States of America* **106**, 17271–5 (2009).

10. Mgharbel, A., Delanoë-Ayari, H. & Rieu, J.-P. Measuring accurately liquid and tissue surface tension with a compression plate tensiometer. *HFSP journal* **3**, 213–21 (2009).

11. Kalantarian, A. *et al.* Axisymmetric drop shape analysis for estimating the surface tension of cell aggregates by centrifugation. *Biophysical journal* **96**, 1606–16 (2009).

12. David, R., Ninomiya, H., Winklbauer, R. & Neumann, A. W. Tissue surface tension measurement by rigorous axisymmetric drop shape analysis. *Colloids and surfaces. B, Biointerfaces* **72**, 236–40 (2009).

13. Guevorkian, K., Colbert, M.-J., Durth, M., Dufour, S. & Brochard-Wyart, F. Aspiration of Biological Viscoelastic Drops. *Physical Review Letters* **104**, 1–4 (2010).

14. Foty, R. A., Forgacs, G., Pfleger, C. M. & Steinberg, M. S. Liquid properties of embryonic tissues: measurement of interfacial tensions. *Physical review letters* **72**, 2298–2301 (1994).

15. Hegedüs, B., Marga, F., Jakab, K., Sharpe-Timms, K. L. & Forgacs, G. The interplay of cell-cell and cell-matrix interactions in the invasive properties of brain tumors. *Biophysical journal* **91**, 2708–16 (2006).

16. Foty, R. A., Pfleger, C. M., Forgacs, G. & Steinberg, M. S. Surface tensions of embryonic tissues predict their mutual envelopment behavior. *Development (Cambridge, England)* **122**, 1611–20 (1996).

17. Schötz, E. *et al.* Quantitative differences in tissue surface tension influence zebrafish germ layer positioning. *HFSP journal* **2**, 42–56 (2008).

18. Norotte, C., Marga, F., Neagu, A., Kosztin, I. & Forgacs, G. Experimental evaluation of apparent tissue surface tension based on the exact solution of the Laplace equation. *EPL (Europhysics Letters)* **81**, 1–6 (2008).

19. Frenkel, J. Viscous flow of crystalline bodies. *J Phys* **9**, (1945).

20. Shaler, A. Seminar on the Kinetics of Sintering (with discussion). *J. Met., 1* (1949).

21. Pokluda, O., Bellehumeur, C. T. & Vlachopoulos, J. Modification of Frenkel's model for sintering. *AIChE journal* **43**, 3253–3256 (1997).

22. Jakab, K. *et al.* Relating cell and tissue mechanics: implications and applications. *Developmental dynamics: an official publication of the American Association of Anatomists* **237**, 2438–49 (2008).

23. Douezan, S. *et al.* Spreading dynamics and wetting transition of cellular aggregates. *Proceedings of the National Academy of Sciences of the United States of America* **108**, 7315–20 (2011).

24. Michel F, S. M. Kinetics of the JKR experiment. *CR Acad Sci Paris* **Série 2**, 17–20 (1990).

25. Bershadsky, A., Chausovsky, A., Becker, E., Lyubimova, A. & Geiger, B. Involvement of microtubules in the control of adhesion-dependent signal transduction. *Current biology : CB* **6**, 1279–89 (1996).

Chapter 3

Physical properties - Fine tuning of tissues' viscosity and surface tension through contractility: a new role for α-catenin

What governs tissue organization and movement? If molecular and genetic approaches are able to give some answers on these issues, more and more works are now giving a real importance to mechanics as a key component eventually triggering further signaling events [1,2].

As developed in the introduction chapter of this manuscript, Steinberg and co-workers proposed a long time ago an analogy between liquids and tissues and showed that indeed tissues possess a measurable tissue surface tension and viscosity. In the study presented in this chapter we question the molecular origin of these parameters and we give a quantitative measurement of adhesion versus contractility in the framework of the differential interfacial tension hypothesis (DITH).

We show that a tunable surface tension and viscosity can be achieved easily through the control of cell-cell contractility compared to cell-medium one. Moreover we show that α-catenin is crucial for this regulation to occur: these molecules appear as a catalyser for the remodeling of the actin cytoskeleton underneath cell-cell contact, enabling a differential contractility between the cell-medium and cell-cell interface to take place.

3.1 Introduction

3.1.1 Origin of tissue surface tension and viscosity

Thanks to the pioneer's work of M. Steinberg, tissue surface tension (TST) has appeared as a very robust tool to predict tissue envelopment behavior [3]. TST reflects intercellular cohesion and predicts cell rearrangement in tissues.

However, the microscopic origin of this surface tension is not clear. Steinberg proposed the Differential Adhesion Hypothesis (DAH) to explain the origin of surface tension and the variation from tissue to tissue. He gave a predominant role to the adhesion energy due to surface adhesion proteins [4], such as cadherins [5], and postulated that surface tension was directly a measurement of the cadherin-cadherin interactions.

From expressing different levels of cadherins in cells, Foty and Steinberg got a linear relationship between the cadherin expression level and the surface tension [3].

To estimate the magnitude of the surface energy due to specific cadherin-cadherin expression one needs estimate of the cadherin density (cadherin/μm^2) and the bond energy (in k_BT or Joules).

Using a surface force apparatus and N-, E- and C-cadherins covalently attached to supported lipid bilayers, Prakasam et al. [6] measured mean bond energies of all possible cadherin pairs (homo- or heterotypic). The stronger energies are obtained when extracellular domains EC3 between opposed cadherins are aligned (D = 38.3 nm between the two bilayers including 2x1.5 nm of the His-Tag linker). Surprisingly, heterotypic bond energies are not lower than homotypic ones and the mean bond energy is about 6 k_BT (~ $25*10^{-21}$ J).

There are very few studies where cadherin densities are estimated. Li et al. [7] use an anti-E-cadherin modified AFM tip pressed against hES cells and performed quantitative force spectroscopy. They found densities of 11, 42, 85 and 200 cadherins/μm^2 for the ectoderm, mesoderm, endoderm and undifferentiated cells respectively. These quantities are at the same level as the average expression of N-, E- and P-cadherins transfected in L929 cells reported by Foty et al. [3] using quantitative flow cytometry. The authors report the range 25000-250000 cadherins/cell which corresponds to 50 to 500 cadherins/μm^2 when assuming a cell area of 500 μm^2. Using the later range of values and the mean bond energy of cadherin pairs measured by surface force apparatus [6], one obtains the following range of surface energies: 10^{-3}-10^{-2} mN/m. This is almost three orders of magnitude lower than the measured range of surface tensions in the same work: 1-6 mN/m [3].

This simple estimate clearly demonstrates that the origin of the measured surface tension may not be simply due to the trans-interaction between single molecules. Moreover,

cadherins are not completely recovering the adhesion zone but often form patches. These cadherin patches might have this role to bring in close contact the two cell membranes. One may therefore have to add other type of specific adhesion or even unspecific adhesion between the rest of the membranes in between these cadherin clusters which may be high, as membranes seem there in close contact. Van der Waals or depletion forces might play a role, as the contact zone distance will entail exclusion of a part of the big molecules that the medium may contain.

Different complementary experimental approaches suggest that cell sorting in vivo and in vitro is not governed solely by protein-level differences in cadherin adhesion [6,8]. But already in 1976, Harris pointed out that surface tension may have different origins. He, in particular, proposed a differential contraction hypothesis [9]. This idea will be later used for computer simulations of cell sorting [10].

And recent studies have indeed highlighted the important role of the contractile actin system in the organization of tissues [10,11]. In the light of these findings, one can question again Foty's experiments and ask whether modifying the expression level of cadherins was not also modifying the contractility at the cell-cell, cell-medium interfaces.

One of the goals of our study is to have a better understanding on the respective roles of adhesion and contractility on tissue surface tension. Moreover, pursuing this fluid analogy, it appears that another parameter is of great importance if we want to understand the dynamics of tissue reorganization: the tissue viscosity.

Different techniques were proposed to measure this parameter. Forgacs and co-workers interpreted their force relaxation behavior in a tissue surface tension measurement as a viscoelastic relaxation from where they could deduce a viscous parameter [12]. Other researchers analyzed the kinetics of fusion of two aggregates [13–15] in order to measure the visco-capillary velocity $v_P = \sigma/\eta$. Recently, relative viscosity values were measured in two different geometries by Brochard and co-workers, namely the aspiration of aggregates in capillary tubes [16], and the spreading of aggregates on adhesive substrates [17]. Gathering data obtained from these different studies (Table 3.1), is hard to find any correlation between viscosity and TST. The range of viscosity values is between 0.2 and $1.5*10^6$ Pa.s, which is orders of magnitude larger than reported viscosities of individual cells [18,19]. These individual cell values depend on cell types, on shear rate [20] and on the probe size (intercellular probe or whole cell measurements [19]). Largest values (*i.e.*, $\eta = 10^4$ Pa.s) were measured for individual fibroblasts and endothelial cells [18].

Cell Line/Tissue Type	σ/η Frenkel (*10^{-7}cm/s)	σ/η corrected (μm/min)	σ (mN/m)	η (*10^{6} Pa.s)
Heart 5 days [13,21]	13.4	0.38	8.5	1.47
Liver 5 days [13,21]	27.5	0.79	4.6	0.35
Liver fragment rounded [13,21]	7.2	0.21	4.6	1.34
Cardiac cushion [14]		0.64	16	1.5
Neural retina fusion [21,22]		0.21	1.6	0.47
Neural retina rounding [21,22]		0.06	1.6	1.6
Murin sarcoma (S180) [16]		1.8	6	0.19

Table. 3.1: *Aggregate literature values for σ, η and σ/η respectively. As explained in [15], the original Frenkel's equation [23] has to be corrected by a factor 2π/3 in order to calculate the correct value for the visco-capillary velocity* $v_P = \sigma/\eta$. *For a detailed comparative description of the fusion and rounding processes, see [24].*

In case of aggregates, no systematic measurements were performed as a function of cadherin expression or cell contractility, and that is what we tested here (for the contractility dependence) using the fusion assay experiment.

If we want to understand the dependence of surface tension or viscosity on the underlying properties of the actin network, we really need a comprehensive description of the very dynamic and very complex interplay between cadherins and the cytoskeleton. Many reviews have been written around these issues recently [25–28].

Let's put here a special emphasis on one of the key partner in the adhesive complex: α-catenin. This protein has long been thought as the one protein which mediated the link between cadherin and the actin cytoskeleton. However, later on in vitro, it was shown that α-catenin could indeed bind either to the β-catenin-cadherin complex or to actin, but not to both at the same time [29]. If the link has to be done, we will have to find another protein. EPLIN might play this role [30].

To make the scene even more complicated, it appeared recently that α-catenin was also a tension transducer [31] and was able to change conformation under tension and to recruit vinculin while stretched at the adhesion zone [32].

But if one wants to really understand the cadherin-actin complex, it is not just the eventual physical link which has to be considered but much more the dynamics of the reorganization of the entire network underneath the contact zone which occurs during the formation of cell-cell contact. Yamada and Nelson have thus studied the growing E-cadherin contacts between MDCK cells [33] and observed a complete remodeling of the actin network at the first stage of contact formation : the actin cortex bundle which normally surrounds the cell is literally dissolved leaving actin bundles bracketing the expanding edge contact. If myosin

was reported to be present at cell-cell junctions [34], activated (phosphorylated) myosin is only found on cell periphery [33].

What do we know about the regulation of this remodeling? Formin has been shown to be associated with α-catenin [35], and so it is envisioned that it favors the apparition of actin bundles, while Arp2/3 was shown to be activated on the side of the cadherin-adhesion zone, favoring the growing of the contact (for a review, see [26]).

We will show here that not only α-catenin is essential for the remodeling to occur but moreover that it is an essential element for the regulation through contractility of tissue's essential parameters that are viscosity and surface tension.

3.1.2 Strategy

In order to investigate the role of α-catenin, we used $F9^{(\alpha-/-)}$ cells which have been knocked out for α-catenin. This loss does not change the level of cadherin expressed by F9 cells [36] (Fig. 2.2).

To get further information on the role of contractility, we also investigated and quantified the effects of three different drugs, nocodazole, Y-27632 and blebbistatin, with opposed actions on the cytoskeleton. The first one, nocodazole, is expected to indirectly increase stress fiber contractility by inhibiting microtubule dynamics and activating the rho kinase pathway [37]. The enhancement of cell contractility is achieved in a cadherin independent manner. In opposition to nocodazole, the second drug we exposed our aggregates to, Y-27632 dihydrochloride monohydrate is known as a selective inhibitor of Rho-associated protein kinases (ROCK-I and ROCK-II), thus implies a decrease in cell contractility [38]. Finally, the third drug we used, blebbistatin, is a selective inhibitor of non-muscle myosin II [39]. We wanted to interfere with contractility with a negative effect (decreasing contractility), however the results with blebbistatin and Y-27632 that we found in the literature are exactly the same [40–51]. Therefore, even though some experiments were made using blebbistatin, we decided to study in a larger extent the drug shutting off the rho kinase pathway (*i.e.,* Y-27632) to have a clear opposite to the one activating this pathway (*i.e.,* nocodazole).

Combining these two approaches (drugs affecting the cytoskeleton together with the cancer cell line genetically invalidated for the stable expression of proteins responsible for the binding cytoskeleton-cadherins) has enabled us to measure quantitatively the respective role of adhesion and contractility on tissue surface tension and viscosity and to highlight the essential role of α-catenin.

3.2 Quantitative dependence of TST on contractility - Surface tension measurements

3.2.1 Force and shape relaxation during compressions

In order to study the relative contribution of adhesion and contractility on surface tension we measure TST using the compression plate tensiometry [52,53].

Aggregate compression experiments on the tissue tensiometer allow us to estimate aggregate surface tension by recording the force signal when a plateau is reached and the shape parameters of aggregates (See Materials and Methods section).

It has been already shown that the surface tension is independent of the number and magnitude of compression up to 50% compression rate [54] (see also Fig. 2.6 in the Materials and methods chapter). This allows us to have a large choice in the range of number and magnitude of compression steps and these values are varying from one experiment to another depending on each aggregate size.

Fig. 3.2 shows aggregate profiles as measured by the side stereomicroscope of our tissue tensiometer at different steps of compression (of 30 µm each) for a F9 WT cell aggregate (approximately 370 µm in diameter) exposed to 10 µM Y-27632 2 hours before the experiment. Each step of compression is separated by an interval of 30 minutes but the aggregate shape reaches equilibrium more quickly.

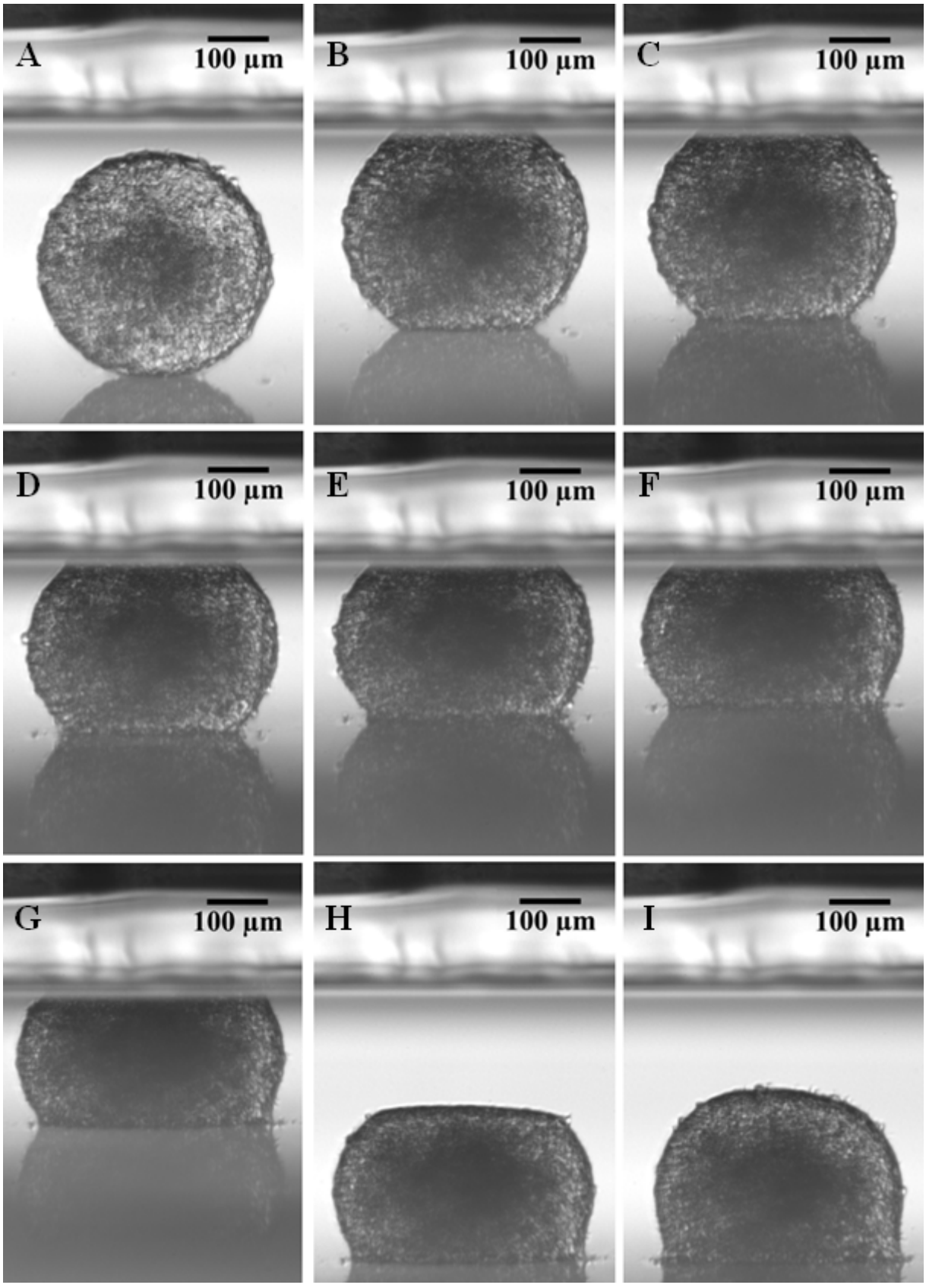

Fig. 3.2: *Side view on a stereomicroscope of a F9 WT aggregate exposed to Y-27632 compressed between two parallel plates: before compression (A), while approaching it to the*

upper plate (B), after 5 steps of compression of 30 µm each (C-G), after lowering the lower plate at the end of the compression series (H) and 30 minutes after lowering the plate (I).

In the followings, typical force signals for F9 WT (Fig. 3.3), F9 WT treated with 10 µM Y-27632 (Fig. 3.4) and F9 WT treated with 1 µM nocodazole (Fig. 3.5) are presented.

We first record for different periods of time the reference signal, that is when no force is introduced in the system (dark blue symbols). Thereafter, compressions steps are performed. The peak of force just after a compression is followed by a force relaxation.

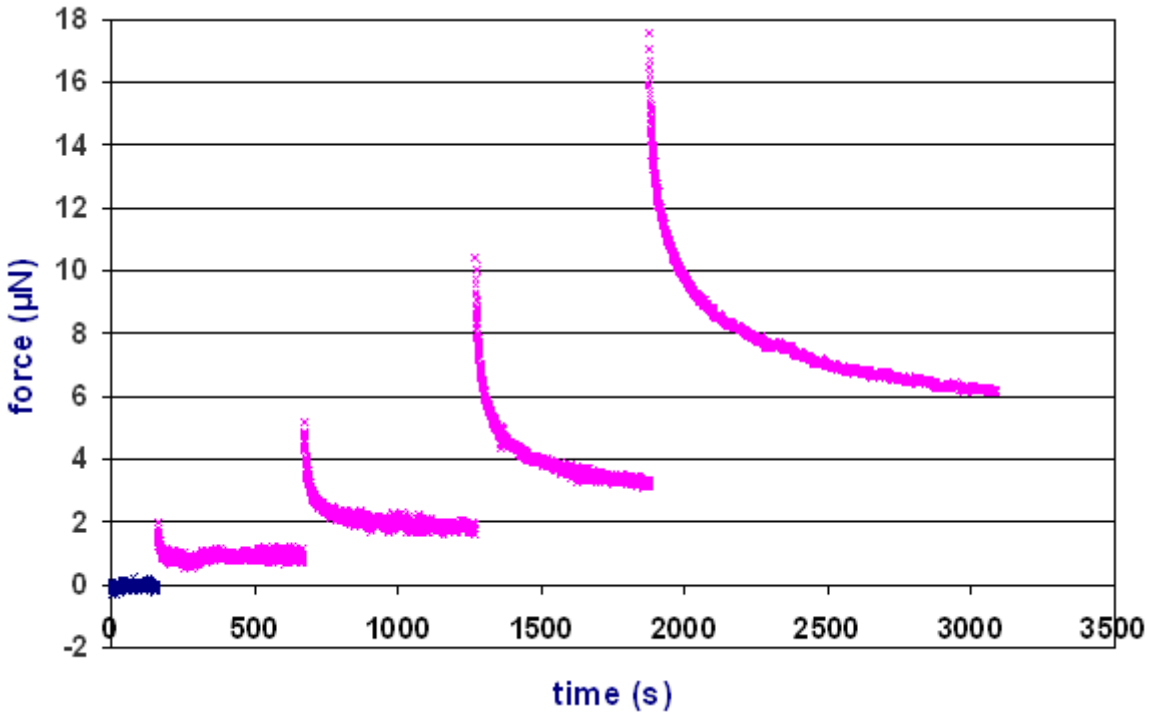

Fig. 3.3: *Force signal of a F9 WT subjected to 4 compressions in steps of 40 µm each. The dark blue color corresponds to the several minutes before performing the first compression and the pink color corresponds to the four compressions with 10 minutes interval between each step. The experiment is stopped 20 minutes after the fourth compression.*

In this first example (*i.e.*, F9 WT), the aggregate was not exposed to any drug before or during the experiment. The repulsive force after one or two compressions of 40 µm reaches approximately 1 and 2 µN respectively (Fig. 3.3).

Treating the aggregate with 10 µM Y-27632 decreases cell contractility, thus we expect that the force value will also decrease accordingly. In this next example, the aggregate was exposed to the drug an hour before the experiment. As the drug is expected to induce a change in the aggregate's behavior, after each step of compression we waited for a longer period of time than usual (*i.e.,* 2 hours) in order for the aggregate to reach force and shape equilibrium. We can indeed see that the value of the force is less important than for the

previous experiment. It is barely measurable after one compression and reaches about 0.5 µN after two compressions of 45 µm each (Fig. 3.4). Very similar force signals were obtained for F9 WT cell aggregates treated with 10 µM blebbistatin (not shown).

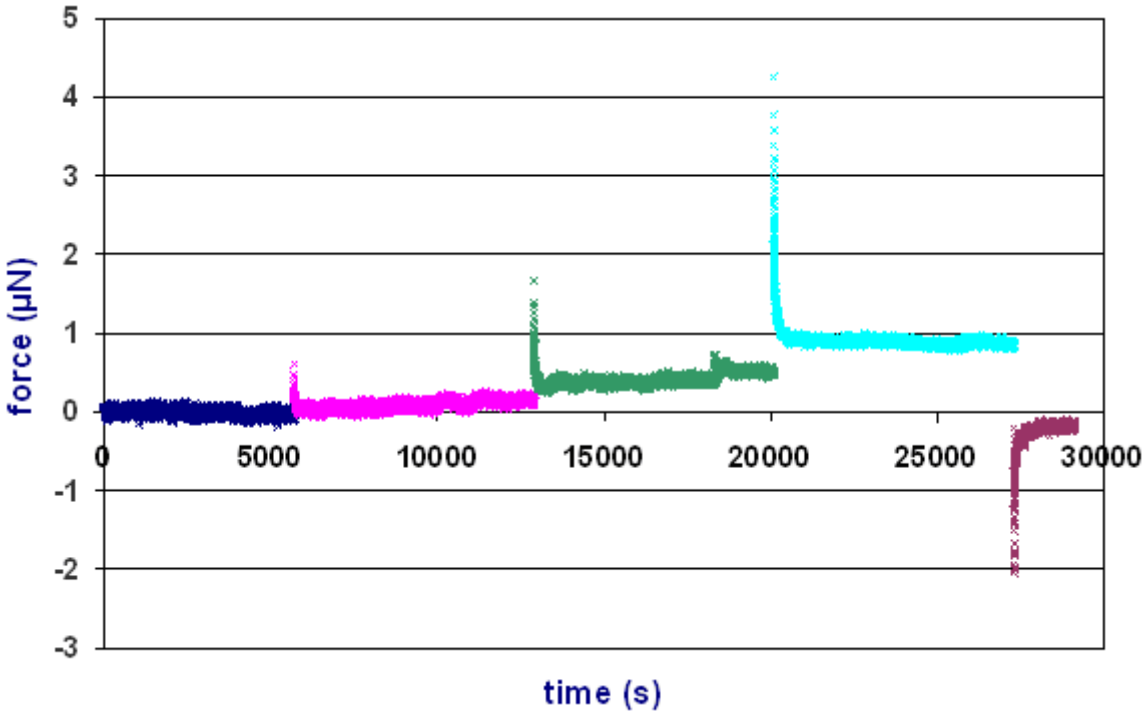

Fig. 3.4: *Typical force signal of a F9 WT treated with 10 µM Y-27632 and subjected to 3 compressions in steps of 45 µm each. The dark blue color corresponds to the period of time before performing the first compression. Pink, green and light blue colors correspond to the three compression steps. At the end of the experiment, we released the aggregate and we recorded the force signal for 30 minutes (represented in purple).*

The treatment with 1 µM nocodazole should also change the force amplitude but in an opposite way than Y-27632. This is what we obtain: about 2 and 5-6 µN after one and two 50 µm compression steps respectively (Fig. 3.4). However, even if we allow the aggregate to relax for 2 hours after each step of compression, the force after the second and the third step doesn't reach equilibrium.

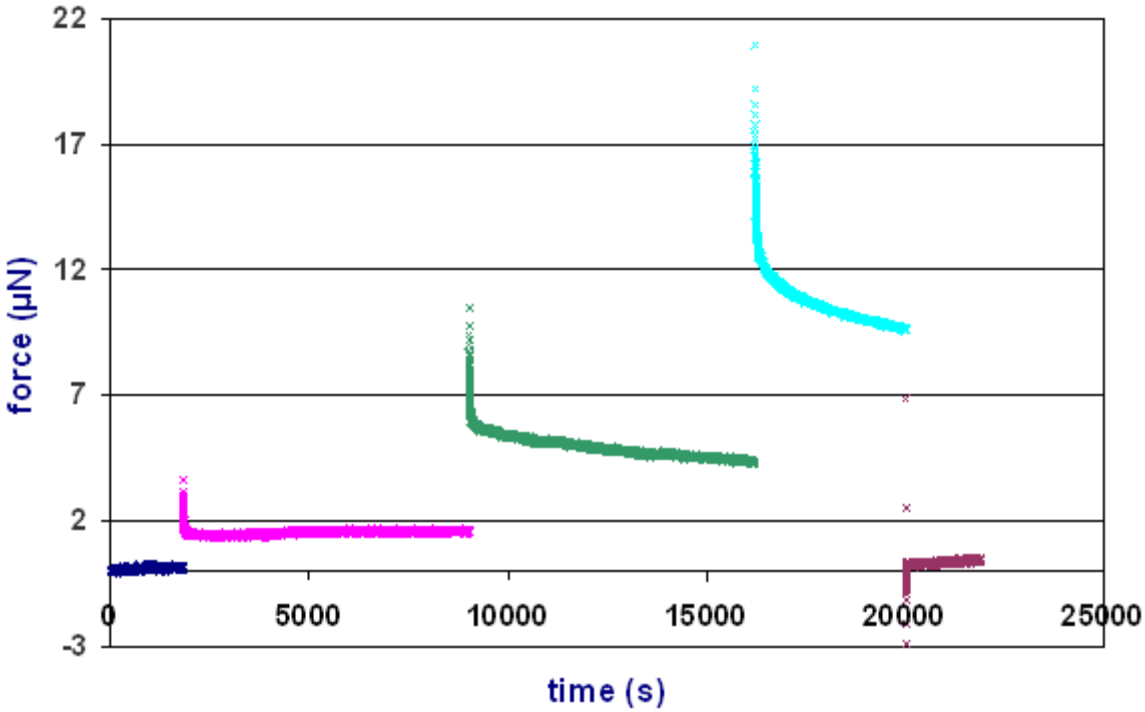

Fig. 3.5: *Force signal obtained when subjecting a F9 WT aggregate to 3 successive compressions of 50 µm each after being exposed to 1 µM nocodazole two hours before the experiment. The dark blue color corresponds to the period of time before performing the first compression. Pink, green and light blue colors correspond to the three compression steps. At the end of the experiment, we released the aggregate and we recorded the force signal for 30 minutes (represented in purple).*

3.2.2 Surface tension as a function of aggregate size

From the force relaxation curves and the shape of the compressed aggregates, we have computed TST values (σ). For most experimental conditions (cell type or presence of drugs), we have repeated at least 5 times the surface tension measurement with aggregates of various sizes. We already show that TST was independent of the compression step, here we show that the TST is also independent of the aggregate's volume (Fig. 3.6), indicating that we are measuring a true surface tension.

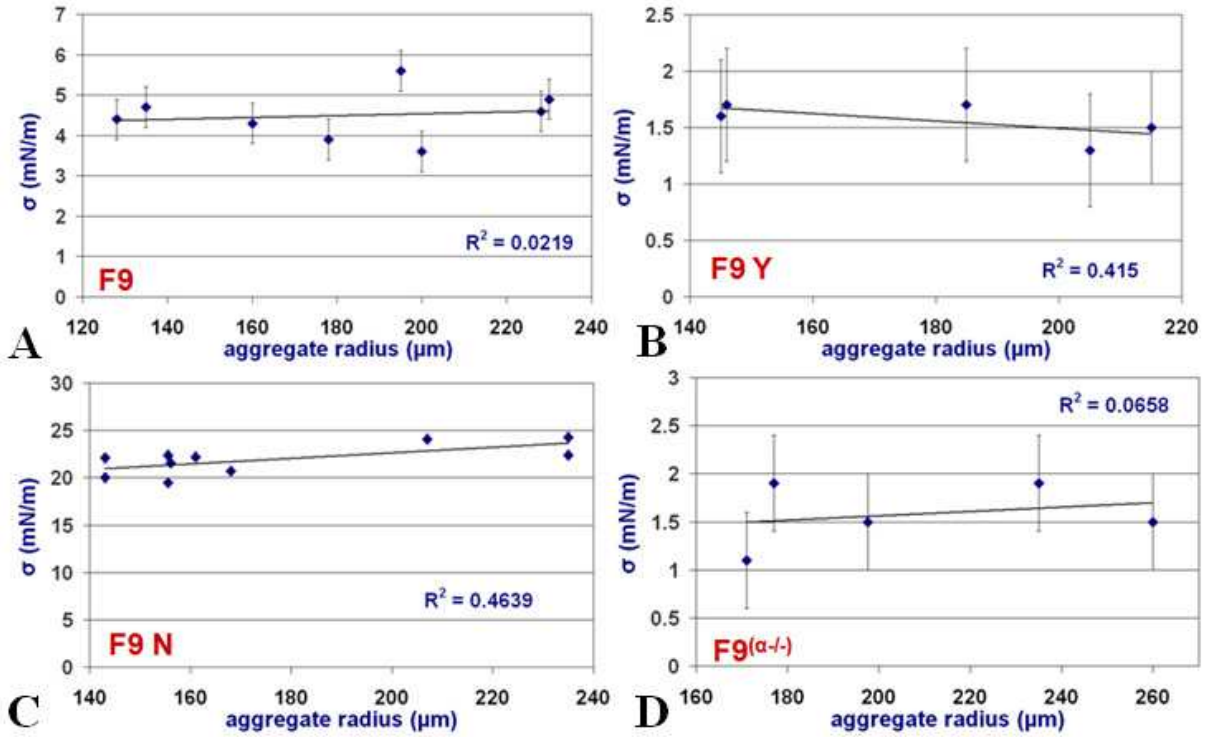

Fig. 3.6: *TST measurements Vs. aggregate radius. (A) TST of F9 WT cell aggregates as a function of aggregate radius. (B) Representation for F9 WT cell aggregates treated with 10 µM Y-27632. (C) Representation for F9 WT cell aggregates treated with 1 µM nocodazole. (D) Representation for F9$^{(\alpha-/-)}$ cell aggregates. TST values are independent of the aggregate size (radius). The error bars are given by the 95% confidence interval given on the linear fit of Force Vs aggregate's geometrical parameters data. The coefficients of determination are 0.0219 (A), 0.415 (B), 0.4639 (C) and 0.0658 (D).*

3.2.3 Surface tension values

The mean values obtained from TST experiments are summarized in Fig. 3.7.

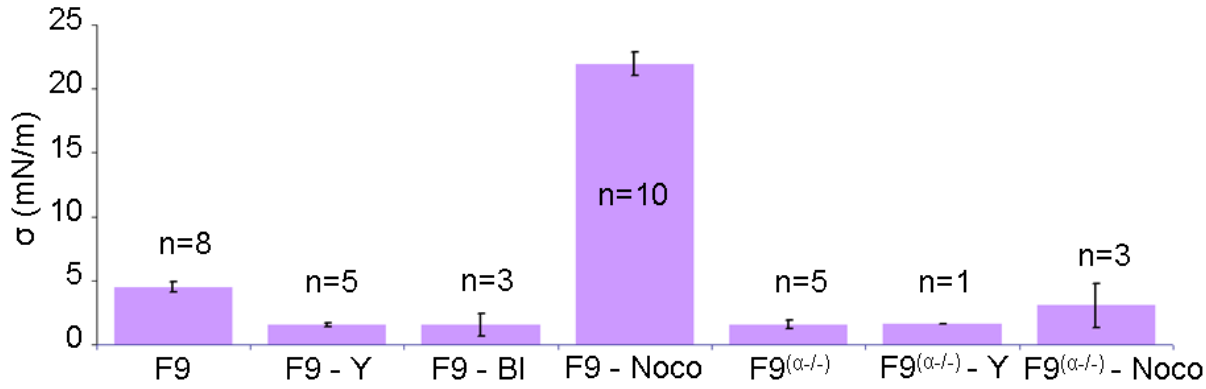

Fig. 3.7: *The value of the TST for different cell lines and drugs as obtained from tissue surface tensiometry experiments. Error bars represent the standard errors of the mean (95%*

confidence interval of the mean) and n is the number of experiments, each experiment corresponding to several successive compressions.

All our results present quite small error bars because experimental dispersion is rather low (see also Fig. 3.6). All differences with the parent cell line F9 are statistically significant, as determined by using Student's t-tests where $p < 0.01$. They come to confirm that surface tension strongly depends on cell contractility.

Previously obtained values in our team (PhD thesis of A. Mgharbel [24]) for the TST (not included in the summary of Fig. 3.7) were 10 ± 3, 4.9 ± 0.5 and 1.5 ± 0.7 mN/m for respectively F9 treated with 1µM nocodazole, F9 WT and $F9^{(\alpha-/-)}$ cell aggregates (in this case, the errors bars represent standard deviations estimated on a series of compressions for each cell aggregate type) [24]. Hence, except for nocodazole, these results are very robust. But when using nocodazole, equilibrium is not reached as the force is continuously decreasing even after two hours of relaxation (Fig. 3.5). However, having done the analysis at different stages of the relaxation time, we can still state that the values for the surface tension are much larger than for non-treated aggregates.

The reference value for the TST is the one obtained for the F9 WT: 4.5 ± 0.41 mN/m (n = 8 aggregates).

The surface tension for F9 WT cell aggregates decreases when exposed to 10 µM Y-27632 and to 10 µM blebbistatin down to 1.56 ± 0.16 mN/m (n = 5 aggregates) and 1.53 ± 0.86 mN/m (n = 3 aggregates) respectively. As expected, the surface tension largely increases when F9 WT cell aggregates treated with 1 µM nocodazole up to 21.93 ± 0.91 mN/m (n = 10 aggregates), as shown in Fig. 3.7.

The TST for $F9^{(\alpha-/-)}$ 1.58 ± 0.32 mN/m (n = 5 aggregates) is almost identical with the one for the WT treated with 10 µM Y-27632.

Also, we have a slight increase of the surface tension for $F9^{(\alpha-/-)}$ aggregates when we exposed them to 1 µM nocodazole 3.06 ± 1.73 mN/m (n = 3 aggregates).

Preliminary tests with $F9^{(\alpha-/-)}$ aggregates treated with 10 µM Y-27632 gave a surface tension of 1.6 mN/m (n = 1 aggregate).

From measurements on F9 WT, we have seen that the surface tension is highly dependent on the contractile behavior of cells, whereas in the case of $F9^{(\alpha-/-)}$, this dependence disappeared.

3.3 Evaluation of cortical contraction and adhesion energy - Interpretation of results in the DITH framework

3.3.1 General DITH framework

We can interpret the results obtained using the Differential Interfacial Tension Hypothesis (DITH) framework, which has been introduced several years ago now in order to accommodate for both the role of adhesion and contractility [55–57]. It relates TST to the tension along the edges of individual cells.

The surface tension is a differential in interfacial energy, whatever the origin. So, one can assign an energy to the interface of the cell, which we could write [58] :

$$E = \sum_{\text{int}\,erfaces} (-J_{ij} + T_{ij} + T_{ji})\, A_{ij} + \sum_{cells} (\lambda_p (A_i - A_0)^2) \quad \text{(Eq. 1)}$$

The definition of the different parameters is exemplified on Fig. 3.8. For aggregates with only one cell type, J_{ij} is the adhesion energy in the sense of Steinberg between cells which is taken positive ($J_{CC} \geq 0$) or between a cell and external medium M which is taken as the reference energy ($J_{CM} = 0$). T_{ij} are the cortical line tensions along the side between cells or cell and medium. Thus, the contact area of two cells is increased by the adhesion energy and decreased by the cortical tensions induced by the contractility of the membrane and of its underlying cytoskeleton.

$\lambda_p(A_i - A_0)^2$ corresponds to an elastic cortex term (here written uniform for all cells). The interfacial tension γ_{ij} is the energy needed to increase an interface by one unit. Mathematically, this will write down as: $\gamma_{ij} = \frac{\partial E}{\partial A_{ij}}$. Hence, $\gamma_{CC} = -J_{CC} + T^c_{CC}$ and $\gamma_{CM} = T^c_{CM}$ where $T^c_{ij} = T_{ij} + 2\lambda_p (A_i - A_0)$ is an effective cortical contraction. One can even refine the model and have λ_p depending on the contact line. In the followings, we will not discuss these issues; we will not be able even to tell what the prominent part of the cortical contraction T^c_{ij} is: the line tension term (T_{ij}) or the elastic term proportional to the perimeter. This point is discussed in other studies [59].

The TST σ is defined as the energy required to separate an interface between cells and to create an interface between cell and medium. At the cell-extracellular medium interface the interfacial tension γ_{CM} is given only by the cortical tension T^c_{CM} as there is no adhesion in this site [11,60]. The interfacial tension γ_{CC} results from the difference between the cortical tension T^c_{CC} and the adhesion energy *J*.

$$\sigma = \gamma_{CM} - \frac{\gamma_{CC}}{2} = T^c_{CM} - T^c_{CC} + \frac{J_{CC}}{2} \qquad \text{(Eq. 2)}$$

If contractility is the motor of surface tension, it immediately implies that the contractility at the cell medium interface is higher than the one at the cell-cell interface.

The origin of J_{CC} is now discussed. As stated in the introduction of this chapter, quantitative estimates of the number of cadherins per cell and of the mean bond energies do not favor strictly speaking the hypothesis proposed by M. Steinberg a while ago that surface tension values (and hence the J_{CC} term) are dominated by the interaction between cadherins. If the molecular interaction between two cells is highly nonspecific then the adhesion energy will clearly be linked to the average distance in between cells (that is where cadherins play an indirect role by making it possible for membranes to be in close contact and to maintain a controlled distance in between the membranes). So as long as the number of cadherins (whatever the distribution) stays roughly the same at the surface, the adhesion energy can be considered constant in between the different conditions.

For the different cell types investigated (*i.e.*, F9 WT and F9$^{(\alpha-/-)}$), it was shown that the number of cadherins expressed at the surface stays the same [36]. In the same way, we used different drugs for which we knew that the number of cadherins expressed at the surfaces stays the same: blebbistatin and Y-27632 [42], and also nocodazole [61]. Note also that the distribution of cadherins stays homogeneous as shown by the β-catenin staining in the case of F9$^{(\alpha-/-)}$ (compare Fig. 3.8 A and B). That is why we make the hypothesis that for all these conditions the adhesive term J_{CC} remains the same and it will always be noted $J_{CC} = J$ hereafter. We will see that this is very robust to the interpretation of our data.

3.3.2 Interpretation of data

Using this approach, one can readily interpret our data. For the F9 WT cell aggregates exposed to 10 µM Y-27632 or 10 µM blebbistatin, myosin II is inactivated, therefore the cell contractility is removed. The surface tension is given only by the adhesion energy $\sigma = J/2$, as the cortical contraction between two neighbor cells and the cortical contraction between one cell and the external environment are both equal to zero $T^c_{CC} = T^c_{CM} = 0$.

In order to simply understand the results previously mentioned on F9$^{(\alpha-/-)}$, we formulate the following hypothesis. The membrane of a cell with no contacts is surrounded by a cortical mesh which is contracted by myosin activity. What do happen when a contact is being formed? That is what is schemed on Fig. 3.8 E-F. When α-catenin is present, the entangled cortex mesh is completely remodeled to form actin bundle whose contractility can be regulated, whereas when α-catenin is absent the meshwork stays more or less as it was before the initiation of the contact. α-catenin appears as a key regulator which enables the complete remodeling of the cortex underlying the adhesive contact zone. Without it the cortex remains uniform in the cell and $T^c_{CC} = T^c_{CM}$.

This hypothesis is also supported by the histological cuts presented in Fig. 3.8 A-B. The cells in a $F9^{(\alpha-/-)}$ aggregate (B), appear much more rounded (uniform tension on every side, no remodeling) compared to a F9 WT aggregate (A) where some remodeling seems to have occur as the contact zones can be very well assimilated to straight lines. Using this hypothesis $T^c_{CC} = T^c_{CM}$ in Eq. 2 leads again to $\sigma = J/2$ for $F9^{(\alpha-/-)}$.

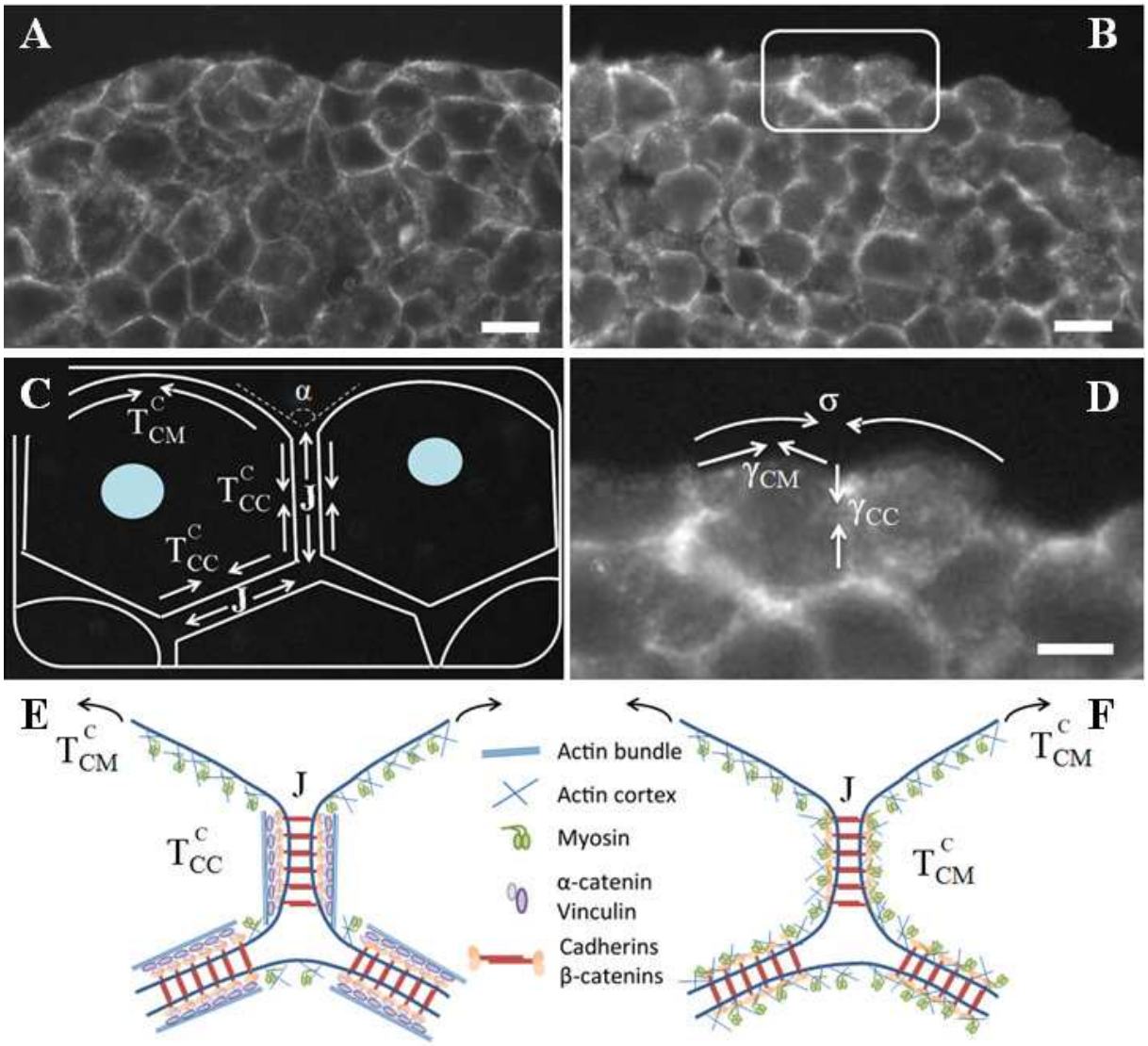

Fig. 3.8: *Cross sections of a F9 WT aggregate (A) and of a $F9^{(\alpha-/-)}$ aggregate (B). (The staining is for β-catenin, scale bars, 10 μm.). (C) Schematic representation of the cortical contractions at the cell-extracellular medium interface (T^c_{CM}), at the cell-cell interface (T^c_{CC}) and of the adhesion energy J. T^c_{CM} and J increase the tissue surface tension, whereas T^c_{CC} decreases it. (D) Closer view of two $F9^{(\alpha-/-)}$ cells in contact. The difference between the interfacial tensions at the cell-cell γ_{CC} and cell-extracellular medium γ_{CM} interfaces gives the aggregate surface tension (σ). γ_{CM} increases the surface tension whereas γ_{CC} decreases it* [56]*. Scale bar, 5 μm. (E-F) Cartoons of cell-cell contacts in the case of F9 WT cells (E) and*

$F9^{(\alpha-/-)}$ cells (F). The presence of α-catenin at cell-cell junction is described as a catalyzer for actin reorganization at cell-cell junctions.

The fact that F9 WT cell aggregates exposed to 10 µM Y-27632 or to 10 µM blebbistatin and $F9^{(\alpha-/-)}$ aggregates possess a same surface tension (1.56 ± 0.16 mN/m and 1.58 ± 0.32 mN/m respectively) is coherent with our assumption that nor the absence of α-catenin neither the addition of the drug modify the expression level of cadherins (so as already stated, *J* is unchanged in all conditions).

Hence, we obtain a value for *J* of the order of 3 mN/m. As seen in the introduction, this is much lower than the value expected if we only take into account the trans-interaction between the extracellular domain of cadherin (see also [62]). However, one can expect that computing adhesion between the two surfaces may not be simply due to the trans-interaction between single cadherin, there will also be lateral specific or unspecific interactions, pleading in favour of the unspecific origin of the adhesion energy.

Finally, our biological (parent line together with mutant and drugs) and physical model also allows us to separate the adhesion energy from the cortical tensions and thus to compute for the F9 WT cells the difference between the two cortical contractions. From Eq. 2 and using a J = 3 mN/m value independent of cell type as discussed above and σ = 4.5 mN/m, we can calculate $T^c_{CM} - T^c_{CC} = \sigma - \frac{J}{2}$ = 3 mN/m. Importantly one can see that the cortical tension difference is of same order than *J* and that $T^c_{CM} > T^c_{CC}$ (*i.e.*, the cell-medium interface is more tensed than the cell-cell interface).

3.3.3 Supplementary parameter estimation by contact angle measurements

If we assume a local mechanical equilibrium at the three phase cell/cell/medium contact line (origin of the angle α on Fig. 3.8 C), the following relation should hold:

$$2T^c_{CM}\cos\alpha/2 = 2T^c_{CC} - J \qquad \text{(Eq. 3)}$$

Hence, in principle by measuring the angle α we have a supplementary equation that allows the determination of all effective cortical contraction parameters T^c_{ij}.

The histological cuts allowed us to estimate the contact angle between cells for the two different cellular types. For F9 WT cell aggregates the angle α (see Fig. 3.8 C) appears to be close to 180° while for the $F9^{(\alpha-/-)}$ cell aggregates this angle becomes smaller, around 120°.

Unfortunately, we could not perform an extensive statistical analysis of angles mostly because an insufficient number of images were taken when cross-sections were performed.

We also did not exposed aggregates to drugs before doing sections. Any supplementary parameter estimation with Eq. 3 is hence limited to F9 WT and F9$^{(\alpha-/-)}$ aggregates.

We completed these estimations with the analysis of aggregates' rugosity. Fig. 3.9 shows F9 WT and F9$^{(\alpha-/-)}$ cell aggregates after two days in hanging drops and another two days on the gyratory shaker. We can see that it is possible to just evaluate by eye the two images to state that F9$^{(\alpha-/-)}$ cell aggregates present a more accentuated profile rugosity. Using exponential curve fitting we measured for the F9 WT a value of 0.48 ± 0.04 µm^2 (n = 30 areas) and for F9$^{(\alpha-/-)}$ the value of 1.82 ± 0.16 µm^2 (n = 16 areas). These roughness values are compatible with the angle estimates: *i.e.*, the smoother F9 WT aggregates present angles close to 180°.

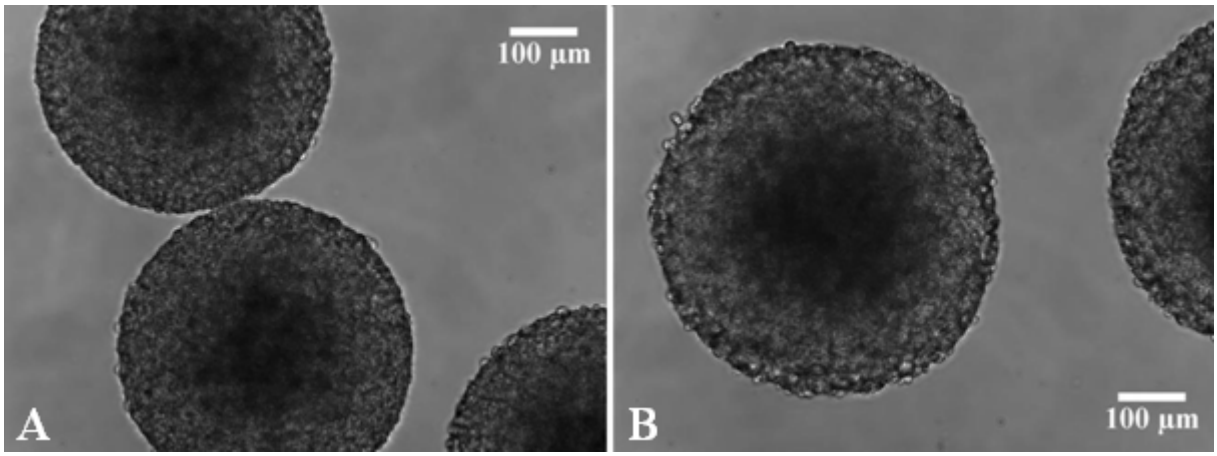

Fig. 3.9: *Optical microscopy images of F9 WT (A) and F9$^{(\alpha-/-)}$ (B) cell aggregates of same age which serve for the estimation of the profiles' rugosity. The outlines prove that there is an evident difference between the two cell lines.*

If we reinject Eq. 3 in Eq. 2, we obtain: $\sigma = T^c_{CM}(1-\cos\alpha/2)$.

We then obtain that T^c_{CM} for F9 WT is equal to 4.5 mN/m and T^c_{CC} = 1.5 mN/m, whereas for F9$^{(\alpha-/-)}$, $T^c_{CC} = T^c_{CM} = J$ = 3 mN/m. It is not surprising here to obtain a different and lower value of T^c_{CM} in the case of the mutant as it has been shown that depleting α-catenin often also induce a change in the ultrastructure of actin [63]. The fact that T^c_{CC} for F9 WT is smaller than the one for the mutant is consistent with our view that α-catenin remodels the cytoskeleton and decreases cell-cell cortical tension. In other words, the surface tension of the mutant F9$^{(\alpha-/-)}$ is decreased because T^c_{CC} is twice larger and T^c_{CM} is lower.

In conclusion, surface tension measurements combined to geometrical analysis appear to be a really powerful tool as to obtain all the desired tension parameters characterizing a cell line.

3.4 Contractility dependent TST still predicts sorting out and envelopment

We performed segregation assays in order to test whether the relative spatial positions adopted by two distinct adhesive cell populations which are mixed together (sorting-out) or by two separate aggregates brought in contact (envelopment) correlate with their surface tension. These phenomena are reminiscent of viscous liquids.

The DAH predicts that in the case of two different tissues, the one of a higher surface tension should be surrounded by the less cohesive one, which has a lower surface tension [64].

3.4.1 Sorting out

We tested the ability of two distinct cell populations to sort out according to their surface tension, by generating aggregates using mixed suspensions of fluorescent F9 (named F9) and $F9^{(\alpha-/-)}$ cell lines. Easily evaluated by eye after several hours, the sorting-out process showed that F9 cells tend to adopt an internal position while $F9^{(\alpha-/-)}$ cells fill the external space of the newly formed aggregate (Fig. 3.10 B).

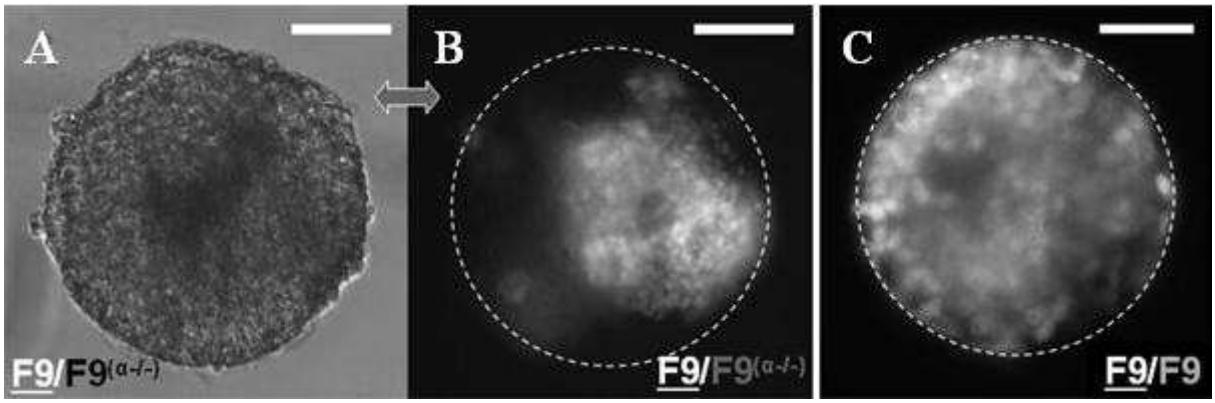

Fig. 3.10: *Phase contrast and fluorescence images representing the sorting out process. (A-B) Phase contrast and fluorescence images correspond to 72 hours after mixing F9 and* $F9^{(\alpha-/-)}$ *dissociated cells in hanging drops. (C) Control fluorescence of a F9/F9 mixture after 72 hours as reported in* [24]*. Left right thick double arrow indicates simultaneous recording in phase and fluorescence. The dashed line circles represent the intuitive outline of aggregates. Scale bars, 100 µm.*

3.4.2 Envelopment

Following the same concept, we combined F9 and $F9^{(\alpha-/-)}$ already formed spherical aggregates as presented in Fig. 3.11 A. After 29 hours in hanging drop culture at 37 °C and 5% CO_2 we evaluate the envelopment and we state that the F9 aggregate is completely

surrounded by the $F9^{(\alpha-/-)}$ one forming a partial "sphere within a sphere" configuration (Fig. 3.11 B).

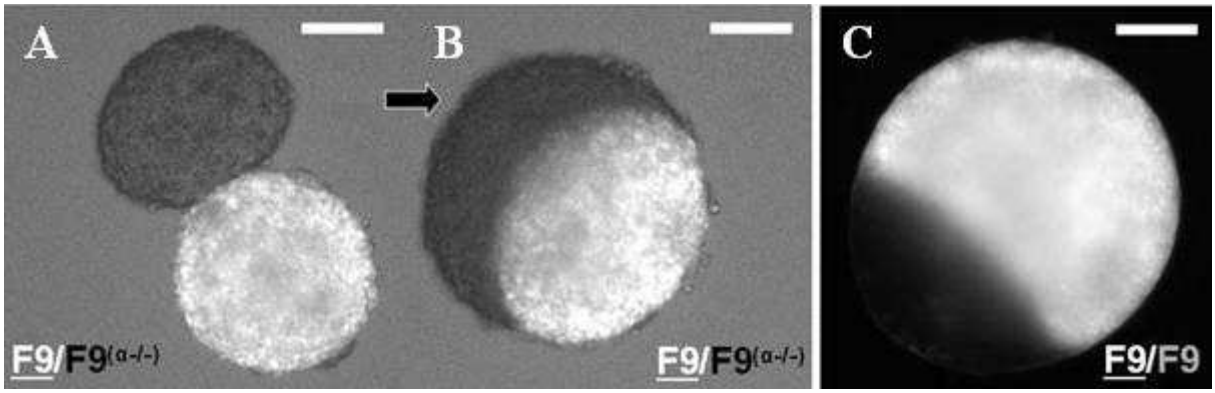

Fig. 3.11: *Fluorescence images representing configurations at different stages of the envelopment process. (A-B) Engulfment of a F9/* $F9^{(\alpha-/-)}$ *pair of aggregates 3 hours (A) and 29 hours (B) after the aggregates were brought in contact and allowed to fuse. (C) Final configuration (72 hours) of a F9/F9 pair of aggregates (control) as reported in* [24]*. Rightwards thick arrow indicates evolution with time. Scale bars, 100 μm.*

For both segregation assays, control experiments were previously made in our team using a single cell line (*i.e.*, F9 and GFP labeled F9 cells) [24]. No sorting could be detected, as even after several hours following the formation of the aggregate, the cells still present a mixed configuration (Fig. 3.10 C). In the envelopment assays the two fusing aggregates maintained their boundaries (Fig. 3.11 C) confirming that the model we used is reliable. This also certifies that the GFP labeled F9 cells present the same physical properties as the F9 line and didn't suffer any changes in terms of surface tension or viscosity, following their transfection (direct measurements of the TST of the GFP labeled F9 cell line confirmed this point [24]).

Combining these two methods, we can conclude that F9 WT cells are more cohesive than $F9^{(\alpha-/-)}$ ones. These results come to confirm the TST measurements presented above.

3.5 Fusion measurements – Tissue fluidity versus contractility

3.5.1 Scaling of viscosity using different models

The sorting out, rounding up and fusion of cell aggregates processes are driven by the tissue surface tension σ and resisted by the tissue viscosity η. The fusion assay offers a quick and convenient way to estimate viscous forces (Fig. 3.12 A and B). The time dependence of the square of the radius neck X^2 is linear at short times (Fig. 3.12 C) as expected from the

Frenkel's modified equation (see Materials and Methods) valid for purely viscous fluids (Newtonian).

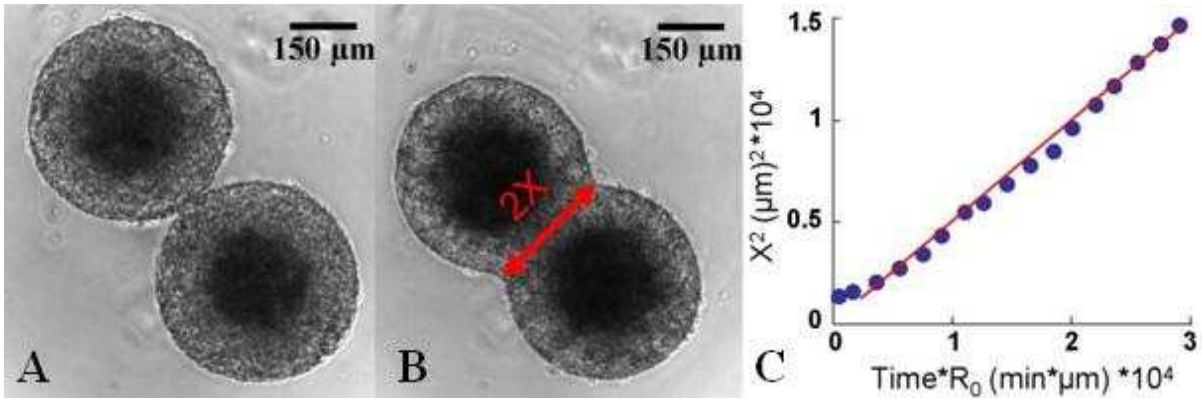

Fig. 3.12: *(A-B) Images of two fusing F9 WT aggregates corresponding to the beginning (A) and the end (B) of the analyzed period, showing in red the neck's diameter 2X. (C) Plot of X^2 versus $t*R_0$ (time*aggregate initial radius) from the fusion experiments. Blue points represent experimental data and red line represents linear fit with the slope defining the visco-capillary velocity v_P.*

Thus, from the analysis of aggregate shape relaxation kinetics we estimate the visco-capillary velocity v_P which is the ratio of the tissue surface tension σ to the viscosity η [65].

The visco-capillary velocity of untreated F9 aggregates remains constant at 0.46 ± 0.02 µm/min (n = 27 pairs) over more than a 3-fold range of diameters as shown in Fig. 3.13.

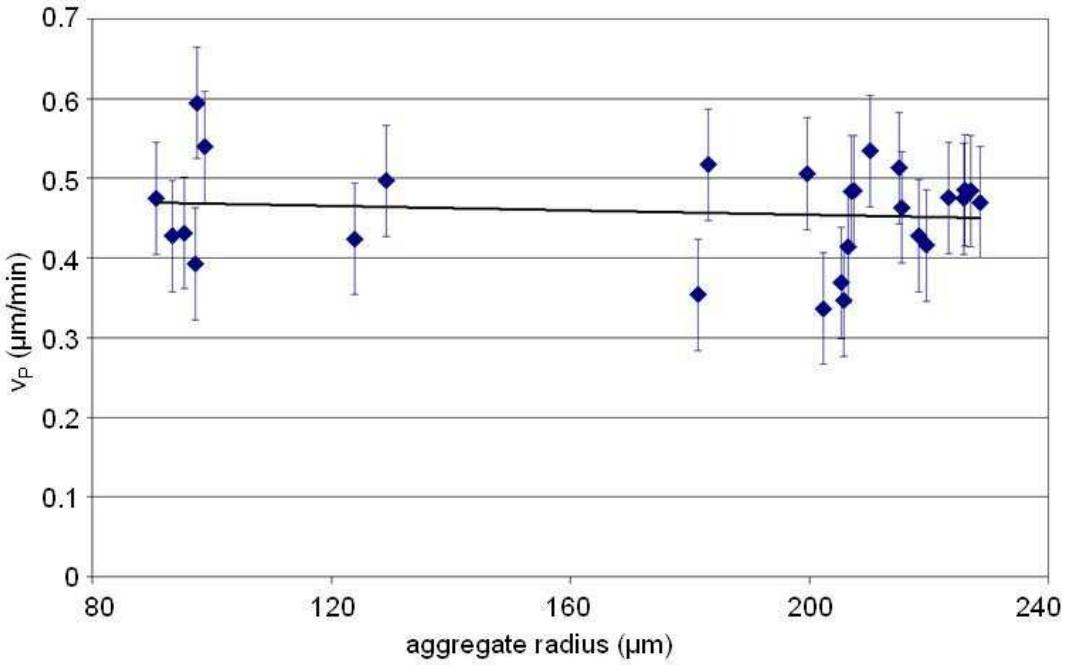

Fig. 3.13: *F9 WT cell aggregate visco-capillary velocity v_P measurements as a function of aggregate radius. v_P values are independent of the aggregate size (radius). The coefficient of determination is 0.0129.*

A different way to fit our data is using the model $X^3 = \alpha \frac{W_{CS}}{\eta} t R_0^2$ presented in [17] (see Materials and Methods chapter). This law is first derived for the spreading of soft viscoelastic polymeric beads [66] and Douezan and co-workers used it expecting it to describe the early stages of spreading dynamics for both complete and partial wetting regimes of cell aggregates on a solid substrate. It enables the estimate of the characteristic velocities W* (ratios $\alpha \frac{W_{CS}}{\eta}$) where W_{CS} is the cell-substrate adhesion energy per unit area.

We have used this non linear model to test whether the fusion of our aggregates could exhibit a similar scaling. In that case, W_{CS} has to be replaced by the TST σ. The slope of the contact radius *Vs*. $t^{1/3}$ is reasonably linear and the corresponding values of the slopes W* are only slightly decreasing with aggregate radius. For example, for F9 WT cell aggregates the new mean value is W* = 0.36 ± 0.02 µm/min compared to v_p = 0.46 ± 0.02 µm/min obtained using Frenkel's equation.

Nevertheless, when representing these values as a function of aggregate radius (Fig. 3.14), we can observe that we have the same distribution as with the Frenkel's model and we obtain very similar coefficients of distribution, similar orders of magnitude of the visco-capillary and characteristic velocities.

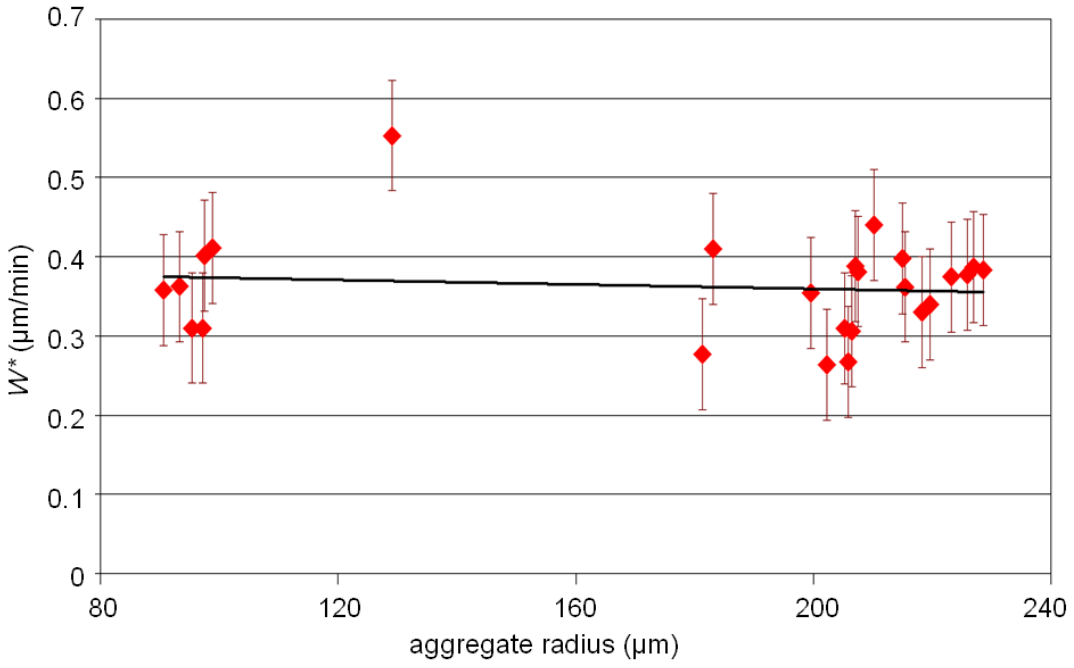

Fig. 3.14: *F9 WT cell aggregate characteristic velocity W* measurements as a function of aggregate radius. W* values are obtained using the model presented in Douezan et al.* [17] *and are independent of the aggregate size (radius). The coefficient of determination is 0.0144.*

Thus, either of the two models can provide trustful values and we cannot decide for a better model. We will however choose the Frenkel description, more familiar to our team, for the rest of the manuscript.

3.5.2 Influence of cell contractility on tissue viscosity

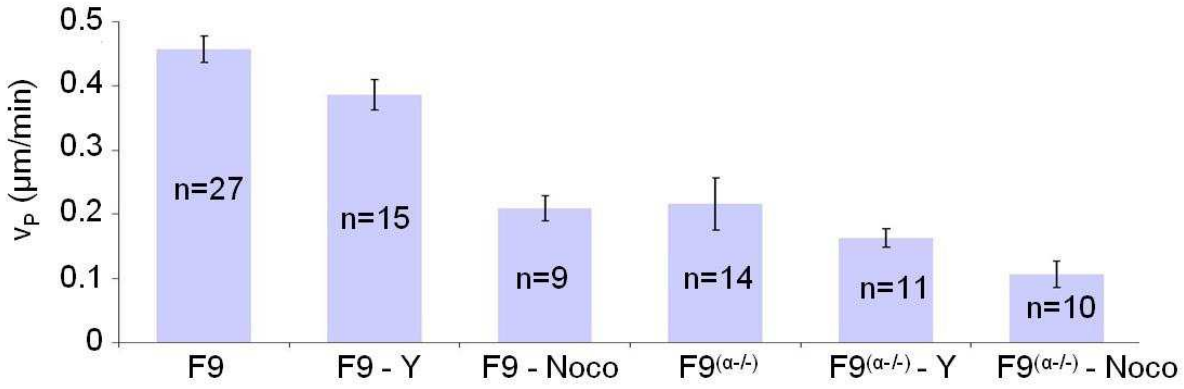

Fig. 3.15: *Measurements of v_P for different cell lines and drugs as obtained from the aggregate shape relaxation kinetics. Error bars represent the standard errors of the mean (95% confidence interval of the mean) and n is the number of experiments.*

Fig. 3.15 summarizes all the results on our two cell lines treated or not with contractile drugs. F9 WT cell aggregates are characterized by a $v_p = 0.46 \pm 0.02$ µm/min. For $F9^{(\alpha-/-)}$, v_P is approximately twice smaller at 0.22 ± 0.04 µm/min (n = 14 pairs). The use of 10 µM Y-27632 generates a slight decrease in v_P for both cellular types: 0.39 ± 0.02 µm/min (n = 15 pairs) for F9 WT and 0.16 ± 0.01 µm/min (n = 11 pairs) for $F9^{(\alpha-/-)}$. Aggregates treated with 1 µM nocodazole displayed a lower v_P than untreated ones: 0.21 ± 0.02 µm/min (n = 9 pairs) for F9 WT and 0.11 ± 0.02 µm/min (n = 10 pairs) for $F9^{(\alpha-/-)}$.

To confirm the fact that our results are reproducible, we can compare them to the previously obtained values for F9 WT, $F9^{(\alpha-/-)}$ and $F9^{(\alpha-/-)}$ treated with 1µM Nocodazole respectively [24]. The three reported ratios σ/η were 0.48 ± 0.10, 0.22 ± 0.02 and 0.11 ± 0.03 µm/min respectively (in this case, the errors are given by standard deviations). We can see that these results are in perfect agreement with the ones we obtained.

One striking feature emerging from the graph of visco-capillary velocities values is the fact that the highest speed is obtained for the wild type condition, and whatever the drugs or genetic modification targeting the cytoskeleton contractility does not accelerate the process as if in the native condition a kind of optimization was attained.

3.5.3 Possible microscopic origin of tissue viscosity

Using the mean TST and v_P experimental values of Fig. 3.7 and Fig. 3.15, we can calculate tissue viscosity or tissue fluidity 1/η which is just the inverse of viscosity (Fig. 3.16).

For untreated F9 WT cell line, we obtain a high viscosity value of $6.26*10^5$ Pa.s in the range of values obtained in the literature [13–16] (see Table 3.17).

Adding Y-27632 on the F9 cell line significantly increases fluidity. The absence of α-catenin as well increases slightly but significantly the fluidity as compared to the parent cell line. The difference is not significant between $F9^{(\alpha-/-)}$ cells treated or not with Y-27632.

The results obtained with nocodazole are consistent with the global tendency that fluidity is negatively correlated with cell contractility: fluidity is always lowered by adding nocodazole which increases contractility both in F9 and $F9^{(\alpha-/-)}$ cell lines.

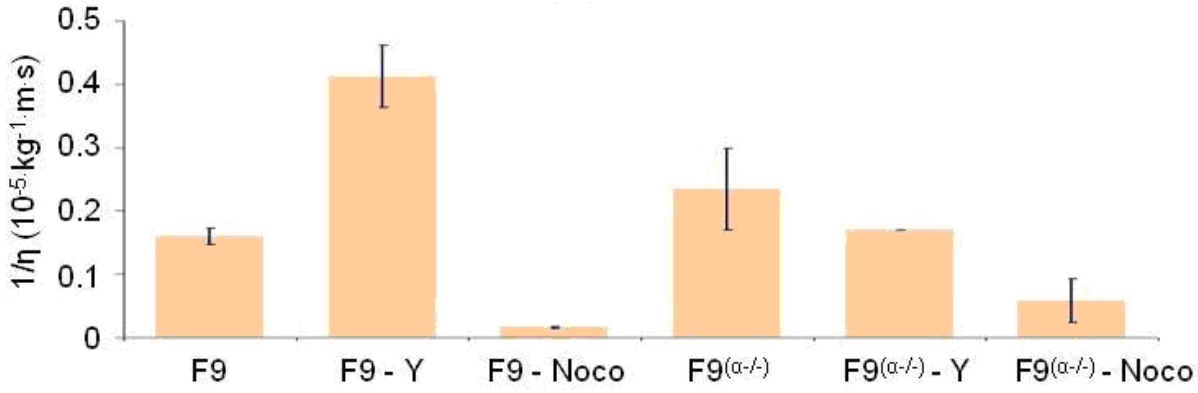

Fig. 3.16: *Fluidity deduced from v_P and σ (i.e., defined as v_P/σ) for untreated and treated aggregates and interpreted as the inverse of the viscosity.*

Cell Line	**1/ η** ($*10^{-5}$ kg^{-1}.m.s)	**η** ($*10^5$ Pa.s)
F9 WT	0.16 ± 0.01	6.26 ± 0.47
F9 WT + 10µM Y-27632	0.41 ± 0.05	2.42 ± 0.29
F9 WT + 1µM nocodazole	0.02 ± 0.001	62.95 ± 6.44
$F9^{(\alpha-/-)}$	0.24 ± 0.05	4.24 ± 0.99
$F9^{(\alpha-/-)}$ + 10µM Y-27632	0.17	5.89
$F9^{(\alpha-/-)}$ + 1µM nocodazole	0.06 ± 0.03	16.92 ± 9.79

Table. 3.17: *Values for fluidity (1/η) and effective tissue viscosity (η) as determined by combining TST and fusion measurements.*

To interpret these results, it is interesting to propose a theoretical framework even rudimentary to model tissue viscosity. Tissue viscosity represents the resistance to relative motion between tissue components. When the interior of the aggregate is reorganized, cells

move relative to each other. This motion requires that cells break and reform their adhesive contacts with their neighbors that cytoskeleton remodels. As cytosol viscosity is generally orders of magnitude smaller than tissue viscosity [67], it is generally assumed that tissue viscosity is of intercellular origin: the greater the binding energy between adhesion molecules, the more stable these contacts will be and the higher the viscosity [12,14,17,22]. Note that this assumption seems to hold in Potts model simulations using adhesive energies only (G. Thomas, UFRGS, Brasil, Personal communication).

A simple dimensional analysis of the viscosity reveals that it can be written as $\eta \sim E_B\tau/\lambda$ where E_B, τ and λ are respectively the average bond energy per unit area, the average lifetime of cell-cell contacts and the average linear cell size [14]. One can interpret the parameter λ/τ as a characteristic protrusive velocity due to the locomotory ability of cells to protrude and retract in a 3D environment in order to move their own size. There are several alternatives for E_B:

(1) The energy cost to break a bonds might be just $\Delta\gamma_{CC}=J$ by assuming cortical tensions are not affected by cell-cell sliding and contact remodeling (this is an exact result in the frame of the DAH where cortical tensions do not play any role). In that case $\eta=J\tau/\lambda$ is not directly proportional to surface tension σ. If we assume that J is a constant, one should find a constant viscosity which is not the case experimentally (see Table 3.17)

(2) The rupture of bond might locally totally modify the cortex and transiently relax the cortical tension from T^c_{CC} to T^c_{CM} exactly as when we compute σ. In that case, $E_B= \sigma$ and the hydrocapillary velocity σ/η is a constant equal to the protrusive velocity. But, experimentally, the hydrocapillary velocity σ/η is not constant (Fig. 3.16).

The fact that none of the alternatives is describing the experimental data indicates that there is a possible different origin to tissue viscosity than intercellular.

Obviously, this origin could be intracellular, cell motility in tissues might be related to cell contractility and cytoskeleton remodeling, not attachment and detachment rates.

Much more experimental and theoretical work is necessary to understand the origin of tissue viscosity.

3.6 Influence of the temperature on the measured physical quantities

We were also interested in finding out if the temperature has an effect on the physical quantities we measure. For this, we performed our experiments at different temperatures, below and above 37 °C.

3.6.1 Surface tension and temperature

Preliminary tests at 35 °C with F9 WT aggregates show that the TST remains more or less the same. For three different experiments, each corresponding to 4 steps of equal compressions on similar size aggregates (*i.e.,* 330, 332 and 395 µm), we obtained a mean value of 4.13 ± 1.15 mN/m. Comparing it to the value of 4.48 ± 0.59 mN/m obtained for experiments at 37 °C we can't state that the surface tension changes with temperature.

3.6.2 Viscosity and temperature

To complete the view, it is interesting to consider the effect of temperature on the visco-capillary velocity. The results obtained testing the two cell lines are summarized in Fig. 3.18 for four different values of the temperature T (*i.e.*, 35, 37, 38 and 39 °C).

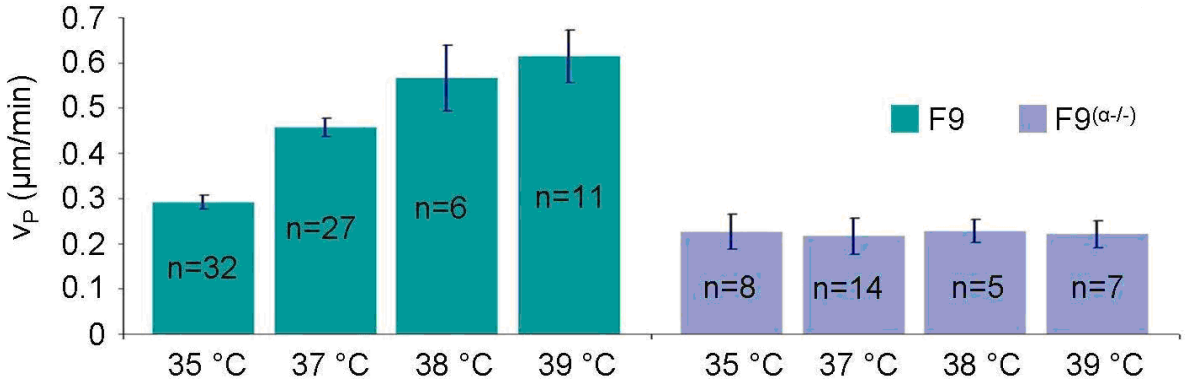

Fig. 3.18: *Measurements of v_P as a function of temperature for F9 WT and F9$^{(\alpha-/-)}$ aggregates. Error bars represent the standard errors of the mean (95% confidence interval of the mean) and n is the number of experiments.*

In the case of F9 WT cells it seems that temperature T has a strong effect as v_P increases almost linearly with T with a ~ 33% increase per degree. This indicates that as expected the viscosity is regulated by active biological processes.

On the other hand, the F9$^{(\alpha-/-)}$ cell line does not present any temperature dependence, as if α-catenin was essential for these active processes to occur.

We also performed these temperature - dependent experiments with treated aggregates and the results are summarized in Fig. 3.19 A for F9 WT cell aggregates and in Fig. 3.19 B for F9$^{(\alpha-/-)}$ cell aggregates.

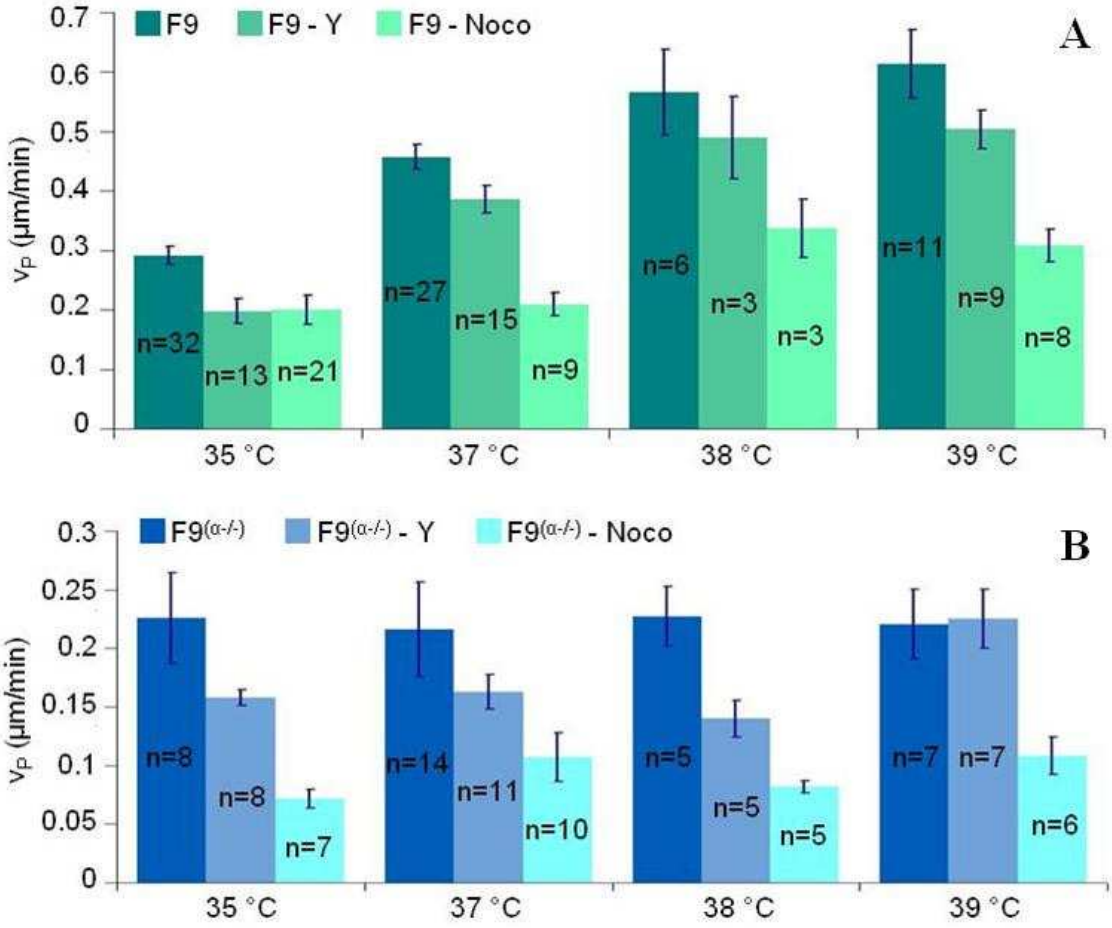

Fig. 3.19: *Visco-capillary velocity v_P measurements as a function of temperature for F9 WT (A) and F9$^{(\alpha-/-)}$ (B) cell aggregates untreated or exposed to 10 µM Y-27632 and 1 µM nocodazole. Error bars represent the standard errors of the mean (95% confidence interval of the mean) and n is the number of experiments.*

With very few exceptions, the tendency of v_P values for each temperature is similar to that found at 37 °C. The highest value is for non-treated aggregates, followed by the one for aggregates exposed to 10 µM Y-27632 and finally, the one for aggregates exposed to 1 µM nocodazole.

Temperature / Cell line	35 °C	37 °C	38 °C	39 °C
F9 WT	0.29 ± 0.01	0.46 ± 0.02	0.57 ± 0.07	0.61 ± 0.06
F9 WT + 10µM Y-27632	0.2 ± 0.02	0.39 ± 0.02	0.49 ± 0.07	0.5 ± 0.03
F9 WT + 1µM nocodazole	0.2 ± 0.02	0.21 ± 0.02	0.34 ± 0.05	0.31 ± 0.03
F9$^{(\alpha-/-)}$	0.23 ± 0.04	0.22 ± 0.04	0.23 ± 0.02	0.22 ± 0.03
F9$^{(\alpha-/-)}$ + 10µM Y-27632	0.16 ± 0.01	0.16 ± 0.01	0.14 ± 0.02	0.23 ± 0.03
F9$^{(\alpha-/-)}$ + 1µM nocodazole	0.07 ± 0.01	0.11 ± 0.02	0.08 ± 0.01	0.11 ± 0.02

Table. 3.20: *Values of v_P measured at different temperatures for non-treated and treated aggregates.*

Finally, we wanted to go further on the dependence of the visco-capillary velocity on temperature and we performed fusion assays at temperature values much lower the already presented ones.

We started with T = 21 °C and what we observed is that F9 WT aggregates no longer fuse, even if we wait for a large amount of time. Rather than observing fusion, we noted a different behavior. In Fig. 3.21 two pairs of F9 WT aggregates are presented in the initial and the final stage of the recorded process. The change in shape and dimensions can be due to cell division within the aggregates. However, even though the contact line between the two aggregates seems to become larger we cannot state that there is a real fusioning process occurring.

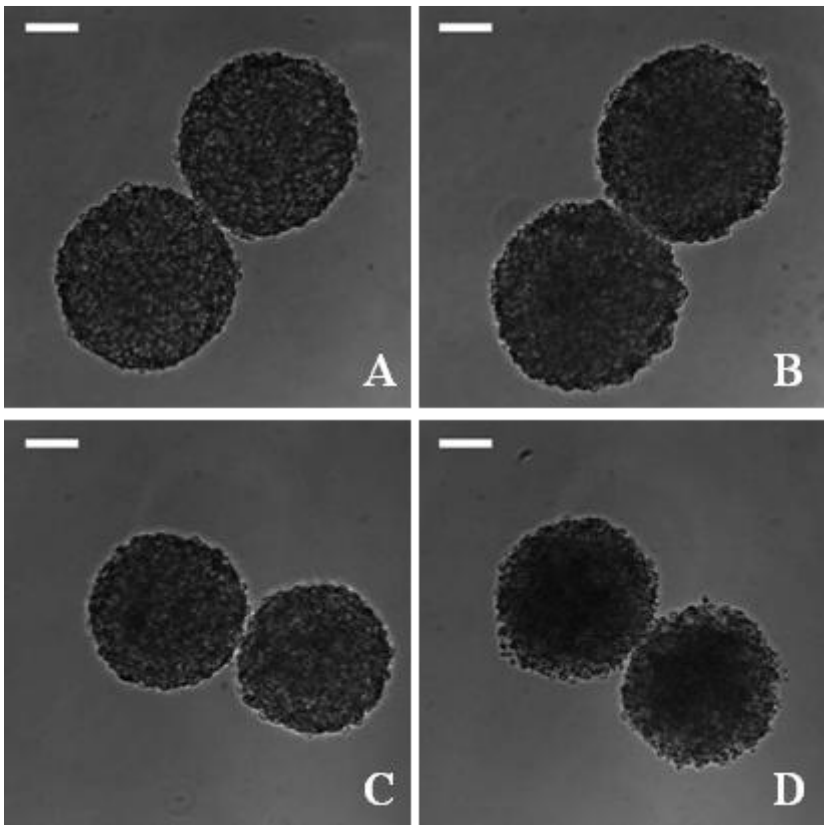

Fig. 3.21: *Initial and final stage of the fusion process at 21 °C for two different pairs of F9 WT aggregates (A-B for the first pair and C-D for the second one). Scale bars, 200 µm.*

Increasing the temperature up to 31 °C allows the fusion process to take place but the measured values of the visco-capillary velocity for both cell lines are significantly smaller than for 35 °C. Thus, we obtained 0.087 ± 0.01 µm/min for F9 WT aggregates (N=4) and an almost twice smaller value of 0.03 ± 0.028 µm/min for $F9^{(\alpha-/-)}$ aggregates (N=3).

Performing experiments at an intermediate temperature between 31 and 35 °C could maybe provide the missing link to complete our understanding of the dependency of fusion dynamics on the temperature.

3.7 Preliminary decompression observations

During this thesis, we concentrated our rheological experiments to the new shear geometry (next chapter) and we could not perform a rheological study of compressed aggregates with the compression tensiometer as done during the PhD thesis of A. Mgharbel [15,24]. However, it appears that such a study would be very interesting as indicated by the following preliminary observation.

In Fig. 3.22 three different instants of a compression experiment devoted to TST measurement are presented: images (A-C) show the initial stage, before any compression is performed, images (D-F) correspond to the moment just after we move down the lower plate, thus releasing the aggregate and images (G-I) are recorded at the end of the experiment, after approximately 30 minutes after lowering the bottom plate with the sample. The three columns correspond to F9 WT, F9 WT treated with 10 µM Y-27632 and F9 WT treated with 1 µM nocodazole.

Comparing the second and the third columns with the first one it appears that the exposure to drugs changes in a significant way the external morphology of aggregates implying that there is a true effect of either drug. The recorded shapes after 30 minutes are all very distinct from one another.

Exposure to Y-27632 seems to "fluidize" the aggregate which keeps longer a "pancake shape" and exhibits a lower amplitude and a slower elastic relaxation than the others. The aggregate exposed to Y-27632 seems also to present a larger adhesion with the substrate as it will further spread on the lower surface.

The treatment with nocodazole gives the opposite effect, as expected. It even appears that several cells (possible "dead" ones) "try" to detach from the aggregate, changing its shape to a "raspberry-like" one.

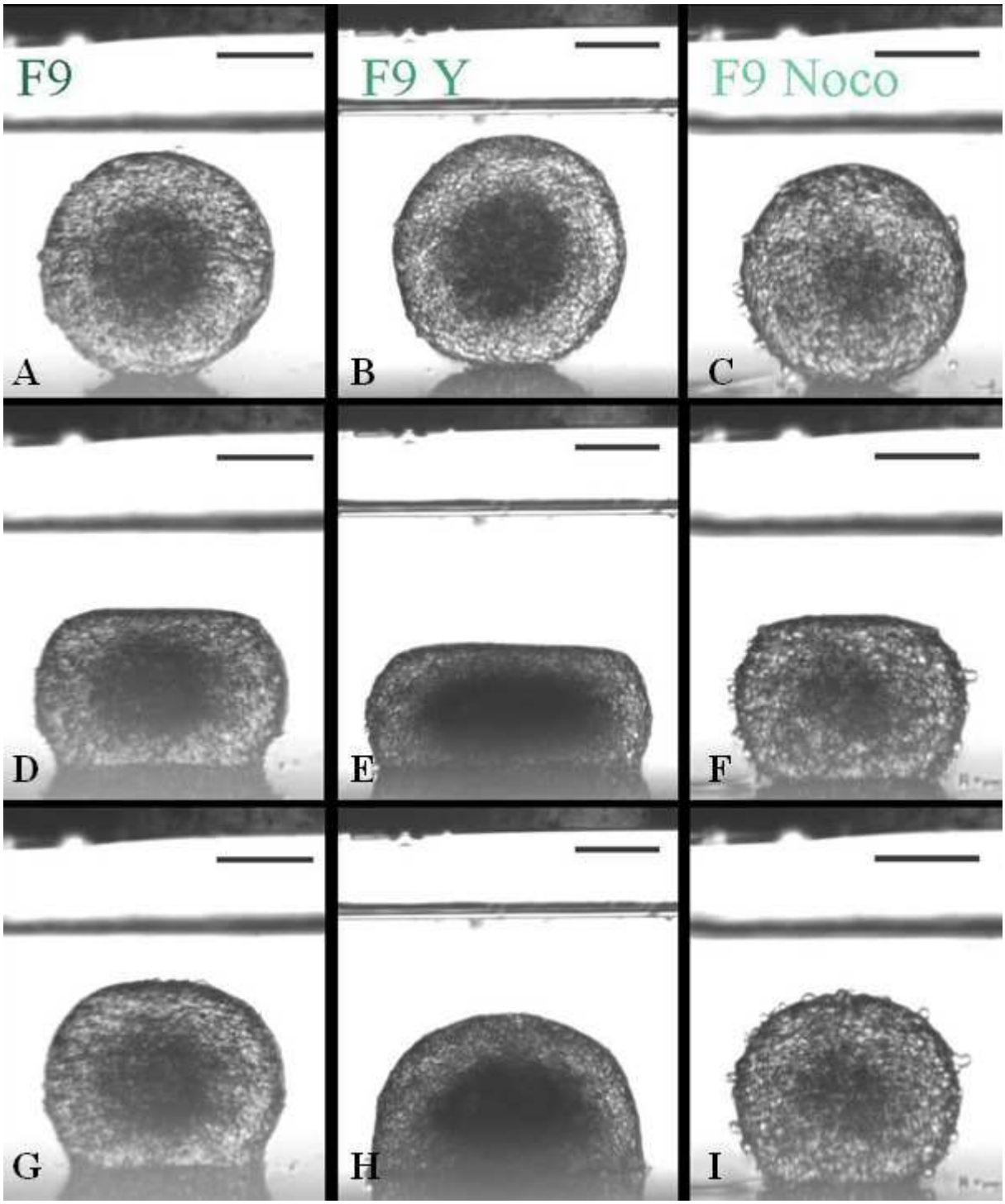

Fig. 3.22: *Different morphologies of F9 WT cell aggregates treated or not with drugs from TST experiments: before compression (A-C), just after releasing the aggregate by lowering the plate at the end of the series of compression steps (D-F) and 30 minutes after (G-I). The first column presents an aggregate which was not exposed to any drug before or during the experiment. The second column presents an aggregate which was exposed to 10 µM Y-27632 an hour before the experiment. The third column presents an aggregate which was exposed to 1 µM nocodazole 2 hours before the experiment. Scale bar 150µm.*

3.8 Conclusion and perspectives

We presented here two different important physical quantities characterizing a fluid material: surface tension and viscosity. One is an equilibrium quantity (minimization of an excess thermodynamical potential), and the other concerns dissipation and dynamics. We pose here the questions of the underlying microscopic origin of these two quantities which actually could have common origins such as cell-cell adhesion.

By combining TST measurements and modification of contractile properties of cells, we have seen that our data were fully compatible with the DITH framework. From there, we got a direct measurement of J and ($T^c_{CM} - T^c_{CC}$).

Supplementary experiments through angle analysis enable us to finally get all the parameters. AFM or micropipette aspiration may give also access to T^c_{CM} independently and so would be very interesting to fully validate the proposed DITH framework.

We have also seen that both surface tension and fluidity were very dependent on contractility, and that α-catenin was essential for this fine tuning of the macroscopic parameters.

In the same order of idea, we have seen that the ratio σ/η is very dependent on temperature for F9 WT, whereas the one of $F9^{(\alpha-/-)}$ cells is not which means that, α-catenin is essential for a spreading of cells upon one another through active processes, and removing this essential protein lead to a passive spreading through physical interaction (most certainly non specific J).

We can imagine how important it is during morphogenesis for the organization of tissues to have a mean to finely tune the fluidity of one tissue relatively to its neighbor. It appears here that the subtle reorganization of the actin network triggered by α-catenin gives the tissue such a possibility simply by regulating its contractile activity.

We think that we presented in this chapter interesting evidence for the surface tension on the respective contribution of adhesion and contractility. If the results are for now difficult to interpret in terms of modeling for viscosity, we believe that this work presents very interesting and robust measurements which will be very useful for the community and it really points out the important role of α-catenin for controlling these parameters.

References:

1. Butler, L. C. *et al.* Cell shape changes indicate a role for extrinsic tensile forces in Drosophila germ-band extension. *Online* **11**, 859–864 (2009).

2. Käfer, J. *et al.* Cell adhesion and cortex contractility determine cell patterning in the Drosophilaretina. *Proceedings of the National Academy of Sciences* **104**, 18549 (2007).

3. Foty, R. A. & Steinberg, M. S. The differential adhesion hypothesis: a direct evaluation. *Developmental biology* **278**, 255–63 (2005).

4. Steinberg, M. S. Reconstruction of tissues by dissociated cells. Some morphogenetic tissue movements and the sorting out of embryonic cells may have a common explanation. *Science* **141**, 401–408 (1963).

5. Takeichit, M. & Steinberg, M. S. Experimental specification of cell sorting , tissue spreading , and specific spatial patterning by quantitative differences in cadherin expression. *Proc Natl Acad Sci USA* **91**, 206–209 (1994).

6. Prakasam, A. K., Maruthamuthu, V. & Leckband, D. E. Similarities between heterophilic and homophilic cadherin adhesion. *October* **103**, (2006).

7. Li, Z. *et al.* Spatially resolved quantification of E-cadherin on target hES cells. *The journal of physical chemistry. B* **114**, 2894–900 (2010).

8. Shi, Q., Chien, Y.-H. & Leckband, D. Biophysical properties of cadherin bonds do not predict cell sorting. *The Journal of biological chemistry* **283**, 28454–63 (2008).

9. Harris, A. K. A. K. Harris - 1976 - Is cell sorting caused by differences in the work of intercellular adhesion A critique of the Steinberg hypothesis.pdf. *Journal of Theoretical Biology* **61**, 2–3 (2010).

10. Krieg, M. *et al.* Tensile forces govern germ-layer organization in zebrafish. *Nature cell biology* **10**, 429–36 (2008).

11. Käfer, J. *et al.* Cell adhesion and cortex contractility determine cell patterning in the Drosophila retina. *Proceedings of the National Academy of Sciences of the United States of America* **104**, 18549–54 (2007).

12. Forgacs, G., Foty, R. A., Shafrir, Y. & Steinberg, M. S. Viscoelastic Properties of Living Embryonic Tissues : a Quantitative Study. *Biophysical journal* **74**, 2227–2234 (1998).

13. Gordon, R., Goel, N. S., Steinberg, M. S. & Lawrence, L. W. Gordon et al. - 1972 - A rheological mechanism sufficient to explain the kinetics of cell sorting.pdf. *Journal of theoretical biology* **37**, 43–73 (1972).

14. Jakab, K. *et al.* Relating cell and tissue mechanics: implications and applications. *Developmental dynamics: an official publication of the American Association of Anatomists* **237**, 2438–49 (2008).

15. Marmottant, P. *et al.* The role of fluctuations and stress on the effective viscosity of cell aggregates. *Proceedings of the National Academy of Sciences of the United States of America* **106**, 17271–5 (2009).

16. Guevorkian, K., Colbert, M.-J., Durth, M., Dufour, S. & Brochard-Wyart, F. Aspiration of Biological Viscoelastic Drops. *Physical Review Letters* **104**, 1–4 (2010).

17. Douezan, S. *et al.* Spreading dynamics and wetting transition of cellular aggregates. *Proceedings of the National Academy of Sciences of the United States of America* **108**, 7315–20 (2011).

18. Thoumine, O. & Ott, A. Time scale dependent viscoelastic and contractile regimes in fibroblasts probed by microplate manipulation. *Journal of Cell Science* **2116**, 2109–2116 (1997).

19. Yamada, S., Wirtz, D. & Kuo, S. C. Mechanics of living cells measured by laser tracking microrheology. *Biophysical journal* **78**, 1736–47 (2000).

20. Tsai, M. a, Frank, R. S. & Waugh, R. E. Passive mechanical behavior of human neutrophils: power-law fluid. *Biophysical journal* **65**, 2078–88 (1993).

21. Foty, R. A., Pfleger, C. M., Forgacs, G. & Steinberg, M. S. Surface tensions of embryonic tissues predict their mutual envelopment behavior. *Development* **122**, 1611 (1996).

22. Mombach, J. C. M. *et al.* Rounding of aggregates of biological cells: Experiments and simulations. *Physica A: Statistical and Theoretical Physics (Amsterdam)* **352**, 525–534 (2005).

23. Frenkel, J. Viscous flow of crystalline bodies. *J Phys* **9**, (1945).

24. Mgharbel, A. Physique et rhéologie des agrégats cellulaires embryonnaires. (2009).

25. Giannone, G., Mège, R.-M. & Thoumine, O. Multi-level molecular clutches in motile cell processes. *Trends in cell biology* **19**, 475–86 (2009).

26. Papusheva, E. & Heisenberg, C.-P. Spatial organization of adhesion: force-dependent regulation and function in tissue morphogenesis. *The EMBO journal* **29**, 2753–68 (2010).

27. Rauzi, M. & Lenne, P.-F. Cortical forces in cell shape changes and tissue morphogenesis. *Current topics in developmental biology* **95**, 93–144 (2011).

28. Yonemura, S. Cadherin-actin interactions at adherens junctions. *Current opinion in cell biology* (2011).doi:10.1016/j.ceb.2011.07.001

29. Drees, F., Pokutta, S., Yamada, S., Nelson, W. J. & Weis, W. I. Alpha-catenin is a molecular switch that binds E-cadherin-beta-catenin and regulates actin-filament assembly. *Cell* **123**, 903–15 (2005).

30. Abe, K. & Takeichi, M. EPLIN mediates linkage of the cadherin – catenin complex to F-actin and stabilizes the circumferential actin belt. (2007).

31. Yonemura, S., Wada, Y., Watanabe, T., Nagafuchi, A. & Shibata, M. alpha-Catenin as a tension transducer that induces adherens junction development. *Nature cell biology* **12**, 533–42 (2010).

32. le Duc, Q. *et al.* Vinculin potentiates E-cadherin mechanosensing and is recruited to actin-anchored sites within adherens junctions in a myosin II-dependent manner. *The Journal of cell biology* **189**, 1107–15 (2010).

33. Yamada, S. & Nelson, W. J. Localized zones of Rho and Rac activities drive initiation and expansion of epithelial cell-cell adhesion. *The Journal of cell biology* **178**, 517–27 (2007).

34. Zhang, J. *et al.* Actin at cell-cell junctions is composed of two dynamic and functional populations. *Journal of cell science* **118**, 5549–62 (2005).

35. Kobielak, A., Pasolli, H. A. & Fuchs, E. Mammalian formin-1 participates in adherens junctions and polymerization of linear actin cables. *Nature cell biology* **6**, 21–30 (2004).

36. Maeno, Y. *et al.* α-catenin-deficient F9 cells differentiate into signet ring cells. *American Journal of Pathology* **154**, 1323 (1999).

37. Brevier, J., Vallade, M. & Riveline, D. Force-Extension Relationship of Cell-Cell Contacts. *Physical Review Letters* **268101**, 98–101 (2007).

38. Omelchenko, T., Vasiliev, J. M., Gelfand, I. M., Feder, H. H. & Bonder, E. M. Rho-dependent formation of epithelial "' leader '" cells. *Proceedings of the National Academy of Sciences of the United States of America* **100**, 10788–93 (2003).

39. Kovács, M. *et al.* Mechanism of blebbistatin inhibition of myosin II. *The Journal of biological chemistry* **279**, 35557–63 (2004).

40. Charras, G. T., Yarrow, J. C., Horton, M. A., Mahadevan, L. & Mitchison, T. J. Non-equilibration of hydrostatic pressure in blebbing cells. *Nature* **435**, 365–9 (2005).

41. Nelson, C. M. *et al.* Emergent patterns of growth controlled by multicellular form and mechanics. *Proceedings of the National Academy of Sciences of the United States of America* **102**, 11594–9 (2005).

42. Shewan, A., Maddugoda, M. & Kraemer, A. Myosin 2 is a key Rho kinase target necessary for the local concentration of E-cadherin at cell-cell contacts. *Molecular biology of the cell* **16**, 4531– 4542 (2005).

43. Guo, W., Frey, M. T., Burnham, N. a & Wang, Y. Substrate rigidity regulates the formation and maintenance of tissues. *Biophysical journal* **90**, 2213–20 (2006).

44. Bischofs, I. B., Klein, F., Lehnert, D., Bastmeyer, M. & Schwarz, U. S. Filamentous network mechanics and active contractility determine cell and tissue shape. *Biophysical journal* **95**, 3488–96 (2008).

45. Kippert, A., Fitzner, D., Helenius, J. & Simons, M. Actomyosin contractility controls cell surface area of oligodendrocytes. *BMC cell biology* **10**, 71 (2009).

46. Ayollo, D. V., Zhitnyak, I. Y., Vasiliev, J. M. & Gloushankova, N. a Rearrangements of the actin cytoskeleton and E-cadherin-based adherens junctions caused by neoplasic transformation change cell-cell interactions. *PloS one* **4**, e8027 (2009).

47. Tinevez, J.-Y. *et al.* Role of cortical tension in bleb growth. *Proceedings of the National Academy of Sciences of the United States of America* **106**, 18581–6 (2009).

48. Rossier, O. M. *et al.* Force generated by actomyosin contraction builds bridges between adhesive contacts. *The EMBO journal* **29**, 1055–68 (2010).

49. Patla, I. *et al.* Dissecting the molecular architecture of integrin adhesion sites by cryo-electron tomography. *Nature cell biology* **12**, 909–15 (2010).

50. Salmerón-Sánchez, M. *et al.* Role of material-driven fibronectin fibrillogenesis in cell differentiation. *Biomaterials* **32**, 2099–105 (2011).

51. Tse, J. M. *et al.* Mechanical compression drives cancer cells toward invasive phenotype. *Proceedings of the National Academy of Sciences of the United States of America* **109**, 911–6 (2012).

52. Foty, R. A., Forgacs, G., Pfleger, C. M. & Steinberg, M. S. Liquid properties of embryonic tissues: measurement of interfacial tensions. *Physical review letters* **72**, 2298–2301 (1994).

53. Hegedüs, B., Marga, F., Jakab, K., Sharpe-Timms, K. L. & Forgacs, G. The interplay of cell-cell and cell-matrix interactions in the invasive properties of brain tumors. *Biophysical journal* **91**, 2708–16 (2006).

54. Mgharbel, A., Delanoë-Ayari, H. & Rieu, J.-P. Measuring accurately liquid and tissue surface tension with a compression plate tensiometer. *HFSP journal* **3**, 213–21 (2009).

55. Harris, A. K. Is cell sorting caused by differences in the work of intercellular adhesion? A critique of the Steinberg hypothesis. *Journal of Theoretical Biology* **61**, 267–285 (1976).

56. Graner, F. Can surface adhesion drive cell-rearrangement? Part I: Biological cell-sorting. *Journal of theoretical biology* **164**, 455–455 (1993).

57. Brodland, G. W. The Differential Interfacial Tension Hypothesis (DITH): A Comprehensive Theory for the Self-Rearrangement of Embryonic Cells and Tissues. *Journal of Biomechanical Engineering* **124**, 188 (2002).

58. Käfer, J. Des cellules aux tissus: modélisation physique du comportement collectif des cellules embryonnaires. (2008).

59. Cavey, M., Rauzi, M., Lenne, P. & Lecuit, T. A two-tiered mechanism for stabilization and immobilization of E-cadherin. *Nature* **453**, 751–6 (2008).

60. Lecuit, T. & Lenne, P. Cell surface mechanics and the control of cell shape, tissue patterns and morphogenesis. *Nature reviews. Molecular cell biology* **8**, 633–44 (2007).

61. Stehbens, S. J. *et al.* Dynamic microtubules regulate the local concentration of E-cadherin at cell-cell contacts. *Journal of cell science* **119**, 1801–11 (2006).

62. Evans, E. Physical Actions in Biological Adhesion. *Science* **1**, 723–753 (1995).

63. Benjamin, J. M. *et al.* AlphaE-catenin regulates actin dynamics independently of cadherin-mediated cell-cell adhesion. *The Journal of cell biology* **189**, 339–52 (2010).

64. Foty, R. A., Pfleger, C. M. C. M., Forgacs, G. & Steinberg, M. S. Surface tensions of embryonic tissues predict their mutual envelopment behavior. *Cell* **1620**, 1611–1620 (1996).

65. MOMBACH, J. *et al.* Rounding of aggregates of biological cells: Experiments and simulations. *Physica A: Statistical Mechanics and its Applications* **352**, 525–534 (2005).

66. Michel F, S. M. Kinetics of the JKR experiment. *CR Acad Sci Paris* **Série 2**, 17–20 (1990).

67. Rieu, J. P. J.-P. & Sawada, Y. Hydrodynamics and cell motion during the rounding of two dimensional hydra cell aggregates. *The European Physical Journal B - Condensed Matter* **27**, 167–172 (2002).

Chapter 4

Rheology – Cell aggregates under shear

After having initiated some preliminary studies of the compression-decompression cycles of embryonic aggregates during the PhD thesis of Abbas Mgharbel, we wanted to go further in the rheological characterization of these tissues and thus we started to study in details the stress-strain relationship when applying shear to sets of several hundred or even thousands of cell aggregates, which to our knowledge has never been performed before. We conducted these rheological measurements using a commercial Anton Paar MCR301 rheometer with a parallel-plate configuration in close collaboration with Pr. Catherine Barentin (Liquids @ Interfaces Team, LPMCN, UCBL, Villeurbanne) which performs an important activity on non-biological complex fluids.

The great advantage of performing rheology on cell aggregates as compared to single cells is that it allows us, through different experiments, to study both the behavior of single cells and, at the same time, the intercellular one (*i.e.*, cell-cell rearrangements). Thus, at low deformations, we probe the mean intracellular rheology and at large deformations one begins to found the signature of intercellular reorganizations. We believe that our large amount of data brings robust (ensemble averaged) information on both single cell rheology and cell-cell rearrangements.

We present a simple model to represent the evolution of responses of our aggregates at different stresses (controlled shear rate or controlled shear stress experiments) that qualitatively describes all features of the measured macroscopic rheological curves.

4.1 Short introduction to the rheology of complex fluids

4.1.1 Typical rheological curves of non Newtonian fluids

To characterize some typical non-Newtonian fluids, one can study their responses with the rheometer by applying different protocols and one can find several distinct behaviors.

As explained in chapter 2, a rheometer allows us to have access to many variables, including the strain (γ), the shear rate ($\dot{\gamma}$), and the shear stress (σ) exerted by the rheometer to the fluid. We recall the reader that : (1) the strain is calculated following the equation $\gamma = R\theta / e$ expressed in %, where R is the external radius of the parallel plates (R=2.1456 cm), θ is the rotation angle and e is the distance between the two surfaces of the rheometer (gap); (2) the shear rate is the speed of deformation in a shear mode with $\gamma = \dot{\gamma} t$; (3) the shear stress given by the rheometer (maximal shear stress at R) is deduced from the torque measurement.

Several types of experiments are possible. Among them, the rheometer can perform oscillation experiments as a function of the frequency. The data at low frequencies describe the behavior of the sample at slow changes of stress. In opposition, the behavior at fast load is expressed at high frequencies. During the frequency sweep test, the frequency is varied while the amplitude of the deformation (strain) is kept constant at a few %, the shear stress is measured and the two components of this stress are deduced: G' which is in phase with the deformation and represents the elastic response and G" which is out of phase and represents the viscous response. The value of one over the other tells us the rather elastic or viscous behavior of our sample.

4.1.1.1 Viscoelastic fluids

Viscoelastic fluids such as molten polymers present two different behaviors according to the frequency range at which the study is being conducted: a viscous behavior at low frequency range (G" > G') and an elastic behavior at high frequency range (G' > G"). Otherwise said, if molten polymers are stretched they will elastically lengthen but if one waits for sufficient long time they will start flowing.

In the example of Fig. 4.1, the oscillations are done at a constant strain of γ = 5%.

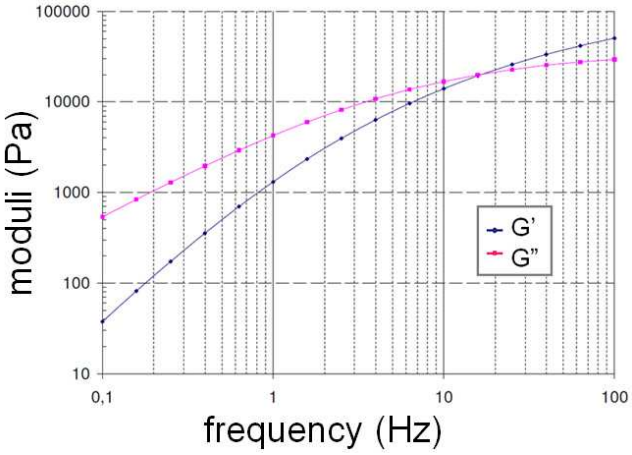

Fig. 4.1: *Frequency sweep of the molten polymers' response to an oscillating deformation at 5%.*

4.1.1.2 Yield stress fluids

Another characteristic non-Newtonian fluid is the yield stress fluid. The Carbopol 1% is a good example and it has been studied for a while in the Fluids @ Interfaces team at LPMCN by Pr. Catherine Barentin.

The Carbopol is a microgel of polymer whose microstructure is composed of jammed interconnected blobs of polymers [1] (see also subsection 4.6.1 in this chapter). It seems it cannot flow as long as the stress exerted does not exceed a certain stress threshold σ_S (known as the yield stress) and it presents a viscous behavior for $\sigma > \sigma_S$. It is described by the Herschel-Bulkley law:

$$\sigma = \sigma_S + k\dot{\gamma}^n \ ,$$

where σ_S is the yield stress, k is the consistency and n is the Herschel-Bulkley exponent (n=0.5 for the Carbopol 1%).

Together with the experiment previously presented, Pr. Catherine Barentin and her team also performed two types of experiments in order to determine σ_S :

- One can shear the sample with a ramp of decreasing shear rates. The yield stress will be the stress at very small velocities (Fig. 4.2 A).

- One can also impose an oscillating shear, at a given frequency and by varying the amplitude. For the analysis, the storage modulus G' and the loss modulus G" are plotted as a function of the strain γ or of the shear stress σ. Thus, σ_S will correspond to the shear stress at the intersection of these two curves (Fig. 4.2 B), while the moduli in the linear viscoelastic region at low deformation characterize the structure at rest of the sample. This second method is less precise in the determination of σ_S .

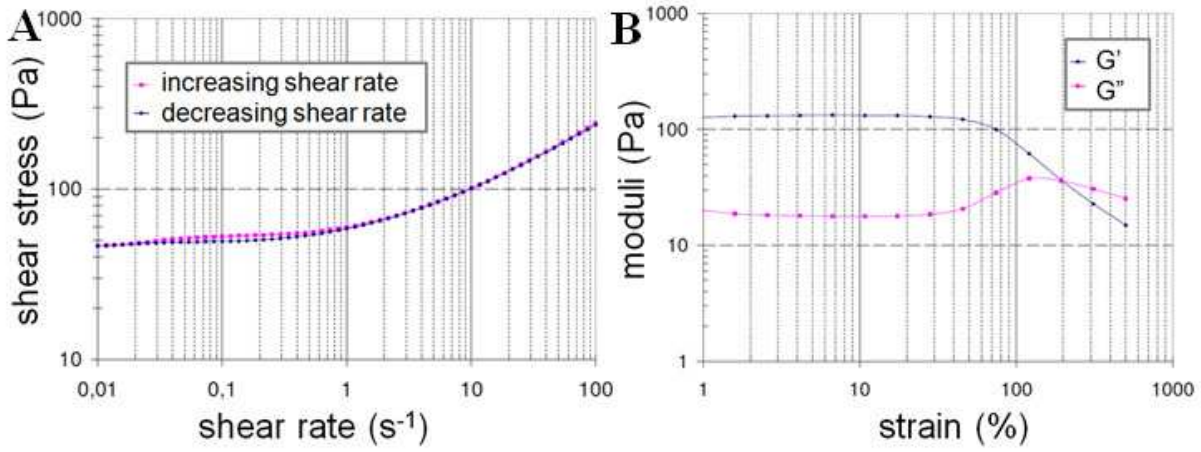

Fig. 4.2: *(A) Flow curve of Carbopol 1%: evolution of the shear stress as a function of a variable shear rate. Here, σ_S ~ 47 Pa. (B) Response of Carbopol 1% to an amplitude sweep test in order to estimate the yield stress value. The oscillatory strain sweep is performed at 1 Hz. In this example we obtain a yield stress value of approximately 50 Pa.*

A third type of experiment exists to determine the yield stress, which we haven't performed. It is a creep experiment, where one applies a constant stress and waits to see the flow (by analyzing the strain response of the system). Let's mention here that creep experiment could be extremely powerful if a strong dependence of the system in frequency is to be observed and where an extensive study of amplitude and frequency sweep would be required. Indeed, the creep experiment enables to excite the system with a full range of frequency in a single experiment (from f_{min} which is the inverse of the rising time to f_{max} which is the inverse of the time during which the stress is being applied). Moreover, mathematical relations exist which enable to relate the creep compliance to G', G'' (see for example [2]).

4.1.2 Non-linear rheology

The linear domain in rheology is defined as the domain where G', G'' are not depending on the amplitude of the applied strain and the non-linear domain is outside (see Fig. 4.3).

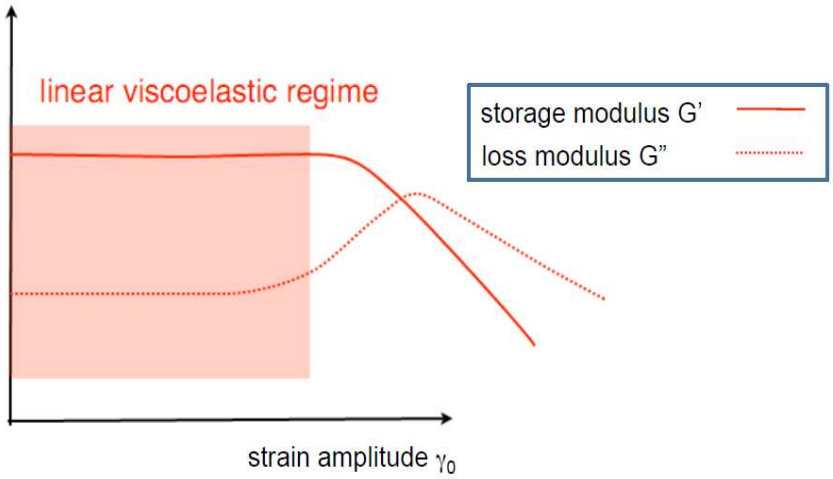

Fig. 4.3: *Linear viscoelasticity. Data is acquired at constant frequency and increasing stress/strain.*

When studying cells, one cannot ignore these non-linearities and the dependence of the response of the system on the applied stress [3–10].

However, if one wants to study precisely the non linear regime, one has to be very careful as standard oscillatory protocols as presented above may fail to reveal interesting features.

Indeed it has been shown that during the time of measurement, even if a nice sinusoidal strain is imposed, the stress component may not be sinusoidal anymore, meaning that in this case G' and G'' are ill-defined [11] (see Fig. 4.4).

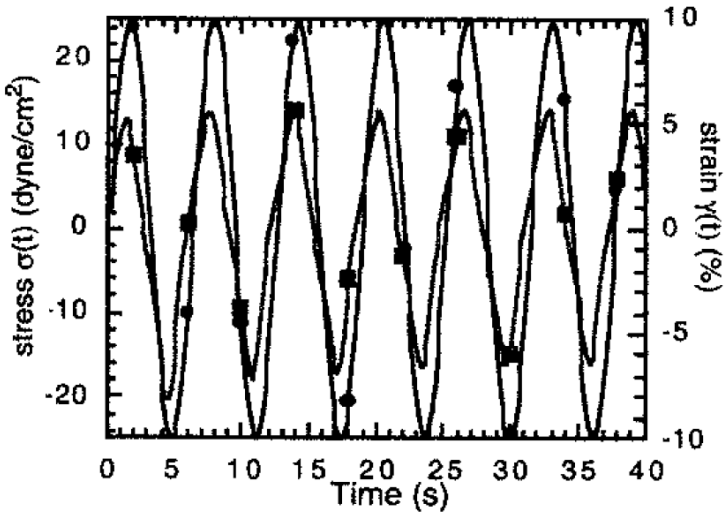

Fig. 4.4: *Mechanical behavior of F-actin networks subjected to oscillatory deformations. Networks were subjected to sinusoidal deformations, $\gamma = \gamma_0 \sin\omega t$, of fixed frequency $\omega=1$ rad/s and increasing deformation amplitude γ_0. Time-dependent strain, $\gamma(t)$ (●), and induced stress, $\sigma(t)$ (■), for F-actin alone; $\gamma_0=10\%$. Taken from* [11].

In this case, different kinds of protocols and analysis have been proposed to be able to extract interesting and relevant features:

1. LAOS (Large Oscillations) analysis using Lissajoux curves (non elliptic cyclic stress/strain curves) where new moduli geometrically characterizing the curves are defined [12].

2. Prestress protocols: A steady prestress, σ_0, is applied on which a small amplitude oscillatory stress, $\delta\sigma(t) = \delta\sigma exp(i\omega t)$ is superposed at a given frequency ω. Usually, $\delta\sigma$ is at most 10% of the steady prestress, and people confirm that the response is linear in $\delta\sigma$ for all σ_0. The complex differential or tangent viscoelastic modulus is determined from $K^*(\omega, \sigma_0) = \frac{\delta\sigma}{\delta\gamma}$. The prestress method was designed to quantify the nonlinear response of viscoelastic solids. This method, however, may not always be suitable for systems that exhibit a significant amount of creep in which the flow induced by a steady stress can lead to restructuring, which might in turn affect the mechanical properties of the system. If these changes occur during the timescale of the measurements, the differential modulus will again be ill-defined.

3. Stress pulses experiment: small stress pulses with increasing stress value are applied to the system, and relaxation of the system is allowed in between the pulses. If creeping is sufficiently small, elastic behavior can be extracted from the compliance curve at fixed timescale (see [13]).

4. Shear rate ramp experiment: In principle, this represents the most direct method to probe the stress–strain behavior of a material, since the stress is measured as a function of an applied strain that increases linearly with time. However, the shear rate is a parameter which has to be varied as, it has been reported for example that pure F-actin solutions exhibit a nonlinear response that depends strongly on the shear rate [14].

Are all these protocols equivalent? Of course not and usually a combination of them would be necessary to be able to give a reasonable picture of the material under study.

Recently for example, Broedersz *et al.* tried to make a rigorous comparison of protocols 2 and 4 (see [15]). They clearly explain that the prestress method measures the nonlinear mechanical response at a specific frequency, while the strain ramp probes the system at a specific rate, and it thus probes the response over a range of frequencies. Both the high-rate strain ramp and prestress protocols measure the fast nonlinear elastic response and may be equivalent if creep could be negligible, while at low rates the stress measured during a strain ramp is the relatively fast elastic response convoluted with stress relaxation processes.

In any cases, as already stated, if creep modifying mechanical properties occurs at short timescales, protocol 2 could not be used anymore and protocols 3 and 4 will require advanced modeling of the creeping process in order to extract rheological parameters from the stress-strain curves.

Nevertheless, these protocols have been used successfully on F-actin solutions, where creeping was not too important. They could observe stress stiffening of the network [13] (increase of *1/J* with stress, with J = γ/σ, Fig. 4.5).

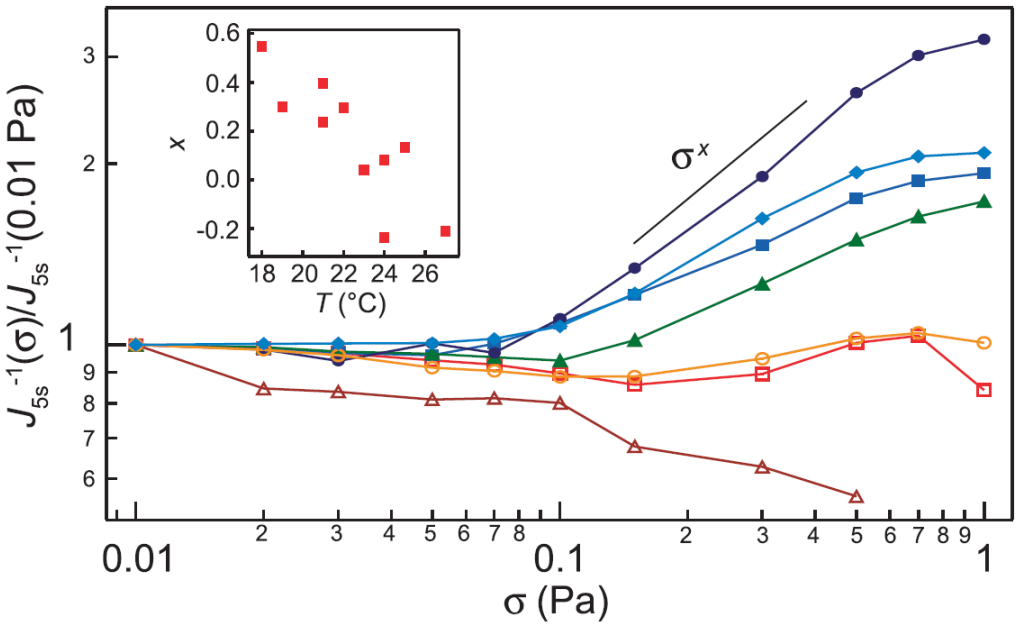

Fig. 4.5: *Non linear rheology of F-actin solutions. Temperature-induced transition from shear softening to shear stiffening (σ-pulse protocol). The inverse of the creep compliance, J, normalized by J(0.01 Pa), as a function of the applied stress σ for various temperatures: T [°C] = 18 (filled circles), 19 (filled squares), 21 (filled diamonds), 22 (filled triangles), 23 (open circles), 25 (open squares), 27 (open triangles) and actin concentration c_A = 9.5 μM, polymer length L = 21 μm. (Inset) Apparent power-law stiffening exponent x of $1/J(\sigma) \propto \sigma^x$ Vs. temperature T. Positive values of the exponent x correspond to shear stiffening while negative values correspond to shear softening. Taken from* [13].

We were wondering if we could see such kind of behaviors using our cellular aggregates. But, directly from the above Fig 4.5, one can see that at physiological temperature, such stiffening may be hard to see. Indeed, the authors claimed there was a time-temperature superposition principle, and consequently, at 37 °C stiffening would only be observed at very short timescales absolutely inaccessible for our rheometer (as we are limited by the instrument and sample inertia).

We will mainly use in the followings protocols 3 and 4 as we will rapidly see that creep modifying the mechanical properties of our sample is occurring on our shortest timescales available (which is only around 0.1 s in our case).

4.2 Controlled shear stress experiments

We began the first series of experiments on aggregates, with protocol 3: we imposed a series of pulses of increasing intensity and we imposed a null stress in between to allow for relaxation.

4.2.1 First experiments: null stress in between pulses

The goal is to obtain the deformation reached after a given time for each pulse. If the deformation was only elastic this would give us directly access to the elastic modulus as a function of strain.

In our protocol, we apply stress pulses from 3 up to 10 seconds, depending on the series of pulses. These pulses are separated by 1 or 10 minutes, depending on the experiment and show an increasing intensity. Each experiment is programmed to stop if the measured deformation exceeds 50%, so as not to damage the aggregates.

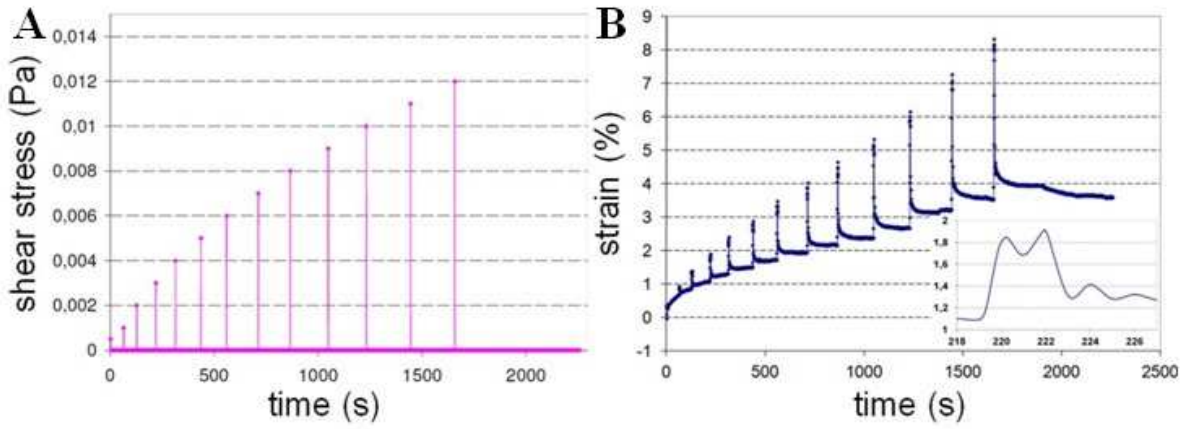

Fig. 4.6: *(A) Imposed increasing shear stress pulses. (B) The evolution of strain when applying increasing shear stress pulses (3 seconds) for a zero stress of variable duration imposed between two pulses. Inset: zoom on the deformation reached for the 4th pulse, with the visualization of the creep-ringing phenomenon (see 4.2.4).*

The first experiments readily informed us that creep was occurring during the pulse itself: we can note that the deformation does not return to zero when the stress is brought to zero, meaning that plasticity phenomena occur in the system (see Fig. 4.6).

Thus, there was no way for us to claim that we would get access here to the direct elastic properties of our aggregates. It appears that we got here the exact unfavorable state where the protocol would fail to give us some reliable information on the eventual non linearities, as creep is occurring at very short timescales.

Nevertheless, it will give us the apparent global reaction of cell to stress at the timescale of seconds in physiological conditions, which could be after all very interesting if we want to give numbers to people trying to model tissues.

4.2.2 Problem of imposing null stress – elastic meniscus

These first experiments were not realized with a large number of aggregates, and it appeared that the elastic modulus of the meniscus at the edge of the plates was not negligible for aggregates when applying a null global stress by the rheometer, and will be sufficient to lead to a global creep of our sample. We thus preferred to apply a null strain in between the pulses.

4.2.3 Null strain in between pulses - apparent softening

When imposing a zero strain between the pulses (see Fig. 4.7 A), we see that after each pulse the stress presents a negative value but is rapidly going back to zero or more exactly to a slightly negative value which we will take into account for the calculus of the exact amplitude of the stress pulse.

We can plot the imposed shear stress as a function of maximum strain reached for every pulse (Fig. 4.7 A). Thus, we can note an apparent softening of our aggregates as a function of strain. Indeed, the applied stress pulses are linearly increasing, while the slope of the recorded strain decreases. This means that while the sample gets more and more deformed, the stress needed to deform it a little more will be less important. We will see hereinafter that this result is in agreement with the results obtained for controlled shear rates (Fig. 4.10), which are themselves consistent with the results found in literature [5].

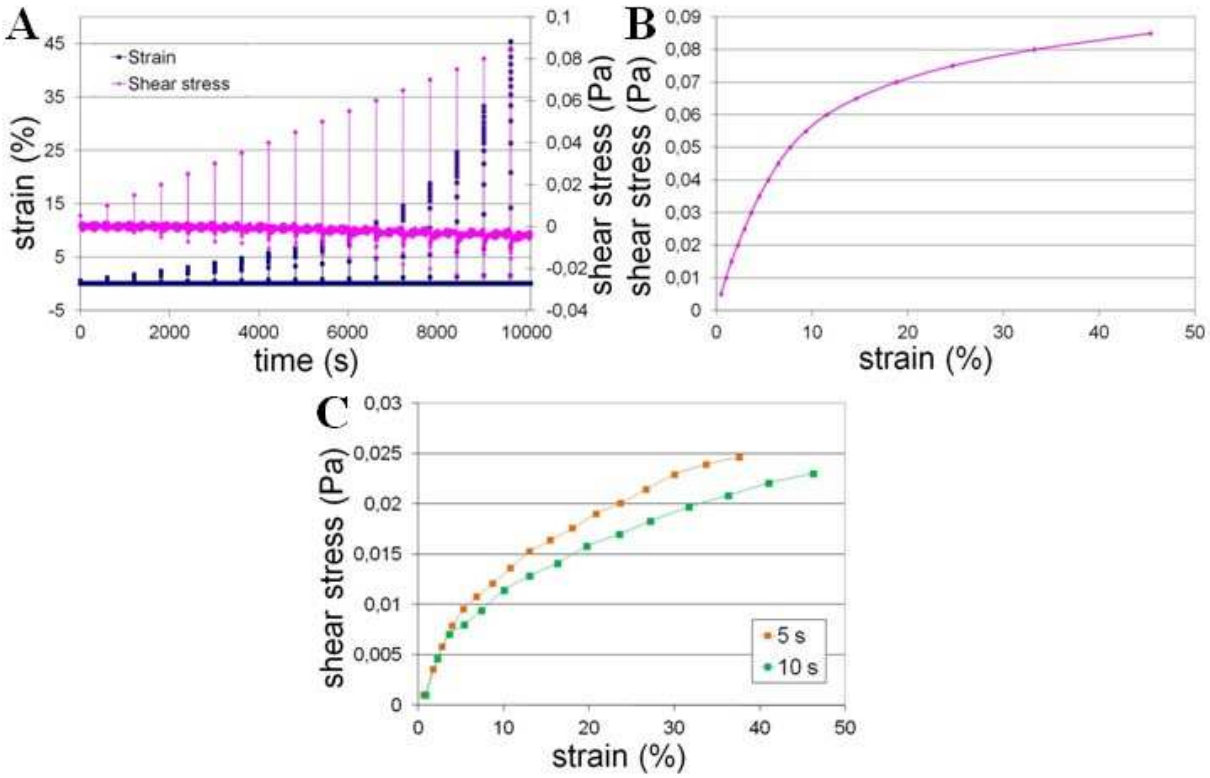

Fig. 4.7: *(A) The evolution of strain when imposing shear stress pulses (3 seconds) for a zero strain of 10 minutes imposed between two pulses. (B) Imposed shear stress as a function of maximum strain reached for every pulse. (C) Comparative softening experimental curves for shear stress pulses of 5 and 10 seconds, showing that the global behavior does not depend significantly on this specific parameter (i.e., duration of the stress pulse).*

However, if Semmrich *et al.* [13] found a hardening behavior as a function of strain for the actin solution, it's certainly due to the fact that they performed experiments at smaller temperatures and higher strain.

4.2.4 Deformation during pulses

Nevertheless, another aspect of this study concerns what happens during the pulses. Thus, we plot the strain during the pulse, as a function of time. We can note two different types of regimes:

- The oscillatory regime, which tends to a plateau (Fig. 4.8 A). This regime is noted at small pulses: it does not have to reach more than 4% of strain. The oscillations are due to a phenomenon called creep-ringing [16]. It is related to the acceleration and the inertia of the rheometer.

- The linear regime, where we can note two distinct slopes (Fig. 4.8 B). It is the case of pulses for which the deformation produced is higher than 4%. Once the transitory regime linked to inertia is passed, we are observing creeping of our system under stress.

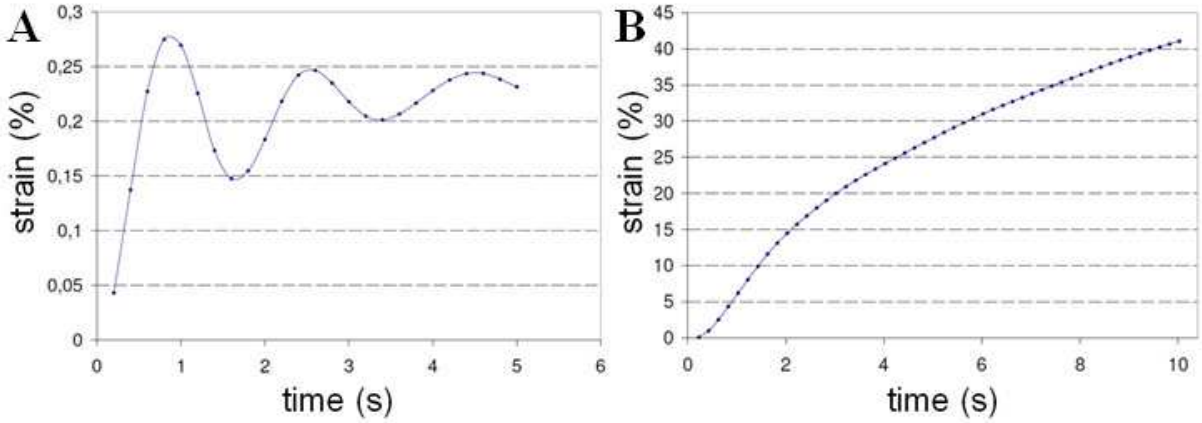

Fig. 4.8: *The evolution of strain during a 10 seconds pulse of 0.004 Pa (A) and a 5 seconds pulse of 0.014 s (B).*

This transition from plateau to creep is clearly showing that there is a yield stress (or strain?) in our system, which we are able to measure using this technique, but which is rather small (for γ ~4%).

4.3 Controlled shear rate experiments – Constant rate cyclic loading

We will study here using controlled cyclic shear rate experiments the influence of the history of loading onto the rheological behavior of our aggregates. As we have already seen that important creep was happening while submitting aggregates to stress, we are in the worst scenario for a direct interpretation of data. It is indeed tricky because all the curves are the results of the convolution of elastic properties and creep. However, we will see that a simple modeling of how this creep may occur enables us to catch the main features of the curves obtained in this section.

We are deforming the aggregates at a constant shear rate. The rheometer allows us to study the behavior of aggregates for values of the shear rate in the range of $5*10^{-5}$ up to 1 s^{-1}. However, the experiments at 1 s^{-1} that we performed give rheological curves which are too difficult to analyze, as too noisy (see Fig. A.1 in the appendix). At the opposite, the minimal value that we tested, $5*10^{-5}$ s^{-1}, gives a very long total experimental time, which allows the visualization of cell death after approximately 14 hours (see Fig. A.2 in the appendix).

Thus, for the majority of cases we study for the same series of aggregates three successive shear rates: 0.001, 0.01 and 0.05 s^{-1}.

Regarding the deformation, we chose, in a first step, to stop shearing when the strain was reaching 30%. This is a rather arbitrary value. At the beginning we did not want to be too harsh on cells, so as to be able to repeat several time the experiments with the same set of aggregates.

To shortly describe what happens during a classical experiment:

- We deform the system up to 30% at each given shear rate for 300, 30 and 6 seconds respectively and immediately after we come back to the initial position with the same shear rate, meaning that the total time of each loading strain is 10 minutes, 1 minute and 12 seconds respectively.

- After each cycle we allow the sample to relax for 10 minutes, by imposing a zero strain.

- This cycle is repeated ten times for each value of the shear rate.

A graphical representation of the input strain-time can be observed in Fig. 4.9.

It is important to mention here that after each series of ten cycles for a given shear rate we let the system relax, imposing a 0% strain for a large amount of time, starting from 2 and up to 5 hours if necessary, in order for the cell aggregates to be able to come back to the closest possible to their initial state before launching another series for a different value of the shear rate. We can then plot in two different ways the shear stress: as a function of strain or as a function of time.

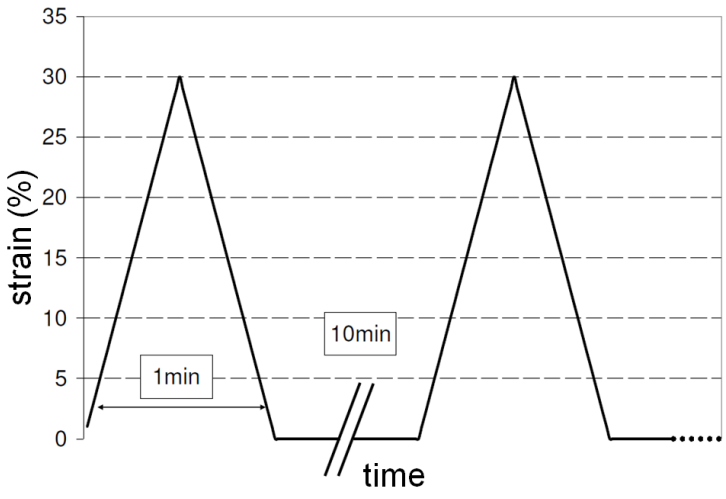

Fig. 4.9: *The input strain-time function as used for controlled shear rate experiments at 0.01 s^{-1}.*

4.3.1 Results of controlled shear rate experiments on F9 WT cell aggregates

In Fig. 4.10 (A-C) we present experimental curves obtained for F9 WT aggregates. The shear stress is plotted as a function of strain for each successive cycle at three different values of the shear rate: 0.001 (Fig. 4.10 A), 0.01 (Fig. 4.10 B) and 0.05 s^{-1} (Fig. 4.10 C). The three series of ten cycles for each value of shear rate are performed on the same sample and are separated by 5 hours at imposed 0% strain. After the 3rd series we waited here only for 3 hours.

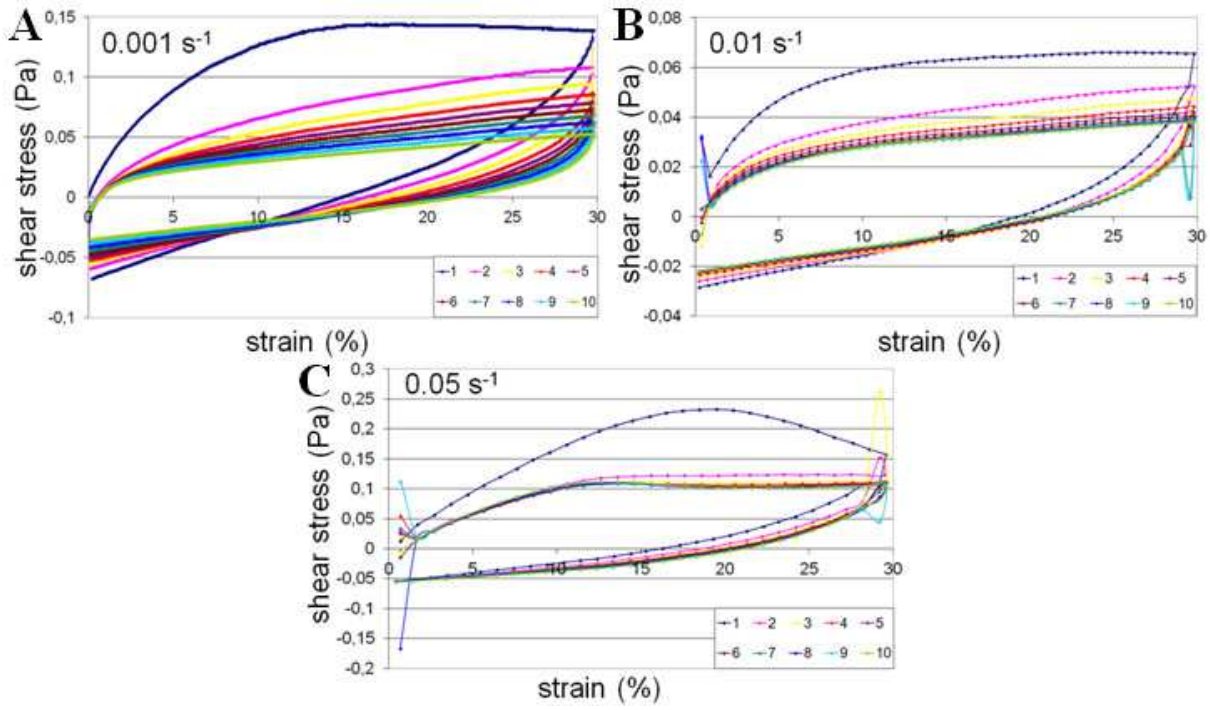

Fig. 4.10: *Shear stress for F9 WT cell aggregates as a function of strain for every cycle. The strain is increased up to a value of 30% and then it is decreased down to 0%. We repeat this step 10 times, with each color representing one cycle (the exact order is specified in the small legend down-right). The ten minutes of relaxation after each cycle are not shown. Experiments have been done for three different shear rates: 0.001 (A), 0.01 (B) and 0.05 s^{-1}(C), with 5 hours of imposed zero strain in between.*

We can observe that the first cycle is very different from the following ones and that the system quickly reaches afterwards a limit cycle behavior. This behavior is mostly independent of the shear rate value.

Moreover, we have seen that if we start again a series of cycles immediately after (*i.e.*, without the long relaxation time), the characteristic bump of the first cycle disappears. However, if we wait for several hours before restarting, the bump will appear again.

Finally, one can notice that after each loading strain, the shear stress does not return to its initial value (*i.e.*, 0 Pa) but reaches a negative stress, which we will call backstress as in [17]. By performing experiments at different shear rates we have also seen that the backstress presents no dependence (or a very small one) on the shear rate (see Fig. 4.10 A-C).

Comparing the response for each value of the shear rate we obtain systematically differences in amplitude for the rheological curves. But, as such, the factor by which the shear rate is increased in between two experiments does not stand alone to explain these differences and some other phenomena should have an important contribution to this.

The advantage when representing the shear stress as a function of time is that we can also visualize the ten minutes of relaxation in between each cycle and also the long relaxation at the end of the ten cycles. Thus, the experimental curves for the same experiments previously described present the following shapes as a function of time:

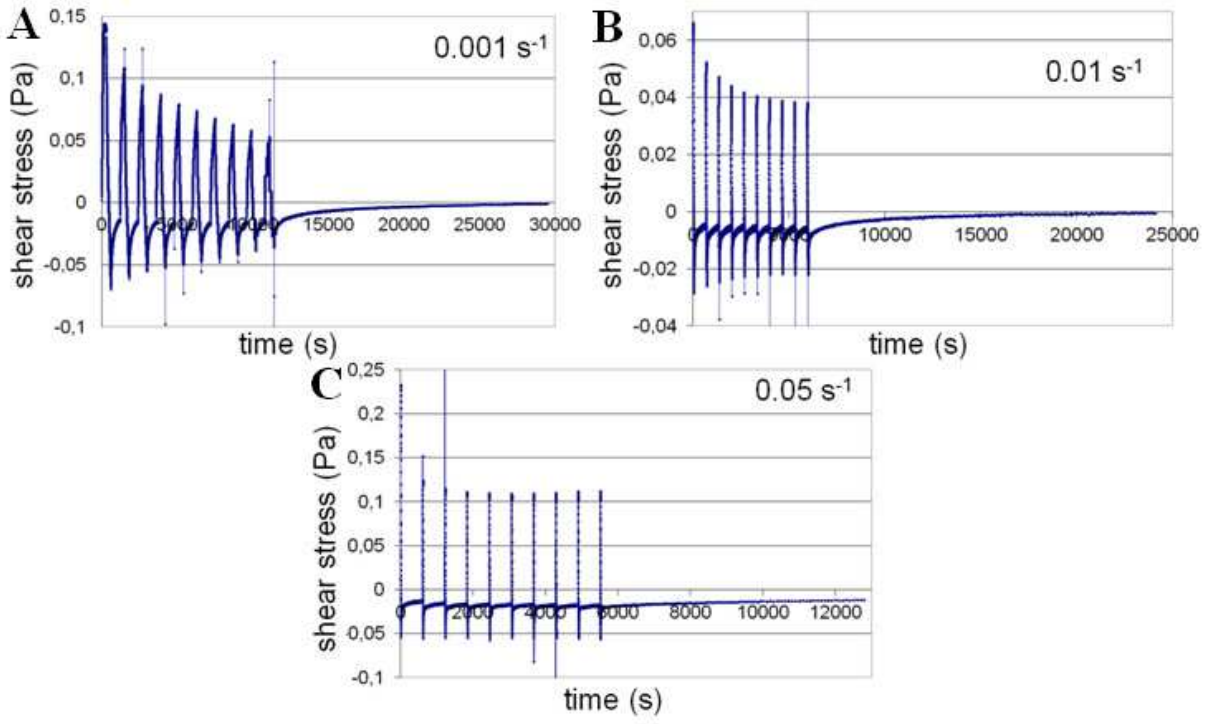

Fig. 4.11: *Shear stress for F9 WT cell aggregates as a function of time for every cycle of deformation. The graphs correspond to the same experiments presented in Fig. 4.10.*

The first cycle presents higher amplitude in shear stress, while the next ones describe the limit cycle. We can note that there is a very long relaxation time at the end of the ten cycles until the shear stress reaches a value close to 0 Pa.

One very interesting feature highlighted here concerns the difference in the relaxation behavior in between the different shear rates experiments. At high shear rates (0.05 s^{-1}), the relaxation in between cycles (after the backstress, during the waiting time) is very fast and

reaches rapidly a plateau which will be the same during the long relaxation and which is very different from 0 (has it something to do with a yield stress?). On the contrary for smaller shear rates, the 10 min relaxation time is not enough to reach a steady state, and during the 5 hours of relaxation, the system seems to be able to reach a state where the stress is null.

This means that there is certainly two different processes occurring at the same time, one triggered by high frequencies which is relaxing quite rapidly (cytoskeleton creeping?) and one triggered at low frequency which may have something to do with cell-cell contacts, which involve much longer timescales. This is also confirmed by a closer analysis of the relaxation (Fig. 4.12). If the first 1 or 10 minutes could eventually be fitted with a power law (Fig. 4.12 B), this is not possible for the next decade (5 hours of relaxation) (Fig. 4.12 C-D). Of course the hypothesis that two types of relaxation exist and that at least one has something to do with cell-cell rearrangements will have to be confirmed by other tools (for example two-photons microscopy).

However, we have to mention that the global relaxation process is relatively well fitted by a logarithmic curve. Curiously enough, such logarithmic relaxation has also been observed in solids [18,19].

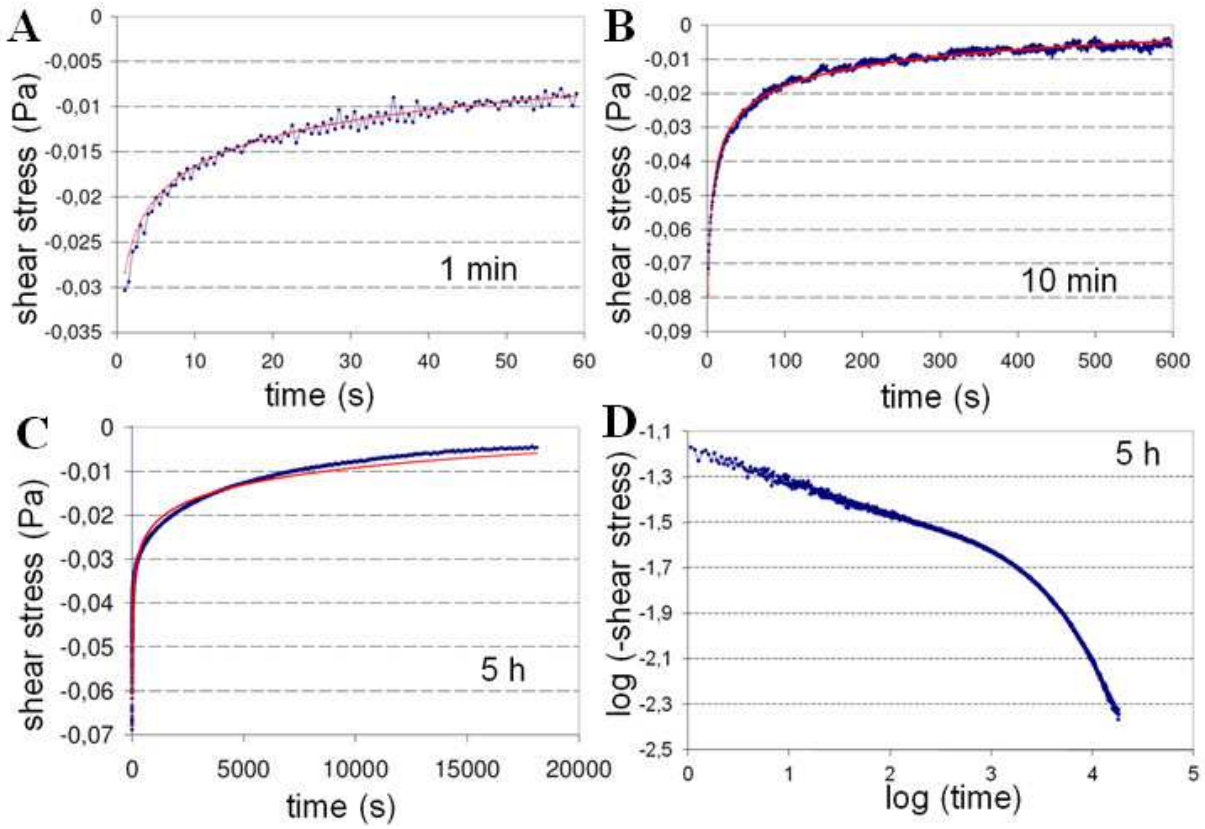

Fig. 4.12: *Relaxation of aggregates at zero strain between two cycles: for 1 minute (A), for 10 minutes (B) and for 5 hours (C). The experiment is performed at 0.01 s^{-1} shear rate. (D) Log-log representation of the shear stress-time curve for a 5 hours relaxation.*

4.3.2 Results of controlled shear rate experiments on F9$^{(\alpha-/-)}$ cell aggregates

We are interested to test whether the internal configuration of cell aggregates, or more precisely the intercellular properties, can induce changes in the overall rheological behavior of our sample. Studying the response obtained when shearing F9$^{(\alpha-/-)}$ cell aggregates could help for confirming that we are really getting information about the single cell behavior and not about the aggregate as a whole.

In order to compare the two cell lines, we performed the same type of experiments on F9$^{(\alpha-/-)}$ cell aggregates. Their behavior is presented in Figs. 4.13 and 4.14.

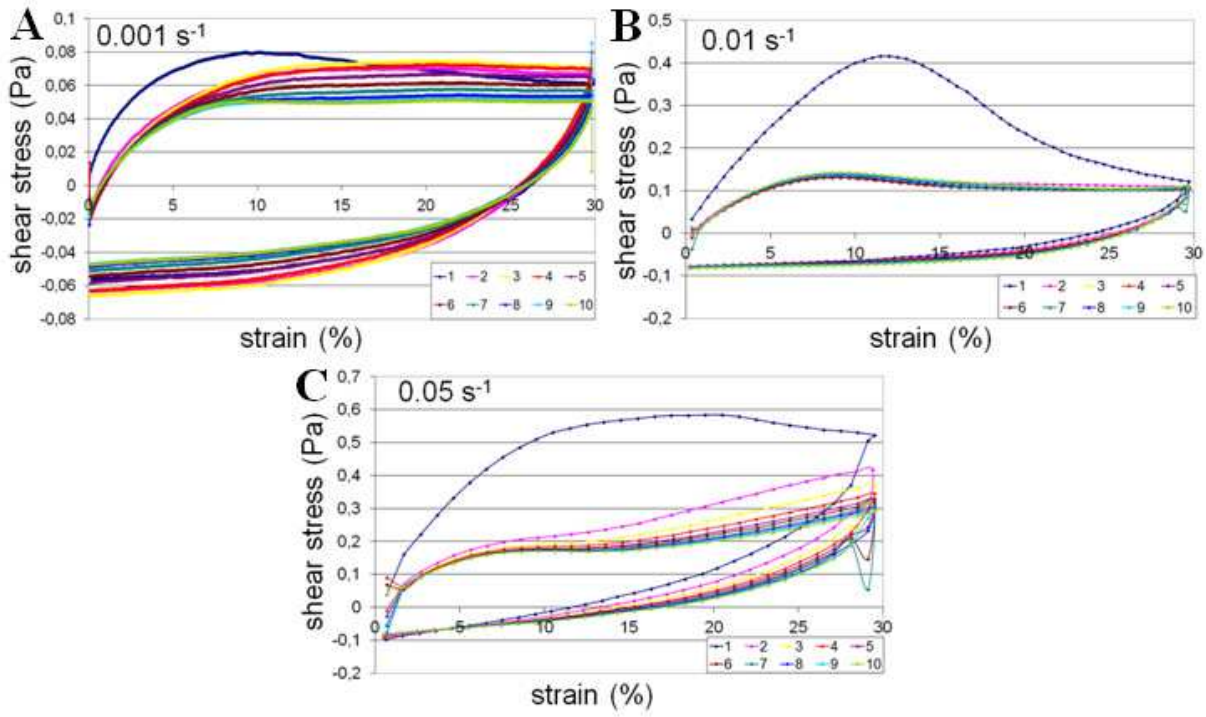

Fig. 4.13: *Shear stress for F9$^{(\alpha-/-)}$ cell aggregates as a function of strain for every cycle. We kept the same experimental parameters as in the case of controlled shear rate experiments performed on F9 WT cell aggregates, previously described (see Fig. 4.10).*

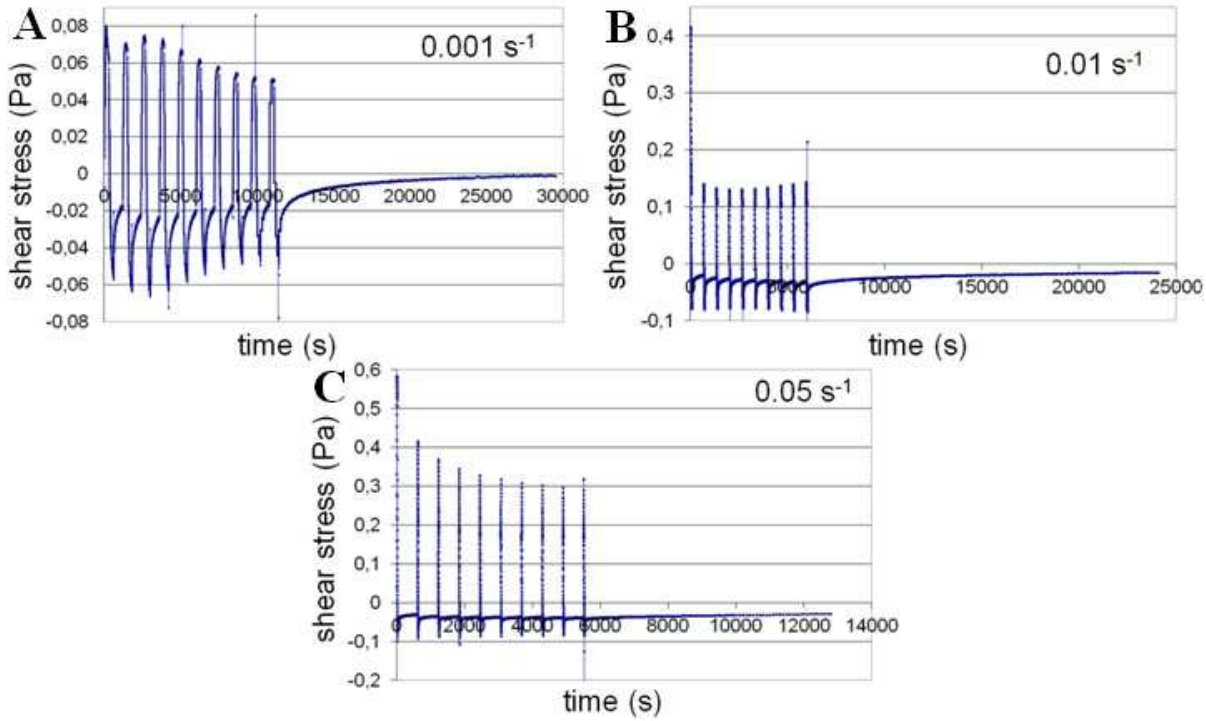

Fig. 4.14 *Shear stress for F9$^{(\alpha-/-)}$ cell aggregates as a function of time for every cycle of deformation. The graphs correspond to the same experiment presented in Fig. 4.13.*

If no striking difference could be notice in the overall shape of these curves and the one obtained for the WT, nevertheless, it is interesting to notice that for the shear rate 0.01s^{-1} where the relaxation curve was going back to zero at long time scale for the WT here it seems we obtain a plateau, indicating that we may have a difference in the triggering of cell-cell movement if our initial hypothesis linking this long relaxation to cell rearrangements happens to be true.

4.3.3 The effect of drugs in controlled shear rate experiments

As mentioned in the Materials and Methods chapter, we are interested to test the effect of different drugs on the rheological behavior of aggregates.

On both cellular types, we first tested the effects of nocodazole, Y-27632 and ATP inhibitor. We obtained no remarkable difference between untreated aggregates and treated ones, as shown in Fig. 4.15. This might indicate that the behavior of aggregates at constant strain depends only on the actin network.

We present here only the result obtained for F9$^{(\alpha-/-)}$ exposed to drugs when imposing a shear rate of 0.01 s^{-1}.

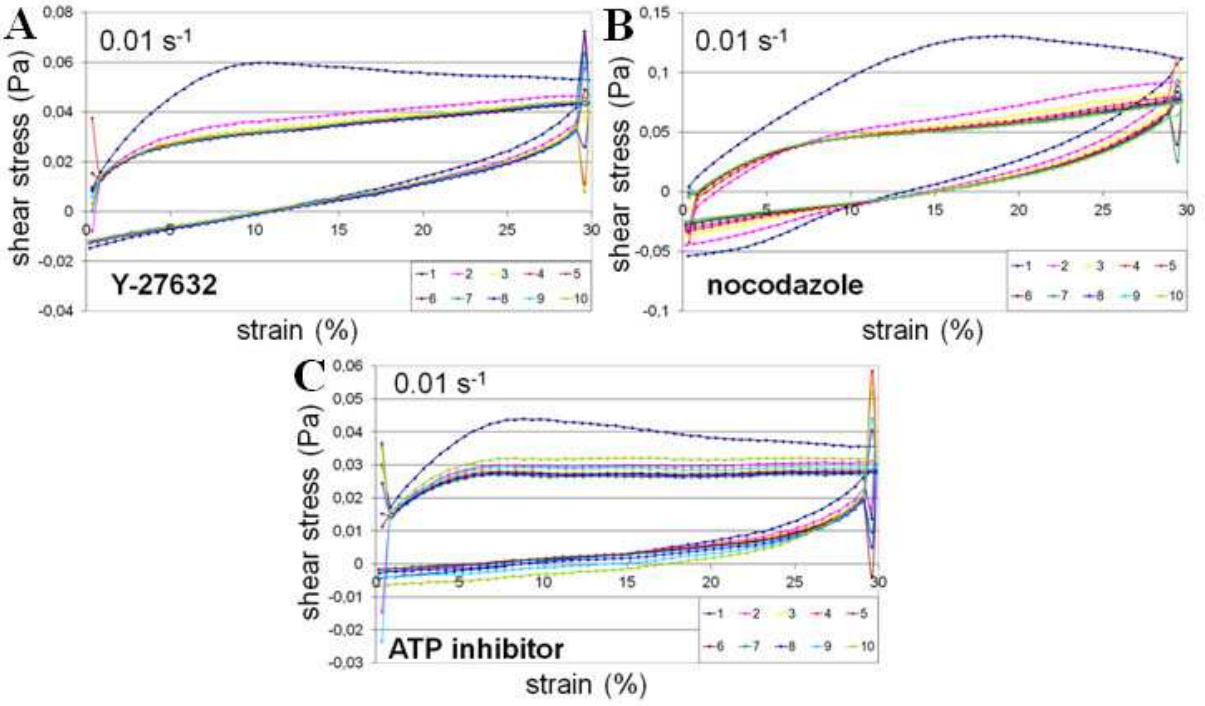

Fig. 4.15: *Rheological curves (shear stress as a function of strain) for F9$^{(\alpha-/-)}$ cell aggregates exposed to Y-27632 (A), nocodazole (B) and ATP inhibitor (C).*

We then decided to interfere with actin polymerization. To do this we exposed our aggregates to 1 µM latrunculin A, which is a very well known drug acting as an inhibitor of actin polymerization.

As presented in Fig. 4.16 for F9 WT cell aggregates, the results show this time, as expected, a remarkable qualitative difference. The shape of the rheological curves for the first series of cyclic loading, at 0.001 s^{-1} (Fig. 4.16 A), suggests a clearly different behavior, as a result of the exposure to the drug. However, we can see that starting from the second series of cyclic loading, corresponding to a shear rate of 0.01 s^{-1} (Fig. 4.16 C) and more remarkably on the last series which corresponds to the highest shear rate, 0.05 s^{-1} (Fig. 4.16 E), the curves regain their usual shape, with a first cycle different from the others, which will follow a limit cycle. This could be interpreted as a loss in the efficiency of the drug, as the timescales for each series is quite long (*i.e.*, approximately 8 hours for the first series, more than 6 and a half hours for the second one and 3 and a half hours for the last one). We also remind here that we usually wait for two hours after depositing the aggregates and approached the two glass surfaces, before starting any other manipulation.

In any case, it would be very interesting to redo the experiment and start first with the highest strain rate.

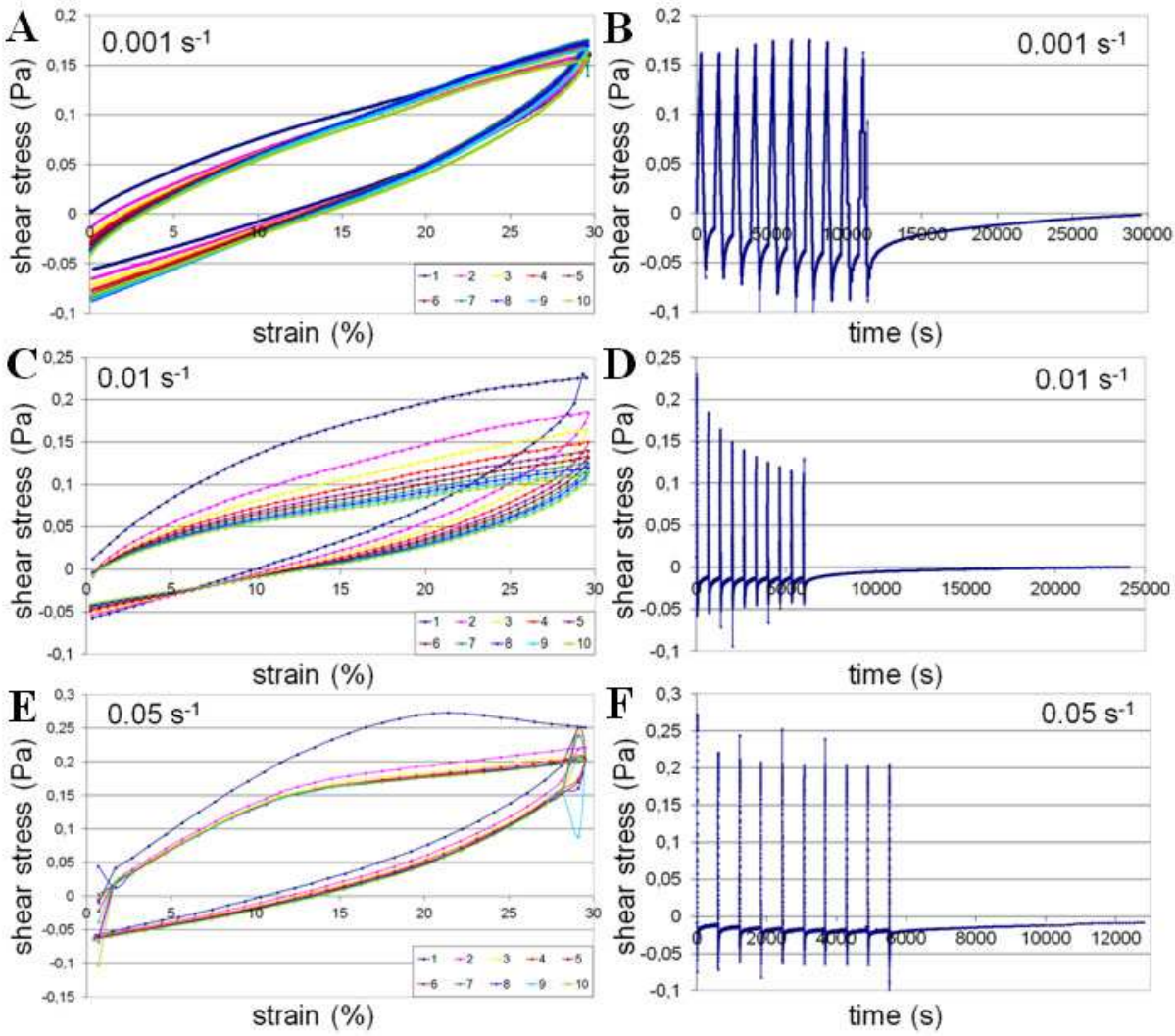

Fig. 4.16: *Shear stress as a function of strain (left) and as a function of time (right) for F9 WT cell aggregates exposed to 1 µM latrunculin A. As usual, the same parameters have been used for the experiments at each value of shear rate.*

We also obtained the same qualitative results on $F9^{(\alpha-/-)}$ cell aggregates exposed to 1 µM latrunuclin A (see Fig. A.3 in the appendix).

Thus, only the first series of cyclic loading is representative for aggregates whose actin polymerization is inhibited and its corresponding rheological curves present different shapes compared to the control experiments in Fig. 4.10 or 4.13. Stress-strain curves are rather linear, which is a signature of a rather rigid-elastic material. We however recover the limit cycle and the backstress is quite important, meaning that there might be some internal plasticity and reorganization inside aggregates.

4.3.4 Controlled shear rates – 50 cycles

It is also interesting to study the behavior of cell aggregates under shear by imposing a large number of cycles at a given shear rate.

We performed a series of 50 successive cycles of deformation for an imposed shear rate of 0.001 s^{-1}, with the usual 10 minutes of zero strain in between. The results obtained for F9 WT and F9$^{(\alpha-/-)}$ cell aggregates are presented in Fig. 4.17 A-B.

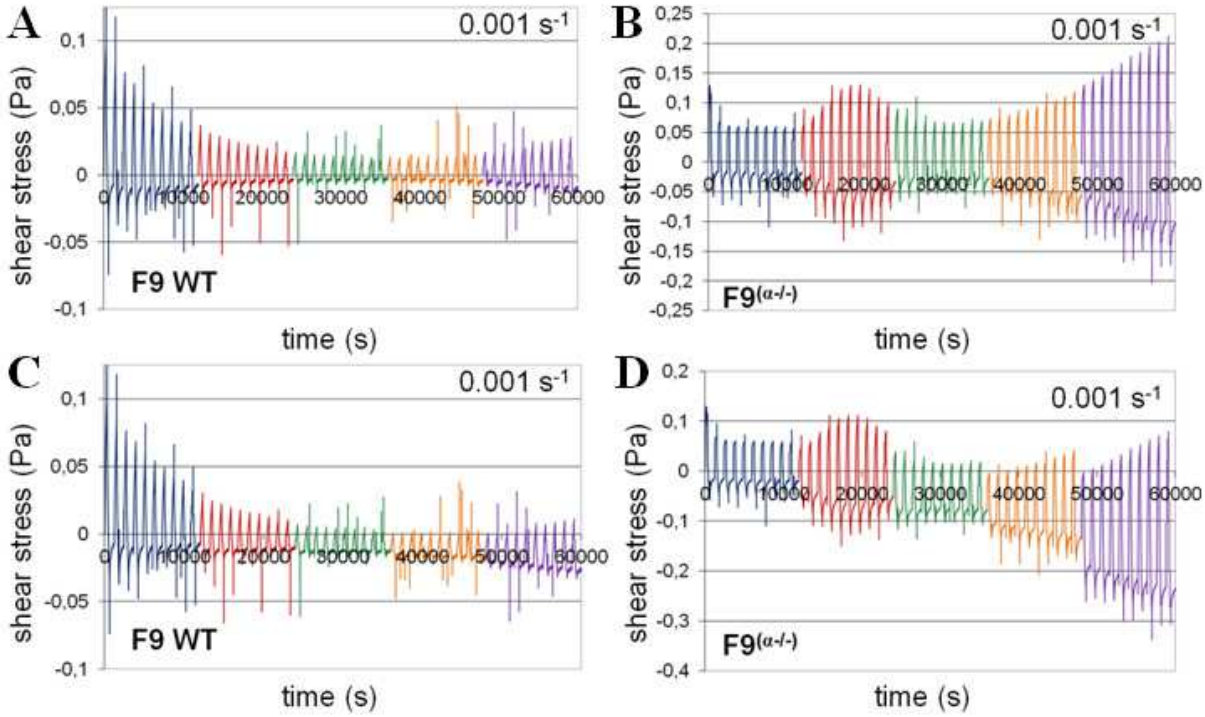

Fig. 4.17: *Shear stress as a function of time for 50 successive cycles for F9 WT (A) and F9$^{(\alpha-/-)}$ (B) cell aggregates. Corrected curves for shear stress after each series of 10 cycles are represented in (C) for F9 WT and in (D) for F9$^{(\alpha-/-)}$ cell aggregates. Each color corresponds to a number of ten cycles.*

Due to some limitations of the software, we had to concatenate five series of ten cycles each. In between two successive series, it seems, if we look at the graphical representations, that the rheometer resets the shears stress to a value close to zero, which makes this data not so reliable. However, if we try to correct the shear stress, we can see in Fig. 4.17 C-D that the curves present a certain drift whose explanation can be found by making the hypothesis that over these large timescales some evaporation of the medium might have occurred, increasing the contribution of the meniscus at the plates' outline. The large timescale can also provide the explanation for the increasing stress in Fig. 4.17 D over the last cycles represented in purple, assuming that cell death occurs.

4.3.5 Controlled shear rates with different imposed timescales at maximum deformation

In order to see if the value of the backstress might depend on the timescale at which the aggregates are being subjected to deformation, we performed experiments where we vary the period of time at maximum strain. After three usual loading strains, where we impose no time, we continue with two cycles with 10 seconds of maximum strain, two with 100 seconds and finally, two with 500 seconds (see Fig. 4.18 for a schematic representation of the strain-time function).

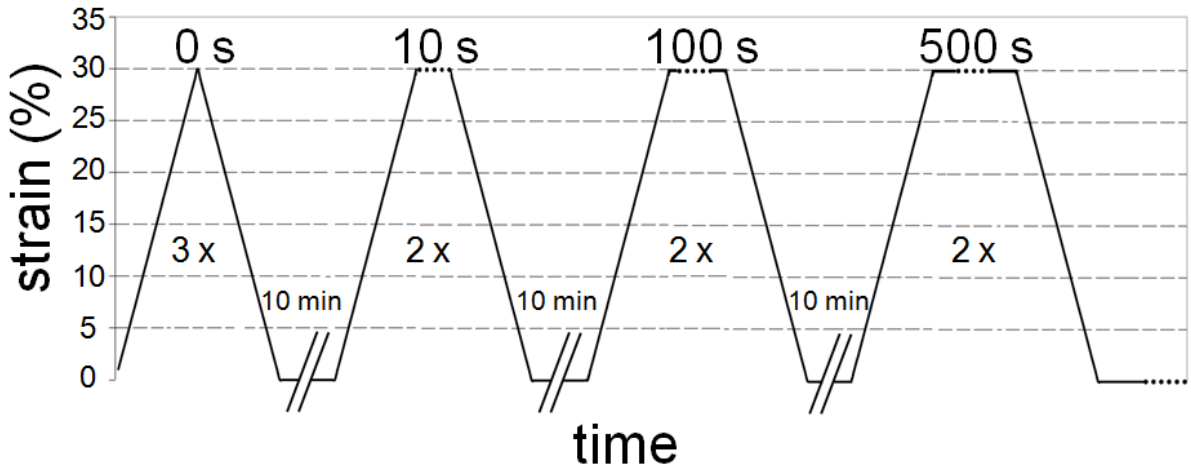

Fig. 4.18: *The input strain-time function as used for controlled shear rate experiments with different imposed timescales at maximum deformation.*

We performed this experiment at a controlled shear rate of 0.01 s^{-1} and we deform our sample up to 30%. The results obtained are resumed in Fig. 4.19.

It seems that the backstress does not depend on this parameter (*i.e.*, the time spent at maximum deformation), which could indicate that the backstress is related to phenomena which are faster than the ones we tested.

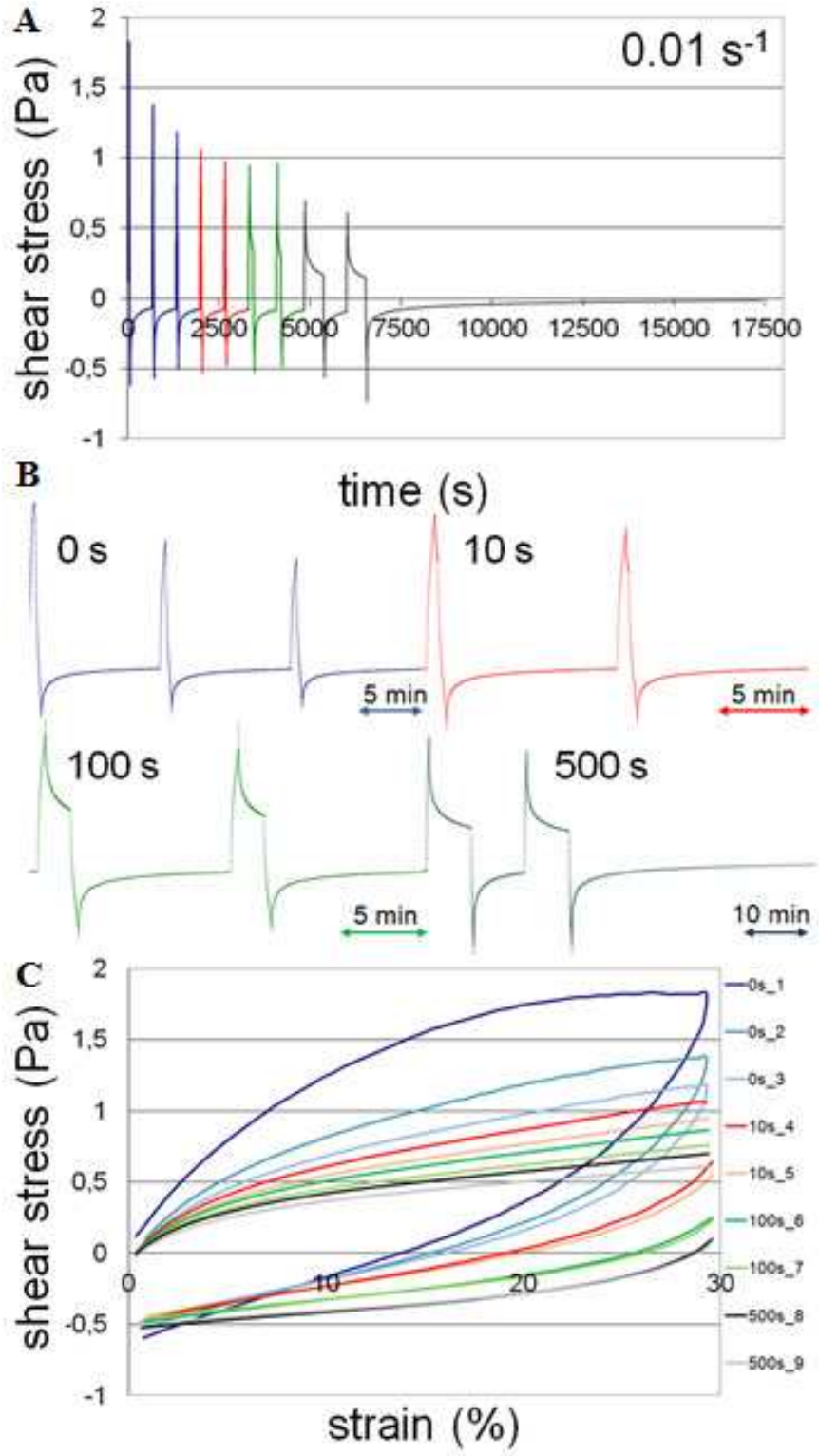

Fig. 4.19: *(A) Shear stress as a function of time for 9 successive cycles for F9 WT cell aggregates. (B) Representation helping for a better visualization of the signal but which does not take into consideration the real scales (X and Y axes). In A-B, each color corresponds to a different value of the period of time at which the maximum strain of 30% is being imposed: blue, 0 s, red, 10 s, green, 100 s and black, 500 s. (C) Shear stress as a function of strain for the same experiment. Here, each color corresponds to a cycle and the order is represented in the legend situated at right.*

4.3.6 Controlled shear rate experiments – Large deformations

We wanted to go further in the analysis of the rheological behavior by imposing large deformations (*i.e.*, up to 200%) to our sample. The idea is of course to be able to measure a clear signature of cell-cell rearrangements.

We tested the response of aggregates when imposing steps of deformations with the increasing strain in the range 0 up to 200%, more specifically successive steps of 0, 2, 5, 10, 15, 30, 60, 100, 130, 160 and 200%, as represented in Fig. 4.20 A. Each step is followed by 10 minutes of relaxation.

3 hours after, we imposed a decreasing variable strain in the same range (*i.e.*, from 200 down to 0%) (Fig. 4.20 B).

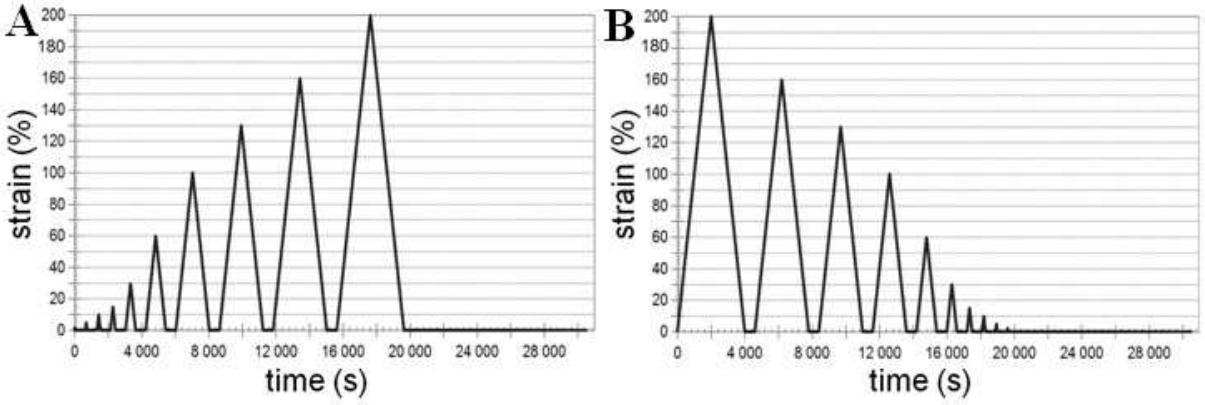

Fig. 4.20: *The input strain-time function as used in controlled shear experiments with ranges in steps of deformation. (A) Increasing and (B) decreasing strain.*

For both increasing and decreasing strains, experiments have been carried at 0.001 and 0.01 s^{-1} shear rates.

The data show that the history influences the recorded stress: increasing or decreasing the strain gives rise to very different behaviors (Fig. 4.21, Fig. 4.22). Curves are superposing starting from the second cycle during the decrease in strain (curves B, D) which is absolutely not the case for the strain increase (curves A, C). The first cycle in the decreasing strain is different due to the long waiting time in between the two phases, increase and decrease in strain.

We also note that there are no striking differences between F9 WT and $F9^{(\alpha-/-)}$ cell aggregates.

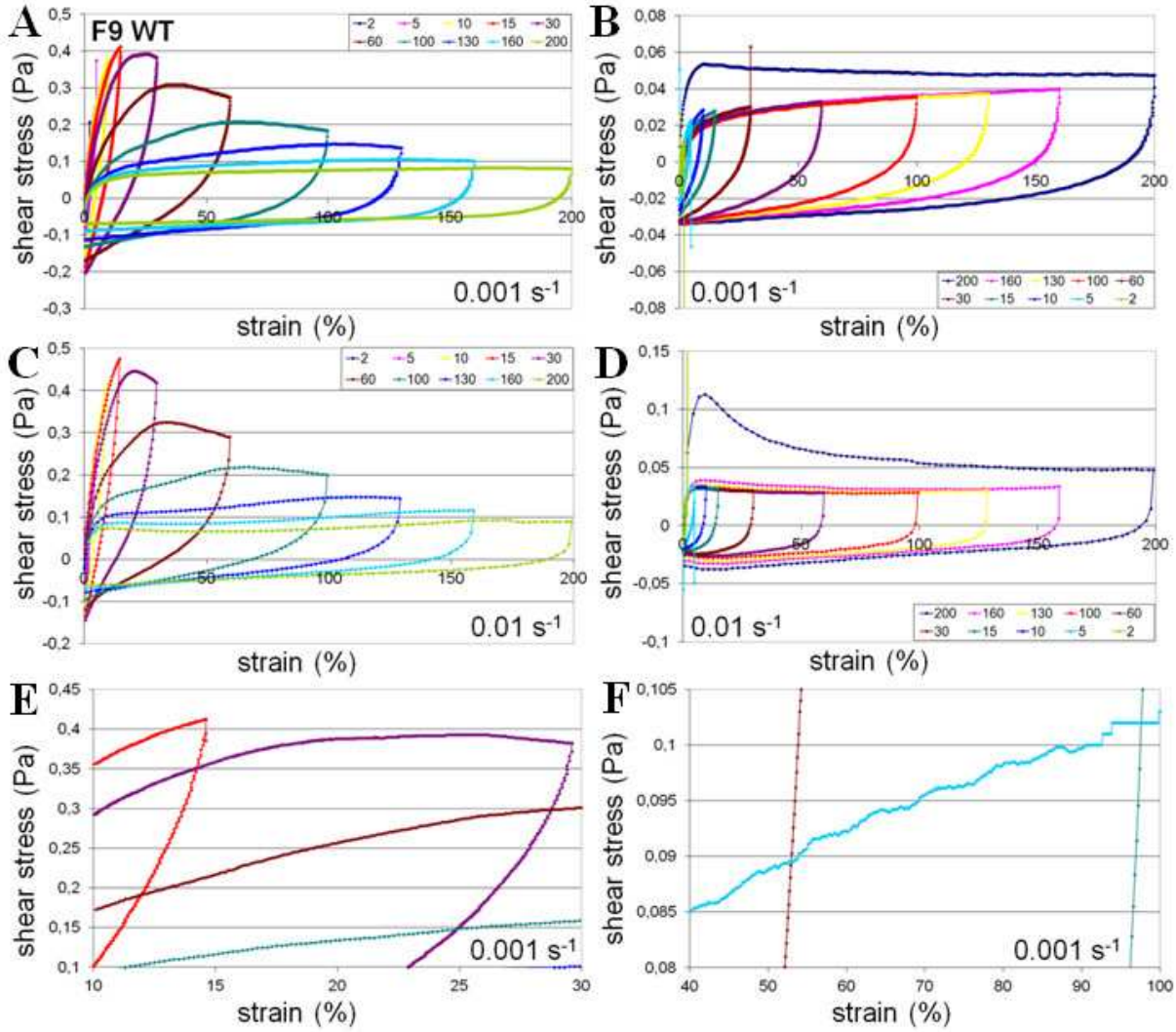

Fig. 4.21: *F9 WT cell aggregates response to increasing (A and C) and decreasing (B and D) strain (values are given in % in the legend box) for different values of shear rate (i.e., 0.001 s^{-1}(A-B) and 0.01 s^{-1}(C-D)).(E-F) Zooms on the rheological curves showing that behaviors of aggregates at different deformations are not similar in the phase of increase in strain.*

When we take a closer look on the curves presented in Fig. 4.21 A for the increase in strain we can note two different behaviors characterizing the aggregates (Fig. 4.21 E-F). While at small deformations there is no new striking feature emerging from the curves (Fig. 4.21 E), when going up to larger deformations we can see several jumps (Fig. 4.21 F) which might indicate that some aggregates are detaching from the surfaces. This would be very reassuring as this would mean that the global detachment of aggregates (which is not what we want to measure) can be monitored and is only appearing at high deformations.

It is also very interesting to see that probing different strain amplitudes and shear rates, we can get different curvature of the stress-strain curve (we will call it differential modulus *K* which is time dependent and is a combination of creep and elasticity). We see that we can observe in a single experiment different behaviors (which could be similar to ones already

observed in the literature : kinematic hardening (Fig 4.21 C brown curve 60%) [17] or even stress stiffening (Fig 4.21 C turquoise curve 100%) [20].

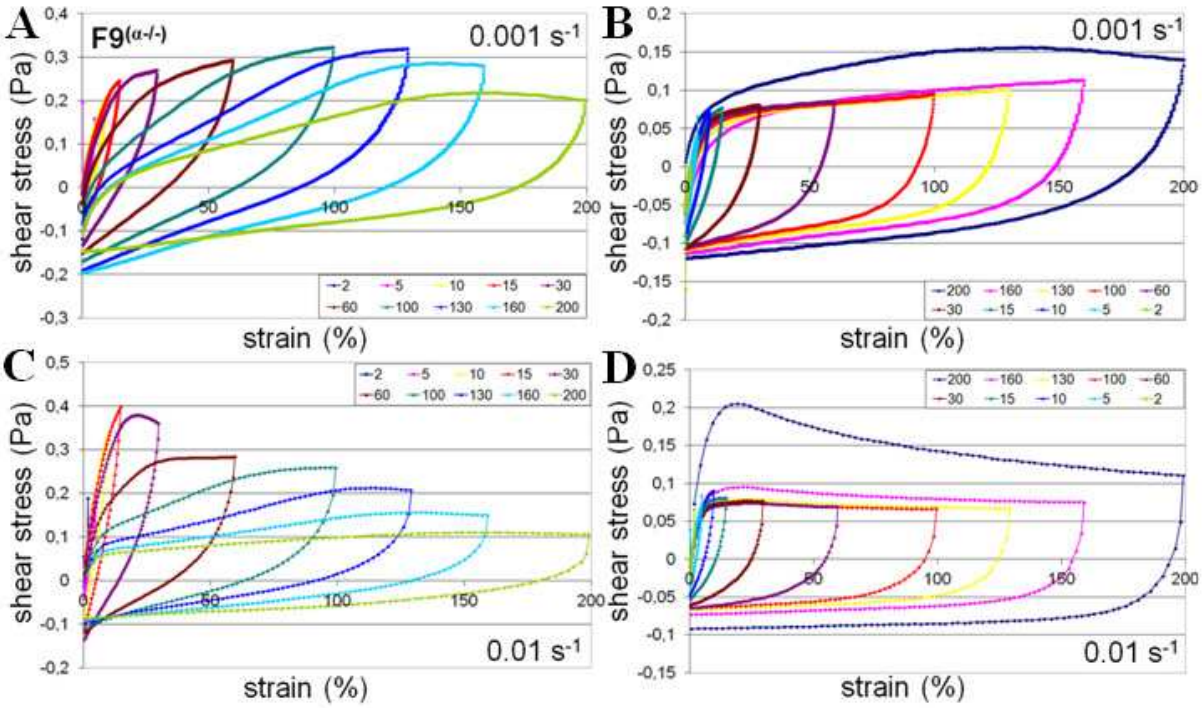

Fig. 4.22: *$F9^{(\alpha-/-)}$ cell aggregates response to increasing (A and C) and decreasing (B and D) strain for different values of shear rate (i.e., 0.001 s^{-1}(A-B) and 0.01 s^{-1}(C-D)).*

Graphical representations of the shear stress as a function of time together with results for both cell lines treated with drugs (Y-27632 and nocodazole) and showing no significant differences can be found in the appendix (Fig. A.4 – A.9). Note that Fig. A.1.8 representing $F9^{(\alpha-/-)}$ cell aggregates response to increasing and decreasing strain while exposed to 10 µM Y-27632 shows a very important change in the rheological curves but it is quite possible and we don't exclude that some other uncontrolled parameters might have influenced these results. We will have to redo this type of experiment.

4.4 The model of parallel springs

4.4.1 Choice of the model

In order to understand and explain our rheological curves at short timescales and small deformations we developed a relatively simple scalar model based on parallel springs. This model was developed by Hélène Delanoë-Ayari and Catherine Barentin from discussions with Lydéric Bocquet, Sham Tlili and François Graner.

The choice of this model is explained by several factors which led us in this direction:

- First of all, our experiments are performed at short times and it has been already shown that cellular rearrangements inside the aggregates are slow phenomena, taking place at longer timescales [21]. Thus, we will not take them into account for the modeling.

- In addition, the cytoskeleton's structure containing the actin filaments, the microtubules and the intermediate filaments, some of which are relatively long proteins (for more details, see the Introduction chapter), is often compared to that of interconnected springs.

- Furthermore, preliminary oscillation experiments allowed us to see that for the range of deformations of interest, the elastic modulus G' is higher than the loss modulus G" which represents the viscous component. Thus, the idea of an elastic model is once again preferred.

In our model, we represent the cells forming the aggregates by *N(t)* springs, whose number may vary from one experiment to another but also within one single experiment and which is always larger than the total number of cells within aggregates. The springs are assumed to be in parallel, as the signal obtained is proportional to the number of aggregates involved. They all have the same stiffness k_0 and the same no-load length l_0 (see Fig. 4.23). Under shear they are all deformed by the same length δ_x with respect to l_0.

For the moment, we are assuming that k_0 is not depending on the level of stress (so no stress stiffening could be seen). However, we plan in a close future to incorporate some stress dependence enabling to model this important behavior. Moreover, we have seen that cells are certainly constituted of different networks (for example actin cortical network and cytoplasmic actin network) whose k could be different. So we could easily render the complexity by adding other springs (also in parallel, with a different k), but this will not be done in this first study in order to extract the basic important features.

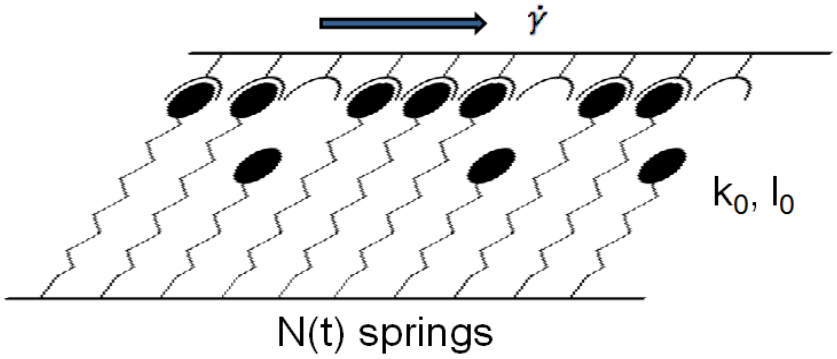

Fig. 4.23: *Identical parallel springs model.*

Initially, there is a maximum number of operating springs but their number will decrease under stress. It is not yet clear if the "real springs" detach to the walls (*i.e.*, at the

contacts with the rheometer's glass surfaces) or if they break within the aggregate. However experiments at large stresses, where the detachment of aggregates could be monitored make us think that the springs are really modeling the cytoskeleton. We will also assume that broken springs could repair themselves and become operational again, at a certain time interval. Thus, the number of springs strongly evolves over time.

4.4.2 The equations

Once we have all our variables defined, we can put into equations the variation of the number of springs and the variation of shear stress.

In our experiments, we measure σ (*i.e.*, the shear stress) and γ (*i.e.*, the strain or the deformation). These two physical measures can be related by using the force exerted by the aggregates which will be denoted as

$$F = \sigma S = N k_0 \delta_x \qquad \text{(Eq. 1).}$$

Here, *S* is the surface of the aggregates which is in contact with the planes of the rheometer and

$$\delta_x = \gamma e = \dot{\gamma} t e \qquad \text{(Eq. 2),}$$

where $\dot{\gamma}$ is the shear rate, *t* is the time and *e* is the distance between the two glass surfaces (*i.e.*, the imposed gap). The force exerted by the aggregates is therefore proportional to the number of operational springs (see subsection 2.4.7 in chapter 2 for more explanations concerning the absolute values of measured physical quantities and the variation of the strain in a plate-plate geometry).

As previously stated, the number of aggregates deposited between the two plates can vary from one experiment to another. Therefore, the surface *S* can also strongly vary. The force being proportional to *S*, in this part of the study we are only interested on the shape of the curves obtained and not in their absolute value.

By applying Kramers' theory for reaction kinetics to bond rupture [22], one assumes next that the bond energy landscape as a function of a position coordinate (relative spring deformation δ_x) presents at least a sharp barrier *Er* (blue line in Fig. 4.24). In order to break a spring, it is necessary to provide an energy, which is the rupture or the detachment energy, which we represent by *Er*. In the absence of any force exerted on the spring, it will require a time τ_r (detachment time) before breaking, with $\tau_r = \tau_0 \exp(\frac{E_r}{\xi})$, where τ_0 is a microscopic time linked to the curvature of the well (see also references [23–25]) and ξ is a fluctuation energy, also noted kT for the effective thermal energy in the literature [26]).

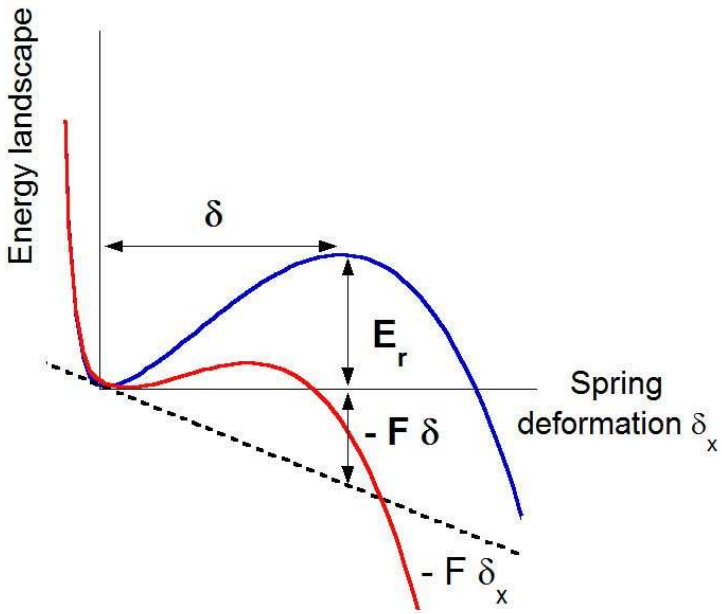

Fig. 4.24: *Spring energy landscape as a function of the spring deformation coordinate. In blue, the landscape in the absence of external force, in red the landscape when a mechanical work –Fδx (dotted line) is added. The energy barrier Er is then basically lowered by the amount of mechanical work –Fδ where δ is the barrier width.*

When exerting a force on the springs, the energy landscape is decreased by the mechanical work *-F* δ_x (dotted line in Fig. 4.24) and the energy barrier is lowered by this external mechanical energy. The new barrier height depends on the barrier shape and force, but roughly if the shape of the barrier is sharp as compared to the mechanical energy, then the barrier is lowered by *-F* δ where δ is the barrier width, a parameter of microscopic origin (as *Er*).

Therefore, the mean detachment time $\tau_r(F)$ when an external force is applied will write down as $\tau_r(F) = \tau_0 \exp(\frac{E_r - \frac{F}{N}\delta}{\xi})$ with $\frac{F}{N}$ being the force of one spring (the springs are parallel and each of them undergoes $\frac{F}{N}$).

The more important the force is, the larger is the number of broken springs. We can therefore calculate the variation of the number of springs as a function of time:

$$\frac{dN}{dt} = -\frac{N}{\tau_r(F)} = -\frac{N}{\tau_r}\exp\left(\frac{F\delta}{N\xi}\right)$$

This equation will describe only the shape of stress-strain cycles when strain is increased. To be able to model the decreasing strain part, we will add a constant (*i.e.*, *C*) which will model the spontaneous spring reattachment rate.

Thus, the main equation of the force dependant parallel spring model will be:

$$\frac{dN}{dt} = -\frac{N}{\tau_r(F)} = -\frac{N}{\tau_r}\exp\left(\frac{F\delta}{N\xi}\right) + C \qquad \text{(Eq. 3),}$$

The equation depends solely on *N(t)* because we make the assumption that all the springs preserve the same stiffness k_0 until the moment they detach. There is no plasticity as well in the springs.

4.4.3 Solving the equations

Using Equations 1-3 we can calculate the evolution of the force and of the number of springs as a function of time.

In the cyclic loading experiments we impose a fixed shear rate $\dot{\gamma}$. In this case, the evolution of the deformation with time is $\delta_x = l_0\dot{\gamma}t$ and the force is written as

$$F(t) = N(t)k_0 l_0 \dot{\gamma} t \,.$$

By reinjection in the Eq. 3 and taking

$$\tilde{t} = \frac{t}{\tau_r} \,, \dot{\tilde{\gamma}} = \tau_r \dot{\gamma} \,, F_1 = k_0 l_0 \text{ et } F_0 = \frac{\xi}{\delta} \,,$$

we obtain

$$\frac{dN}{d\tilde{t}} = -N \exp\left(\frac{F_1}{F_0}\dot{\tilde{\gamma}}\tilde{t}\right) + C.$$

As already stated, the *C* constant allows one to find the limit cycle, by describing the decreasing step in the strain.

We can numerically solve this equation and get *N* as a function of *t* (Fig. 4.25 A).

From the analytical expression of *N(t)* we can get the one of *F(t)* (Fig. 4.25 B).

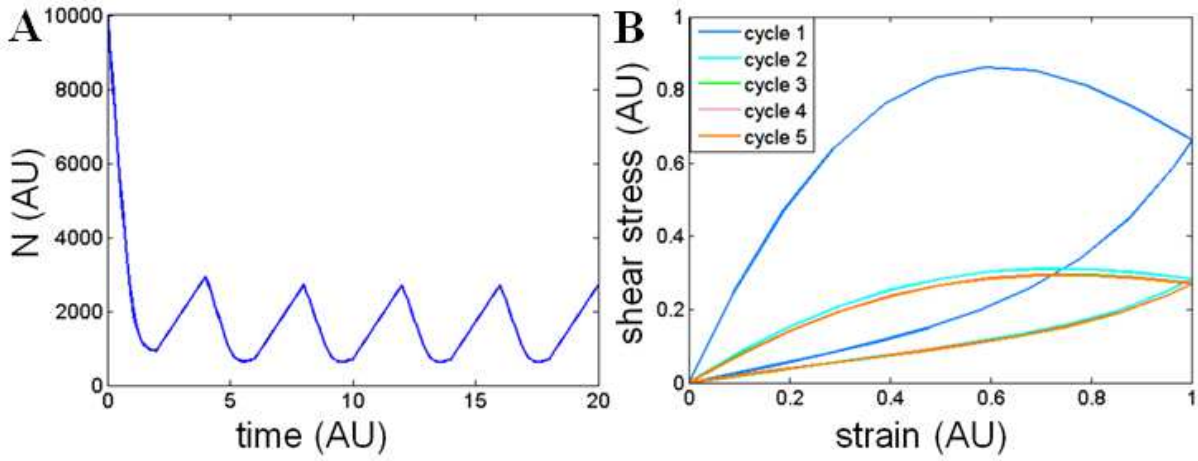

Fig. 4.25: *(A) Evolution of the number of springs as a function of time in arbitrary units during the first five cycles {$F_0 = 3*10^{-4}$; $F_1 = 1$; $N_0 = 10000$; $C = 1000$}. (B) Evolution of the stress as a function of time in arbitrary units for the first five cycles {idem}.*

The force *F* is a competition between the strain, which makes it increase at short time scales and the detachment of springs, which makes it decrease at long time scales. Thus, the characteristic bump of the first cycle (Fig. 4.25 B) is the result of this competition.

Furthermore, at the end of the first cycle, the number of springs left N_1 will be much less important than the number of springs N_0 present before the first cycle. The ten minutes of

relaxation being largely insufficient for the springs to be able to reattach we will always have about N_1 springs before starting the second cycle, with $N_1 < N_0$. The force exerted during this second cycle will be less important (because it is proportional to the number of springs). We therefore have a less important, almost invisible bump for the second cycle. And it is the same for the next 8 ones (in the simulations presented earlier, the next three ones).

Finally, the largest number of springs is broken in the first cycle. During the next ones they will break much less, because the force is much smaller. This explains that the first cycle is very different from the next 9 ones which are almost stackable.

4.4.4 Modeling the backstress

This simple model of springs can account for the shape of the experimental curves but does not provide the understanding of the backstress.

Indeed, according to the model, when decreasing the strain down to 0%, the force (and hence the shear stress) would turn to 0, which is not the case on the experimental curves (Fig. 4.10). What we actually can observe on the curves is that the force does not return to its initial value, but to a negative value (*i.e.*, the backstress).

To try to improve our model, we propose a hypothesis for the attaching springs that we will develop hereinafter.

Thus, we cannot obtain the backstress if the springs attach at their initial stress. This stress being an elastic one, it is always positive for a given positive strain. To get the negative stress we need to have a negative strain because the only supposed measured stress is the elastic one. There is no physical reason for a spring to attach at the same stress as before the detachment. If the spring represents the cytoskeleton then we can imagine that the spring's detachment corresponds to the cytoskeleton flow. When it reassembles again, we can assume that it is at zero strain, implying a zero elastic stress.

Now, when the springs reattach during the decreasing strain phase, having the same no-load length, they will be subjected to a negative strain and thus create a negative elastic stress that can explain the backstress in the curves.

We make the assumption that the reattachments take place spontaneously. Fig. 4.26 presents a cartoon to explain these different steps.

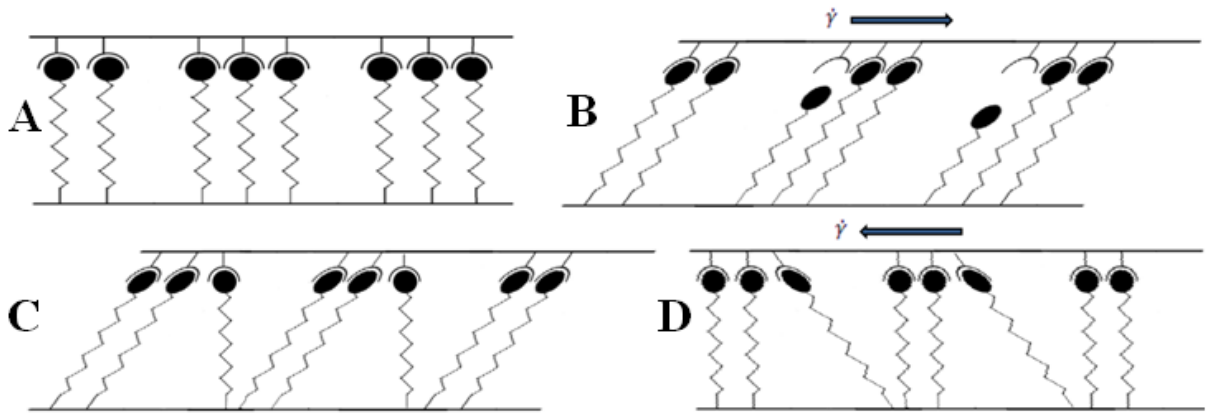

Fig. 4.26: *Cartoon of the parallel springs model summarizing the different steps during one deformation cycle. (A) Initially, the system is only composed by parallel springs with the same no-load length. When shearing, a number of springs can detach (B) and then reattach at zero deformation (C). In the second part of the cycle, when the strain decreases, the springs attached earlier, at zero deformation, will create a negative elastic stress, which can account for the backstress.*

Compared to the simpler model presented before where we used only differential equations, for this version we also use a Monte Carlo simulation process.

Now, each spring has its own deformation denoted γ_i, that can be different from spring to spring, depending on the spring's detachment and reattachment history.

In this scenario, the time is binned and for each time step the deformation of the spring γ_i is updated to $\gamma_i + \dot{\gamma}dt$ (here, $\dot{\gamma}$ is the same shear rate as described for the previous version of the model).

For each time step *dt*, each spring has a probability to detach and the rate of detachment is given by $\frac{dN}{dt} = -N * P_r$, with $P_r = \frac{1}{\tau_0}\exp(\frac{|\gamma_i|}{\xi})$. We use an absolute value in the exponential because we model a tensorial shear with a scalar model and there is no physical difference between a negative shear stress and a positive one. For the sake of simplicity, in our model we will note $\frac{1}{\tau_0}$ with *A*. Thus, the larger *A* is, the easier it is for the springs to detach.

For each time step, each detached spring has a constant probability *B* to reattach at zero deformation and the reattachment could be a signature of the mean time for the reorganization of the cytoskeleton.

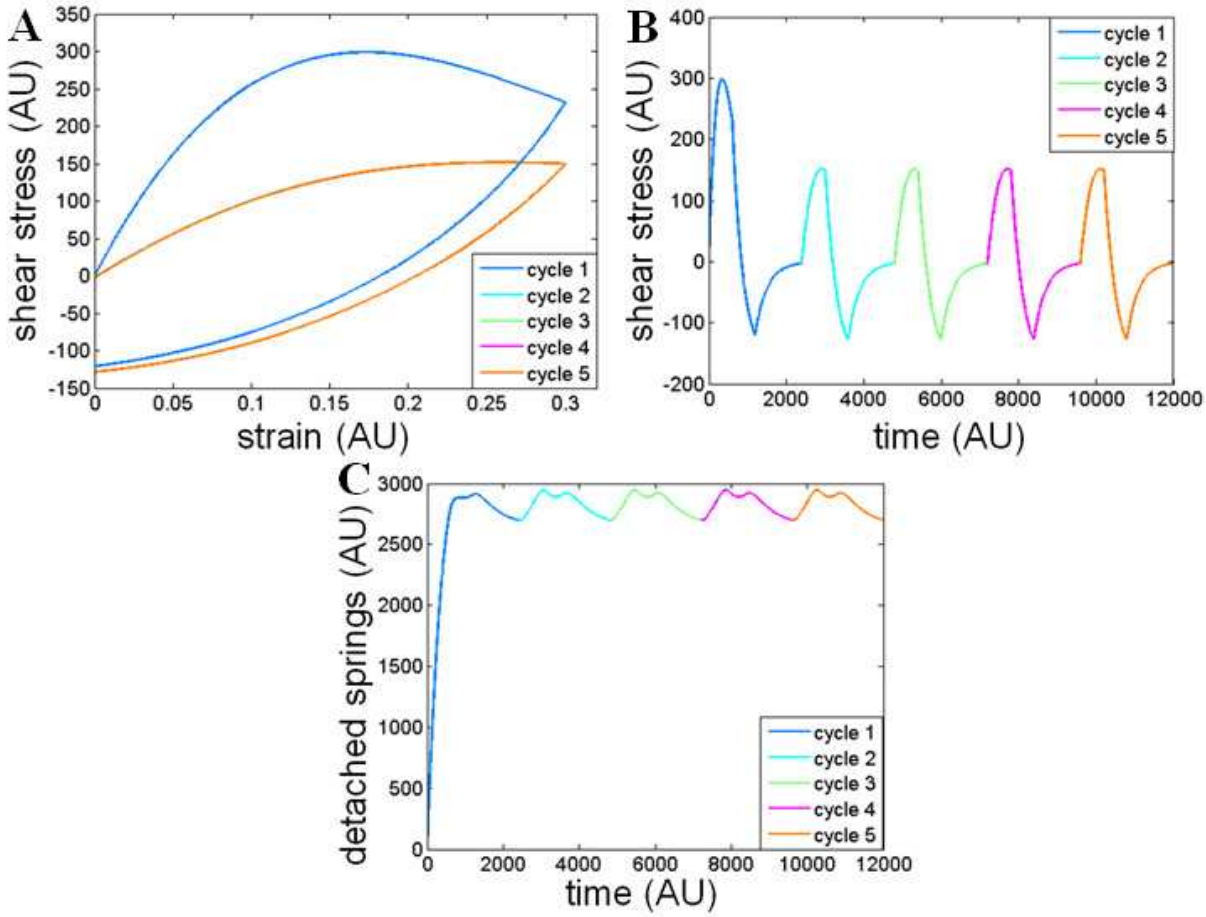

Fig. 4.27: *(A) Evolution of the stress as a function of strain in arbitrary units for the first five cycles {A = 2*10^{-3}; B = 1*10^{-3}; ξ = 0.35; N_0 = 4000}. (B) Evolution of the stress as a function of time in arbitrary units for the first five cycles {idem}. (C) Evolution of the number of detached springs as a function of time in arbitrary units during the first five deformation cycles {idem}.*

We define the number of broken springs by the following equation:

$N_0 - N_{attach} = N_r$, where N_0 is the initial number of operating springs and N_{attach} is the number of repaired springs. The evolution of the number of broken springs is represented in (Fig. 4.27 C), where we plot according to the model, in arbitrary units, the number of detached springs as a function of time. This number decreases when the strain decreases.

The parameters introduced in the model are A, B, ξ. The ratio between A and B determines the ratio between the amplitude of the first stress cycle and the next one, while ξ influences the shape of the rheological curves representing the stress. We show the influence of these parameters in Fig. 4.28.

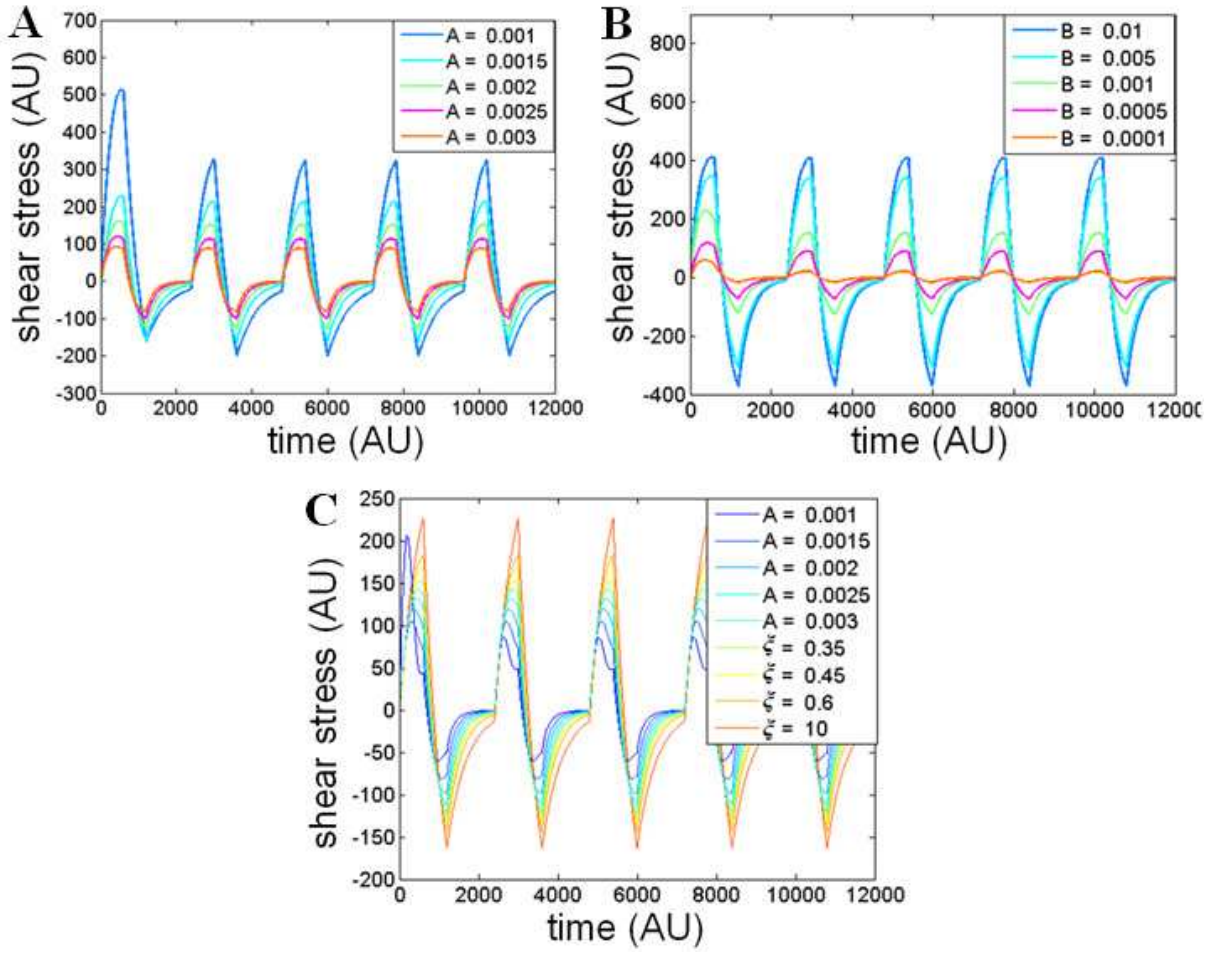

Fig. 4.28: *Influence of the different parameters of the model on the evolution of the stress as a function of time in arbitrary units for the first five cycles. In (A) we vary A for* $B = 1*10^{-3}$ *and* $\xi = 0.35$. *In (B) we vary B for* $A = 2*10^{-3}$ *and* $\xi = 0.35$. *In (C) we vary A and* ξ *for* $B = 1*10^{-3}$.

With this model we are able to describe the backstress and also the relaxation between two cycles. Thus, it captures most of the physical important parameters we wanted to investigate.

If we use the model to fit one of our rheological curves, we can see in Fig. 4.29 that the experimental stress has a similar shape as the one given by the model.

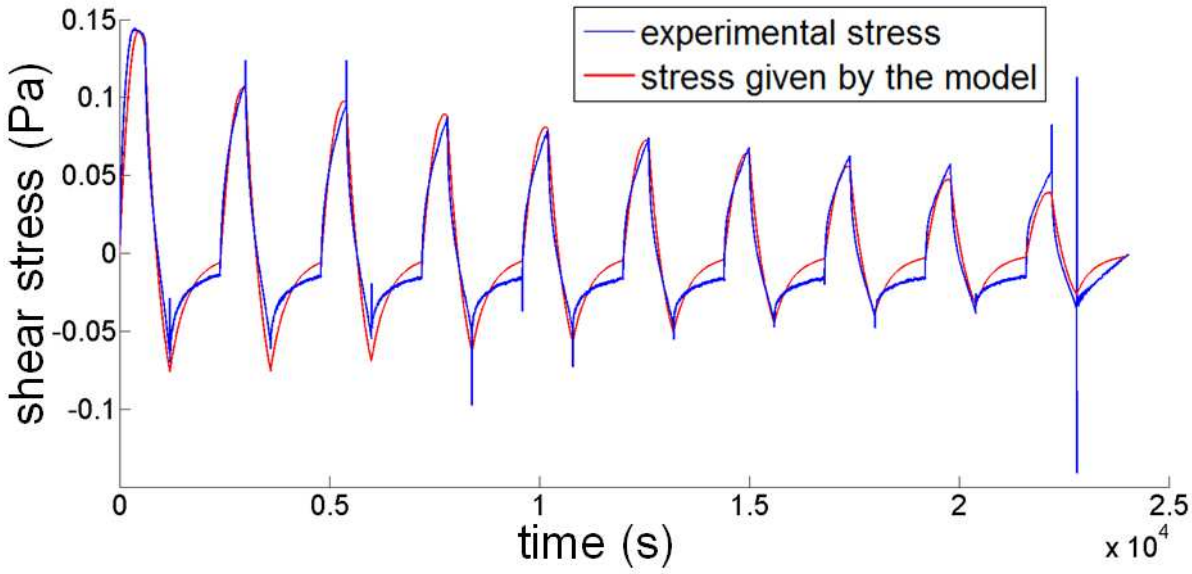

Fig. 4.29: *Fit of the rheological curve previously presented in Fig. 4.11 A, using the model of parallel springs that break and reattach at zero deformation. Here, a new term which models the apoptosis process is added. In blue we represent the experimental stress and in red, the stress given by the model.*

The shapes of the rheological curves presented in subsection 4.3 makes us state that this simple model of springs that may stretch and break can also be used to explain the behavior of aggregates treated with different drugs acting on the cytoskeleton of the cells, meaning that it allows us to cover all aspects of a controlled shear rate.

4.4.5 Back to controlled shear stress experiments

All the experimental results can be very well interpreted using our simple model. We also have to take into account the experimental "imperfections" of our system (such as meniscus and inertia effects).

Let's go back first to the experiments where a null stress was applied in between pulses. The increasing residual strain observed in between pulses can very well be explained, if the small elastic torque of the meniscus is taken into account. In this case:

$$\sigma_{rheo} = \sigma_{agg} + \sigma_{meniscus} = 0$$

If $|\sigma_{meniscus}|$ is inferior to the yield stress then $\gamma = -\frac{\sigma_{meniscus}}{Nk} = cte$ and will be increasing during the experiment as N is decreasing while stress pulses are imposed on aggregates (see Fig. 4.6).

If $|\sigma_{meniscus}|$ is superior to the yield stress then γ will be also increasing in between pulses. We also observed this situation (see Fig. 4.30).

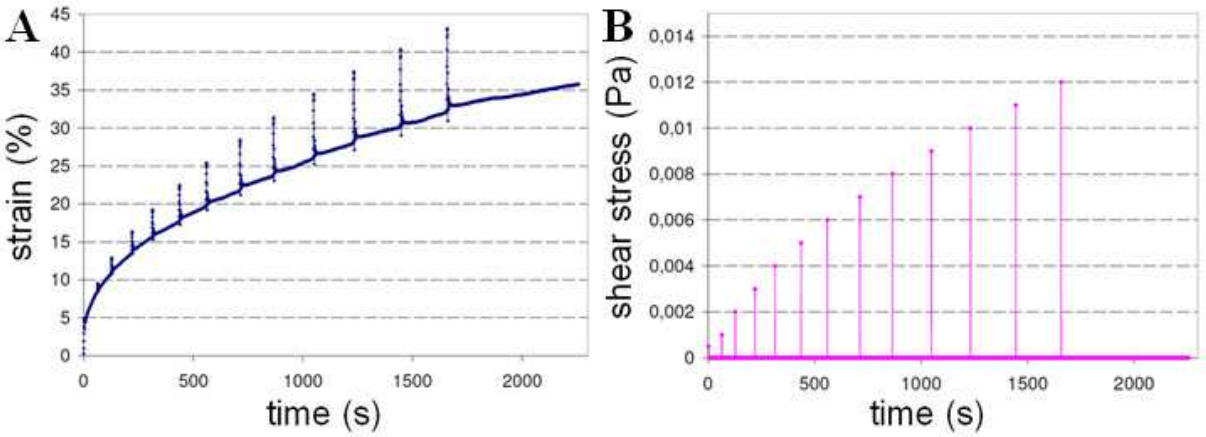

Fig. 4.30: *(A) The evolution of strain when applying increasing shear stress pulses (3 seconds) for a zero stress of variable duration imposed between two pulses. (B) Imposed increasing shear stress pulses. Note that during the period the stress returned to zero, the strain is constantly increasing.*

Considering now what is happening during pulses, two different slopes (see Fig. 4.8 B) are observed when the yield stress is passed. As already explained, to model the first slope one would have to take into account the rheometer inertia and the second slope could be very well modeled by our equations. In conclusion, this set of data could also easily be used to constrain the model and to fit the parameters of our model. That is what we plan to do, in the next following months.

4.4.6 Open questions - Influence and modeling of cell division

Another important point we have to take into consideration is that during each experiment the spacing between the plates remains constant and we estimate there is a non-negligible change in the volume of the sample, as cell division occurs at large timescales (see in Fig. 4.31).

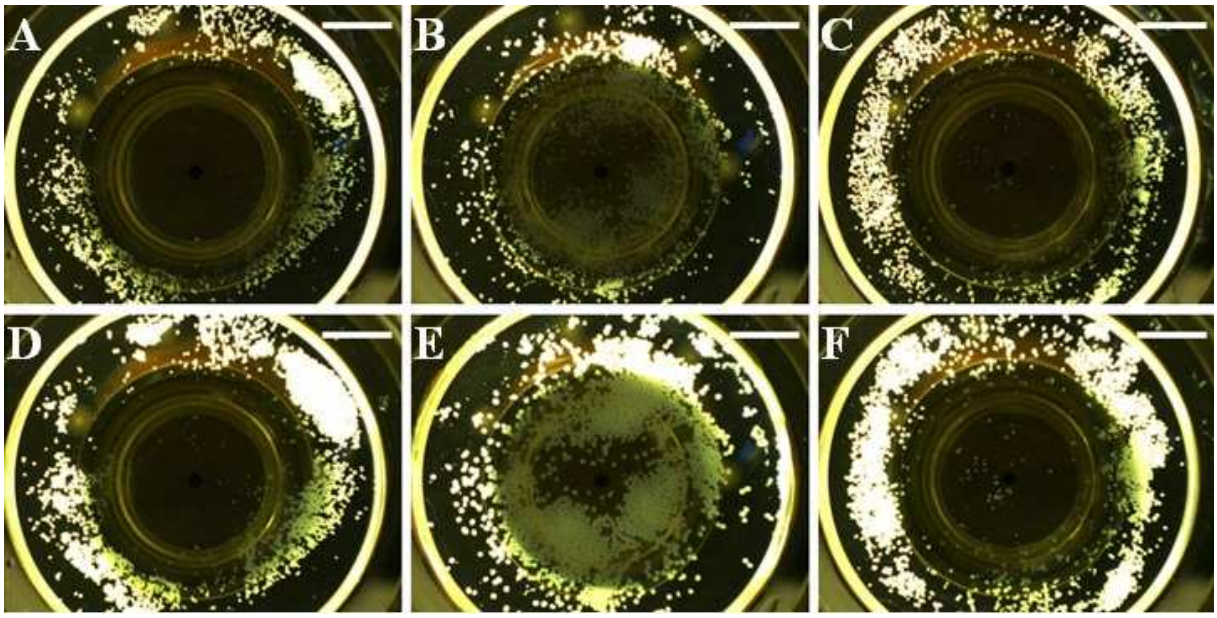

Fig. 4.31: *Different depositions of aggregates between the two parallel plates, all corresponding to a gap of 250 μm. The aggregates are surrounded by the CO_2 independent medium and the evaporation of the medium is avoided by adding a mineral oil ring. The images A-C correspond to the beginning of the experiment and the images D-F correspond to approximately 24 hours after. A certain difference regarding the shape and volume of the sample can be noticed between the two stages. Scale bars, 1 cm.*

Thus, depending on the duration of an experiment, any proposed physical model has to handle the effects of aggregate's growth due to cell division within each aggregate. Indeed, one of the advantages of our model is that it allows us to easily include the cell division process by adding the division rate to the initial number of operating springs.

4.5 Analogy to rheology of classical complex fluids

4.5.1 Carbopol polymers - Results of controlled shear rate experiments

We also wanted to compare our biological system to another system, a passive one, and we chose to study in a little extent the Carbopol, which is a non-aging suspension of micro-gel-based polymer (Fig. 4.32).

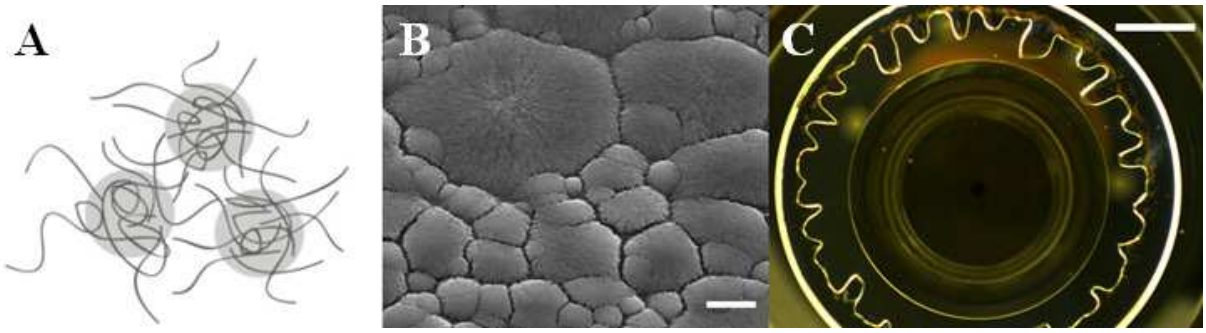

Fig. 4.32: *(A) Patterns of the microstructures of a polymer micro-gel. (B) Carbopol $(C_3H_4O_2)_n$ imaged by scanning electron microscopy (SEM)* [27]*. Scale bar, 5 µm. (C) Sample of Carbopol between the two parallel glass plates of the rheometer while performing the gap (approaching the surfaces). Once the desired gap is reached, the finger-like shape is no longer present, the Carbopol taking a spread configuration with a ring-shaped outline. Scale bar, 1 cm.*

The choice was made taking into consideration the fact that, as previously mentioned, the Carbopol is widely used in literature as a viscoplastic fluid model [27–30] well described by the Herschel-Bulkley's law. It is well known to possess a yield stress beyond a critical concentration (see subsection 4.1.1.2) and also, it is relatively easy to prepare and to obtain a large range of rheological parameters only by adjusting its polymer concentration.

Thus, we performed the controlled shear rate experiments on a sample of Carbopol 1% which was prepared the same day (see the appendix for preparation protocol). These experiments were conducted in collaboration and with the great support of Pr. Catherine Barentin and Baudouin Geraud from LPMCN.

We estimated the gap between the two glass surfaces at 300 µm, by averaging the values we usually impose for our aggregates. We also had to preshear our sample at 500 s^{-1} for 1 minute, in both directions (clockwise and counter clockwise) in order to make it homogeneous. The experiments are performed at temperatures of approximately 25 °C.

When representing the shear stress as a function of strain (Fig. 4.33) we can observe that qualitatively, we recover the first different cycle, followed by the nine next ones describing the limit cycle, which resemble to the usually obtained rheological curves for biological aggregates. The phenomenon of backstress is also present.

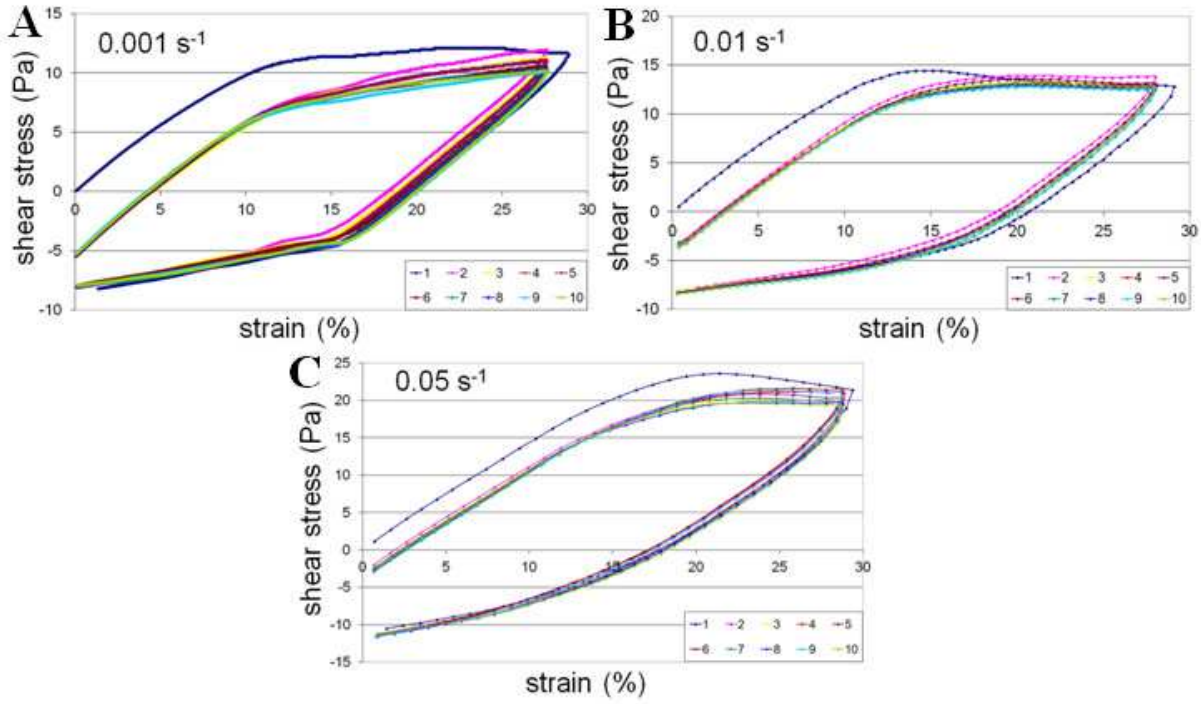

Fig. 4.33: *Shear stress as a function of strain for every cycle for Carbopol 1%. As usual, the same parameters have been used for the experiments at each value of shear rate.*

An interesting feature that we can observe when we plot the shear stress as a function of time (Fig. 4.34) for the Carbopol 1% is that the relaxation process during the 10 minutes describes a qualitatively different relaxation curve that the one obtained with cell aggregates (Fig. 4.34 D). This is typical for the Carbopol as it behaves the same on compression-relaxation experiments also (data not shown), showing different reproducible dynamics with a sequence of different relaxation times and plateaus (possibly explained by broken weak bonds inside the structure).

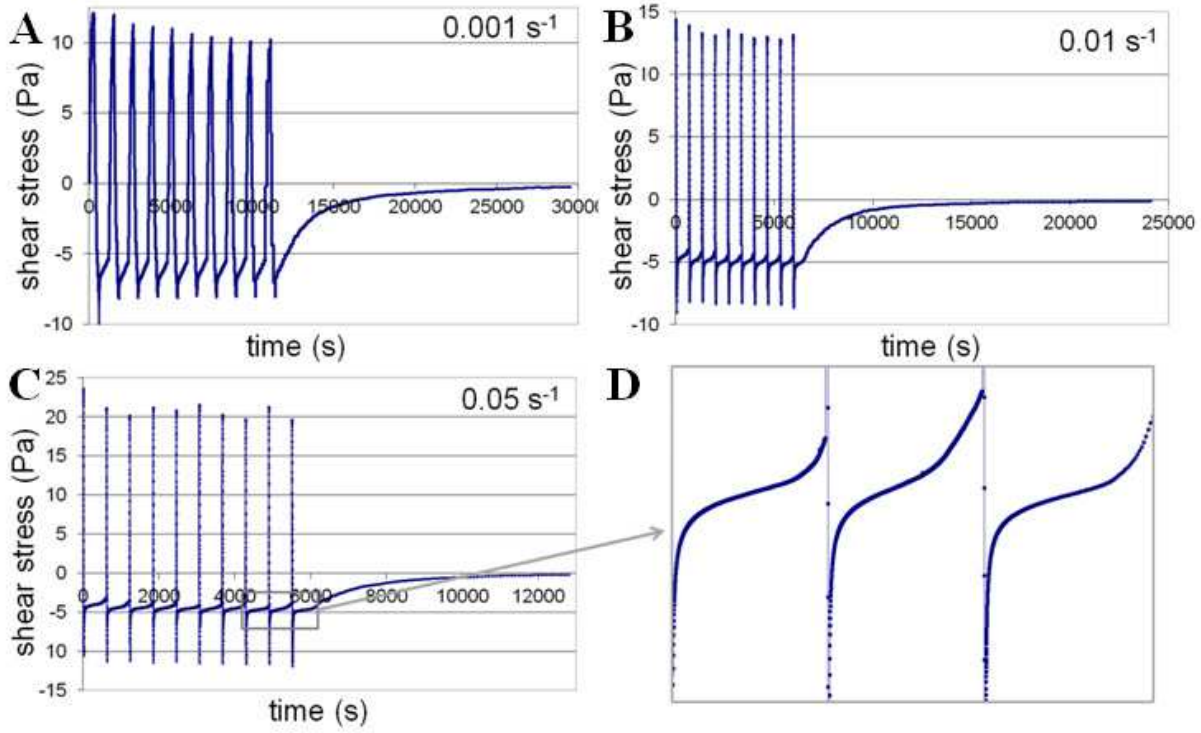

Fig. 4.34: *Shear stress as a function of time for every cycle for Carbopol 1%. In (A-C) we represent the rheological curves obtained for the usual parameters. The shape of the ten minutes relaxation curve is different than for our biological system. (D) Zoom of (C), here, the Y axis corresponds to a shear stress from -6.4 up to -3.6 Pa, and the X axis corresponds to a time from 4300 up to 6200 seconds.*

Overall, we can see that between an active (cell aggregates) and a passive (Carbopol) system, the response to deformation is quite similar, as we probe both elasticity and plasticity, depending on the timescales and the amplitude of the deformation.

4.6 Conclusions

We have shown in this chapter, that we could obtain information on cell rheology while shearing aggregates using a commercial rheometer.

We have obtained an overall picture, showing that cells are stress softening elements on the timescale of seconds to minutes and hours, which is in complete agreement with the experiments done by the group of Fredberg [5]. We only were able to observe some stiffening signature for high strain amplitudes and with the fastest shear rate used for this experiment. It would be interesting to go even faster or to make experiments at smaller temperature. However, the timescales used (s to min and hours) are the one relevant for cellular movements. The softening process entails that the protocol history serving to probe cell rheology is of high importance. This means that to obtain reproducible results we need to

know from which state we are departing from (for example we waited at least two hours before beginning any experiments). This kind of information is often missing in many rheological tests on cells.

Moreover, we showed that sometimes several hours were often necessary to obtain a complete relaxation of our sample. This makes experiments quite long and requires protocols that maintain cells in good shape for several hours.

We also presented the first measurement of a yield strain for cells, which is of course very small ($\gamma \sim 4\%$). This shows the great sensitivity of our technique.

Finally, we proposed a very simple model to explain this softening behavior: aggregates are made of parallel springs which will break under loading.

We plan now to try to make a clear distinction between the intracellular plasticity and intercellular ones (we indeed think that we get a signature of these processes at very low frequencies). The final goal would be to try to understand what is the "aggregate" viscosity we have measured in fusion experiments, and what is its physical origin.

References:

1. Lee, D. *et al.* Investigating the microstructure of a yield-stress fluid by light scattering. *Physical Review E* **83**, 1–8 (2011).

2. Desprat, N., Richert, A., Simeon, J. & Asnacios, A. Creep function of a single living cell. *Biophysical journal* **88**, 2224–33 (2005).

3. Wertheim, M. G. Mémoire sur l'élasticité et la cohésion des principaux tissus du corps humain. *Extr. des Annales de chimie* **21**, 385–415 (1847).

4. Fernández, P., Pullarkat, P. a & Ott, A. A master relation defines the nonlinear viscoelasticity of single fibroblasts. *Biophysical journal* **90**, 3796–805 (2006).

5. Trepat, X. *et al.* Universal physical responses to stretch in the living cell. *Nature* **447**, 592–5 (2007).

6. Stamenović, D. *et al.* Rheological behavior of living cells is timescale-dependent. *Biophysical journal* **93**, L39–41 (2007).

7. Ito, S. *et al.* Viscoelastic and dynamic nonlinear properties of airway smooth muscle tissue: roles of mechanical force and the cytoskeleton. *American journal of physiology. Lung cellular and molecular physiology* **290**, L1227–37 (2006).

8. Kollmannsberger, P. Nonlinear microrheology of living cells. (2009).

9. Kollmannsberger, P., Mierke, C. T. & Fabry, B. Nonlinear viscoelasticity of adherent cells is controlled by cytoskeletal tension. *Soft Matter* **7**, 3127 (2011).

10. Kollmannsberger, P. & Fabry, B. Linear and Nonlinear Rheology of Living Cells. *Annual Review of Materials Research* **41**, 75–97 (2011).

11. Xu, J., Tseng, Y. & Wirtz, D. Strain hardening of actin filament networks. Regulation by the dynamic cross-linking protein alpha-actinin. *The Journal of biological chemistry* **275**, 35886–92 (2000).

12. Ewoldt, R. H., Hosoi, A. E. & McKinley, G. H. Nonlinear viscoelastic biomaterials: meaningful characterization and engineering inspiration. *Integrative and comparative biology* **49**, 40–50 (2009).

13. Semmrich, C. *et al.* Glass transition and rheological redundancy in F-actin solutions. *Proceedings of the National Academy of Sciences of the United States of America* **104**, 20199–203 (2007).

14. Semmrich, C., Larsen, R. J. & Bausch, A. R. Nonlinear mechanics of entangled F-actin solutions. *Soft Matter* **4**, 1675 (2008).

15. Broedersz, C. P. *et al.* Measurement of nonlinear rheology of cross-linked biopolymer gels. *Soft Matter* **6**, 4120 (2010).

16. Ewoldt, R. H. & Mckinley, G. H. Creep Ringing in Rheometry or How to Deal with Oft-discarded Data in Step Stress Tests! *Rheology* **76**, (2007).

17. Fernández, P. & Ott, A. Single Cell Mechanics: Stress Stiffening and Kinematic Hardening. *Physical Review Letters* **100**, 2–5 (2008).

18. Nabarro, F. R. . The time constant of logarithmic creep and relaxation. *Materials Science and Engineering: A* **309-310**, 227–228 (2001).

19. Pichler, C. & Lackner, R. Identification of Logarithmic-Type Creep of Calcium-Silicate-Hydrates by Means of Nanoindentation. *Strain* **45**, 17–25 (2009).

20. Wolff, L., Fernández, P. & Kroy, K. Resolving the stiffening-softening paradox in cell mechanics. *PloS one* **7**, e40063 (2012).

21. Marmottant, P. *et al.* The role of fluctuations and stress on the effective viscosity of cell aggregates. *Proceedings of the National Academy of Sciences of the United States of America* **106**, 17271–5 (2009).

22. Kramers, H. A. Brownian motion in a field of force and the diffusion model of chemical reactions. *Physica* **7**, 284–304 (1940).

23. Eyring, H. The Activated Complex in Chemical Reactions. *The Journal of Chemical Physics* **3**, 107 (1935).

24. Bell, G. Models for the specific adhesion of cells to cells. *Science* **200**, 618–627 (1978).

25. Evans, E. & Ritchie, K. Dynamic Strength of Molecular Adhesion Bonds. **72**, (1997).

26. Beysens, D. A., Forgacs, G. & Glazier, J. A. Cell sorting is analogous to phase ordering in fluids. *Proceedings of the National Academy of Sciences* **97**, 9467–9471 (2000).

27. Piau, J. M. Carbopol gels: Elastoviscoplastic and slippery glasses made of individual swollen sponges. *Journal of Non-Newtonian Fluid Mechanics* **144**, 1–29 (2007).

28. Oppong, F., Rubatat, L., Frisken, B., Bailey, A. & de Bruyn, J. Microrheology and structure of a yield-stress polymer gel. *Physical Review E* **73**, 1–9 (2006).

29. LUU, L.-H. & FORTERRE, Y. Drop impact of yield-stress fluids. *Journal of Fluid Mechanics* **632**, 301 (2009).

30. Divoux, T., Tamarii, D., Barentin, C. & Manneville, S. Transient Shear Banding in a Simple Yield Stress Fluid. *Physical Review Letters* **104**, 1–4 (2010).

Conclusions and perspectives

This thesis focused on the experimental study of physical properties and biomechanics of embryonic cell aggregates. Before drawing general conclusions, we are listing the main results of this work roughly by order of appearance in this manuscript (in bold) and give for each of them some perspectives.

Summary of the results and perspectives

(i) In chapter 3 we showed that a tunable tissue surface tension (TST) and viscosity can be achieved easily through the control of cell-cell contractility compared to cell-medium one. Moreover we showed that α-catenin is crucial for this regulation to occur: these molecules appear as a catalyser for the remodeling of the actin cytoskeleton underneath cell-cell contact, enabling a differential contractility between the cell-medium and cell-cell interface to take place.

By combining TST measurements, angle measurements at the aggregate surface and modification of contractile properties of cells by properly chosen drugs or knockout mutants, we have seen that our data were fully compatible with the DITH framework (Differential Interfacial Tension Hypothesis, [1–4]). We could hence obtain all cell surface important parameters: cortical tensions *T* and adhesive energy *J*. No other experience so far does give access to such measurements.

This work confirms the remarkable robustness of TST measurements. Of course, it will be interesting to also compare our method (compression plate apparatus) to other methods. Angle estimates as performed in chapter 3 were also very preliminary. For that, we used images of cross-sections of aggregates that were unfortunately not performed initially for such a purpose (actually it was to have an idea of the internal cellular structure of aggregates). It will be necessary to take more images in order to perform a truly statistical analysis of angle distribution for every cell line and drug used. As we could obtain all DITH parameters, it will be interesting to really test the robustness of this method by performing independent measurements of cell-medium cortical tension T^c_{CM}. T^c_{CM} is indeed measurable by AFM [4] or with micropipettes [5]. Perhaps in that case, absolute values of tension could differ from one to

another method, but the ratio between different situations (in the presence or absence of drug) should be comparable.

(ii) We have also seen that both surface tension and fluidity were very dependent on contractility (fluidity was as well very dependent on temperature), and that α-catenin was essential for this fine tuning of the macroscopic parameters.

It would now be very interesting to study in details the biological pathway (involving α-catenin) which enables the restructuration and the control of the actin network underneath the membrane by the triggering of cadherin-cadherin adhesion.

We have also shown that viscosity values are neither proportional to surface tension, nor to the adhesive energy *J*. They cannot therefore be explained by simple models with only cell-cell detachment as a main ingredient. Cell motion within aggregate might also be limited by other mechanisms such as cytoskeleton dynamics. Here, one can expect that numerical simulations such as the extended Potts model [6], may help to understand how to generate cell viscosity values not strictly dependant on cell-cohesion. Detailed and systematic observations with 2-photon confocal microscopy will also give a better view of the kind of cell movements actually occurring in 3D. Preliminary observations during the fusion of two aggregates were performed in the team (PhD thesis of A. Mgharbel). We have also started to get recording of "Brownian" motion in 3D. An analysis of hydra cells in 2D was performed several years ago in the team [7] but in 3D, at least with the current cell line used (F9 cells), movements are much slower and seem mostly arising from cell divisions. Another long dated idea to continue the parallel with the physics of colloidal systems is to analyze a few magnetic cells inside an aggregate under a gradient of magnetic field. If their distribution is initially homogeneous they should move due to the gradient over time and one may expect differences depending on the status of the cell (parents or mutants, with or without drugs).

(iii) An important contribution of this work was also to get a rheological characterization of embryonic tissues by studying the stress-strain relationship when applying shear to sets of several hundred or even thousands of cell aggregates. We showed that at low deformations and short timescales, we are able to probe the mean intracellular rheology, while at large deformations and long timescales one begins to found the signature of intercellular reorganizations.

We believe that our large amount of data brings robust (ensemble averaged) information on both single cell rheology and cell-cell rearrangements. This work opens therefore interesting perspective to study at low deformations and relatively fast shear rate the single cell rheology of virtually any cell type as for most cell types it is possible to prepare cell aggregates.

(iv) On the basis of our results, we proposed a model of parallel springs that under deformation can detach and reattach at zero strain. This simple model can very well reproduce the behavior of our aggregates when submitted to different stresses (controlled shear rate or controlled shear stress experiments).

As a perspective, observations by 2-photon microscopy of cellular reorganizations inside a single sheared cell aggregate (or several) can be performed in order to get a clearer image of the parameters playing a role in the final response of cell aggregates while being subjected to shear.

Conclusions and general perspectives for the use of aggregates for science and biomedical applications

A very satisfactorily result of this thesis is the robustness and reproducibility of measurements with cell aggregates, especially TST measurements but also rheological ones and viscosity measurements to a less extend. Results were very similar to those obtained by Abbas Mgharbel three years before; they did not changed as well when we had to ask new cell vials to our generous suppliers after accidents (Akira Nagafuchi, Nara, Japan and Daniel Riveline, Strasbourg). For anyone working with single cells, reproducibility and large dispersion of the results is often a serious limitation to quantitative measurements. Aggregates are therefore very attractive because their properties depend on the average of thousands cells.

Together with the fact that aggregates mimic better the 3D living environment than single cells on plastic Petri dishes, aggregates have attracted many biologists for the purpose of answering fundamental questions on development, oncology or for biomedical applications (tissue engineering, drug screening, replacement of animal testing…). Surely, the aggregate technology is ready to be transferred to High-throughput screening experiments such as Lab-on-chip and large microfluidic or millifluidic devices.

For the physicist of soft matter, complex fluids, cellular aggregates are especially appealing because they are composed of unit cells that possess their own mobility (effective temperature) that can be tuned by drugs or simply by the thermal temperature, they can be in principle stained and tracked in 3D and also because they are robust. The community of biophysicists and non-linear physicists would certainly have high interest in developing comparative studies on these very interesting “materials” which are cellular aggregates.

1. Harris, A. K. Is cell sorting caused by differences in the work of intercellular adhesion? A critique of the Steinberg hypothesis. *Journal of Theoretical Biology* **61**, 267–285 (1976).

2. Graner, F. Can surface adhesion drive cell-rearrangement? Part I: Biological cell-sorting. *Journal of theoretical biology* **164**, 455–455 (1993).

3. Brodland, G. W. The Differential Interfacial Tension Hypothesis (DITH): A Comprehensive Theory for the Self-Rearrangement of Embryonic Cells and Tissues. *Journal of Biomechanical Engineering* **124**, 188 (2002).

4. Krieg, M. *et al.* Tensile forces govern germ-layer organization in zebrafish. *Nature cell biology* **10**, 429–36 (2008).

5. Hochmuth, R. M. Micropipette aspiration of living cells. *Journal of biomechanics* **33**, 15–22 (2000).

6. Graner, F. & Glazier, J. A. Graner, Glazier - 1992 - Simulation of biological cell sorting using a two-dimensional extended Potts model.pdf. *Physical Review Letters* **69**, 2013–2016 (1992).

7. Rieu, J. P., Upadhyaya, A., Glazier, J. A., Ouchi, N. B. & Sawada, Y. Diffusion and Deformations of Single Hydra Cells in Cellular Aggregates. *Biophysical Journal* **79**, (2000).

Appendix

Supplementary experimental rheological curves and Carbopol preparation protocol

I. Extreme values of shear rate for controlled shear rate experiments (see 4.3)

a) Too fast: too noisy

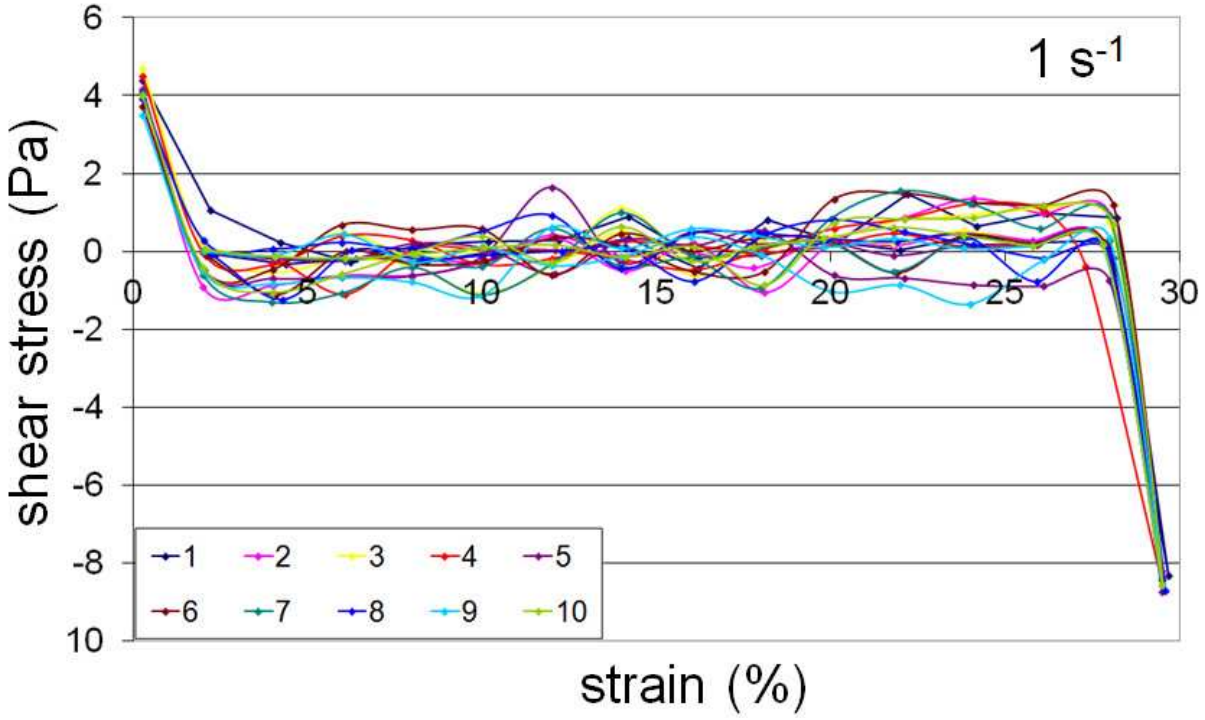

Fig. A.1: *Noisy signal when representing shear stress as a function of strain for F9 WT cell aggregates in a controlled shear rate experiment. The ten cyclic loadings are performed at 1* s^{-1}.

b) Too slow: cell death

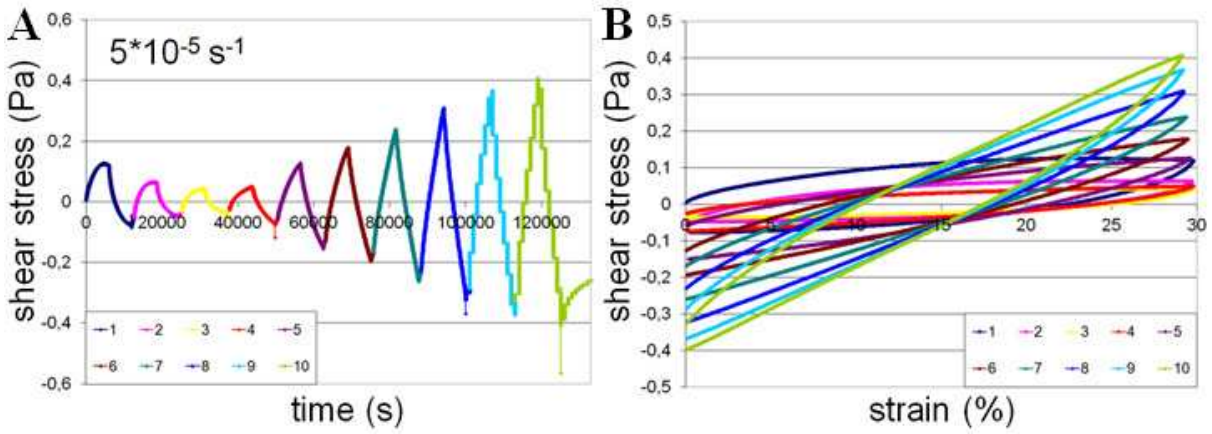

Fig. A.2: *(A) Shear stress as a function of time for F9 WT cell aggregates in a controlled shear rate experiment. The ten cyclic loadings are performed at* $5*10^{-5}s^{-1}$. *Starting from the* 5^{th} *cycle (dark mauve), cell death could explain the significant increase in amplitude of shear stress. (B) Shear stress as a function of strain for the same experiment.*

II. Latrunculin A effect on F9$^{(\alpha-/-)}$ cell aggregates: same effect as on F9 WT cell aggregates (see Fig. 4.16)

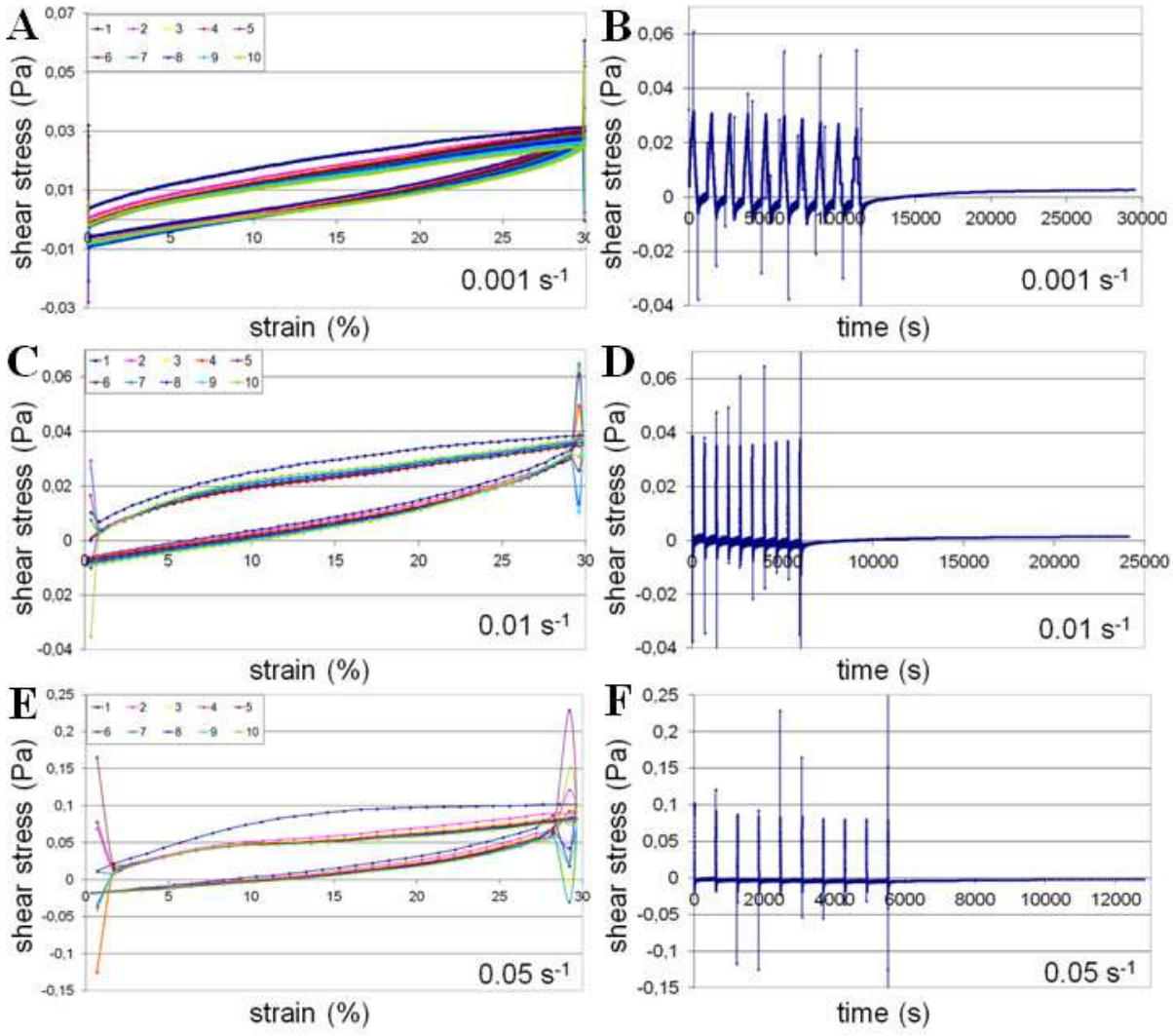

Fig. A.3: *Shear stress as a function of strain (left column) and as a function of time (right column) for F9$^{(\alpha-/-)}$ cell aggregates exposed to 1 µM latrunculin A.*

III. Controlled shear rate experiments – large deformations (see 4.3.6)

a) Time dependence for F9 WT cell aggregates

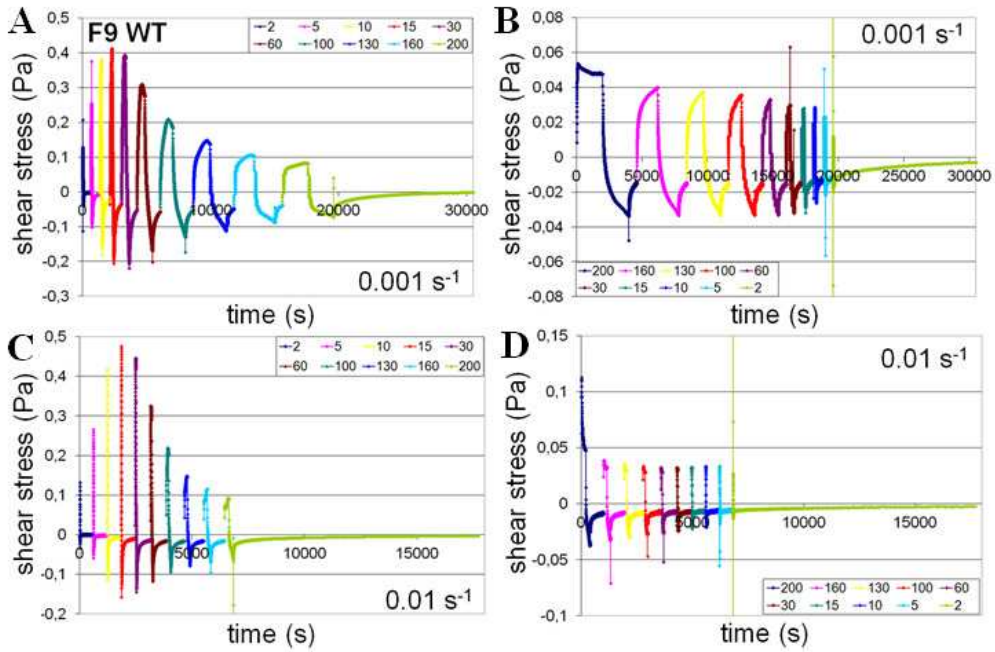

Fig. A.4: *F9 WT cell aggregates response (shear stress as a function of time) to increasing (A and C) and decreasing (B and D) strain for different values of shear rate (i.e., 0.001 s^{-1}(A-B) and 0.01 s^{-1}(C-D)).*

b) Time dependence for $F9^{(\alpha-/-)}$ cell aggregates

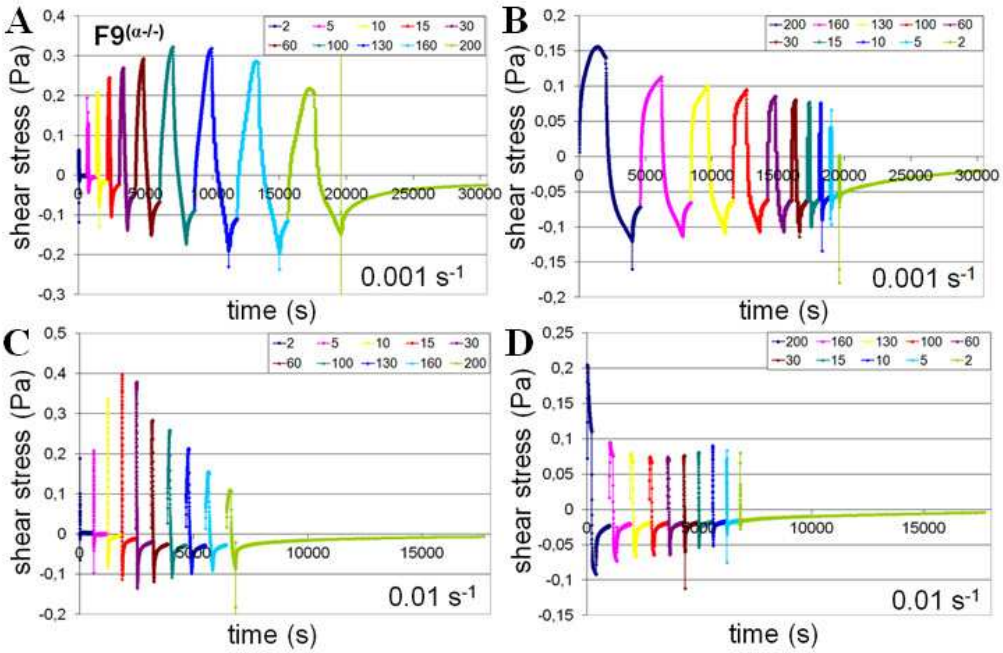

Fig. A.5: *$F9^{(\alpha-/-)}$ cell aggregates response (shear stress as a function of time) to increasing (A and C) and decreasing (B and D) strain for different values of shear rate (i.e., 0.001 s^{-1}(A-B) and 0.01 s^{-1}(C-D)).*

c) Time dependence for F9 WT cell aggregates exposed to 10 µM Y-27632

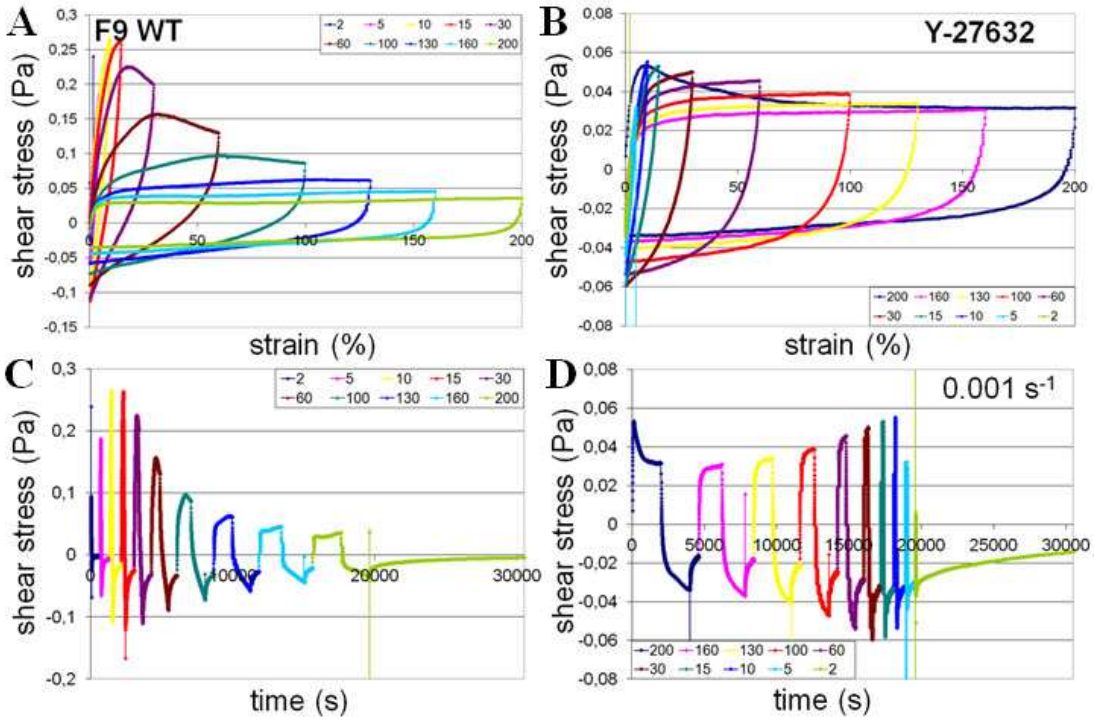

Fig. A.6: *F9 WT cell aggregates response to increasing (A and C) and decreasing (B and D) strain for a 0.001 s^{-1} shear rate when treated with 10 µM Y-27632.*

d) Time dependence for F9 WT cell aggregates exposed to 1 µM nocodazole

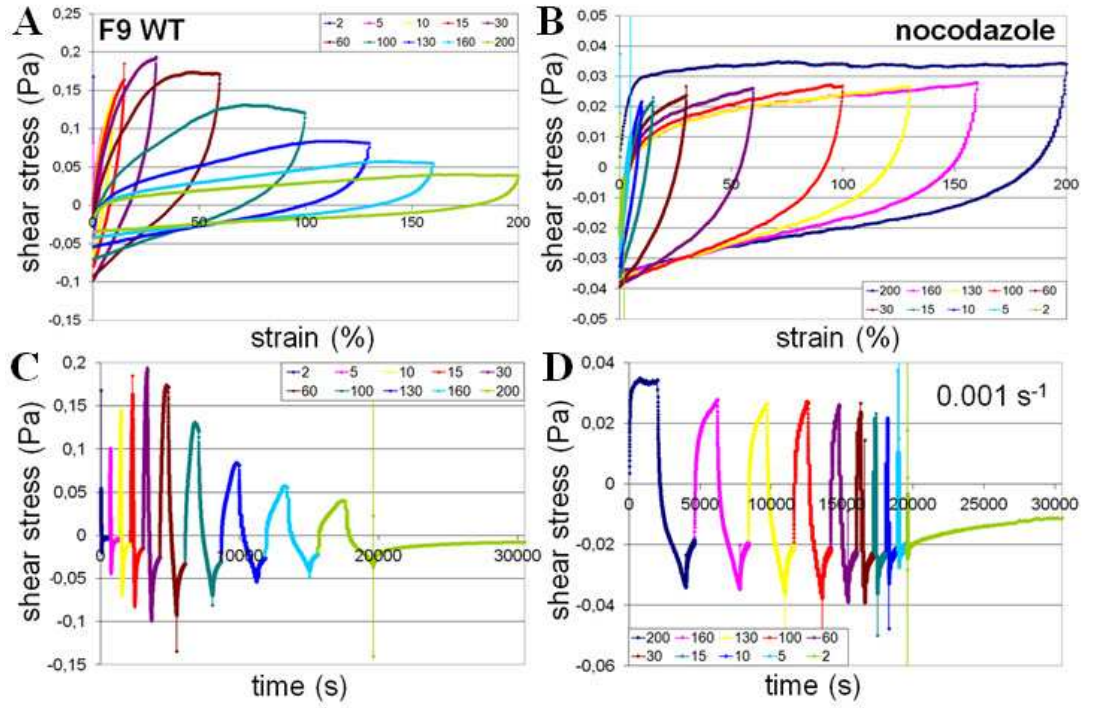

Fig. A.7: *F9 WT cell aggregates response to increasing (A and C) and decreasing (B and D) strain for a 0.001 s^{-1} shear rate when treated with 1 µM nocodazole.*

e) Time dependence for F9$^{(\alpha-/-)}$ WT cell aggregates exposed to 10 µM Y-27632

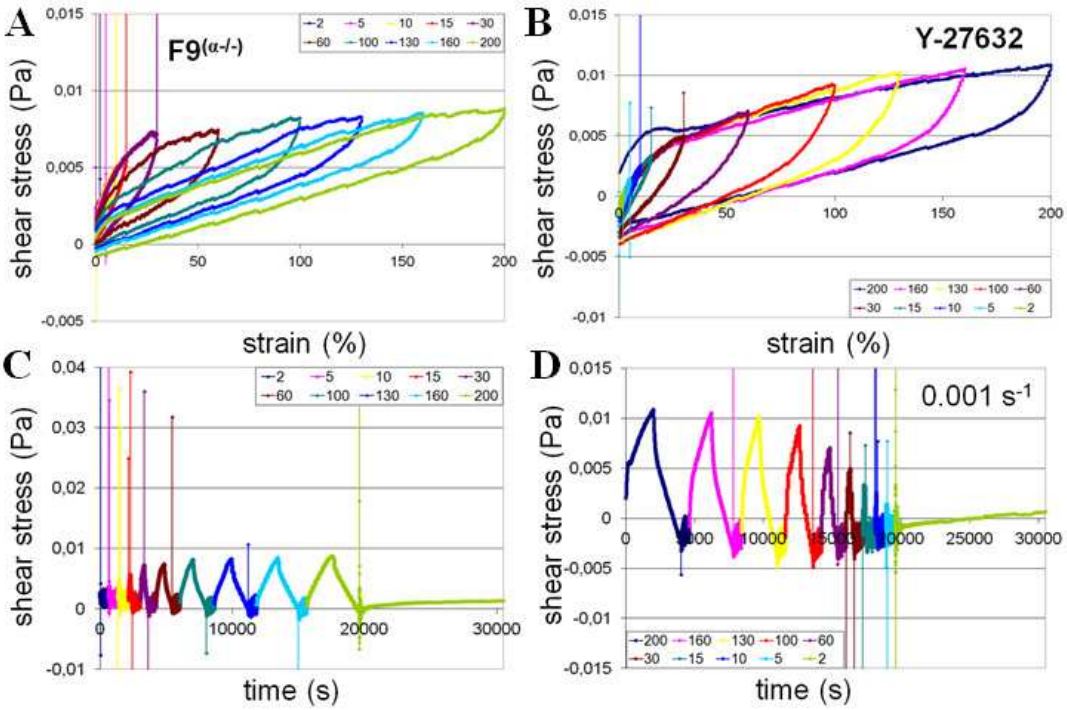

Fig. A.8: *F9$^{(\alpha-/-)}$ cell aggregates response to increasing (A and C) and decreasing (B and D) strain for a 0.001 s^{-1} shear rate when treated with 10 µM Y-27632.*

f) Time dependence for F9$^{(\alpha-/-)}$ WT cell aggregates exposed to 1 µM nocodazole

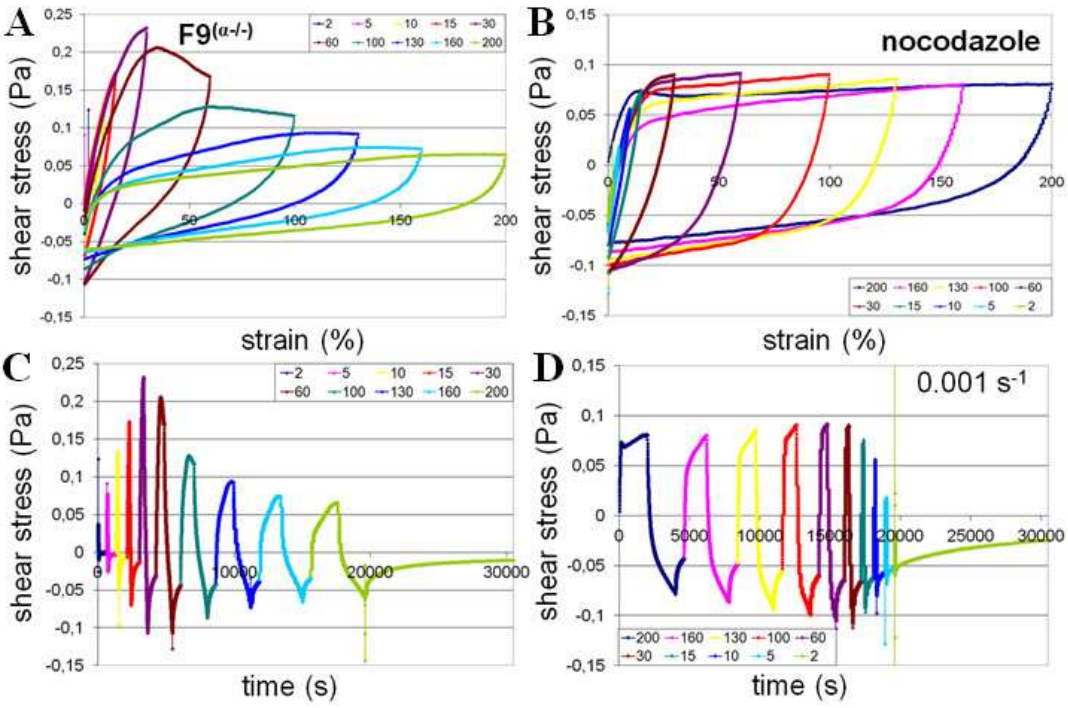

Fig. A.9: *F9$^{(\alpha-/-)}$ cell aggregates response to increasing (A and C) and decreasing (B and D) ire strain for a 0.001 s^{-1} shear rate when treated with 1 µM nocodazole.*

IV. Creep experiments: Single power law failure

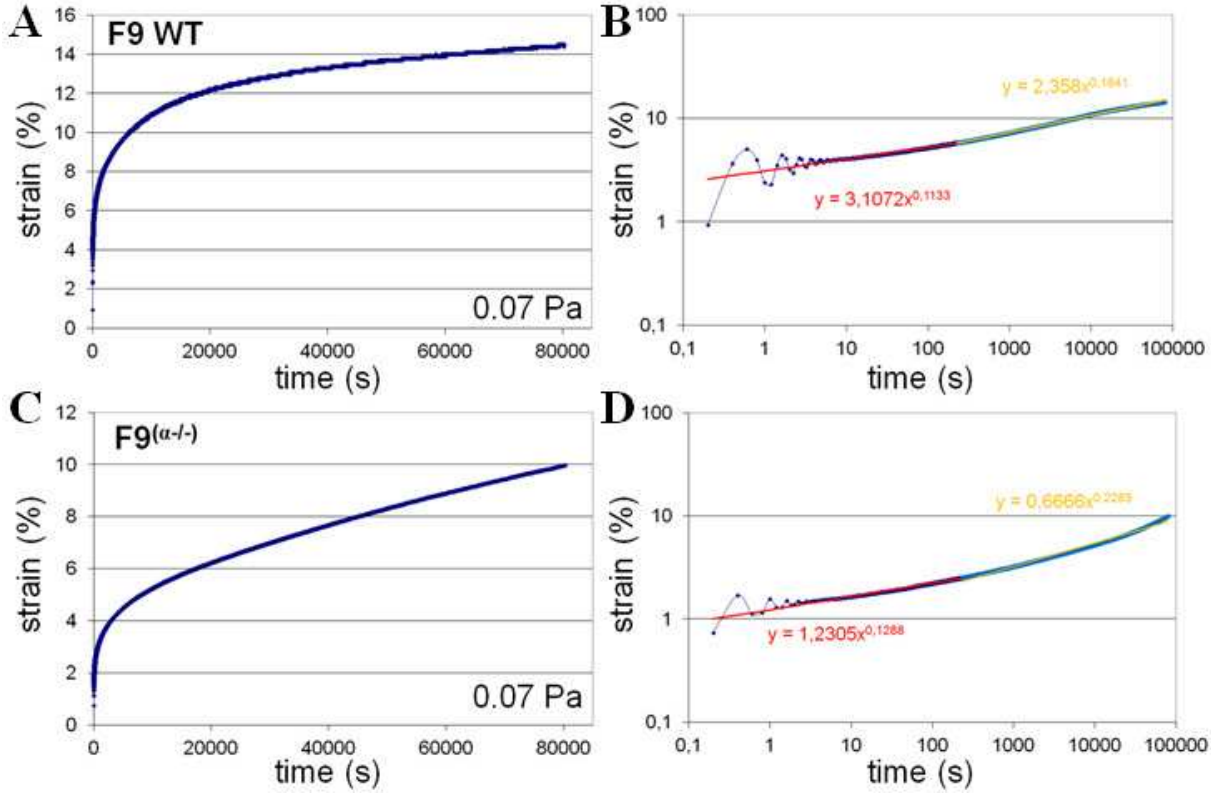

Fig. A.10: *Log-log graphical representation of deformation as a function of time during a shear pulse.*

V. Carbopol 1% preparation protocol

The preparation of Carbopol is a quite easy procedure. A few steps are to be followed:

- weigh the Carbopol one wants to dissolve;
- dissolve the Carbopol in pure water at 50 °C;
- allow the solution to be stirred for 30 minutes;
- let it cool down at ambient temperature;
- determine the pH (acid pH expected);
- while under stirring, add a few drops of until raising the pH up to about 7;
- retrieve the gel in tubes (note date, components, concentration, pH);
- centrifuge at 2500 rpm for 10 minutes;
- refrigerate until used.

Note: If a large volume (usually 50 ml) of Carbopol is prepared for several experiments, centrifugation before each use is necessary in order to remove the possible entrapped air bubbles.